EPFL

# Concrete cancer : characterization of Alkali Silica Reaction early stage products by electron microscopy

Solène Anne-Lise
ALBINSKI, née Barbotin

École
polytechnique
fédérale
de Lausanne

2022

A ma chère famille

« Je bénirai le Seigneur en tout temps,
sa louange sans cesse en ma bouche »
*Psaume 34, 2*

# Remerciements

Un immense merci à vous Lidia et Tiphaine, pour votre chère amitié et votre soutien moral, à tous les niveaux. Vous savez à quel point c'est précieux. Sans oublier les partages enfants qui ont rythmé nos conversations plus ou moins sérieuses. Une bouffée d'air frais au milieu de toutes nos obligations !

Cette thèse doit tout à ma chère famille. A mes frères, Pierre-Yves et Yann, qui m'avez montré le chemin de l'excellence par votre propre parcours. Merci pour tous les bons moments passés ensembles. Yann, tu as tracé la voie en effectuant ton doctorat à l'EPFL, et en t'appliquant à m'expliquer maintes choses scientifiques (ça a porté du fruit ☺). Que de souvenirs ! Merci à Marie, valeur ajoutée de notre famille, qui apporte une bouffée d'air frais non scientifique et féminine, à mon filleul Paul, mes neveux et nièces Benoît, Syméon, Jeanne et Madeleine, pour votre entrain votre joie et tous les jeux que nous avons faits ensemble. A mes parents pour leur soutien indéfectible dans les bons et les mauvais moments, par votre amour et votre éducation vous avez fait de moi ce que je suis aujourd'hui, et j'en suis fière ! Et votre soutien ne s'arrête pas là, vous vous êtes tellement bien occupés de Joseph (et moi-même..!) pour que je puisse venir à bout de cette thèse. Merci du fond du cœur.

Et enfin que serait ce doctorat sans toi cher Matthias (5 ans aussi, et bien plus à venir !), et sans mon Joseph chéri ? Probablement plus complet, plus parfait. L'écriture de cette thèse aurait sûrement été plus facile, mais aussi tellement plus fade…la vie serait tellement moins belle sans vous. Merci d'être là ! Et merci bout de chou de t'être accroché jusqu'à la fin de la thèse ☺

Lausanne, le 10 mars 2022.

# Abstract

Concrete deterioration is a natural process, which has to be carefully monitored over the service life of a structure. The Alkali-Silica Reaction (ASR) is a slow-process degradation, which develops over decades and is therefore difficult to predict. Since its recognition 80 years ago, progress in understanding the fundamental mechanisms has been limited due to many parameters involved in the product formation, and the difficulty to isolate and test them separately. Such parameters include the concentrations of chemical elements in solution, the temperature and the water supply, which can evolve with time.

This thesis focuses on characterizing the initial stages of ASR, in different conditions. First, early-stage products from OPC concrete in standard accelerated conditions are analysed. The existence of two different ASR products was found. One has a granular morphology with an amorphous structure, and the second has a platey morphology with a partially crystalline structure. Both products show similar chemical compositions. Such a study at the nanometer scale was made possible using powerful microscopy techniques which are Scanning Electron Microscopy (SEM) to localize the area of interest, Focused Ion Beam (FIB) to prepare ultra-thin lamellae that can be studied in Transmission Electron Microscopy (TEM) in Scanning mode (STEM) to carry out Energy Dispersive X-ray (EDX) measurements and calculate the compositions, coupled with Selected Area Electron Diffraction (SAED) to analyse the structure.

Besides the first analyses, the influence of three parameters was tested. The temperature in the standard accelerated conditions, were lowered from 60°C to a more field realistic one of 38°C, to evaluate the impact on ASR product characteristics. At 38°C, only amorphous product was found, with different compositions, presumably due to the mixed analysis of a precursor form of the final ASR product (observable at low temperature) and the ASR product itself. In a second experiment, Supplementary Cementitious Materials (SCM) (fly ash and calcined clay), which are known to hinder concrete expansion, have been used as a partial replacement of OPC in the concrete mix. SCM showed no expansion in the first accelerated months, and rare occurrences of ASR products were found. The product composition did not change (no aluminium uptake), although its Ca/(K+Na) ratio slightly increased in comparison to OPC samples. A third experiment studied the addition of alkali to a concrete mix containing calcined clays. No major change was observed in the early stage ASR product formation, despite the fact the product was more easily found in the sample.

Finally, samples from the field and from synthetic production were also analysed. The comparison between field results and accelerated results was necessary to 1) validate the relevance of the accelerated tests and 2) evaluate the differences between early-stage and late-stage products found after the expansion and structure cracking has occurred. They were found to be similar in morphology (granular and platey), composition and structure, the field samples exhibiting an overall stronger crystalline state. The synthetic samples showed a similar morphology and composition but with mainly nanocrystalline to crystalline structure. The comparison validated the relevance and similarity with field and accelerated products. It is advised to focus in the future on amorphous to slightly nanocrystalline products, in order to investigate the expansion mechanism due to ASR formation.

# Keywords

Alkali-Silica Reaction, ASR, early-stage, electron microscopy, characterization, morphology, composition, structure, FIB, TEM

# Résumé

La détérioration du béton est un processus naturel, qui doit être soigneusement surveillé tout au long de la durée de vie d'une structure. La réaction spécifique autogène Alkali-Granulats (RAG) est un processus de dégradation lent, qui se développe sur des décennies et est donc difficile à prévoir. Depuis sa découverte 80 ans plus tôt, peu de progrès sur sa caractérisation ont été réalisés, en raison de nombreux paramètres impliqués dans la formation du produit et de la difficulté de les isoler et de les tester séparément. De tels paramètres concernent les concentrations en éléments chimiques, la température et la disponibilité en eau, qui peuvent évoluer avec le temps.

Cette thèse se concentre sur la caractérisation de la RAG au début de sa croissance, sous différentes conditions. Les produits précoces de RAG du béton contenant du ciment portland (OPC) soumis à des conditions accélérées standards sont d'abord analysés. L'existence de deux produits de RAG différents a été trouvée. L'un a une morphologie granulaire avec une structure amorphe, et le second a une morphologie lamellaire avec une structure partiellement cristalline. Les deux produits présentent des compositions similaires. Une telle étude à l'échelle du nanomètre a été rendue possible grâce à de puissantes techniques de microscopie que sont la microscopie électronique à balayage (MEB) pour localiser la zone d'intérêt, le faisceau d'ions focalisé (FIB) pour préparer des lamelles de béton ultra-minces qui peuvent être étudiées en transmission (résultats plus précis) et la microscopie électronique à transmission (MET) en mode de balayage (MEBT) pour effectuer des mesures par rayons X à dispersion d'énergie (EDX) et calculer les compositions, couplées à la diffraction électronique de zone sélectionnée (SAED) pour analyser la structure.

Outre la première analyse, l'influence de trois paramètres a été testée. Dans une première expérience, la température dans les conditions accélérées standard, a été abaissée de 60 ° C à une température plus réaliste de 38 ° C, pour évaluer son impact sur les caractéristiques des produits RAG. A 38°C, seul un produit amorphe a été trouvé, avec des compositions différentes, vraisemblablement du fait de l'analyse conjointe d'une forme précurseur du produit ASR final (observable à basse température) et du produit RAG lui-même. Dans une deuxième expérience, des matériaux cimentaires supplémentaires (MCS) (cendres volantes et argile calcinée), connus pour entraver l'expansion du béton dûe à la RAG, ont été utilisés en remplacement partiel des OPC dans le mélange de béton. Les MCS n'ont montré aucune expansion au cours des premiers mois accélérés, et de rares occurrences de produits RAG ont été trouvées. La composition du produit n'a globalement pas changé (pas d'absorption d'aluminium), bien que son rapport Ca / (K + Na) ait légèrement augmenté par rapport aux échantillons OPC. Une troisième expérience a étudié l'ajout d'alcalins à un mélange de béton contenant des argiles calcinées. Aucun changement majeur n'a été observé dans la formation du produit à stade précoce de la RAG, malgré le fait que le produit a été plus facilement trouvé dans l'échantillon.

Enfin, des échantillons de terrain et des produits synthétiques ont également été analysés. La comparaison entre les résultats de terrain et les résultats accélérés était nécessaire pour 1) valider la pertinence des essais accélérés et 2) évaluer les différences entre les produits de stade précoce et de stade avancé, trouvés après l'expansion et la fissuration de la structure. Ils se sont avérés similaires en termes de morphologie (granulaire

et en plaques), de composition et de structure, les échantillons de terrain présentant un état cristallin globalement plus prononcé. Les échantillons synthétiques ont montré une morphologie et une composition similaires mais avec une structure principalement nanocristalline à cristalline. La comparaison a validé leur pertinence et leur similitude avec les produits de terrain et accélérés, avec le conseil de se concentrer à l'avenir sur la formation des produits amorphes à légèrement nanocristallins, afin d'approfondir nos connaissances sur le mécanisme d'expansion dû à la RAG.

## Mots-clés

Réaction Alkali-Silice, RAG, stade précoce, microscopie électronique, caractérisation, morphologie, composition, structure, FIB, MET.

# Contents

# List of Figures

# List of Tables

# List of Equations

# Glossary

## Abbreviations of materials and phases

ASR : Alkali Silica Reaction

OPC : Ordinary Portland Cement

SCM : Supplementary Cementitious Material

LC3 : Limestone Calcined Clay Cement

MK : metakaolin

C-S-H : Calcium Silicate Hydrate

AFm : $Al_2O_3 \cdot Fe_2O_3 \cdot$ mono (OH, $SO_3$ or $CO_3$)

## Abbreviations of techniques

SEM : Scanning Electron Microscopy

EDS : Energy Dispersive X-Ray Spectroscopy

FIB : Focused Ion Beam

TEM : Transmission Electron Microscopy

STEM : Scanning Transmission Electron Microscopy

SAED : Selected Area Electron Diffraction

XRF : X-Ray Fluorescence

## Miscellaneous

w/c : Water to Cement ratio

w/s : Water to Solid ratio

RH : Relative Humidity

LOI : Loss On Ignition

# Chapter 1    Introduction

## 1.1    Preamble

The durability of concrete structures is an always critical and outstanding topic, since it can lead to major safety issues as well as high maintenance costs. Recent examples of failure, such as the Morandi bridge collapse in August 2018 in Genoa, Italy, proves our inadequacy in the face of these issues. In most cases, failure is a combination of problems [1], bringing together the loss of performance due to the age of the structure and environmental conditions, the increased traffic load, as well as human error (in design, construction, maintenance, risk assessment, etc.). Fortunately, such problems very rarely occur, due to effective monitoring, and once the complications are identified, repairs can be carried out. However, maintenance of massive structures like bridges or dams is extremely expensive and time consuming. Therefore, a great effort is currently being made worldwide to more fundamentally understand the causes of the deterioration of concrete in the long term, and improve its durability as much as possible.

The most familiar durability issues emerging in concrete service life are the corrosion of embedded steel, deterioration due to freezing and thawing, chemical attack and alkali-silica reactivity. In this study, the specific case of the alkali-silica reaction, also commonly known as concrete cancer, is addressed.

Alkali-Silica Reaction (ASR) is an endogenous chemical reaction occurring in concrete material. It is one of the most important degradation mechanisms affecting concrete structures [2][3]. As mentioned in numerous books and publications, three conditions (Figure 1.1) are necessary for the ASR to occur :

- presence of reactive silica, originating from aggregates.

- presence of water or moisture, mainly from the concrete pore solution, but also from external water supply during the structures life.

- alkali ions, primarily originating from the cement.
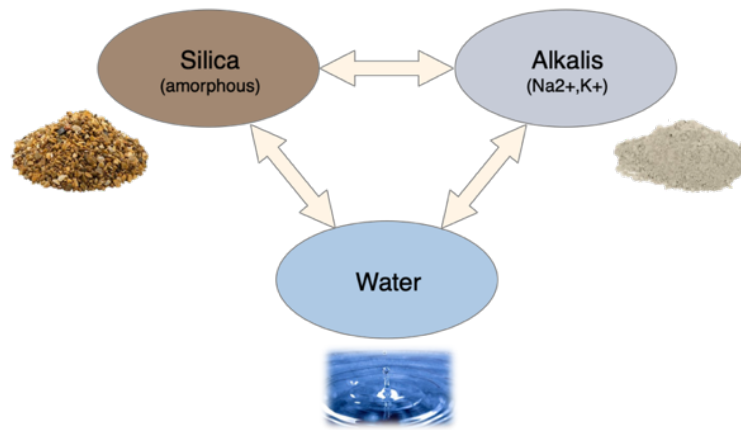
Figure 1.1 : Condition and raw materials needed for the formation of ASR product.

The reaction can be summarized as follows : hydroxyl ions in the pore solution first dissolve the siliceous minerals from the aggregates. The dissolved silica compounds then further react with the alkalis from the pore solution. Due to water uptake during the reaction, the newly formed products expand, leading to stress in the aggregates and subsequent cracking of the structure.

## 1.2    History and identification of the reaction

The first recognition of the problem emanated in the USA from Pearson as "an investigation of dangerous aggregate" as cited by [4]. Followed in the 30s an increased identification of the number of structures presenting severe cracking in the USA. In 1940, Thomas E. Stanton published studies in which he identified alkali from the paste (Na and K) reacted with the silica from the aggregates, to produce a deleterious reaction termed Alkali Silica Reaction [5][6][7]. His publications are considered as the first to recognize the nature of ASR. Concrete structures worldwide have been recognized to suffer from the formation of this deleterious product and exhibit deficiency after a few decades of service life.

In Switzerland, several hundreds of structures are affected [8] and it is a major concern in the field, especially for structures where mechanical properties and dimensions must remain stable over time, like bridges and dams.

After only a few years, signs of ASR may already be seen on the surface of built structures. An example is shown in Figure 1.2, where cracks as wide as 1mm appear. A crack at the microscopic level is also shown in Figure 1.3.

Figure 1.2 : ASR clefts (macroscopic level) in a retaining wall from Brünig area, Bern, CH.
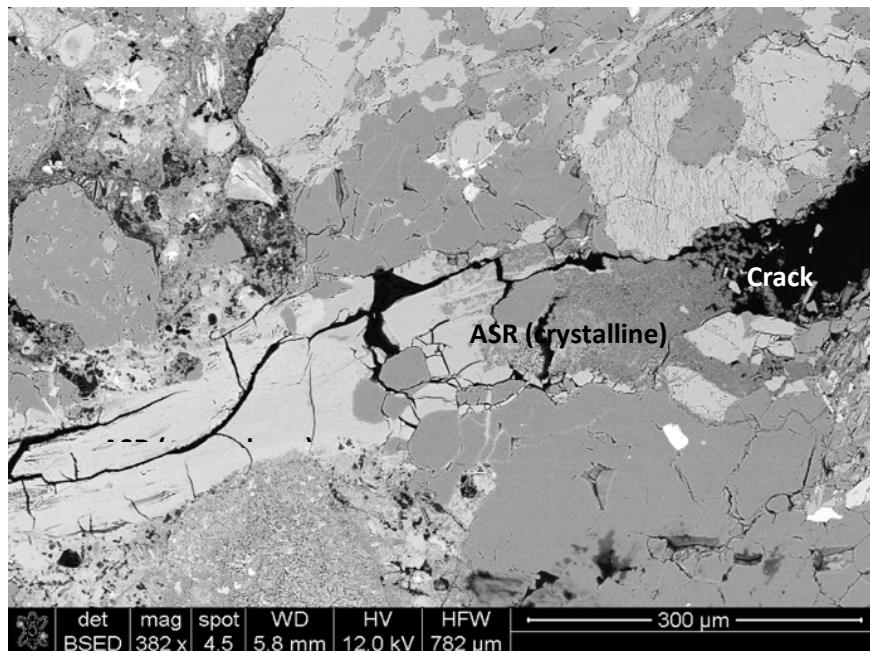


Figure 1.3 : ASR cleft (microscopic level) SEM image in a retaining wall from Brünig area, Bern, CH.

## 1.3    Motivation

As summarized in Figure 1.4, the project is motivated by the identification of a need. Structures experience degradation (Figure 1.4, Issue), and in the last 60 years, knowledge about the ASR product formation has progressed, specifically concerning the late stage product formation. We are able to partially characterize the product formation once damages occurred (Figure 1.4, Available knowledge). Despite abundant research on the product, information is missing, specially about the early stage ASR formation. Is the product forming before the expansion is measurable, similar to the one which has aged? (Figure 1.4, Missing information). A new methodology using diverse electron microscopy techniques has been set up to obtain qualitative and quantitative results about it (Figure 1.4, Results) and will bring information for the modelling part and help designing solutions for future use (Figure 1.4, Input).  The steps are described more in depth in the following paragraphs.
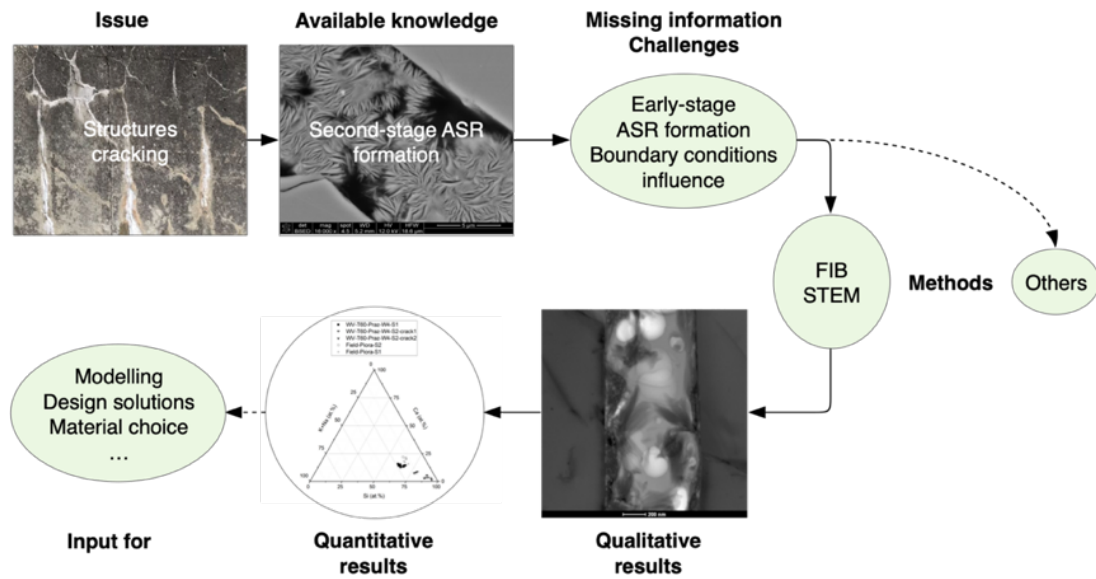
Figure 1.4 : Summary of the project structure, from the statement of the problem to the future input of the research.

**Issue**

A preliminary survey indicated that in Switzerland, more than 400 structures are affected by ASR [8]. Some structures like dams are of critical interest. In Switzerland, they were presumed to be built with non-reactive aggregates, but as they grew older and older, expansion and cracking was noticed. It is estimated that 20-30% of swiss dams are now affected [9]. There is no possibility to stop expansion, and repair of such massive structures is very expensive, rehabilitation techniques consisting of cutting slots along the dam to release stress. There is thus a great need of improving our knowledge about ASR formation in order to prevent it.

**Available knowledge and challenges**

Despite abundant research about ASR products in the past 80 years, the intricacy of the process, its sluggish kinetics, and the heterogeneous nature of concrete mean that the cause of deterioration (particularly swelling) is still contested today. Over the years, several facts and theories have been offered concerning the chemistry of the reaction [10][11][12][13][14], the reaction products main components (Si, K, Na and Ca) and structures [15][16][17][18][19][20][21][22][23] and the mechanisms of expansion [24][25][11][13][26][27][28][29]. They lay the foundation for future research but no mechanism has been shown to be more plausible than the others so far. In addition, ASR rheology, Ca effect, mineral phases dissolution and reaction, the effect of Al for example, are nowadays investigated and debated. It is still difficult to determine if a given aggregate-cement combination will be reactive or not due to the very slow nature of the reaction. The swiss geology is an issue concerning ASR formation as it is made of minerals which are vulnerable to ASR : around 90% of the aggregates were classified as potentially reactive by [9].

A more detailed review of our current knowledge of the reaction will be given in chapter 2.

**Methods and results**

In the light of these statements, it is clear that a more fundamental understanding of the reaction itself is needed and new research aspects should be explored, to find solution to concrete structure failure. The combined use of FIB and STEM to analyse the morphology, composition and structure of the product was successful in generating qualitative and quantitative data.

**Input**

This project is included in a larger project dedicated to ASR investigations, funded by a Swiss National Foundation (SNF) Sinergia project. It is a collaboration between laboratories from EMPA Dübendorf, PSI, and EPFL. It is the subproject n°2 of 6, as in Figure 1.5. The collaboration brings competences from several research fields, to establish a link between chemistry and mechanics, from nano to microscale, and provide the understanding and modelling input needed to design ASR-resistant concrete structures even when the local available aggregates known to be reactive must be used.
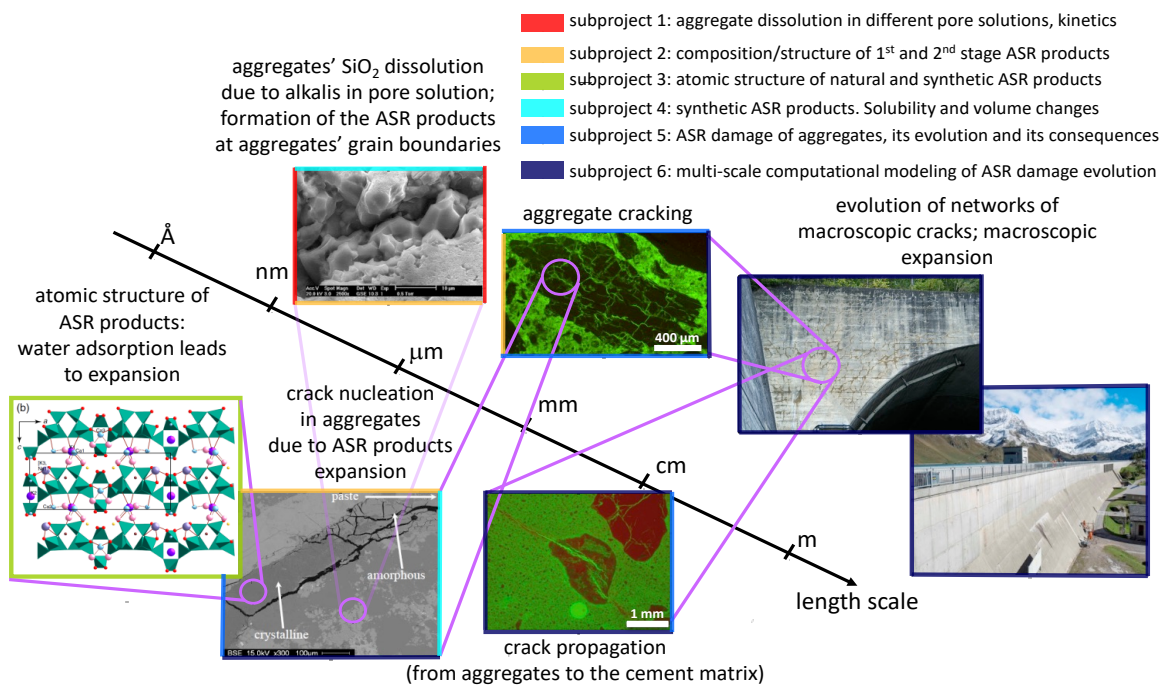


Figure 1.5 : Overview of the aspects of ASR studied within the proposed Sinergia project considering the different length scales.

## 1.4    Objectives of the thesis

The aim of this project is to understand the mechanisms that control the early stage formation of ASR product in concrete. Such knowledge should bring a significant contribution to reducing or even preventing the reaction and subsequent damages in concrete. This early stage product has not been studied so far, and only the larger deposits of products have been characterised, due to their greater availability and volume. Indeed, the small volumes of early stage product available made its analysis difficult with classical techniques like SEM-EDX.

From the second-stage product analysis, as exposed in section 3.2, it is clear that boundary conditions such as available chemical species, temperature and time have an impact on the product formation.

Based on these findings and on the motivation facts exposed above, the following questions set the stage for the thesis :

- What is the product morphology, composition and structure at the very beginning of the reaction?
- What are the differences between the early-stage and late-stage product ?
- What is the influence of boundary conditions and addition of Supplementary Cementitious Materials (SCM) on composition and structure of the initial product?

To reach our objectives, lamellae of the region of interest were cut using a FIB, and TEM analysis was accomplished to assess the morphology and the chemical composition as analysed by EDX. Selected Area Electron Diffraction (SAED) provided information about the crystal structure of the initial product that forms within aggregates, under different boundary conditions.

## 1.5    Research approach and structure of the thesis

**Chapter 1** describes the basics and history of ASR recognition, exposes the motivation and the objectives of the thesis.

**Chapter 2** is a non-exhaustive literature review. It outlines the most recognized models and controversial points, explaining the formation principles of ASR products and its possible expansion mechanisms.

**Chapter 3** is a published paper, which presents the materials needed to conduct the experiments and the method that has been implemented to observe the early stage ASR product. It provides the steps from the SEM observation, the FIB cutting and the TEM/STEM analysis as in Figure 1.6.
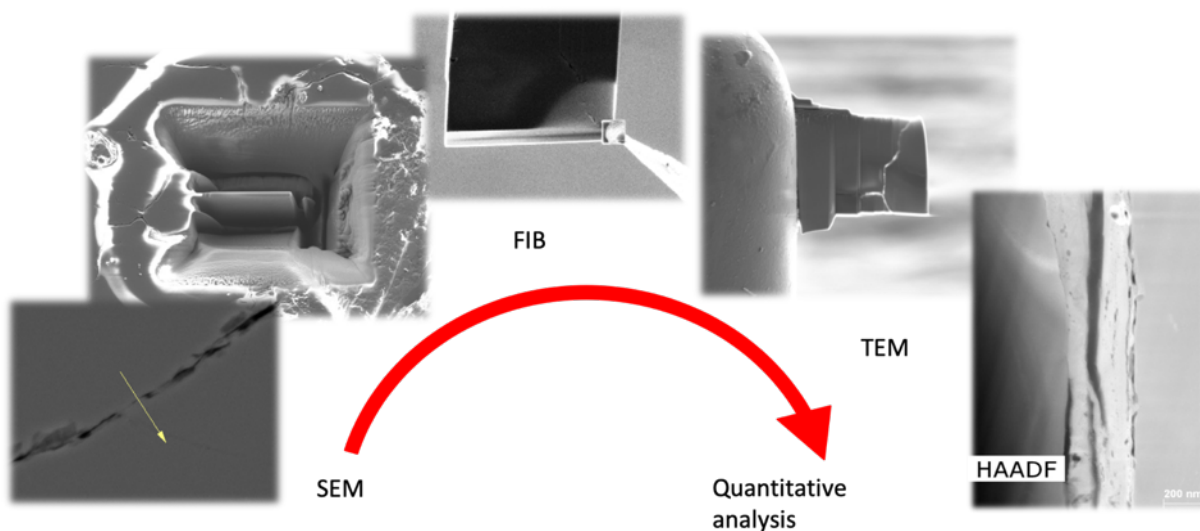


Figure 1.6 : Sample preparation process: localization of an ASR filled crack in SEM, followed by extraction of the product in the form of a thin lamella with FIB for further analysis in the TEM.

The following four chapters present the results and concentrate on assessing the chemical composition and structure of ASR initial product by Transmission Electron Microscopy (TEM). Three different types of samples were studied : samples from accelerated testing conditions in the lab, from the field and from synthetic ASR production.

**Chapter 4** concerns the characterization of ASR early stage products morphology, composition and structure in accelerated laboratory concrete specimens. These specimens are stored according to the swiss standard accelerated process, in water vapour and at 60°C. Composition is analysed by EDX, and structure by Selected Area Electron Diffraction (SAED).

**Chapter 5** is a continuity of the early stage product characterization, in accelerated specimen under more field realistic conditions. Boundary conditions like temperature are estimated to have an impact on the product formation and thus samples are stored at 38°C, either in water vapour or in pore solution to avoid alkali leaching. The difference between the products are evaluated.

**Chapter 6** looks at the effect of SCM addition (calcined clay and fly ash) on the early stage product formation. SCM addition is known to considerably delay and hinder ASR formation, probably due to the presence of aluminium. The effect and interaction of aluminium with the ASR product features is investigated.

**Chapter 7** reports the results of ASR characterization in field samples and additional synthetic products. The field early stage results are compared with the accelerated ones assess the similarity and differences between them. The same comparison is done with the synthetic samples to ensure the transferability of the results. This validation is important, since synthetic samples can be much more easily observed, with a greater variety of techniques.

**Chapter 8** is the concluding chapter. It summarizes the main findings and achievements of the work, the remaining open questions and the perspectives of the future work.

# Chapter 2    Alkali-Silica        Reaction        : controversial points and review of models

## 2.1    Introduction

There is a profusion of results on ASR product characterization. Despite the abundant research on the product, its occurrence under various conditions, environment, mixes and forms, there is no general agreement on the development of the reaction. The ASR product is commonly supposed to swell and generate stress in the aggregates, further leading in most cases to expansion and cracking of the structure. However, it was reported that in some cases the ASR product did not lead to expansion [20]. It seems that significant expansion only occurred with sufficient availability of calcium. However, the precise role of calcium is still not fully understood and a large number of mechanisms have been proposed [10][30][31][32][33][34][29][35][36] [28][37][2][38][39][40].

In this chapter, we will highlight some of the most controversial points and most common models concerning the chemistry of the reaction and the mechanism of expansion, which the work in this thesis seeks to clarify. For a more exhaustive review of the past ASR literature, two complete reviews about the ASR mechanisms and general overview of the reaction are given by Rajabipour et al [41] and Figueira et al [42].

## 2.2    Surface alteration vs. dissolution

Since the 50s, many models about the chemistry of ASR and its expansion have emerged and laid the foundations for understanding these mechanisms [43][11][30][34][36][44][12]. The models are similar with some variation about the calcium involvement and the mechanism of expansion.

First thing to consider is the question of surface alteration versus dissolution. The earliest papers on ASR discussed about the breakdown of silanol bonds and the incorporation of alkalis in those structures, with or without calcium contribution [11][13][34]. Such mechanisms are often mistakenly termed as dissolution, but rather demonstrate a solid-state process. So, following this, several authors have implicitly assumed that the process of gel formation is a solid-state transformation from a glassy network to a network incorporating alkali ions which then imbibes water and swells. On the other hand we know that in the alkaline solution these silicate minerals do completely dissolve [45], and it seems many ASR products are structurally distinct from the original aggregates implying that their formation is governed by a dissolution-precipitation process through solution [36][44][39][40].

The major question is to what extent is the swelling coming from an altered surface layer and to what extent is it coming from products precipitating through solution which then cause swelling ?

## 2.2.1 Surface alteration

Amorphous or crystalline $SiO_2$ present in the aggregates is altered in the presence of hydroxyl ions present in the pore solution (pH between 13.0-13.5). In a more detailed context, $OH^-$ ions hydrolyse the siloxane bonds and neutralise the silanol groups ($\equiv$Si-OH) according to Equation 2.1 and 2.2 respectively. Then, the positive alkali ions in the pore solution are attracted by the negatively charged ions Si-O$^-$ as described by Equation 2.3 and seen in Figure 2.1. This model is stated by Dent-Glasser and Kataoka [11] :

Rupture of siloxane bonds through hydroxyl attack

$$\equiv\text{Si-O-Si}\equiv + \text{OH}^- \rightarrow \equiv\text{Si-OH} + \text{Si-O}^- \qquad \text{Equation 2.1}$$
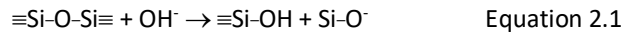
Reaction of the silanol groups on silica surface with the hydroxyl ions of the solution

$$\equiv\text{Si-OH} + \text{OH}^- \rightarrow \text{Si-O}^- + \text{H}_2\text{O} \qquad \text{Equation 2.2}$$
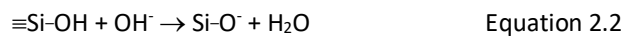
Neutralization of the negative charges on the silica surface by the alkali

$$\equiv\text{Si-O}^- + \text{Na}^+ \rightarrow \equiv\text{Si-O}\cdots\text{Na} \qquad \text{Equation 2.3}$$
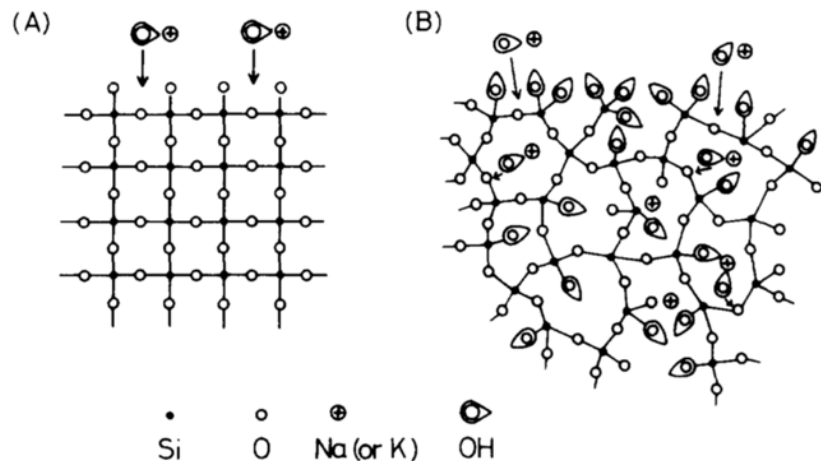


Figure 2.1 : Scheme of the attack of the silicate structure by hydroxyls and alkali ions according to [11]

The first steps of the reactions in Equation 2.1 and 2.2 are well described and are a base for most of the further developed models. We can clearly see here that the alkali (sodium in equation 2.3, but can also be potassium in real systems) penetrate the silicate structure, without dissolution of the silicates in the pore solution. In this case, there is no intervention of the calcium ions along with the alkali, but it involves a similar mechanism with partial replacement of the alkali by calcium ions and will be seen in the subsection 2.3.

## 2.2.2 Dissolution

The full mechanism of silica dissolution is somehow a continuity of the surface alteration model presented above. Dron et al. proposed a model including the dissolution step in the process of ASR formation [36][44]. The silicates resulting from the breaking of siloxane bonds by the alkali end up in solution as ionic silicates in monomeric or polymeric form. These ionic silicates, due to the alkaline hydroxide rich pore solution, will

precipitate with alkali or calcium. Such a mechanism has been more recently supported by Shi et al. [46][47] and Geng et al. [48].

The dissolution step is most of the time implicitly present but has been rarely measured and clearly stated.

## 2.3    The role of calcium

The second point of debate is the role of calcium. Many studies assumed that first of all the product is purely an alkali silica product [11][31][49][50][51]. Nowadays many authors say that there is first formation of an alkali silica product which then reacts with calcium (all other papers). The incorporation of calcium has often been implicated to have a big impact on the product rheology, increasing its viscosity [52]. Vayghan et al. observed that an increase of the Ca/Si ratio shortens significantly the gelation time, while an increase in the Na/Si ratio moderately lengthens it [53]. The rheological properties of ASR gel have not been much studied. Some people have said that alkali silica gels have a low viscosity (very fluid), they flow and with increasing absorption of calcium they stop flowing due to high viscosity [31][43][34]. For example, alkali silicates are formed within the aggregates and then on the outside of the aggregate there is calcium enrichment which blocks the diffusion of the silicate species [54], leading to expansion [55][12][35].

A more clearly established point is that there is a transition from alkali silica products to C-S-H particularly in terms of microstructural observations. Several studies report the presence of ASR products in the aggregates with a calcium gradient increasing towards the cement paste [56][17][22] and then C-S-H in the vein continuity, outside the aggregate [57][47][21]. However the third point which is worth noting, is that all reported analysis of alkali silica products in real structures actually find that there is always calcium as well as alkali [22][18][58][59]. Therefore, a major question is if calcium is always there in the beginning or if it is only there later. Finally, does the (K+Na)/Ca ratio change with time ?

### 2.3.1   Reaction involving calcium ions

The model involving calcium ions generally agrees with the stages presented in 2.2.1, where the dissolution of the silica is initiated by the hydroxide ions and the silica then bonds with the alkali. It is estimated incomplete and that in addition to the alkali, the calcium ions play a role in the product formation. Thomas et al. [38] state that « a number of experimental studies have concluded that significant expansion only occurs when an adequate supply of calcium is available as calcium hydroxide [$Ca(OH)_2$]. In systems with abundant alkali hydroxides and reactive silica, but no calcium hydroxide, silica dissolves and remains in solution. » Equation 2.3 from 2.2.1 is thus generalized as Equation 2.4 (M+ being the alkali Na+ or K+) and completed by Equation 2.5 :

$$\equiv Si–O^- + M^+ \rightarrow \equiv Si–O \cdots M \qquad\qquad \text{Equation 2.4}$$

$$2\equiv Si–O^- + Ca^{2+} \rightarrow \equiv Si–O \cdots Ca \cdots O– Si\equiv \qquad\qquad \text{Equation 2.5}$$
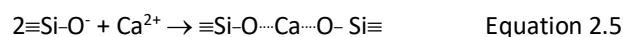
### 2.3.2   Origin of the calcium ions

Most of the calcium ions available in the pore solution come from the dissolution of portlandite. This dissolution mechanism was reported by Wang and Gillott [34] to release OH- ions, which thus influence the

silica dissolution. When there is saturation of calcium ions though, the silica dissolution rate is reported to be reduced due to the formation of a strongly bonded CSH layer [60]. So high calcium ions concentration is reported to lead to two mechanisms :

- Prevention of the diffusion of silicates [30]
- Preferential formation of C-S-H over ASR [61][62][63][64][65][39]

The dissolution of portlandite and thus the concentration of calcium ions present in the concrete pore solution is dependent on the pH of the latter, and so its concentration in alkali ions. In a highly alkaline medium (pH > 13), the calcium ions concentration is low, as measured by Wang and Gillott (Figure 2.2) and Duchesne et al. [66].
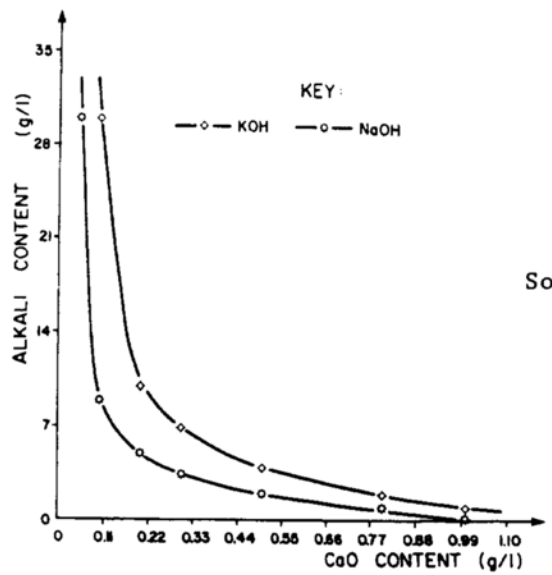


Figure 2.2 : Calcium solubility curve depending on the alkali content in the pore solution [34]

## 2.3.3    Alkali recycling

Calcium ions are also proposed to favour alkali recycling [67][68][69]. Indeed, the calcium ions, which are available in the pore solution, partially substitute the alkali in the formed silico-alkali products as seen in Figure 2.3. The released alkali are available for further penetration in the silica structure and the mechanism stated in 2.2.1 by Equation 2.1, 2.2 and 2.3 can go on.
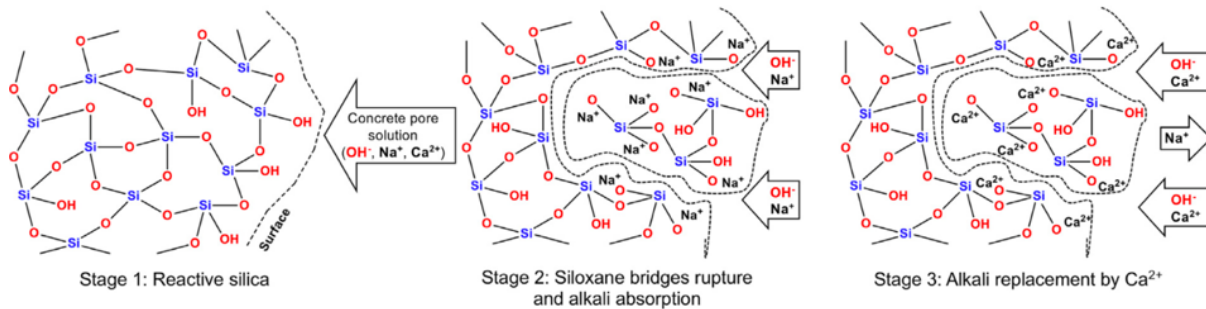


Figure 2.3 : Alkali recycling process due to replacement with calcium from [42]

## 2.4    Common models of the expansion mechanism

The third point of debate of this chapter, concerns the actual expansion mechanism, for which there is no complete explanation.

ASR product formation in general, commonly lead to cracking of the concrete structures. As described in chapter 1, the ASR product - often termed as a "gel" even though it can take both amorphous and crystalline product – forms, principally in the aggregate pre-existing cracks, grain boundaries, close from the cement interface, and at the cement/aggregate interface itself.
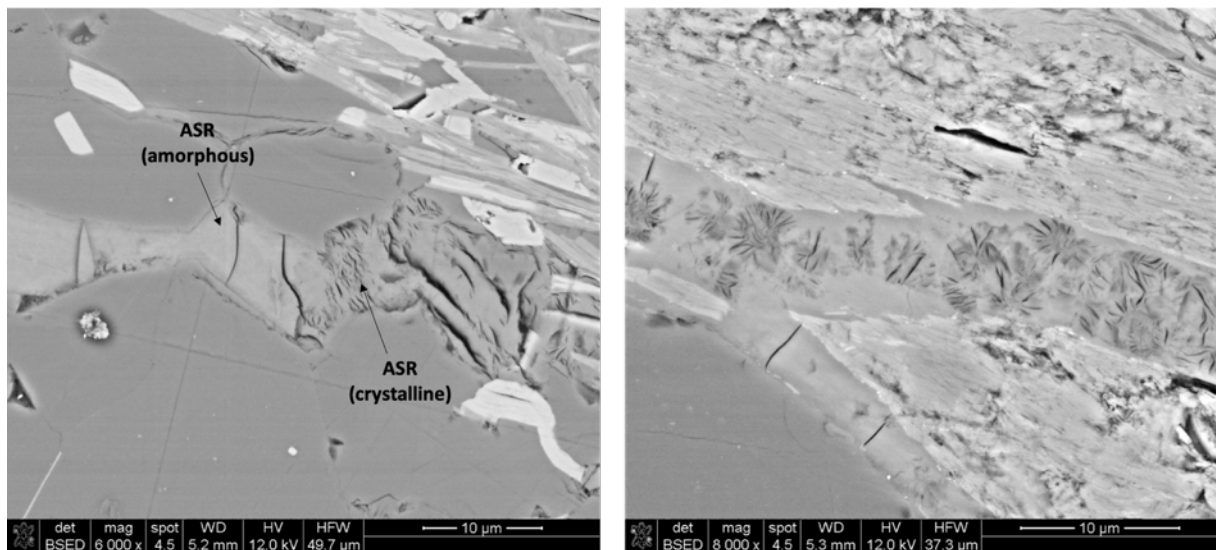


Figure 2.4 : SEM images showing two distinct ASR products morphologies and structures (smooth and amorphous vs. platey and crystalline).

Studies about the characterization of the products are numerous. They highlight the variability of the product morphology, composition and structure. With this variability comes the challenges of identifying the impact of the involved parameters. As previously exposed in subsections 2. and 3., some authors reported that silico-alkaline gels form (in contrast with silico-calco-alkaline gels) and are responsible for the swelling mechanism while others say calcium is necessary to have expansion of the gel. Calcium was also reported to be increasingly incorporated in the product, from the cement paste to the aggregate interior [56][17][22]. The role of calcium is controversial among the scientific community, and appears to be a key in understanding the expansion behaviour. As seen in Figure 2.4, the products also display different structures, amorphous and crystalline.

A review of the main theories is presented in the next sections.

### 2.4.1   Crystallization pressure

The premise of ASR products inducing a crystallization pressure responsible for expansion was highlighted by Dron et al. [14][27].

According to Riecke's principle, the growth pressure is determined not only by the interfacial tension and confinement but also by the degree of supersaturation. As stated by [70], the crystallization pressure P is

described by Riecke's law [71] as the ratio between the change in free enthalpy of the precipitation reaction ΔG and the molar volume of the precipitate formed, $V_m$ (Equation 2.6).

$$P = -\Delta G / Vm \qquad \text{Equation 2.6}$$

The sudden disruption of the metastable equilibrium that exists between the supersaturated solution of silico-alkaline entities (from aggregate dissolution) and the calcium ions (from portlandite dissolution) generates a variation in free enthalpy, which leads to the formation of silico-calco-alkaline products that cause the expansion.

Dron et al. prepared synthetic Calcium Potassium Silicate Hydrate gels (C-K-S-H) by putting reactive sand in contact with a solution containing potassium salt and calcium hydroxide particles.
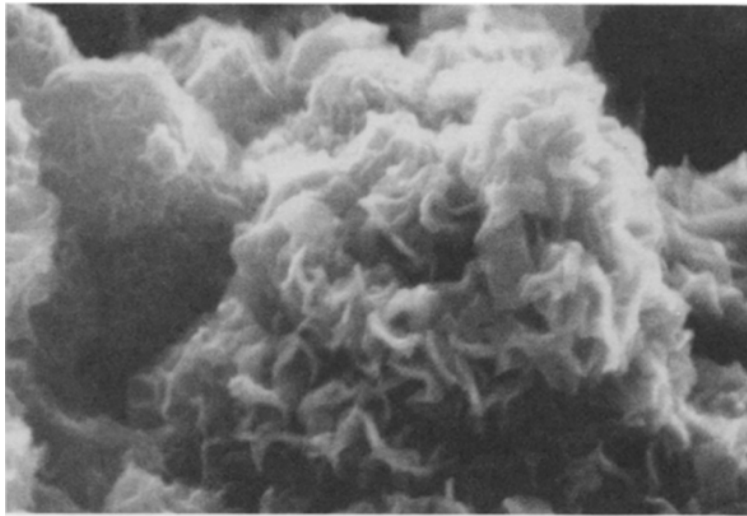


Figure 2.5 : SEM micrograph of prepared synthetic C-K-S-H [44].

The dissolution and formation kinetics were studied and it was established that the formed gel has the deleterious properties of the ASR gel. The energy for expansion does not come from the C-K-S-H product itself, but is released by the reaction of precipitation of the C-K-S-H product. Thermodynamically, the variation of the free energy causes the expansion, and the reaction is generally expressed as in Equation 2.7 :

$$(p + x)SiO_2 + Ca(OH)_2 + xK^+ + xOH^- + \left(q - \frac{3}{2}\right)H_2O \rightarrow CK_xS_{p+x}H_q \qquad \text{Equation 2.7}$$
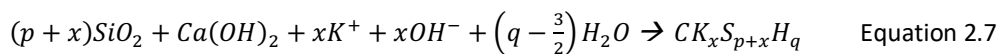
This mechanism of precipitation inducing mechanical energy release and possible expansion is still under consideration. However, when something is forming gradually particularly because the silicates have a very slow dissolution rate, it is very difficult to imagine to get conditions of supersaturation. The latter occur when a reactant is dissolving very fast and the product does not have time to relieve that crystallization pressure. An example is the sulfate attack. The pore solution is quickly saturated with sulfates which react with the alumina in the confined hydrated calcium aluminate phases, leading to ettringite or gypsum formation [72].

In addition, crystallization pressure has to be distinguished with the mechanism of crystal swelling pressure, another hypothesis which has recently been dismissed by [48][47][73].

## 2.4.2 Osmotic pressure

The model based on the swelling of ASR products due to the osmotic pressure has been extensively studied. Many authors have proposed it as the main deleterious mechanism causing expansion [67][13][11][50] [24][25]. It has been described for both types of reaction product (see 2.2.1 and 2.3.1), either silico-alkali or silico-calco-alkali gels.

As previously stated, the alkali ions react with the deprotonated silicates to form a gel. The water contained in the gel has a lower chemical potential than the water from the pore solution, due to its high ionic concentration. To reestablish equilibrium, water from the pore solution will diffuse towards the gel. This diffusion process generates pressure inside the gel network, called osmotic pressure as seen in Figure 2.6. In a confined environment like an aggregate rim or grain boundary, pressure up to 11 MPa are claimed to be possible [74]. The question remains whereas the generated pressure is enough to open up a crack, and if the tests done on synthetic samples are representative of the field.
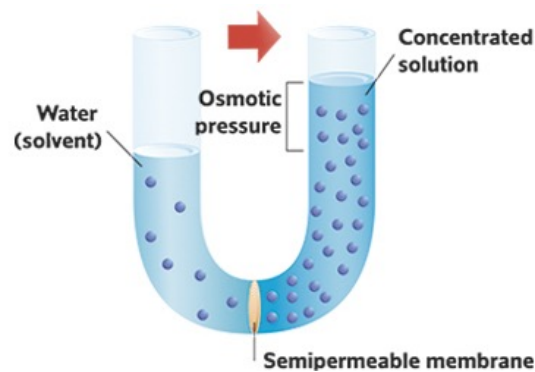


Figure 2.6 : Principle of osmosis, leading to osmotic pressure [75].

Authors like Chatterji reported that calcium is necessary for swelling to occur [30], which is in contradiction with some results [50][24][25][13]. The large number of parameters involved during the formation of the gel hinders a clear definition of the role of calcium and prevents the scientific community from reaching a consensus.

## 2.4.3 Ion diffusion

The ion diffusion mechanism is mainly introduced by Chatterji [76][26][30], but not only [77][78]. They state that the presence of calcium ions is necessary for the reaction to occur. Two scenarios then arise :

- If the alkali concentration is low, there will be precipitation of CSH and thus penetration of the rest of the ions will be limited.
- If the alkali concentration is high, there will not be precipitation of insoluble silicates and cations can penetrate in the silica grain. The calcium ions, will not penetrate so far due to their large hydrated size, and will rather precipitate with silica. It will then hinder the diffusion of the silicate ions, while more cations are diffusing in, creating an expansive force (Figure 2.7). So, it is mainly the calcium preventing the diffusion of silica away from the dissolving aggregate that is responsible for the swelling.

Figure 2.7 : A hypothetical reaction between silica, hydroxyls, alkali and calcium ions by [79]

The plausibility of this mechanism has however not been further investigated.

### 2.4.4 Electrical double layer

The electrical double layer theory was developed by Prezzi et al. [28][80] and envisions the interaction between the entities in solution like colloidal particles. The repulsive forces between these silica colloids govern the gel formation and the built pressures. This mechanism states that the silica is partially depolymerized, silicates colloidal particles are enriching the pore solution. These polymeric or monomeric units in solution presenting negative charges will be balanced by cations interactions. With the concentration increase (silica continue to dissolve and cations keep diffusing towards the attacked area), the double layer thickness will decrease as well as the repulsion forces. It is as predicted by the double layer theory, according to the Gouy Chapmann model (Figure 2.8).



$$\sigma_d = \Sigma(\sigma_{d+} + \sigma_{d-})$$

$$\sigma_o + \sigma_d = 0$$

$\sigma_o$ = Surface charge

$\sigma_d$ = Diffuse layer charge

Figure 2.8 : Model of the diffuse double layer introduced by Gouy-Chapman, from [28]

Despite the repulsive forces, due to the concentration increase and space filling mentioned before, the particles come closer and reach a point where the attractive Van der Waals forces are higher and overcome the repulsive forces. The colloidal particles agglomerate and form a gel. Due to the difference in chemical potential between the highly concentrated ionic gel and the pore solution, the gel will absorb water and expand, similarly to the osmotic pressure mechanism. This hypothesis is more related the way the gel itself is forming, rather than the mechanism of expansion.

## 2.5    Summary

There are still other models that are a little less widespread (e.g. gel dispersion [81][82]), with explanations which overlap with those presented here. Due to their similarity, they were not presented here, in order to keep some clarity on the basic mechanisms suspected of being at the origin of the expansion. A good review of those mechanisms is given in french by [70], and more generally in [41][42].

To summarize, the dual nature of the ASR product complicates our understanding of the mechanisms. They will form and respond differently in a given environment, and it is necessary to understand the characteristic behavior for each. From the above proposed mechanisms, the following statements can be retained :

Crystalline ASR product :

- Precipitation pressure could be responsible for microscopic expansion, but the required supersaturations are unlikely.
- Swelling mechanisms (in general) are not responsible for microscopic expansion.

Amorphous ASR products :

- Swelling mechanisms can be responsible for microscopic expansion.

In the light of these statements, two main modes of expansion need to be investigated : the swelling of the amorphous product and the precipitation of the crystalline product.

## 2.6    Aggregate reactivity

It is difficult to assess the reactivity of aggregates, due to the slow nature of the ASR reaction, as well as the aggregates mineral phases complexity and variety.

Cryptocrystalline or microcrystalline quartz will react more slowly than amorphous silica but can still provoke some deleterious expansion on the long term. Some mineral phases are nowadays known to be reactive, like opal, and a list has been established as seen in Table 2.1.

Table 2.1 : Reactive mineral phases or rocks and their characteristics [38] (from ACI Committee 201, 1991)

| Reactive substance (mineral) | Chemical composition | Physical character |
|---|---|---|
| Opal | $SiO_2 \cdot nH_2O$ | Amorphous |
| Chalcedony | $SiO_2$ | Microcrystalline to cryptocrystalline; commonly fibrous |
| Certain forms of quartz | $SiO_2$ | Microcrystalline to cryptocrystalline; crystalline, but intensely fractured, strained, and/or inclusion-filled |
| Cristobalite | $SiO_2$ | Crystalline |
| Tridymite | $SiO_2$ | Crystalline |
| Rhyolitic, dacitic, latitic, or andesite glass or cryptocrystalline devitrification products | Siliceous with lesser proportions of $Al_2O_3$, $Fe_2O_3$, alkaline earths and alkalis | Glass or cryptocrystalline material as the matrix of volcanic rocks or fragments in tuffs |
| Synthetic siliceous glass | Siliceous, with lesser proportions of alkalis, $Al_2O_3$, and/or other substances | Glass |

The most important deleteriously alkali-reactive rocks (that is, rocks containing excessive amounts of one or more of the substances listed above) are as follows:

| | | |
|---|---|---|
| Opaline cherts | Rhyolites and tuffs | Opaline concretions |
| Chalcedonic cherts | Dacites and tuffs | Fractured, strained, and limestone-filled quartz and quartzites |
| Quartzose cherts | Andesites and tuffs | |
| Siliceous limestones | Siliceous shales | |
| Siliceous dolomites | Phylites | |

NOTE: A rock may be classified as, for example "siliceous limestone," and be innocuous if its siliceous constituents are other than those indicated above.

In the case of Switzerland, mountain formation tends to produce rocks which are vulnerable to ASR, and around 90% of the aggregates were classified as potentially reactive by [9]. Rocks from the alpine region were for a long time considered as non-reactive because they mostly contained quartzite and crystalline rocks (see Figures 2.9, 2.10 and 2.11) and have been extensively used in construction. However, regions of poorly ordered material usually exist at grain boundaries and these regions are vulnerable to attack.
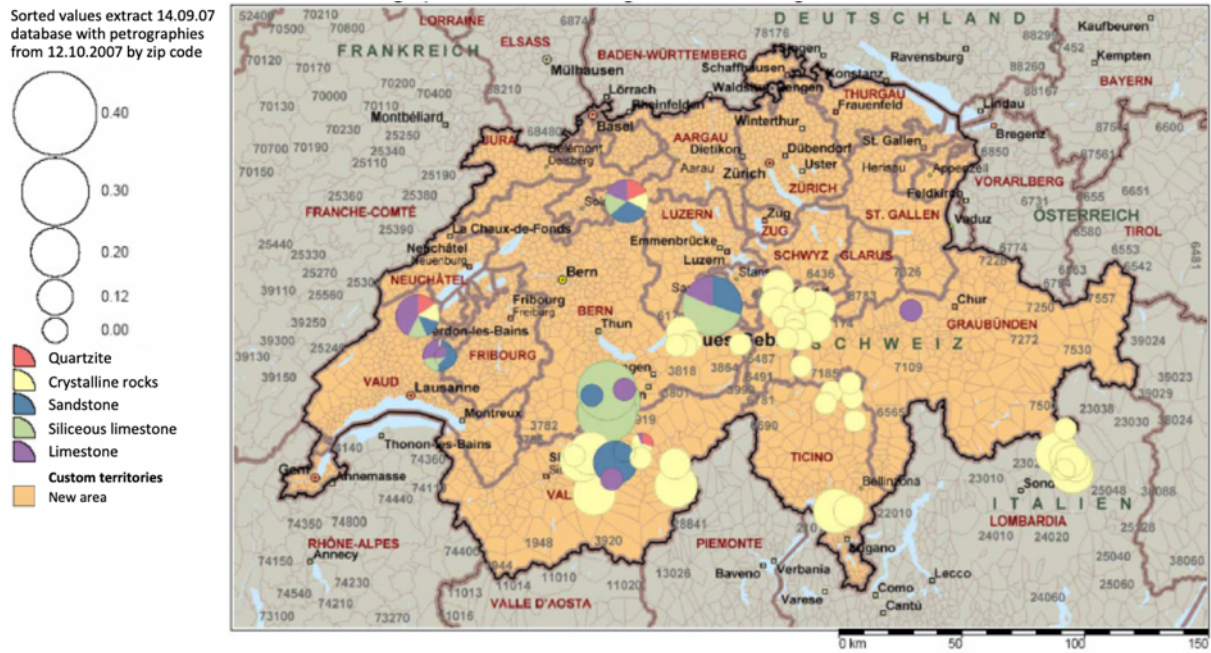
Figure 2.9 : Switzerland petrography of the 16-32 mm aggregates [9].
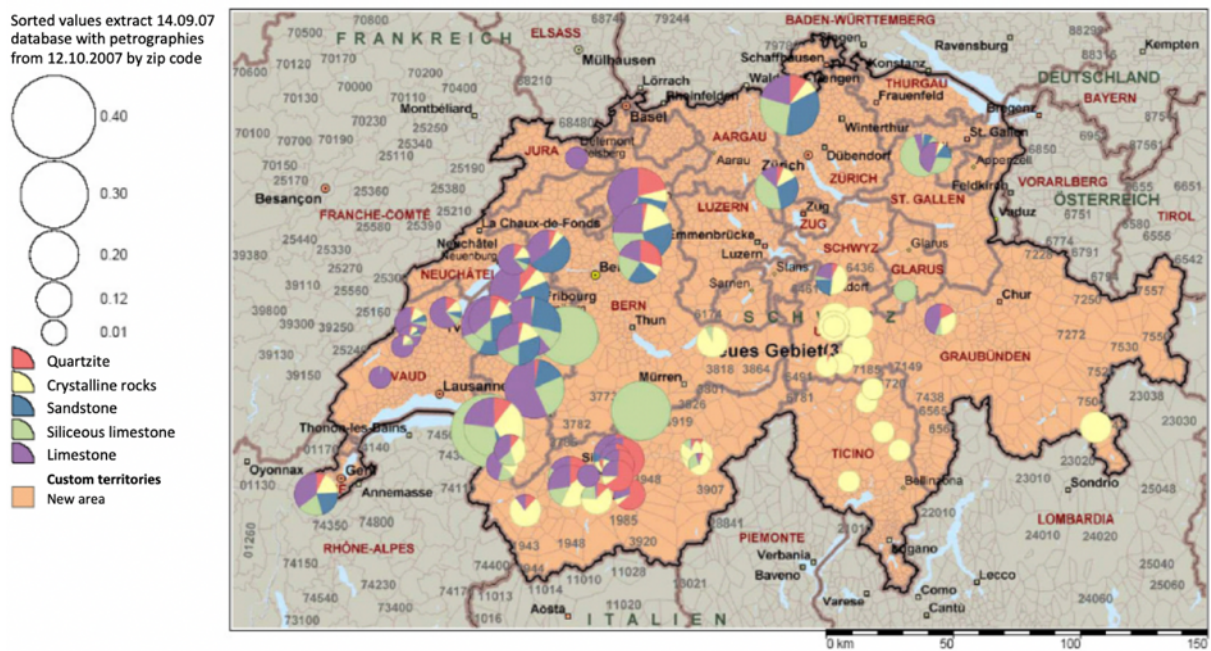


Figure 2.10 : Switzerland petrography of the 4-8 and 8-16 mm aggregates [9].
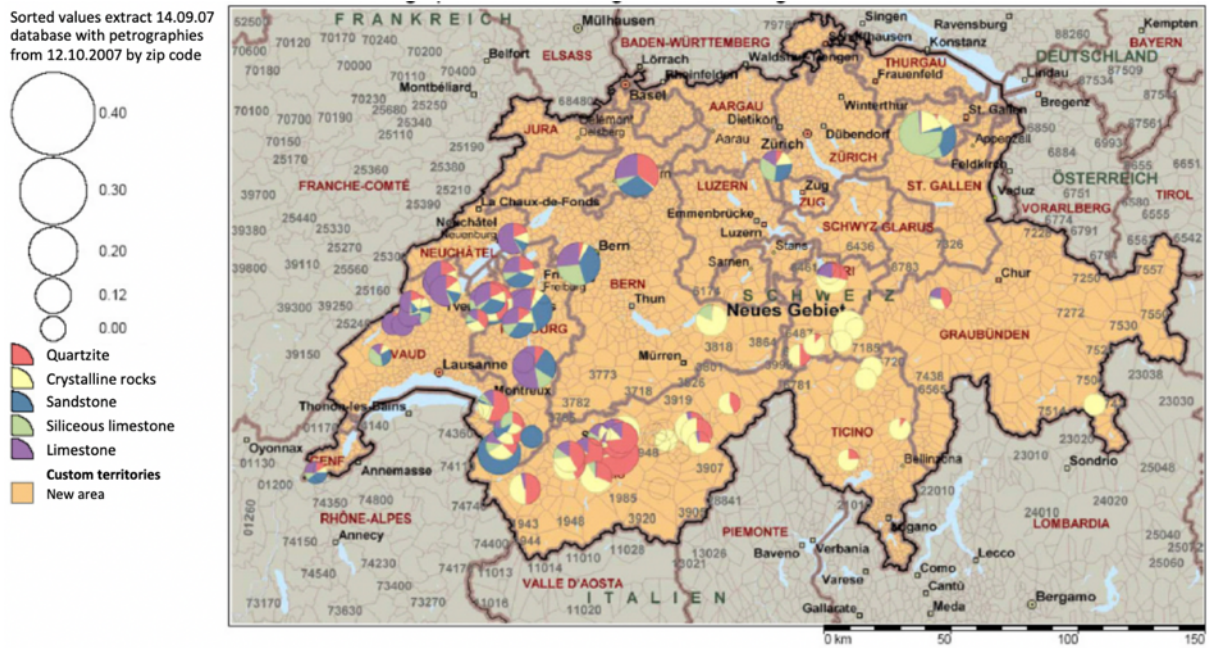
Figure 2.11 : Switzerland petrography of the 0-4 mm aggregates [9].

In the past decades, attempts to characterize aggregate reactivity, ASR products formation and expansion have been conducted in laboratories, with the use of glass as the reactive aggregate. It was from good intention, a way to simplify the model system and better understand the mechanisms. The drawback from such experiments is that glass tends to react strongly on the surface instead of cracking, and is thus not representative of the expansion mechanism leading to structures cracking on field.

Nowadays, more attempts to extend our knowledge and characterise aggregates reactivity are being conducted [83][84][85][3][21][86], with the use of real and locally available aggregates. For a question of local availability, there is a great need to characterise the reactivity of the Swiss aggregates and their mineral phases. In this thesis, early-stage ASR products characterization is not correlated to the aggregate mineralogy, but should be one of the future evaluation steps, as exposed in the perspectives (chapter 8) of the thesis.

# Chapter 3  Adaptation and development of a method to analyse the ASR early-stage product

**Note : This chapter has elements based on an article published in a peer-reviewed journal.**

*E. Boehm-Courjault, S. Barbotin, A. Leemann and K. Scrivener*

# 3.1    Introduction

ASR products have been extensively analysed once they are present in relatively large quantities in cracks > 10 μm [15][16][17][18][19][20][22]. The results often display a large panel of ASR products characteristics. ASR products mainly contains Si, Ca, K and Na, with approximate atomic ratios of 0.15–0.25 for Ca/Si and 0.20–0.35 for (Na + K)/Si (e.g. [18][20]). They also show different structures, amorphous or crystalline, as reported by authors [58][87][88][89][90][91][92]. The large analysed cracks are going through an aggregate and are also continuing in the cement paste, further connecting with other propagating cracks, forming a network. They are referred as second-stage ASR product.

However, it is not sufficient and results about the early stage formation are needed for a better understanding of the mechanism of cracking. The characteristics of the ASR product firstly formed between adjacent mineral grains or narrow cracks [21][93][94] are insufficiently understood. There is only a small volume of product at early stage, generally in the range of a few nanometers up to one micron. It makes its analysis very challenging as it is below the spatial resolution (1–3 μm) of energy-dispersive X-ray spectroscopy (EDS) as used in conventional scanning electron microscopy (SEM).

Transmission electron microscopy (TEM) offers a higher spatial resolution for imaging and chemical analysis compared to SEM-EDS, because the problem caused by the interaction volume of the electron beam with the sample can be significantly reduced due to the thickness of the TEM lamella (approximately 200 to 250 nm) [95]. Moreover, with selected area electron diffraction (SAED) in TEM it can be determined whether the analysed material is crystalline or amorphous, which cannot be done in a SEM.

A combination of SEM – FIB – TEM techniques based on results obtained by [96] was built up to make it possible to reach the required spatial resolution and analyse these early stage products as shown by [23]. The steps and parameters used to reach our goal are described in this chapter.

# 3.2    Raw materials gathering and concrete mix manufacturing

## 3.2.1   Raw materials

The cement used for preparing the accelerated tests concrete is the Normo 4 from Holcim, a Portland cement CEM I 42.5 N. The aggregates come from Switzerland, a quarry in Wallis canton and are termed Praz aggregates. Their localization can be seen in green in Figure 3.1 They are from the alpine region, between the Helvetic domain (light blue) and the crystalline rocks region (pink). As mentioned in chapter 2, they were thought to be non-reactive due to their high crystalline content, and thus have been extensively used for construction. The red locations correspond to the structures in which the field samples have been collected.
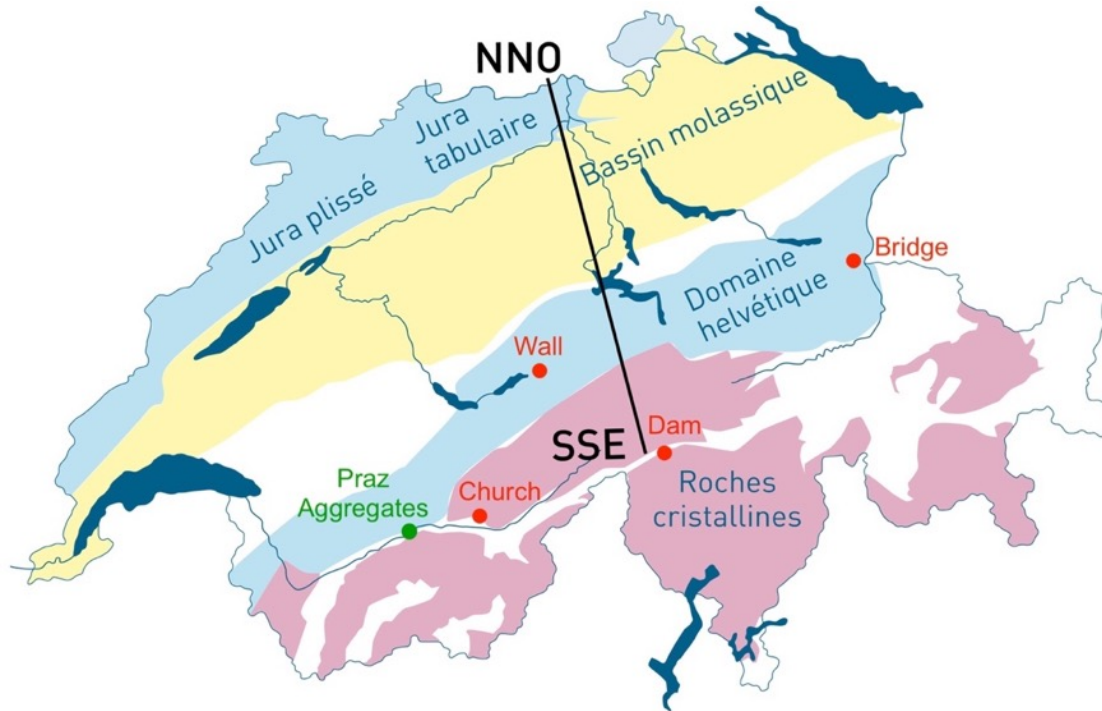
Figure 3.1 : Geological map of Switzerland [NAGRA]

In addition to the cement and aggregates gathered to produce classical concrete, some special concrete batches were prepared, containing Supplementary Cementitious Materials, such as Calcined Clay (LC3) and Fly Ash (FA).

The raw materials composition as analysed by XRF is presented in Table 3.1. The mineralogy of the swiss aggregate is given in Table 3.2 according to [45].

Table 3.1 : XRF results of the raw materials used to produce the concrete.

| In w% | Limestone (Durcal 5) | Calcined clay (Bhuj, India) | Fly Ash (Tarong) | Cement (Normo 4, Holcim) | Praz aggregate (Wallis) |
|---|---|---|---|---|---|
| SiO2 | 0,11 | 49,74 | 50,54 | 20,45 | 67,24 |
| Al2O3 | 0,00 | 41,78 | 24,70 | 4,39 | 4,38 |
| Fe2O3 | 0,04 | 2,30 | 9,29 | 3,01 | 0,76 |
| CaO | 54,96 | 0,20 | 5,07 | 64,48 | 12,13 |
| MgO | 0,20 | 0,10 | 2,88 | 1,66 | 1,48 |
| SO3 | 0,03 | 0,00 | 0,71 | 2,83 | 0,05 |
| Na2O | 0,06 | 0,30 | 1,05 | 0,24 | 0,60 |
| K2O | 0,01 | 0,10 | 4,10 | 0,89 | 1,79 |

| | | | | | |
|---|---|---|---|---|---|
| **TiO2** | 0,01 | 3,40 | 0,95 | 0,34 | 0,10 |
| **P2O5** | 0,00 | 0,09 | 0,00 | 0,28 | 0,00 |
| **MnO** | 0,00 | 0,02 | 0,00 | 0,06 | 0,02 |
| **Others** | 0,00 | 0,00 | 0,00 | 0,10 | 0,08 |
| **LOI** | 42,60 | 1,85 | 0,71 | 1,30 | 10,78 |
| **Na2O eq** | 0,06 | 0,37 | 3,75 | 0,83 | 1,78 |

Table 3.2 : Mineralogical composition of the swiss aggregate by XRD analysis [45]

| Mineral phase | in wt % |
|---|---|
| **Quartz**: SiO2 <br><br> [ICSD 174] | 56,3 |
| **Feldspar:** Albite: NaAlSi3O8 <br><br> [ICSD 87657] | 8,3 |
| **Feldspar:** Microcline: KAlSi3O8 <br><br> [ICSD 83531] | 8 |
| **Feldspar:** Orthoclase: KAlSi3O8 <br><br> [ICSD 9543] | - |
| **Mica:** Muscovite: KAl2(AlSi3O10)(OH)2 <br><br> [ICSD 75952] | 7,5 |
| **Calcite**: CaCO3 <br><br> [ICSD 73446] | 15,4 |
| **Dolomite**: CaMg(CO3)2 <br><br> [ICSD 66333] | 4,6 |
| **Chlorite**: Clinochlore Mg5Al(AlSi3O10)(OH)8 <br><br> [ICSD 66258] | - |

## 3.2.2   Manufacturing

The first step consisted of the raw materials preparation. The aggregates had to be rinsed and dried in oven at 100°C for 4h. They were then sieved according to the granular class defined in the SIA 2042 swiss standard [97] in the proportions listed in Table 3.3.

Table 3.3 : Aggregates proportions for each size class

| Granular class [mm] | Quantity [%] |
|---|---|
| 0.16 – 0.315 | 5 |
| 0.315 – 0.63 | 5 |
| 0.63 – 1.25 | 5 |
| 1.25 – 2.5 | 10 |
| 2.5 – 5.0 | 15 |
| 5.0 – 8.0 | 15 |
| 8.0 – 12.5 | 20 |
| 12.5 – 22.4 | 25 |
| Total | 100 |

Five types of concrete were prepared to investigate the ASR products characteristics, as expressed in the Objectives section. The batches had the composition given in Table 3.4.

Table 3.4 : Concrete mix solid proportions, excluding the aggregates.

| In % | Cement | Siliceous FA | Calcined Clay | Limestone | $Na_2O_{Eq.}$ |
|---|---|---|---|---|---|
| **OPC** | 100 | 0 | 0 | 0 | 0.83 |
| **FA** | 70 | 30 | 0 | 0 | 0.77 |
| **LC3** | 55 | 0 | 30 | 15 | 0.57 |
| **LC3 0.8%** | 55 | 0 | 30 | 15 | 0.8 |
| **LC3 1.25%** | 55 | 0 | 30 | 15 | 1.25 |

An important parameter in the concrete production was the alkali content, expressed in $Na_2O_{Eq}$ mass%. The calculation to determine the amount of alkali $Na_2O$ to add to the concrete mixes to reach the decided Na2O % eq. of 0.8 is done according to the SIA 2042 swiss standard in Equation 3.1 [97] :

$$\partial = \frac{C}{100}[A_m(1 + 2V_c) - A_{ech}] \: [kg/m^3] \qquad \text{Equation 3.1}$$

And simplified to Equation 3.2 due to a lack of data on alkali dispersion :

$$\partial = 0.0025 \cdot C \cdot A_{Ech} \quad [kg/m^3] \qquad \text{Equation 3.2}$$

C cement dosage in concrete

$A_m$ active alkali content of the cement in $Na_2O_{Eq}$ mass%

$V_c$ cement variation coefficient of $Na_2O_{Eq}$ content

$A_{Ech}$ active $Na_2O_{Eq}$ content of the cement sample used to produce the concrete prisms in mass% (with $Na_2O_{Eq}$ = $Na_2O$ + 0.658 $K_2O$)

It can then be converted to a mass of NaOH to add to the mix using the molar masses.

Each concrete batch was prepared at once, and cast in steel molds of size 70 x 70 x 280 mm. Three prisms were cast for expansion measurements purpose and two were cast for microscopic investigations. After 24h curing, the prisms were demolded and placed in accelerated conditions that will be further described in the upcoming chapters.

## 3.3    SEM samples preparation and analysis

### 3.3.1   Cutting

Slices of approximately 1cm thickness are cut in the middle of the accelerated test prisms using a diamond sprayed saw cooled down with water. The prisms are then placed back in accelerated curing conditions. The slices which have the dimension 70 x 70 x 10 mm are resized by removing 1cm of material on two opposite sides, for preparation and handling purpose (fitting in the polishing machine) Figure 3.2. The parallelepipeds of dimension 70 x 50 x 10 mm are then rinsed with water to remove the dirt and dried in oven at 40°C for three days.
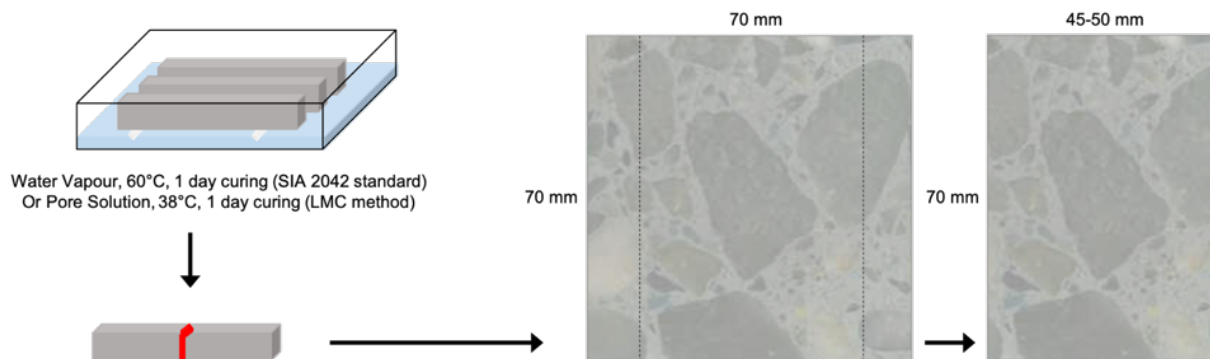


Figure 3.2 : Scheme showing the samples preparation from concrete prisms to microscopy.

### 3.3.2   Impregnation

Samples were impregnated in epoxy resin and hardener mix, containing C and H and no chloride. The resin was dyed with fluorescein, in case some optical microscopy is later of interest. Approximately 1 w% of fluorescein was added to the epoxy mix. The concrete samples were meanwhile placed in a plastic pot in a continuous vacuum $< 5.10^{-1}$ bars for 1h. The pot is then slowly filled through a thin plastic tube with the resin, until all samples are covered by the resin. It is important at this stage to make sure the samples are not touching each other, so that penetration of the resin in the sample is optimal. The resin is added slowly due to degassing under the vacuum: it produces foam which can overflow the pot.

After 1h degassing and penetration in the samples, the vacuum is stopped. The samples are placed one by one in latex socks (for which condoms were used) with approximately 50mL of resin. The latex socks are closed with a simple knot, without air bubble inside.

The whole is placed in a pressure column as seen in Figure 3.3. The column with the samples is filled with water, closed and pressure is manually applied via a pumping gas system. Three levels of pressure are applied, as following:

- 100 bars for 20 min
- 200 bars for 20 min
- 300 bars for 20 min



Figure 3.3 : Pressure column system.

By applying pressure, it is ensured that the resin penetrates deep into the concrete microstructure. Further samples observation showed that resin penetration is > 1mm.

The concrete samples are then taken out of the latex socks, and laid on a rubbery plate in oven at 40°C for 24h. After 24h, the resin is hardened and the samples can be further processed.

### 3.3.3  Polishing

A good impregnation is critical for the polishing steps. Indeed, cutting the samples with the saw damaged the first 0.5mm layer of concrete, and it has to be removed to obtain optimal sample imaging-quality in the SEM. The samples are roughly pre-polished by removing a layer of material ranging from 0.5 to 1mm. The deep impregnation (>1mm) is of critical importance to avoid cement and aggregates crumbling and more damaging of the surface due to polishing. With this method, the damaged top layer is removed, without further degradation since the deeper structure is protected by the epoxy resin stable matrix. The method implemented by Sofia et al. [98] has been validated and proved to yield good quality imaging results [23].

More polishing is done with the following grain size and protocol:

- SiC paper 500 - 10 min manually
- SiC paper 1200 - 10 min manually
- Si wafer with 15µm diamond particle size (spray) – 2h machine
- Si wafer with 9µm diamond particle size (spray) – 4h machine
- Si wafer with 3µm diamond particle size (spray) – 4h machine
- Si wafer with 1µm diamond particle size (spray) - 8h machine

In some rare cases, polishing steps had to be repeated due to very deep and tenacious scratches.

In between each polishing step, the samples are cleaned in ethanol for 5 min in an ultrasonic bath. They are dried with an air gun, and finally placed in a desiccator maintained in vacuum for long term storage.

### 3.3.4  Analysis

The localization of ASR products in the prepared samples was done using a XL-30 ESEM (Environmental Scanning Electron Microscope) from FEI. It features a tungsten filament source allowing secondary electron image resolutions up to 6nm and it is equipped with a backscattered electron (BSE) detector. The large chamber is ideal to host large samples, which is very suitable in the search for ASR in our wide surfaces. An integrated energy dispersive X-ray micro-analysis (EDS) system is available for compositional analysis. Analysis of our samples was done in high vacuum BSE mode to observe the microstructure of polished cross-sections, at a pressure of $1-5.10^{-5}$ mbar, an accelerating voltage of 15keV, a working distance of 12.5 mm and an emission current of 100 µA. The spot size was adapted to fit the conditions of the standard library system factor calibration, in order to be in the same conditions for each EDX analysis. Concerning EDX analysis, the quantification was done referring to a standard for the concerned elements. Comparison between the peak intensities of the sample elements and the standard considers the effect of atomic number, absorption and fluorescence, and correct them in an iterative way. It corrects in the most accurate way available the matrix effects of the sample.

A high voltage of 15keV was chosen, because X-rays, to be generated from an atom, need an incident energy of about 2 times the ionization energy of the concerned atom. In the case of concrete, the element with the

highest ionization energy is iron Fe. The most loosely bound electron in Fe is in $K_\alpha$ shell and $K_{\alpha1}$ energy is 6.4keV. The applied high tension should then be $\geq$ 13 keV [96].

The samples are taken out of the vacuum, coated with carbon (15 nm thick layer) and placed in the SEM for analysis. Regions of interest are visually localized, according to the following criteria:

- Located in the aggregate, a minimum of 100 µm away from the cement-aggregate interface, to avoid intermixing with C-S-H
- In the outer 2 mm of the aggregate (Figure 3.4)
- Located between adjacent quartz grains
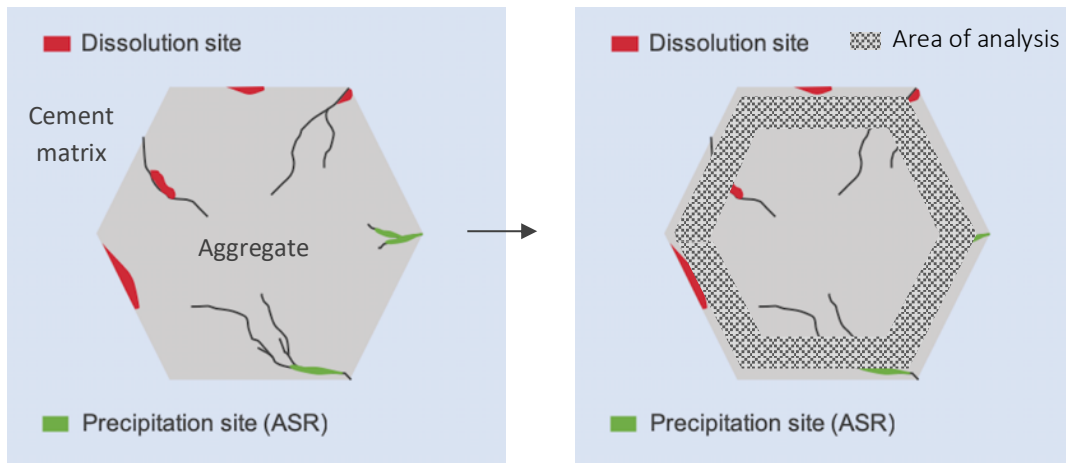


Figure 3.4 : Aggregate area of study.

Each region of interest is confirmed by an EDS analysis, as shown in Figure 3.5. Since it is localized in quartz grain mineral phases (containing only Si and O and traces of other elements), an increase of calcium and alkalis content of a few percent confirms the presence of ASR in the fine crack. A line scan is done according to the yellow arrow on the left image of Figure 3.5.
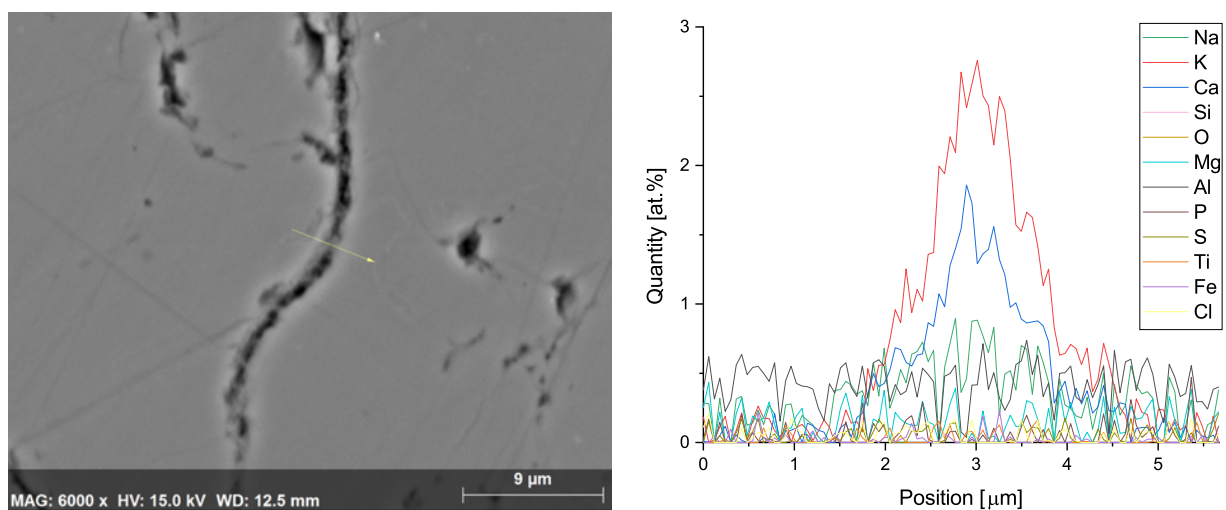


Figure 3.5 : Line scan (yellow arrow) of a crack (left) and its compositional results (right)

Here, the values of concentrations are not quantitatively considered. The important fact is that alkalis and calcium concentrations are increasing in the gap between the two quartz grain walls. The next crucial step is to be able to find the area again. Multiple SEM images are thus taken at different magnifications to be able to later recognize the area in the FIB. Images of the path to reach the area are also taken.

## 3.4    FIB sample preparation

Each sample was then transferred to a focused ion beam microscope (NVision40 FIB, Zeiss) in order to produce TEM lamellae. The dual-beam column of this device allows the isolation and milling of the exact area of interest.

The first stage is to find the area of interest, localized in the SEM. Once found, the stage eucentricity is adjusted, the working distance is set on 5mm and the stage tilt angle on 54° so that the sample surface is perpendicular to the FIB beam. The GIS (Gas Injection System) needle is inserted for the carbon protective layer deposition and a fine rectangle pattern of size 30 x 3 µm and thickness 1.4 µm is set. The voltage and current to build the carbon layer are set 30kV 150pA with a dwell time of 0.8. The pixel fill factor should be around 70% to have the right density and texture in the carbon layer.

### 3.4.1   The excavation

After the carbon deposition, come the milling steps. It is done at a high voltage of 30kV, for a depth of 20µm:

- the main trapezoidal trenches 1, 2 and 3 as seen in Figure 3.6 are milled at 27nA, dwell time 102.4.
- the 2nd step rectangles 4, 5 and 6 at 6.5nA, dwell time 25.6
- further polishing on both sides at 3nA dwell time 12.8, and corrective tilt angle ± 1° (to avoid the trapezoidal effect) to thin the lamella down to approximately 1.5µm.
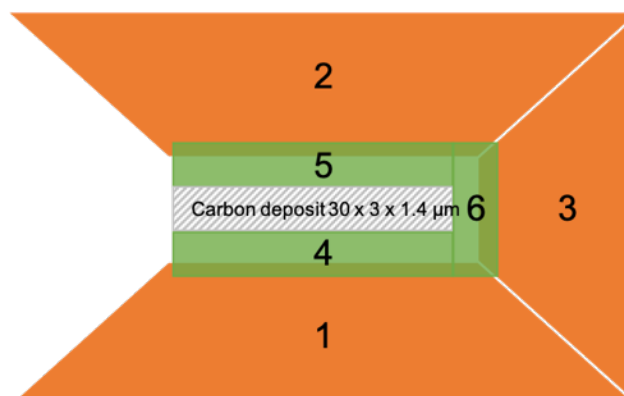


Figure 3.6 : Scheme of the FIB areas to be milled to produce a thin lamella.

### 3.4.2 The key

The sample is tilted at a 9° angle, to carry out "the key", which consist of a pre-cutting of the lamella for extraction purpose. The milled patterns are seen in Figure 3.7. The milling is done at 30kV, 1.5nA, dwell time 3.2.
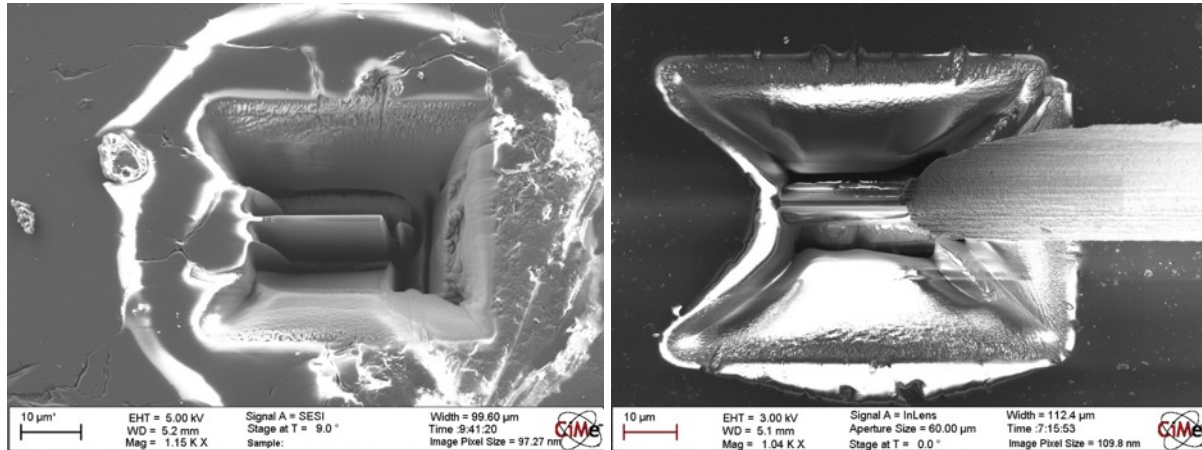


Figure 3.7 : FIB sample with the milled areas (left) and welding to the microneedle (right).

### 3.4.3 The extraction

The extraction itself is done at a 0° tilt angle. A manipulator having a needle shape is inserted using 3 axes movements: retract/insert, up/down and clockwise/counterclockwise, with 6 different possible speeds (mechanical/piezoelectric). It allows the right precision to come in contact with the lamella without breaking it, when carefully proceeded.

The lamella is welded to the needle by carbon deposition with the following characteristics: 2 x 2 µm rectangle deposited at 30kV, 10pA, dwell time 0.4 and pixel fill factor 40%, for 600s.

Once the welding looks satisfying (crosscheck in SEM and FIB to make sure the parts are well connected), the last part of material holding the lamella to the bulk sample is milled at 30kV 1.5nA as previously done. Retracting the needle with the welded lamella has to be executed slowly and step by step to avoid crashing the lamella in the surrounding material (Figure 3.8). The stage can be slightly lowered once the lamella is safe, and the manipulator is then fully retracted.
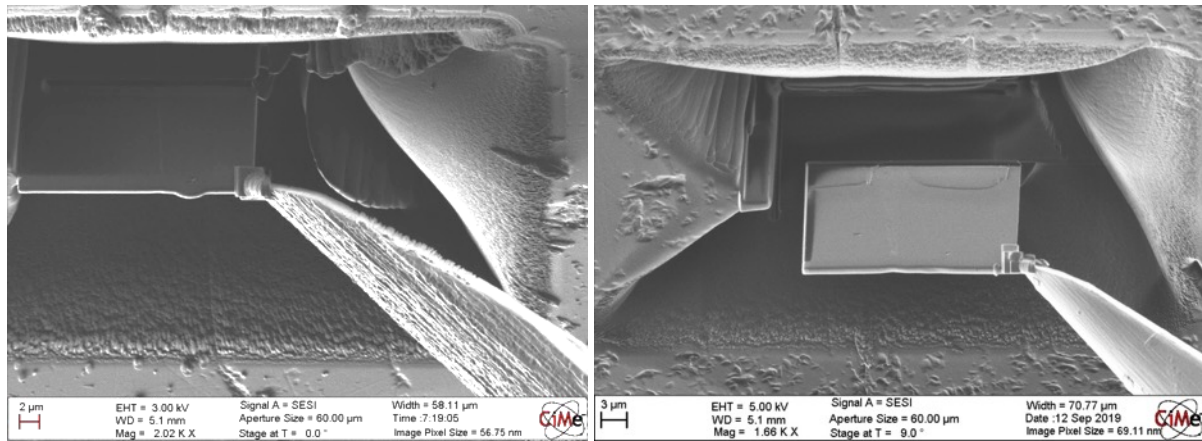
Figure 3.8 : FIB sample welded to the microneedle in the FIB (left) and its extraction (right)

### 3.4.4   The transfer

A TEM copper grid is inserted in the FIB chamber. The stage is placed in eucentric position, and the final tilt angle is 0°, at a working distance of 5mm. The GIS is inserted, and the manipulator is slowly inserted until the lamella welded on the manipulator needle tip comes in contact with the side of one of the grid copper pin as in Figure 3.9. A carbon rectangle 9 x 6 µm is deposited at 30kV 40pA, dwell time 0.2 and pixel fill factor 40-50% for 1200s.

Once the welding again seems satisfying, it is necessary to cut the lamella free from the manipulator needle. It has to be done without delay, since with time it is possible that a slight drifting occurs. The lamella will start bending until a breaking point is reached, generally in one of the welded areas.

The milling is done at 30kV 700pA dwell time 25.6 for 120s.
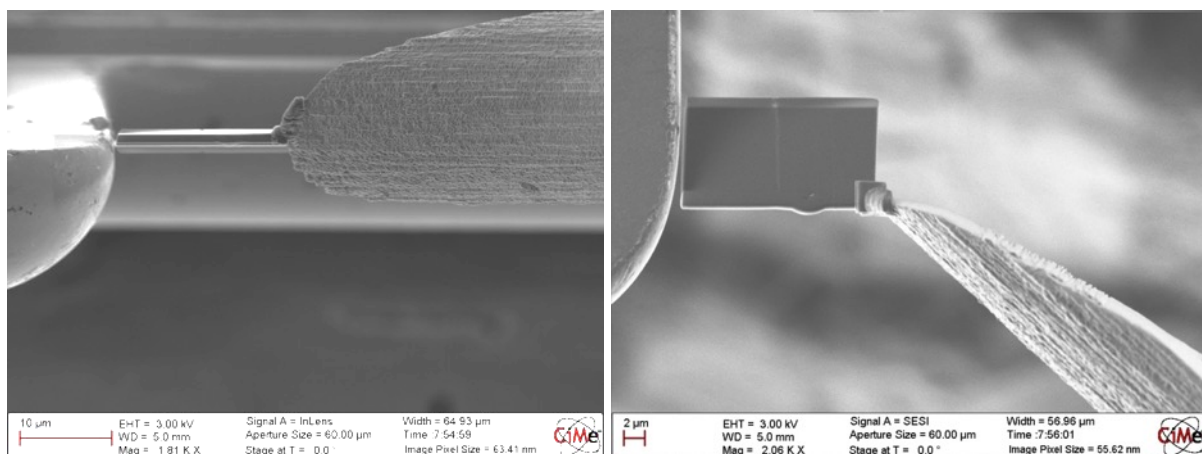


Figure 3.9 : Transfer of the lamella to a copper grid in SEM view (left) and FIB view (right).

After this step, the manipulator and the GIS are retracted, to continue with the lamella thinning.

### 3.4.5    The thinning

Due to the hard nature of the material (aggregate) and the lamella depth (10 to 14 µm depth), it is necessary to apply a correction angle to the original tilt. To be parallel in the z axis with the FIB beam, the tilt has to be 54°, and the lamella should be parallel to the FIB beam, as viewed in Figure 3.10. Now applying the correction angle, when milling the lower face, the tilt is 53° and for the upper face it is 55°.

The milling steps are alternating the faces, and are ordered as following, at 30kV for a width of 20 µm:

- 1.5nA, DT 1.6
- 700pA DT 0.8
- 300pA DT 0.8
- 150pA DT 0.4
- 80pA DT 0.4

The last step, is a cleaning step and is done at 5kV and 80pA for 30s. The sample is tilted of an extra ±5° from the original position and the full face is cleaned to remove possible redeposition occurring during the milling process. The lamella has now a thickness of 200-250nm to reach TEM transparency and is ready to be analysed in the TEM (Figure 3.11).



| 10 µm | EHT = 5.00 kV<br>WD = 5.6 mm<br>Mag = 875 X | Signal A = InLens<br>Aperture Size = 60.00 µm<br>Stage at T = 0.0 ° | Width = 134.1 µm<br>Date :9 Sep 2019<br>Image Pixel Size = 131.0 nm | CiMe |
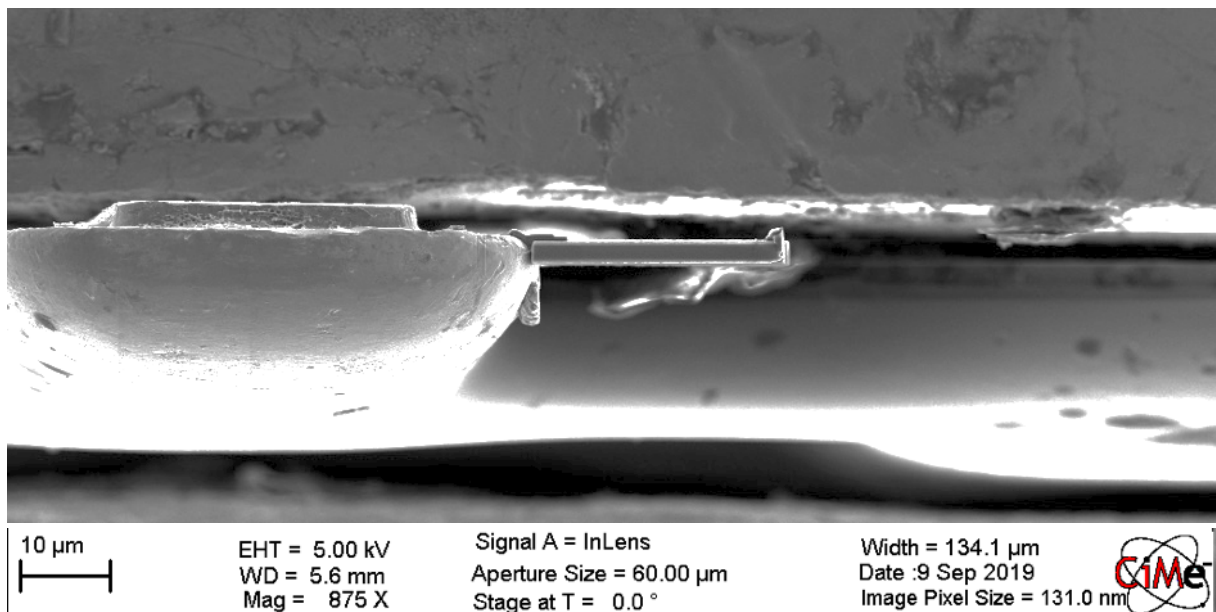
Figure 3.10 : Lamella welded to the copper grid, viewed at tilt=0° in SEM. If tilted at 54°, the same view will be obtained in FIB.
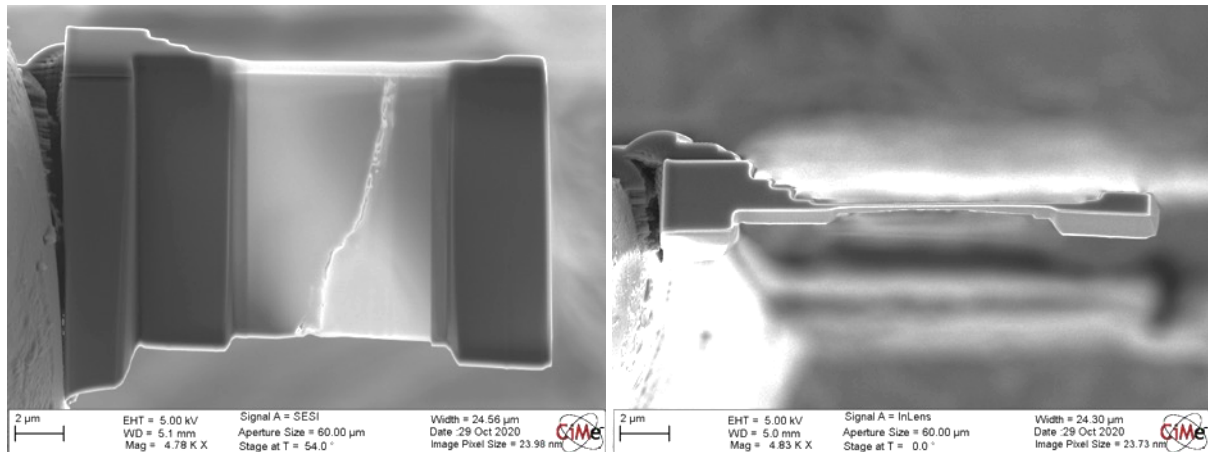
Figure 3.11 : Thinned down lamella in SEM view (left) and FIB view (right).

## 3.5 TEM-STEM analysis

Transmission Electron Microscopy allows a very local and precise analysis of the samples. The resolution limitation encountered in the SEM due to the low quantity of early stage ASR product can be overcome. The samples thinness (thickness < 300 nm), solves the issue of the interaction volume inclusion as illustrated in Figure 3.12. It is possible to analyse an area without contribution of the neighbouring phases.
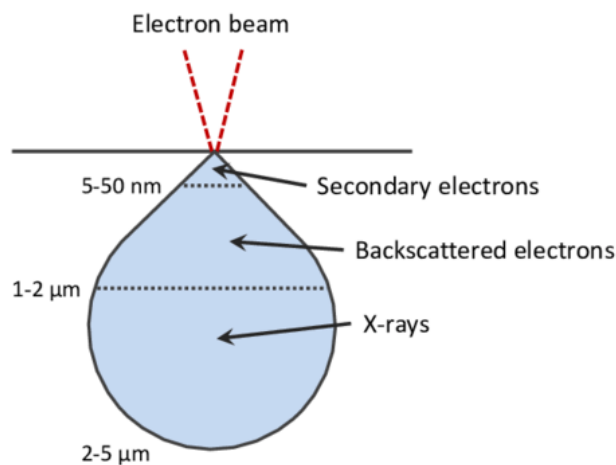


Figure 3.12 : Electron beam interaction volume in bulk samples.

A transmission electron microscope (Tecnai Osiris TEM, FEI) equipped with an EDS detector (Nano XFlash, Bruker) was used for imaging, diffraction and EDS analyses. The chosen operating accelerating voltage is 80 kV (instead of the usual 200kV) and a low current density (corresponding to a very large spot size) in order to limit the extent of potential beam damage and as such to preserve the structure of the ASR products. Two operating modes have been used. The TEM mode, for diffraction analysis, and the STEM mode, for imaging and EDX analysis. A description of the two modes is given in the following two paragraphs.

TEM: an electron beam is transmitted through a very thin sample (< 300nm thick).

In imaging mode, the interactions between the electrons and the atoms of the sample produce an image of high resolution (up to 0.05 nm). In diffraction mode, it is made use of the undulatory nature of the electrons.

Depending on the structural organization of the atoms, the electrons will be diffracted (crystalline material) or not (amorphous material). In the case of crystallinity, the beam will be diffracted in very specific directions (according to the atomic organization). The diffraction pattern is viewed when the back focal plane of the objective lens acts as the object plane for the intermediate magnetic lens. To have an image, the image plane of the objective lens acts as the object plane for the intermediate lens this time. In both cases it is then projected onto the viewing screen Figure 3.13.
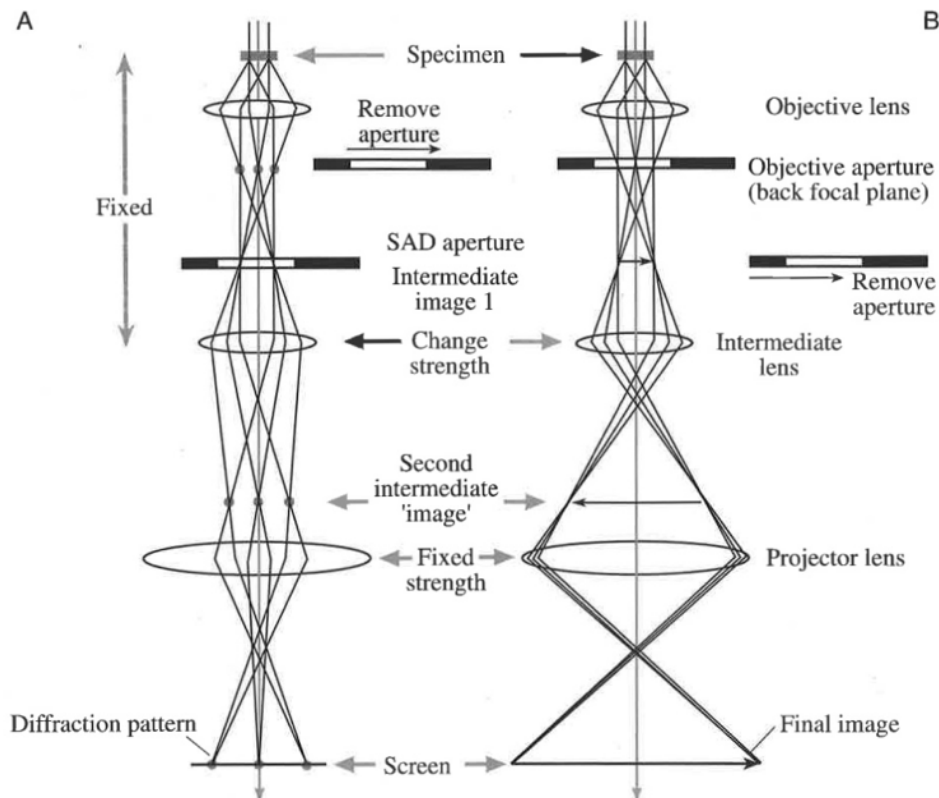


Figure 3.13 : "The two basic operations of the TEM imaging system involve (A) projecting the diffraction pattern on the viewing screen and (B) projecting the image onto the screen. In each case, the intermediate lens selects either the back focal plane or the image plane of the objective lens as its object." [99]

STEM: the electron beam is focalized in a small as possible probe which scans the sample surface. It is the same principle as in SEM, the difference being the sample thickness and thus the interaction volume contribution. It is thus possible to do EDS analysis. It also reduces aberrations for imaging purposes, because it consists of a point by point image reconstruction of the transmitted intensity.

Both Bright Field (transmitted beam) and High Angle Annular Dark Field (diffracted beam, high angles scattered electrons forming Z-contrast images) detectors have been used in this study.

The copper grid with the lamella to be observed is placed in a Single Tilt holder in the TEM.

Due to the beam sensitive nature of ASR, trials to establish convenient working parameters have been conducted. The key parameters are the electron dose and the electron dose rate. The electron dose (cumulative) has been chosen to not exceed $5 \times 10^2$ e/$\text{Å}^2$. In [23] we reported that eventhough this value is not exceeded, there is attenuation of the sample crystallinity. A test was done on field ASR platelets product,

for which the maximal electron dose of $5 \times 10^2$ e/Å$^2$ was reached after approximately 1 minute. There is a slight attenuation of the diffraction pattern. The sample is thus still preserved despite a slight loss of crystallinity as seen in Figure 3.14. After 3 and 5 minutes, dots in the diffraction patterns are still visible but very weakly, and most crystallinity has disappeared.

The investigation parameters presented in the next subparts proved to be successful in maintaining a low enough damage level to observe and have reliable quantifiable data.
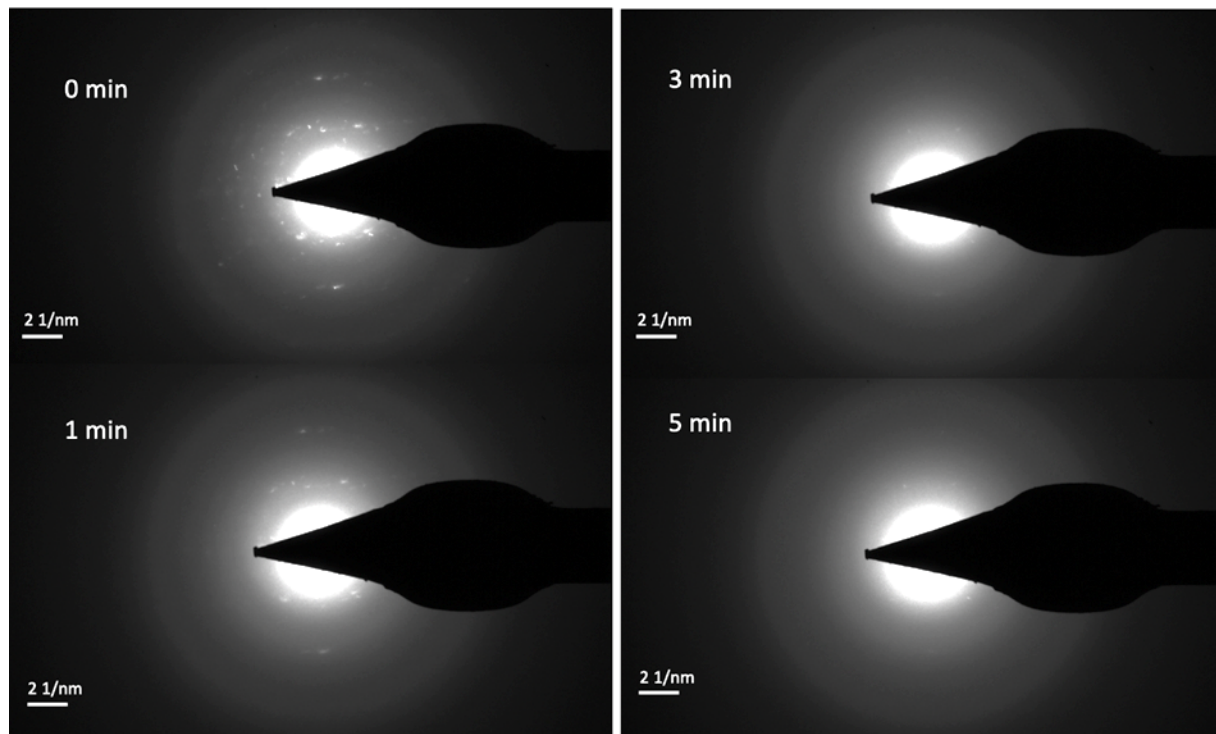


Figure 3.14 : Diffraction pattern dots attenuation of ASR product with time, indicating damages to the material crystalline structure.

## 3.5.1 Imaging

Imaging is done in STEM mode, at 80kV, spot size 8, gun lens 6. Once the classical adjustments are done (condenser aperture, pivot points, rotation center) and the sample is placed in eucentric focus, the High Angle Annular Dark Field (HAADF) and the Bright Field (BF) detectors are inserted. The type of images obtained is shown in Figure 3.15. Astigmatism and final focus can be finalized. Images are acquired at a resolution of 1024 x 1024 and dwell time 6µs to avoid beam damage.
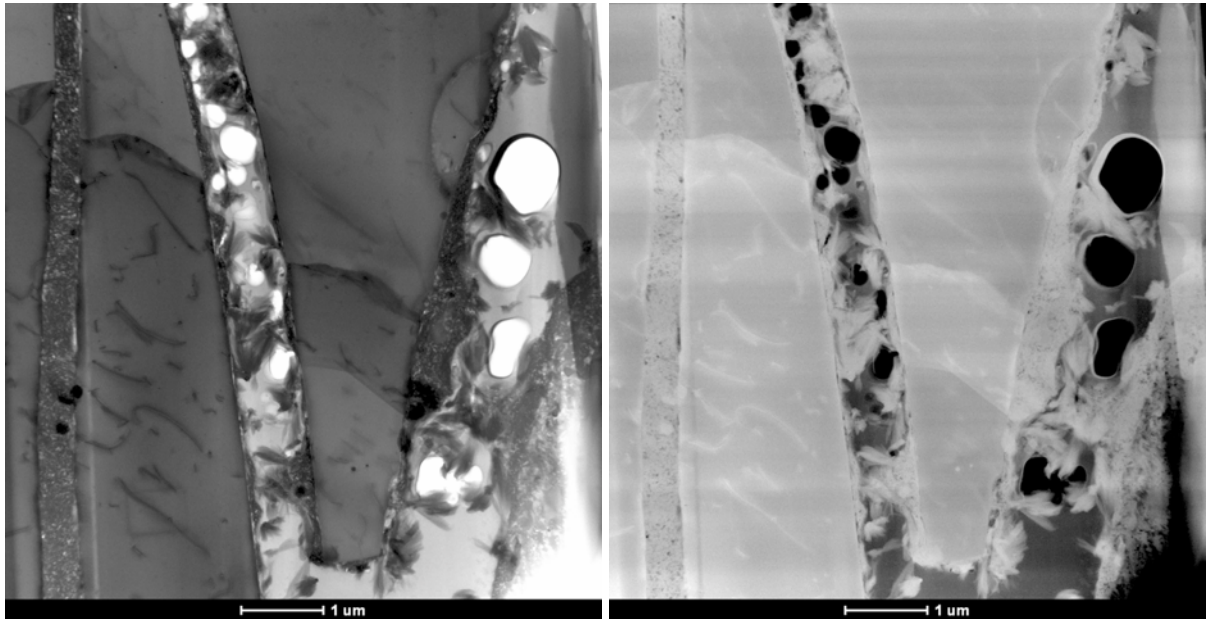
Figure 3.15 : BF (left) and HAADF (right) STEM images of a lamella.

### 3.5.2  Diffraction

Diffraction is done in TEM mode, at 80kV. The parameters are set as following:

- C2 aperture – 70 µm
- Spot size – 8
- Electron dose – < 0,5 e/Å$^2$ which means one can stay 15 mins without exceeding our defined limit value.

To analyse a precise location, a Selected Area Electron Diffraction (SAED) shutter is inserted, size 100nm (smallest available). Once the area of interest is isolated and moving to the diffraction mode, the electron diffraction pattern of the selected area is visible.

In the case of a crystalline sample, it is possible to select a diffraction spot by moving along the X and Y axis the objective aperture in Dark Field, and see which crystalline part has the same orientation, as seen in Figure 3.16.
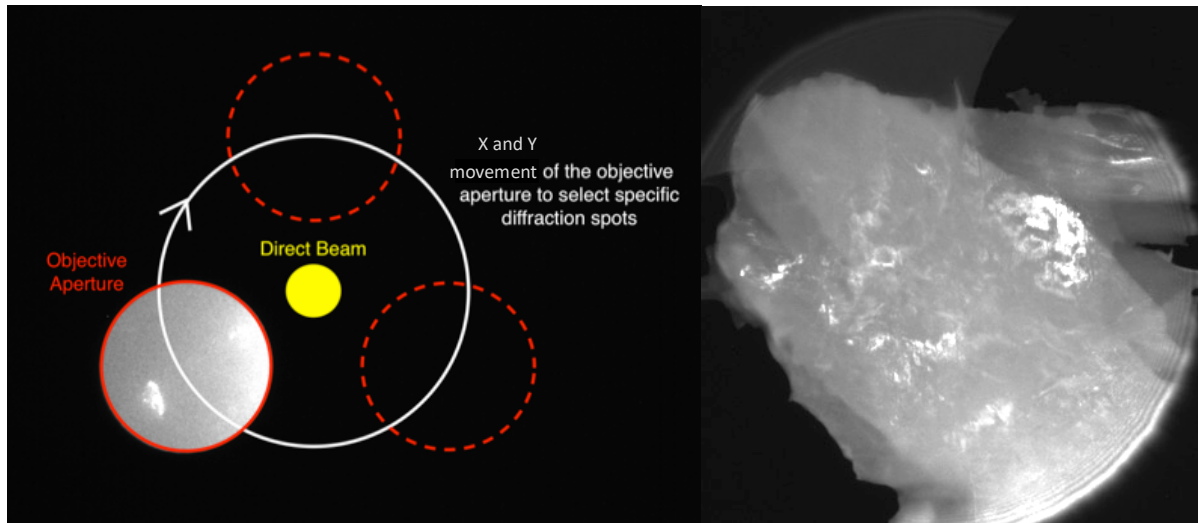
Figure 3.16 : In the diffraction mode, possibility to select a specific area containing a diffraction dot by introducing the objective aperture. The image obtained results of bright areas of the orientation planes corresponding to this diffraction dot.

### 3.5.3   EDS analysis

EDS analysis is done in STEM mode, at 80kV, spot size 8, gun lens 6. The parameters are similar as for imaging. In addition, the sample is tilted of 20° (or -20°) to have a better signal and avoid the shadowing effect described in Figure 3.17. Due to the 20° tilt, two of the four EDX detectors are shutdown, n°3 and 4 (n°1 and 2 if tilt is -20°), because they do not receive any signal as in Figure 3.17.
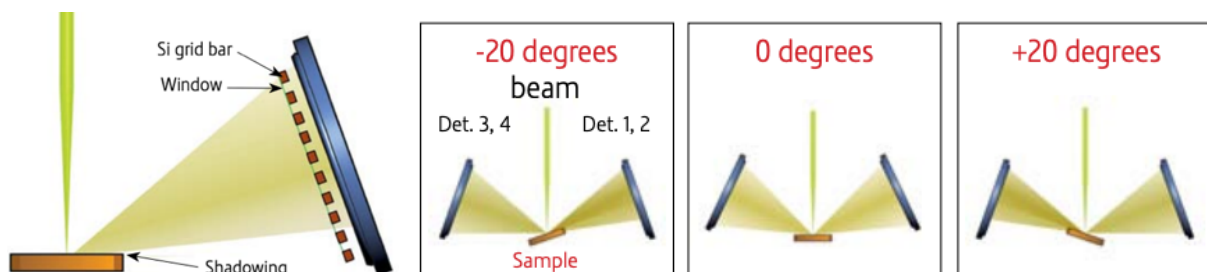


Figure 3.17 : Effect of shadowing in the TEM. Tilting the sample of 20 or -20° will improve quantification with detectors 1,2 and 3,4 respectively, the other two detectors have in parallel to be shut down.

A defocus of approximately 200 nm is done to reduce the sample damages. The counts number should be around 8000. The acquiring parameters are set to:

- resolution imaging = 512 x 512 px
- dwell time imaging = 16 µs
- dwell time mapping = 100 µs

The quantification is done with the Cliff-Lorimer standardless method. The sample thickness is assumed to be small and homogenous, in order to neglect absorption and fluorescence effects, in the case all elements are identified. The method specifies that the X-rays intensities ratio between element A and B is proportional to the mass concentration ratio of those elements as in Equation 3.3 :

$$\frac{C_A}{C_B} = k_{AB} \cdot \frac{I_A}{I_B} \qquad\qquad \text{Equation 3.3}$$

With $\frac{C_A}{C_B}$ the mass concentration ratio between element A and B, $\frac{I_A}{I_B}$ the peak intensities ratio between elements A and B, and $k_{AB}$ a factor considering the instrument parameters.

Acquisition runs for 10 mins. The raw maps are later analysed using the Bruker Esprit software. Areas can be defined for quantification (see Figure 3.18) and give an average of the composition. Due to the small acquisition time, point analysis cannot be done.
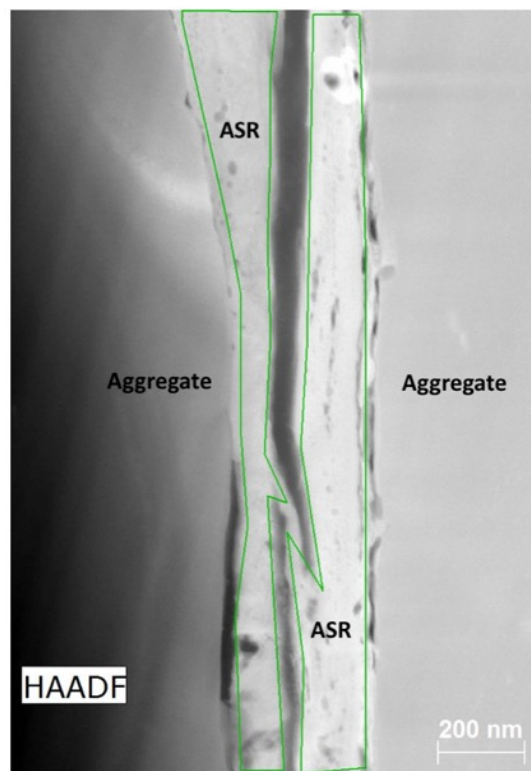


Figure 3.18 : Example of analysed areas in green, in a STEM quantified image. Areas are manually defined.

## 3.6 Validation of the method

It is possible to tune the parameters in TEM to avoid sample damage. It is done by keeping the electron dose to a reasonable level (see subsection 3.5), changing the spot size or the condenser aperture size. The difficult step is to make sure there is no induced damage during the FIB process. Despite the very low currents used to finish the milling in FIB, it was necessary to prove FIB does not damage the ASR product and is suitable for its preparation. Evaluation of the damage due to FIB processing has been evaluated studying a field sample which had a lot of ASR products (seen macroscopically) from which two samples were collected in the following ways:

- SEM – FIB – TEM/STEM method, lamella containing ASR platelets.
- ASR powder collection, dispersed in ethanol and dried on a TEM copper grid for direct TEM/STEM observation.

Both exhibited a clear crystalline behavior as signaled by the diffraction pattern dots seen in Figure 3.19 for the powder sample and Figures 3.20 and 3.21 for the FIB sample. Of course, the FIB sample has a weaker signal compared to the powder one since only small areas were analysed with SAED, as pointed out by the red circles in Figure 3.21. It is also presenting different crystal orientations in comparison with the single ASR platelet, present in Figure 3.19, from the diffraction pattern forming a partial ring shape.

Using the FIB method is thus totally appropriate to observe ASR samples without causing structural damages that would bias the results.
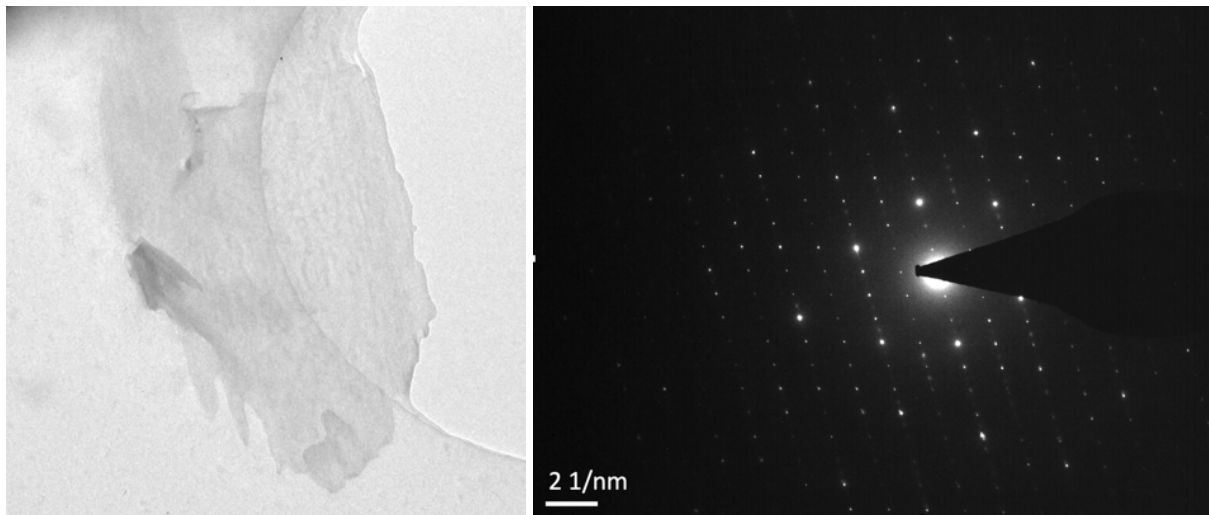


Figure 3.19 : Field ASR platelet analysis (without SAED) from powder dispersion on a TEM copper grid (left) and its crystalline diffraction pattern (right)
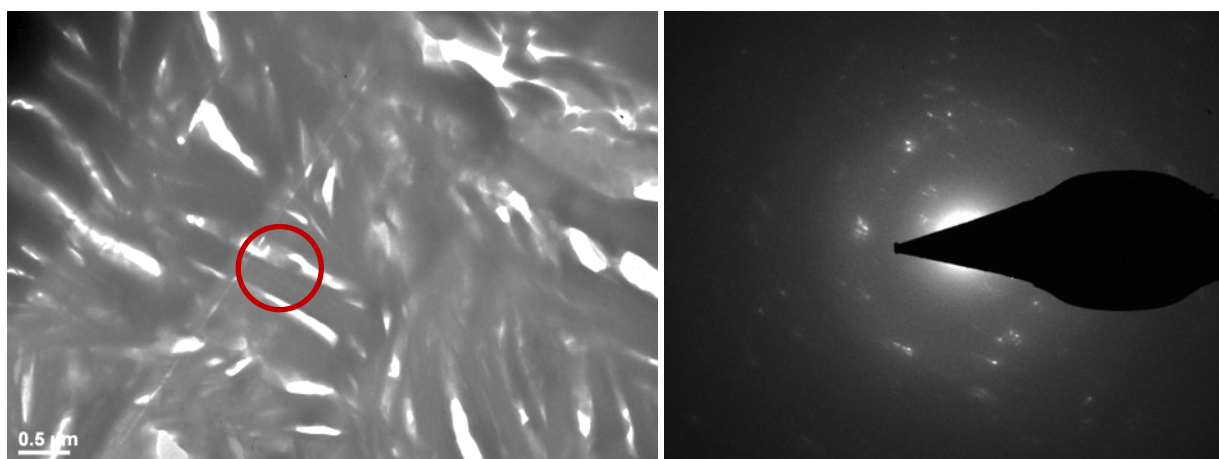


Figure 3.20 : Field ASR platelets analysed area (red circle) from FIB milling (left) and its crystalline diffraction pattern (right)
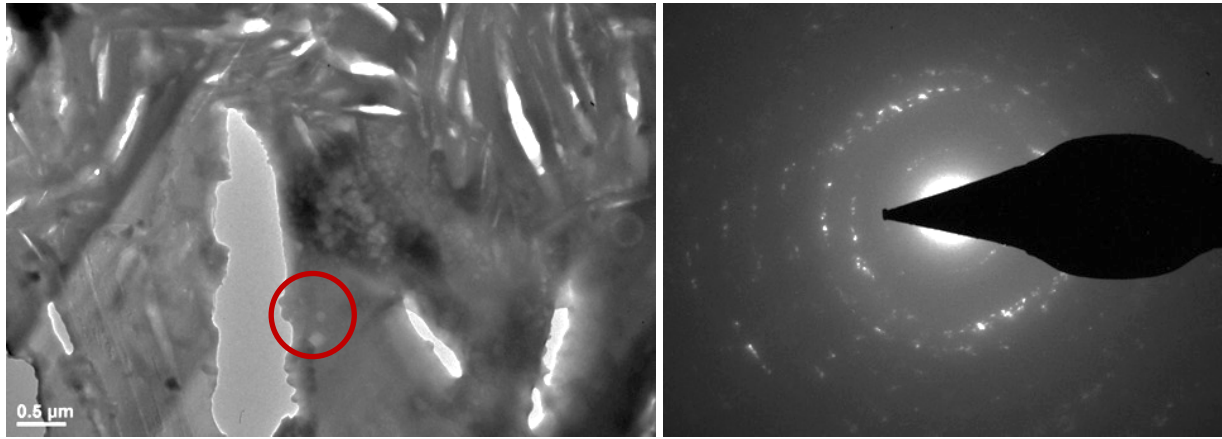
Figure 3.21 : Field ASR platelets analysed area (red circle) from FIB milling (left) and its crystalline diffraction pattern (right)

# Chapter 4   Early   stage   ASR   product evaluation   in   laboratory   concrete   samples containing alpine aggregates

## Abstract

Understanding the early stages of ASR is a key factor for identifying the damage process. New technological approaches provide the opportunity to investigate the very first steps of the reaction. For the analysis of the initially formed products in concrete aggregates, a new method combining FIB and TEM was developed. After only 2 weeks in accelerated laboratory conditions, signs of ASR were already found and the morphology, composition and structure of these products were studied. This reveals the presence of two different morphologies: granular and platey products. Selected electron diffraction indicates them to be amorphous and nanocrystalline, respectively. The composition of all products was very similar, slight differences were related to the position in the cracks, rather than to morphology.

## 4.1    Introduction

Since the discovery of ASR in the 1940s [5][6][7], great progress has been made regarding its characterization. It is generally described as a two-step reaction, involving :

- the dissolution of the silica from the aggregates
- the formation of an alkali-calcium-silica-rich product leading to concrete cracking

Several reaction mechanism have been proposed [11][30][79][34][100][101]. These tend to agree on the basics of dissolution. The OH- ions present in the pore solution break the siloxane bonds of the amorphous or nanocrystalline silica which further reacts with the alkali ions [10], [12], [102] and calcium. Several mechanisms for the swelling mechanism (osmotic pressure [67][13][10][102][24][11], crystallization pressure [14][27], ion diffusion [26][12][77][78], double-layer [28][80]) have been proposed. However, many details of the reaction are unclear. For example :

- The relevance of the amorphous or crystalline nature of the products, which are often found to be intermixed in the same crack, generally close to the ITZ in the aggregates.
- The composition of the products, their homogeneity at nanoscale.
- The different effects of potassium and sodium on expansion.
- The role of calcium in the stress generation and thus expansion, which is particularly controversial.

A major problem is that most observations focus on products found in structures or laboratory specimens after extensive cracking and expansion occurred, thus fairly late on in the process. Analysis of ASR products before expansion is needed to better understand the mechanisms of concrete expansion due to the ASR process. The first ASR products tend to start forming close to the ITZ (interfacial transition zone) in the aggregate. In this state before cracking, the product is present in very small amounts making its analysis difficult. Here, a combination of focused ion beam (FIB) and transmission electron microscopy (TEM) techniques, as described by [23][93][103] and chapter 3 of this thesis, was used to prepare the samples and analyse the early stage reaction products. However, as mainly field samples from structures were used for analysis [23][93][103], aging, and with it a change of characteristics of the initial products, cannot be excluded.

The goal of this study is to analyse the initial ASR products formed in controlled laboratory conditions at various ages. For this purpose, concrete was produced in the laboratory and subjected to the concrete prism test under accelerated conditions. The nanoscale morphology, composition and structure of the initial products was investigated using FIB and TEM.

## 4.2    Materials and methods

### 4.2.1   Concrete mix preparation and conditioning

The concrete was prepared with 430 kg/m$^3$ of cement and a water to cement ratio of 0.46. A Swiss alpine aggregate from the swiss Wallis region (VS) and Portland cement (PC) were used for the concrete production. Their composition as analysed by XRF is presented in Table 4.1. The mineralogy of the aggregate is given in Table 4.2 according to [45]. The concrete prims with dimensions of 70 x 70 x 281 mm were cast according to

the Swiss standard SIA 262-1 (appendix G) [104]. Additional 70 x 70 x 281 mm samples were cast for the microscopy analysis, which was carried out in parallel to the expansion measurements.

Table 4.1 : Chemical composition of the PC and the Swiss aggregates used in the concrete by XRF analysis.

| in wt % | $SiO_2$ | $Al_2O_3$ | $Fe_2O_3$ | CaO | MgO | $SO_3$ | $Na_2O$ | $K_2O$ | $TiO_2$ | $P_2O_5$ | MnO | Others | LOI | $Na_2Oeq$ |
|---|---|---|---|---|---|---|---|---|---|---|---|---|---|---|
| PC | 20,45 | 4,39 | 3,01 | 64,48 | 1,66 | 2,83 | 0,24 | 0,89 | 0,34 | 0,28 | 0,06 | 0,10 | 1,30 | 0,83 |
| Aggregate | 67,24 | 4,38 | 0,76 | 12,13 | 1,48 | 0,05 | 0,60 | 1,79 | 0,10 | 0,00 | 0,02 | 0,08 | 10,78 | 1,78 |

Table 4.2 : Mineralogical composition of the swiss aggregates by XRD analysis [45]

| Mineral phase | in wt % |
|---|---|
| **Quartz**: SiO2 [ICSD 174] | 56,3 |
| **Feldspar:** Albite: NaAlSi3O8 [ICSD 87657] | 8,3 |
| **Feldspar:** Microcline: KAlSi3O8 [ICSD 83531] | 8 |
| **Feldspar:** Orthoclase: KAlSi3O8 [ICSD 9543] | - |
| **Mica:** Muscovite: KAl2(AlSi3O10)(OH)2 [ICSD 75952] | 7,5 |
| **Calcite**: CaCO3 [ICSD 73446] | 15,4 |
| **Dolomite**: CaMg(CO3)2 [ICSD 66333] | 4,6 |
| **Chlorite**: Clinochlore Mg5Al(AlSi3O10)(OH)8 [ICSD 66258] | - |

The Swiss guidelines require curing for one day, demolding of the prisms and placement in boxes stored at 100% relative humidity (WV) at 60°C (T60). Expansion of the prisms is measured at 4, 8, 10, 12 weeks and every 4 weeks up to 1 year in accelerated conditions. For the measurements, the prisms are taken out of the climate chamber, cooled down to 20 °C for 24h in the closed containers before their length is measured. The prisms were then immediately placed back in the above mentioned conditions.

## 4.2.2  Sample preparation

After 2 weeks and at each subsequent time step when expansion was measured (see 4.2.1), slices with thickness around 0.5 to 1 cm were cut from the middle of the prisms cast for microscopy analysis. One centimeter of material was removed from two opposite sides to obtain samples of dimensions 70x50 mm. The size had to be reduced for practical reasons. These samples were dried at 40°C for 3 days. Once dried, the samples were impregnated with epoxy resin under a pressure of 3 bar, cured, polished and finally coated with carbon to be suitable for microscopic observations. Based on the expansion evolution (Figure 4.1), two sets of samples were chosen to assess the first formation of ASR products. In the Swiss standard, an aggregate is considered reactive, if the expansion reaches a value of > 0.20 ‰ within 20 weeks, which is the case here. The plateau in the expansion curve observed in Figure 4.1 after approximately 200 days is due to alkali leaching, since the samples are kept in a water vapour environment at high temperature. Because there is a significant expansion already after 4 weeks, it was decided to look for early-stage ASR product at 2 and 4 weeks where signs of ASR were already evident. No expansion measurements were done at 2 weeks, but considering the already high expansion at 4 weeks, it was expected to find signs of ASR reaction at 2 weeks also.
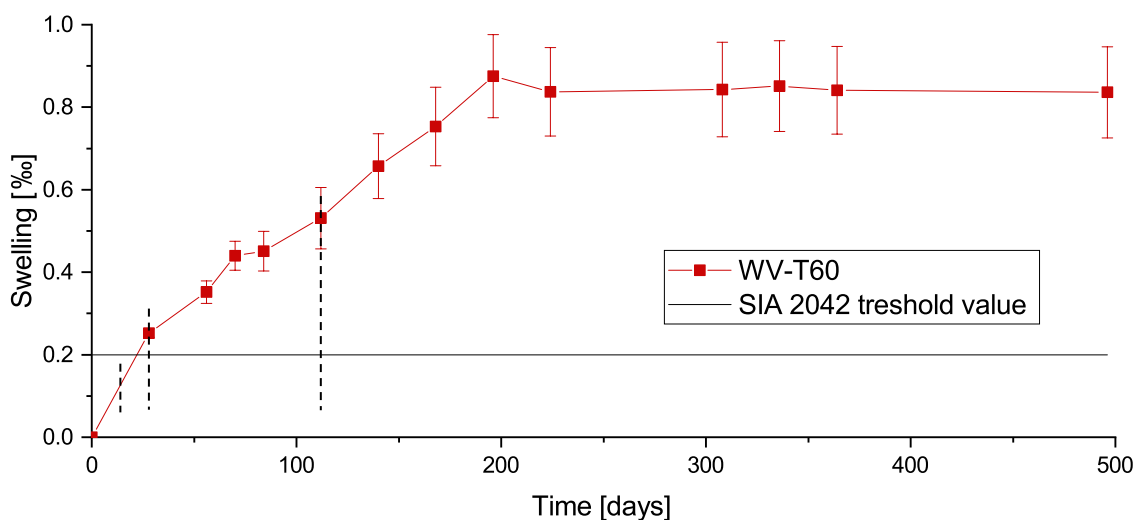


Figure 4.1 : Expansion of concrete prisms according to [104].

Areas of interest were localized in the SEM. In order to facilitate the ASR product localization, only gaps and pre-existing cracks within quartz particles were analysed. Their width is usually in the range of 0.1-1 μm. Cracks between mica or feldspar were not analysed due to the presence of alkalis in these minerals. Areas selected for analysis were localized in cracks in aggregates with a minimum of 100 μm distance from the ITZ to avoid a possible contribution of the cement paste products in the analysis. An increase of potassium (and or sodium) and calcium in cracks indicated the presence of ASR product, as seen in Figure 4.2.

Once areas of interest were identified, they were extracted in the form of lamellae using FIB. The method used is described in chapter 3. Four lamellae were prepared from the 2 weeks old sample (W2) and three lamellae from the 4 weeks old sample (W4). All of them were from fairly preserved aggregates as verified in the SEM, which is an indication that initial product is studied. In addition, a lamella from an aggregate extracted from the quarry and not used for concrete production was selected, to verify the aggregates were

not yet suffering from ASR formation due to storage condition. The lamella prepared from this aggregate served as a reference. The rest of the lamellae are labelled as :

- W2-L1; W2-L2; W2-L3; W2-L4 (sample exposed for 2 weeks in accelerated conditions)
- W4-L1; W4-L2; W4-L3 (Figure 4.2, sample exposed for 4 weeks in accelerated conditions)
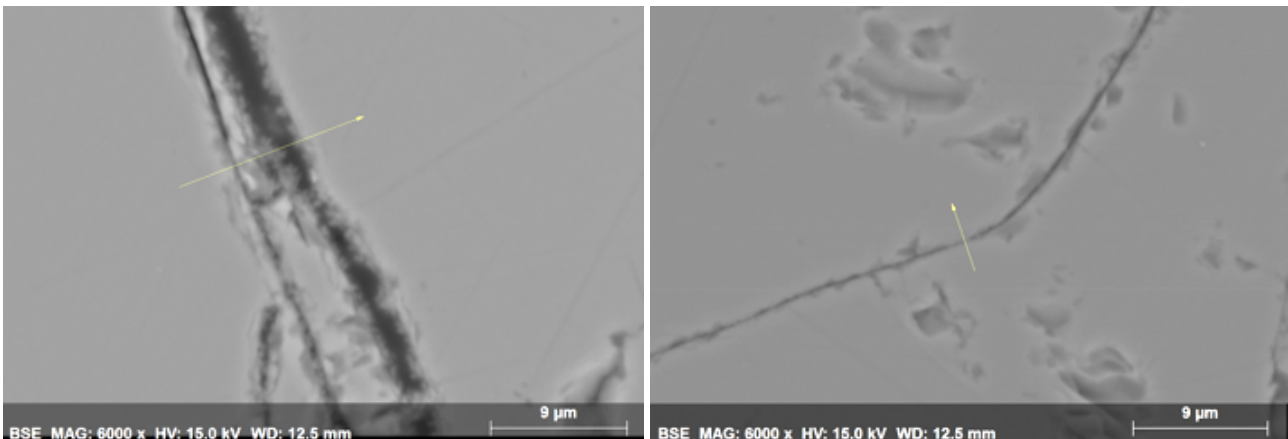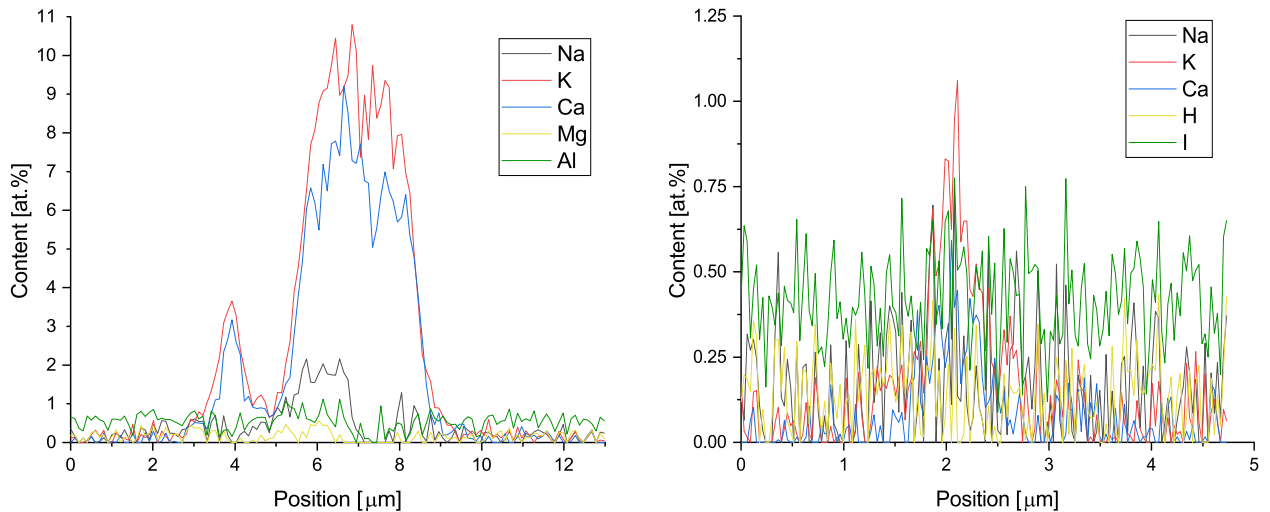


Figure 4.2 : SiO2 mineral phase with ASR product presence in the cracks. There is a calcium and potassium increase as measured by EDX analysis.

## 4.2.3   Analytical method

The lamellae were examined in a Tecnai Osiris TEM from FEI. Due to the sensitive nature of ASR products, the analysis was conducted at a relatively low acceleration voltage of 80kV with an electron dose $\leq 5 \times 10^2$ e/Å$^2$, as described in [23] and chapter 3, for diffraction analysis. For EDX analysis, STEM mode was chosen. Once the EDX maps were generated, small areas were chosen for data extraction as indicated by the green outlines in Figure 4.3. The average compositions in each area are represented by a dot in the ternary diagrams in Figures 4.10, 4.13 and 4.19.
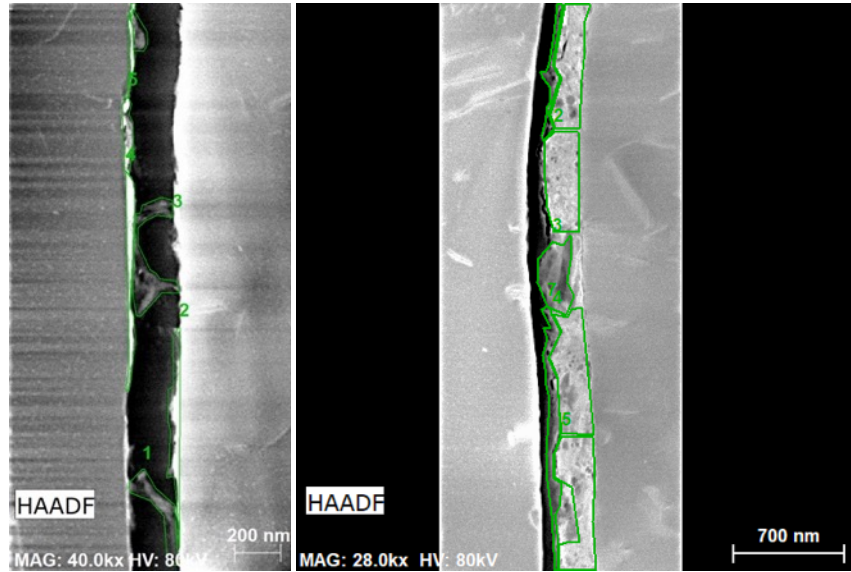
Figure 4.3 : Example of chosen areas after EDS analysis in STEM mode.

The crack orientation plays a significant role for the analysis. It is important to be in a situation as shown in Figure 4.4 (left) rather than Figure 4.4 (right). Due to the interaction volume of the electron beam with the sample, the situation shown in Figure 4 (right) leads to an increased signal of the aggregate (quartz) influencing the signal from the ASR product. This leads to an exaggerated Si content in the analysis.



Figure 4.4 : Different crack orientations: The direction of electron beam (left) is suitable for analysis in contrast to (right).

## 4.3    Results and discussion

### 4.3.1   General

A total of eight lamellae were successfully prepared and analysed. One is from an aggregate in its original state after extraction in the quarry, and serves as a reference. It was necessary to verify that the ASR product did not start to form in the aggregates before concrete preparation, due to poor storage conditions.

As expected, this lamella showed no traces of ASR products. However, the aggregates had many gaps and pre-existing cracks between adjacent quartz grains (Figure 4.5). This observation confirms the one made in [94]. Such gaps and pre-existing cracks provide spaces where the initial ASR products can form.
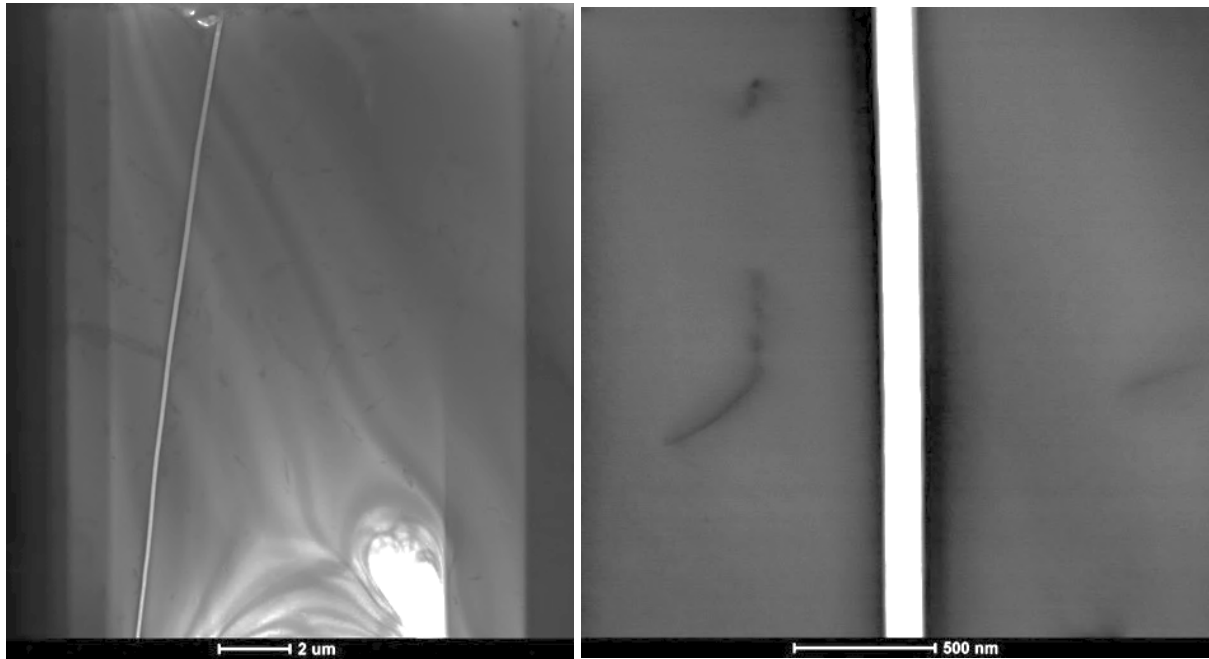
Figure 4.5 : Raw aggregate STEM Bright Field images showing an empty preexisting crack and local defects.

Four lamellae were prepared from W2, and 3 from W4. All lamellae have a crack partially filled with ASR product. In both W2 and W4 lamellae, two ASR products morphologies are observed as seen in Figures 4.6, 4.7 and 4.8 : a granular and a platey product. The difference between the two morphologies is more clearly seen in W4-L1 in Figure 4.8. The reasons favouring one or the other morphology is not yet understood: a possible reason could be the local boundary conditions like available space, temperature or ion species concentration.
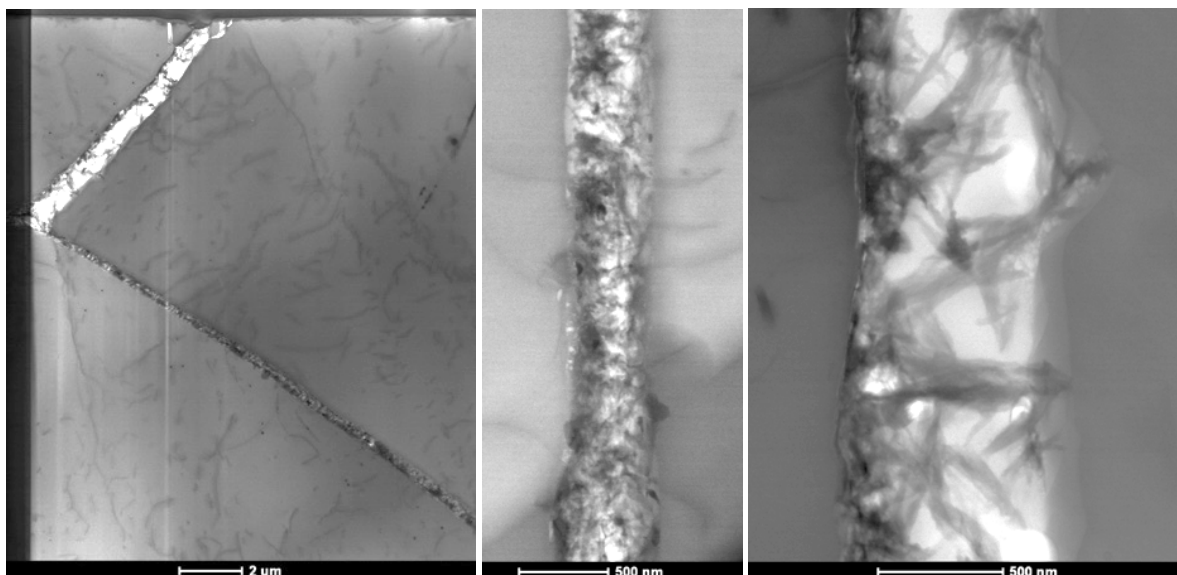


Figure 4.6 : Overview of W2-L1 cracks. (left) At higher magnification, presence of granular product (middle) and a mix of granular – potentially platey product. (right).
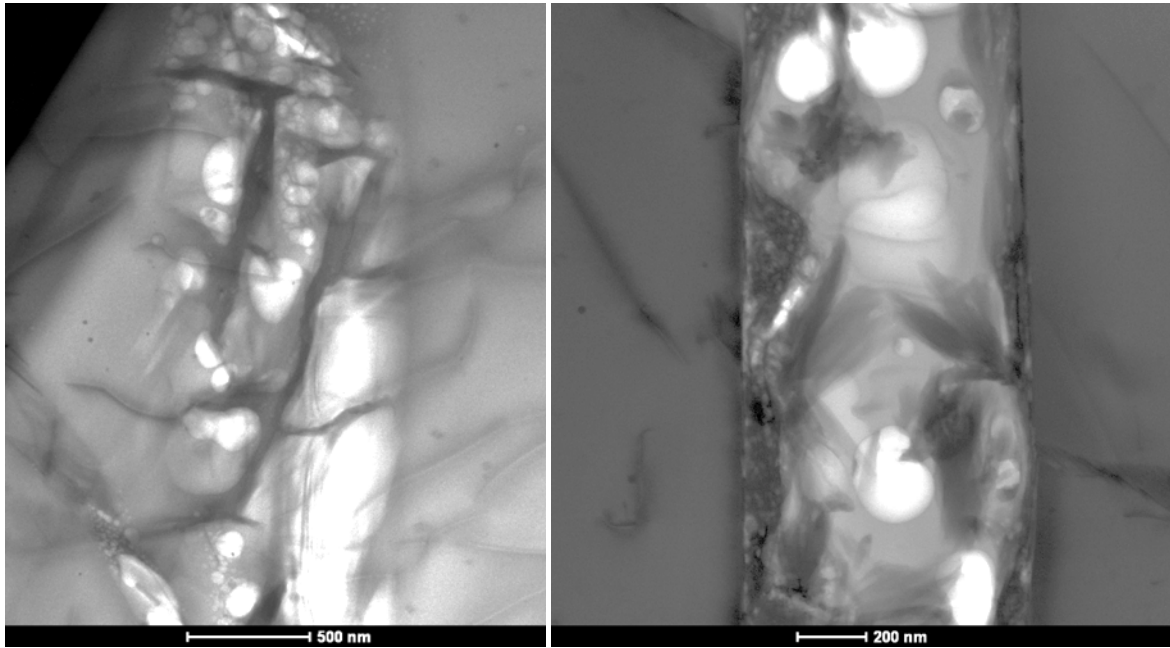
Figure 4.7 : Overview of W4-L1 cracks. (left) At higher magnification, in the same crack, presence of platey product on top of granular product. (right).



Figure 4.8 : In two neighbouring cracks, presence of (left) granular and (right) platey product.

The products found in the rest of the lamellae from W2 and W4 could not be clearly identified in terms of morphology. The first reason is that the product is too scarce to be identified (see Figure 4.9 (a) and (b)), and the second reason is that the product is densely packed (the crack is filled) and the product features are not visible. In Figure 4.9 (d) the product looks similar to platelets, but with contribution of some granular features.
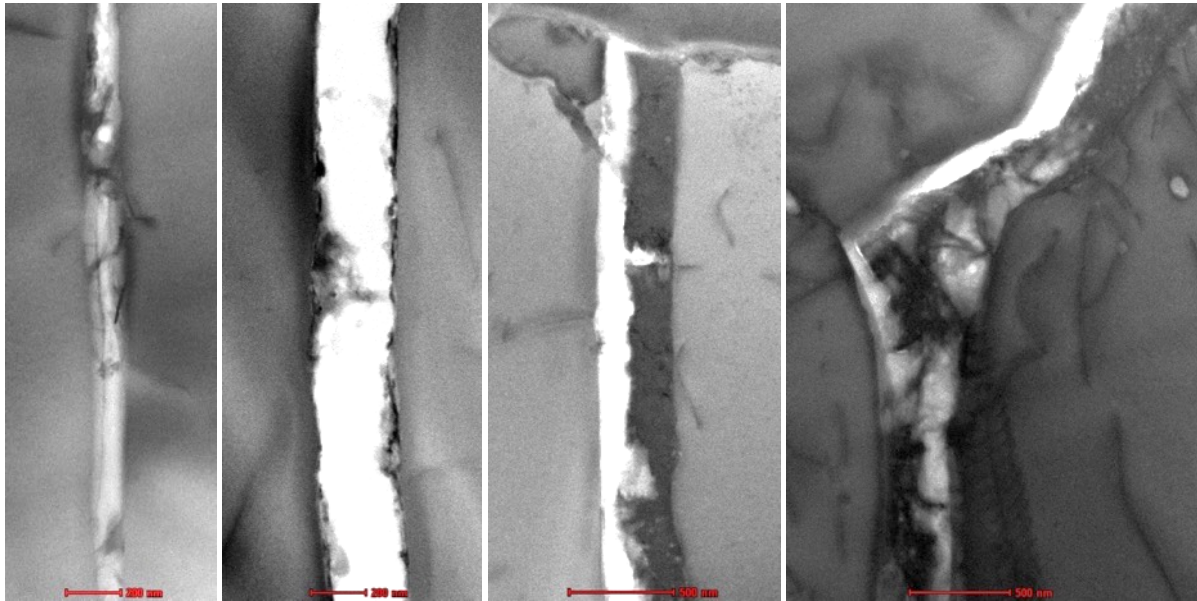
Figure 4.9 : Overview of W2-L2 cracks. (left) At higher magnification, (middle left), (middle right) and (right) some ASR product is visible mainly on the surface of quartz only partly filling the porosity.

One of the first observation in these early-stage samples is that a considerable part of the cracks is empty, which is not surprising considering the existence of many preexisting cracks. Besides, ASR formation will mostly start near the paste-aggregate ITZ, inside the aggregate (very likely in preexisting cracks) due to pH and silica concentration gradients, the gradients being highest within the aggregate adjacent to the paste boundary [43][105]. The cations in solution K+, Na+ and Ca2+ Si4+ are mainly provided by the dissolution of the products from the cement for the alkalis, the portlandite for the calcium and cryptocrystalline SiO2 mineral phases for the silica. ASR products then do not necessarily form where the dissolution occurs, but will form according to gradients mentioned above.

In addition to the morphological results, (see Figure 4.10), the typical average product composition show a (K+Na)/Si and a Ca/Si ratio from 0.15 to 0.35, with in some cases significant variations. The composition of all the products is displayed in the ternary diagram Figure 4.10. From these results, four groups are identified:

- A high alkali and low Si content product (G1).
- A slightly higher calcium content ASR product (G2).
- A slightly higher alkali content ASR product (G3).
- An only alkali and silica content ASR product (G4).

Each group characteristics are investigated in the four following subparts.
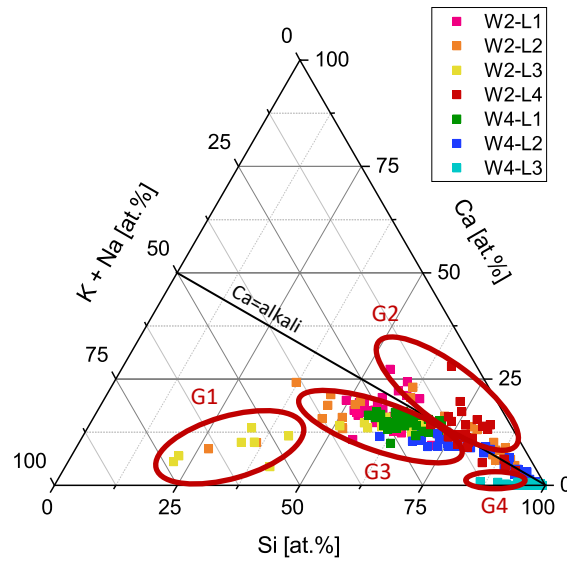
Figure 4.10 : Ternary diagram displaying normalized atomic composition for the elements Si, Ca, K+Na of all 7 lamellae.

## 4.3.2   High alkali and low Si content product G1

This product containing a very high alkali content and low Si content, with a (K+Na)/Si ratio from 1.0 to 3.0, corresponds to very specific areas of the product. It is always found at the edge of the bulky product as in Figure 4.11. In these areas, there is less product observed (as indicated by higher electronic transparency).

A possible explanation is that it corresponds to a growth zone, in which there is product formation when a sufficient Si concentration is reached.
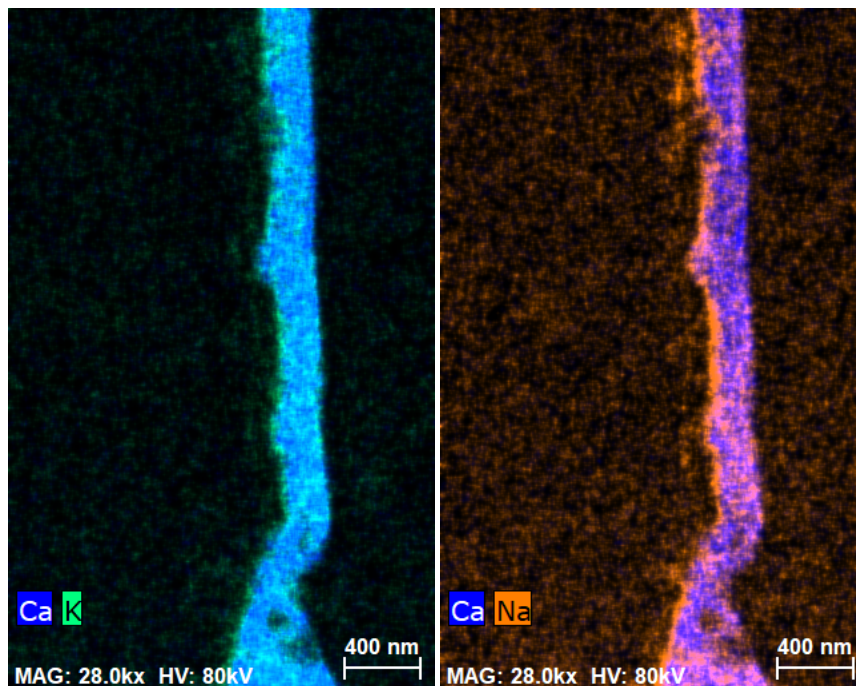


Figure 4.11 : Example in W2-L3 of inhomogeneous distribution of Ca and K (left) and Ca and Na (right) in ASR product. Ca is evenly distributed in the product, whereas K and Na are also accumulated at the product edge.

### 4.3.3 Slightly higher Ca content product G2

A slightly higher Ca/(K+Na) ratio is found in one sample, W2-L4 (see Figure 4.10). In this sample, as seen in Figure 4.12, the crack is very thin, its width is < 100nm. The calcium content was also increasing from one end of the crack to the other end, suggesting local concentration variations. The product is smooth and present most likely a granular morphology.
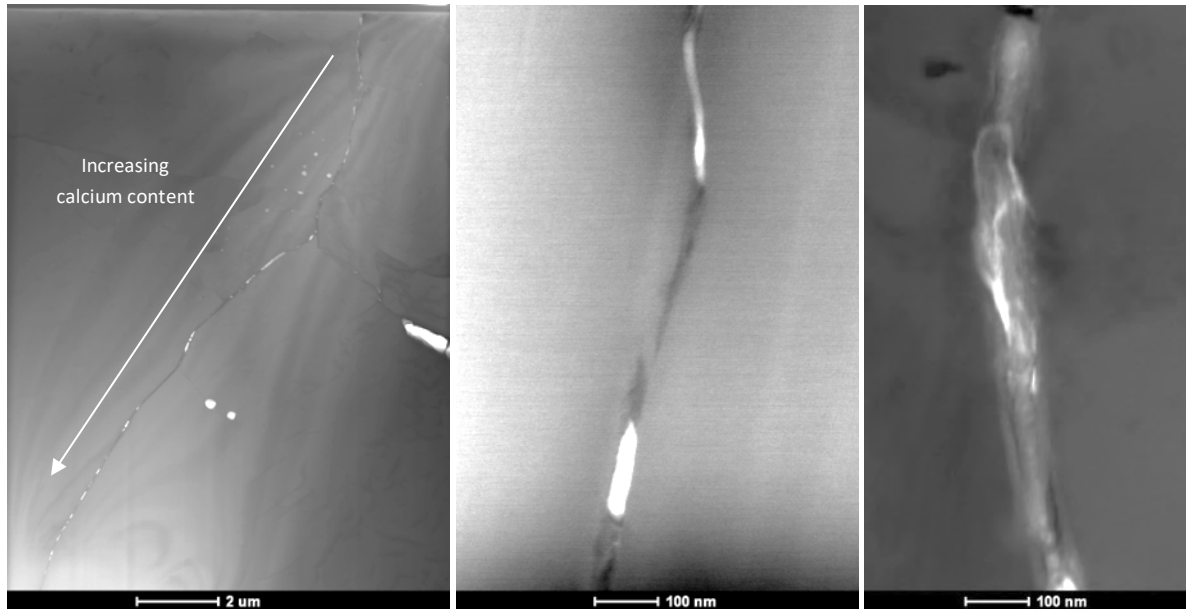


Figure 4.12 : Overview of W2-L4 cracks (left). At higher magnification, (middle) and (right) ASR product is visible.

### 4.3.4 Slightly higher alkali content product G3

The major part of the analysed ASR products has such a composition, with a Ca/(K+Na) ratio between 0.6 and 1.0, and both Ca/Si and (K+Na)/Si ratio between 0.15 and 0.35. Both granular and platey products have this group (G3) composition. A more detailed analysis of the two morphologies led to a small differentiation between the two, as seen in the ternary diagram Figure 4.13.
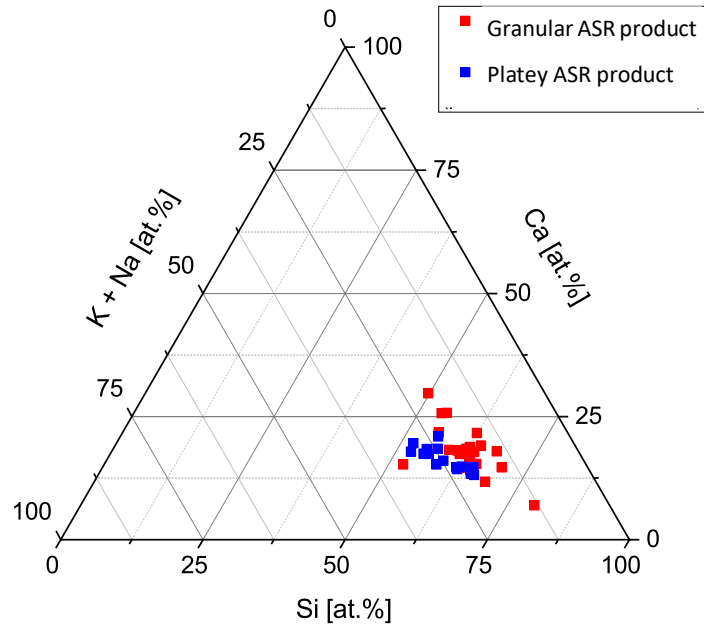
Figure 4.13 : Ternary diagram displaying normalized atomic composition for the elements Si, Ca, K+Na of the granular and platey products.

From all observations, there is a slight tendency of the granular product to contain more calcium than the platey one, with a Ca/(K+Na) ratio of 0.9 to 1.2 whereas the platey one is between 0.6 to 1.0. The granular product in some cases contained more calcium than alkali, thus belonging more to G2 than G3.

In addition, the elemental EDX maps qualitatively showed an inhomogeneity in the distribution of Ca and K (Figures 4.14 and 4.15). This inhomogeneity, which is difficult to detect in the quantitative analysis because it is at the nanoscale range, results in this compositional point scattering among G2 and G3 groups. The compositional difference observed between the granular and platey products is too thin to be validated, and could be influenced by this nanoscale inhomogeneity.

Concerning this inhomogeneous alkali distribution in the ASR products, there is no obvious reason for it. One possible reason could be drying applied during sample preparation. This possibly leads to the precipitation of the alkali-rich sol.
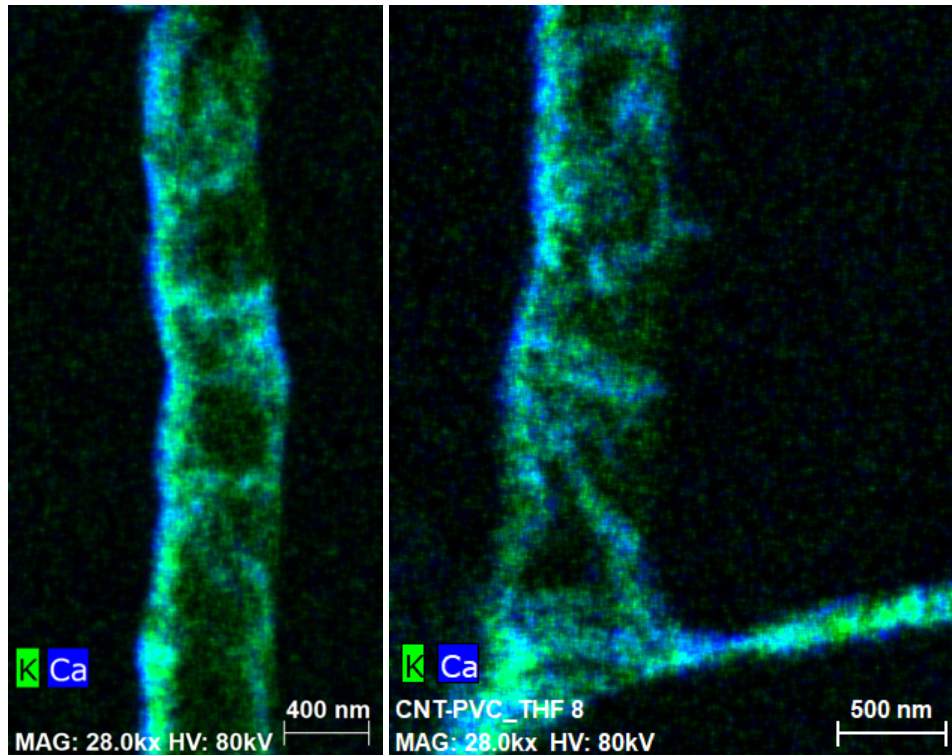
Figure 4.14 : Bright Field image and EDX maps for calcium, potassium and silica in W2-L1. Calcium and potassium confirm the presence of ASR product. Calcium is precisely distributed in the product whereas potassium is more homogeneously distributed in the crack.
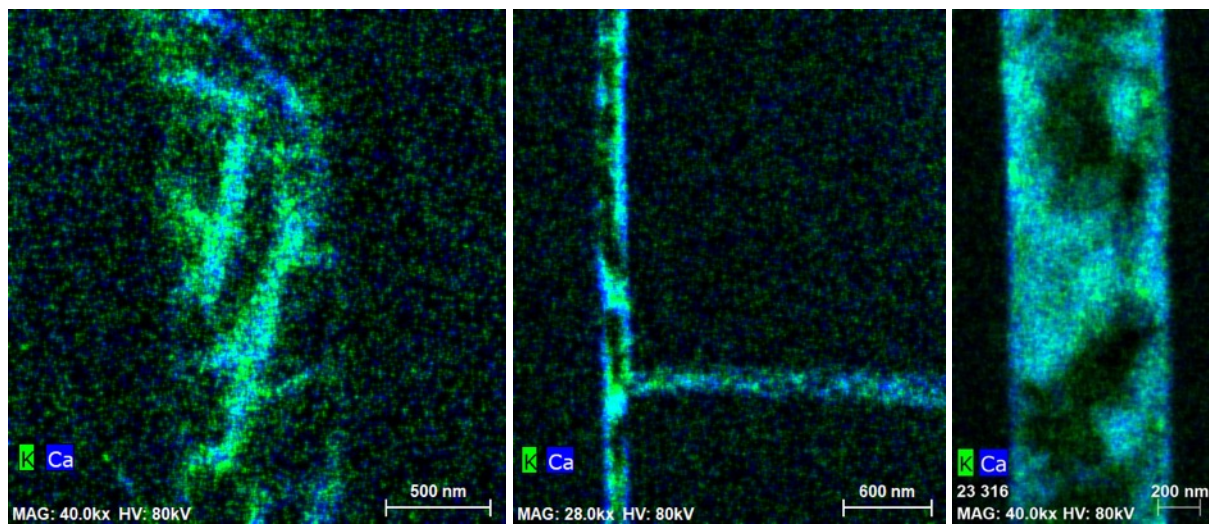


Figure 4.15 : Complementarity Calcium/Potassium. K is more diffuse than calcium.

There is a product inhomogeneity which is not only seen in the product itself. In some cases, for example in Figure 4.16, the alkali are also seen to partially penetrate the silica structure, whereas the calcium remains in the product only.
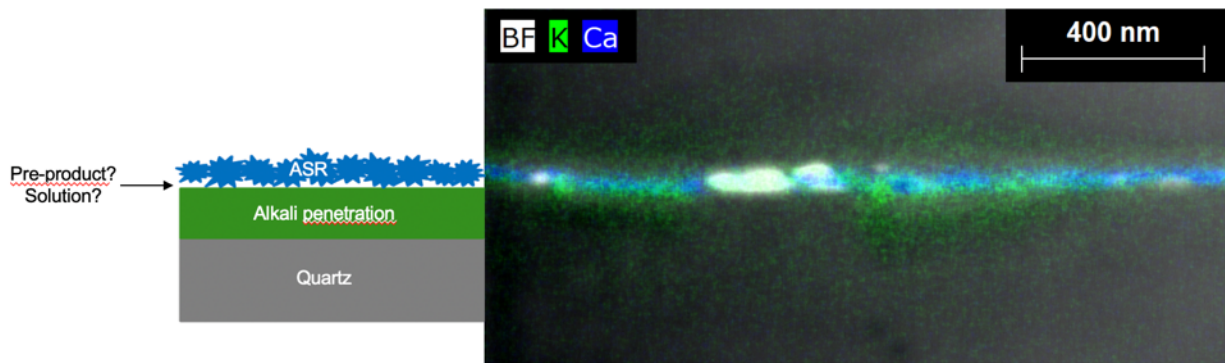
Figure 4.16 : Penetration of K into the silicate structure. Ca does not penetrate and stays in the ASR product.

Both Figures 4.16 and 4.18 indicate the possibility of a two-zone formation mechanism. After dissolution of the first layer of Q4 and Q3 silica tetrahedron (ST) (silanols ionisation or siloxane bonds rupture) by OH- and alkali attack, [11], [12] there is :

- Penetration of the alkali in the $SiO_2$ structure.
- Reaction of the dissolved silica with alkali and Ca to form ASR product.

Two possible explanations are given to explain the preferential penetration of the alkali over the calcium :

- The solubility of the alkaline hydroxyl is much higher than that of portlandite [106], thus the alkali concentration in the pore solution is much higher than the concentration of Ca.
- Alkali have a smaller hydraulic radius than calcium, implying they will diffuse more easily [34].

## 4.3.5  Only alkali and Si content product G4

In lamella W4-L3, where the tip of a crack was localized (Figure 4.17), the composition of the products is different from all other lamellae. Only alkali is present in the crack, with calcium only as traces as qualitatively seen in Figure 4.18 and quantitatively in Figure 4.10.
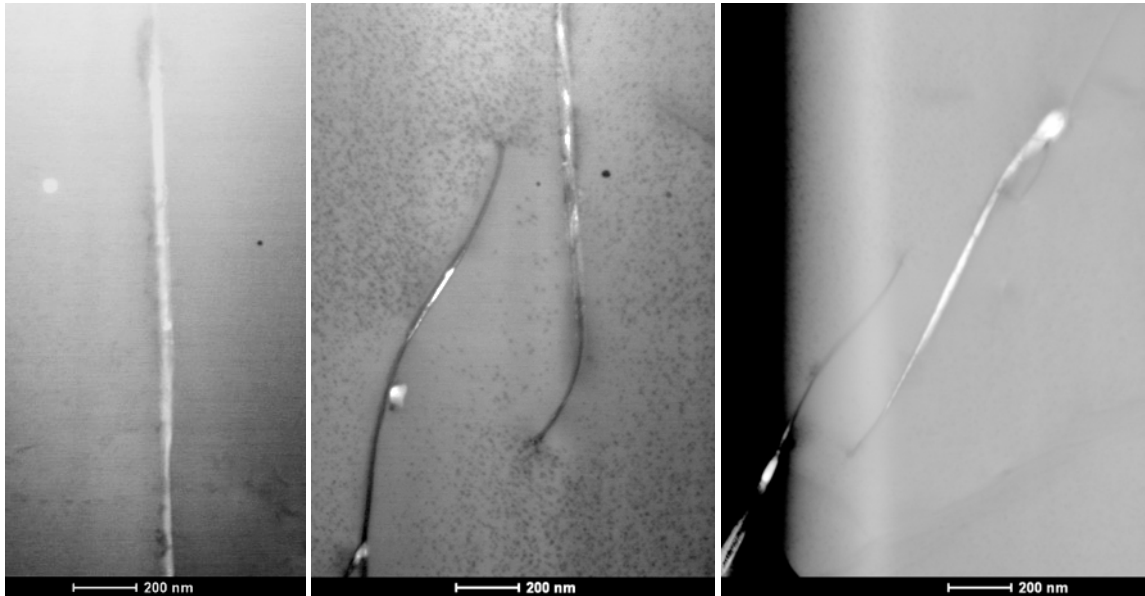
Figure 4.17 : Lamella W4-L3 with very thin crack (left) and (middle) its cracking tip. A second cracking tip is present (right).
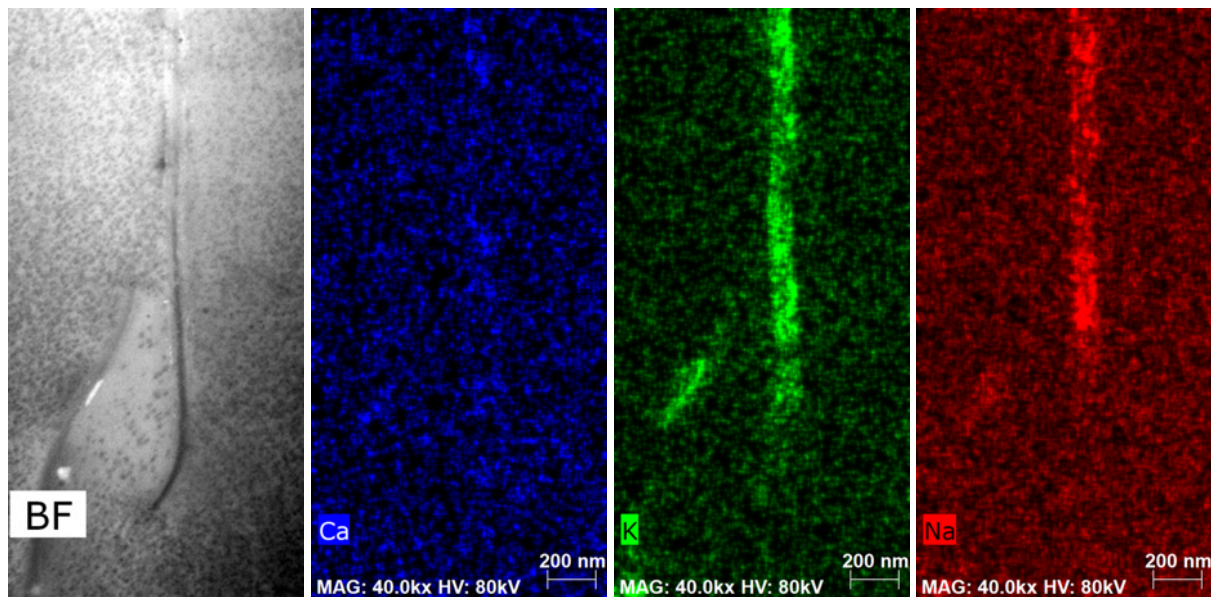


Figure 4.18 : W4-L3 tip of crack EDX analysis (left) Bright Field image, (middle left) calcium, (middle right) potassium and (right) sodium repartition.

Observation of a crack tip suggests that at this stage of reaction and in these local conditions, there is not enough pressure to open the crack.

### 4.3.6 Comparison K and Na

Concerning the difference in K and Na content, the products always contained more potassium (K/Na ratio mainly between 2.0 and 5.0) than sodium (see Figure 4.19). This was expected since the cement used for concrete production contains more K (K/Na ratio approximatively 3.5). There was a drastic increase of sodium concentration with regards to potassium at the product edges. Potassium is distributed more homogeneously in the product. A qualitative example is given in Figure 4.11 where the distribution of calcium, potassium and

sodium is clearly seen. There is a higher concentration of potassium and sodium at the rim of the product, in contrast to calcium, which is only located in the product.
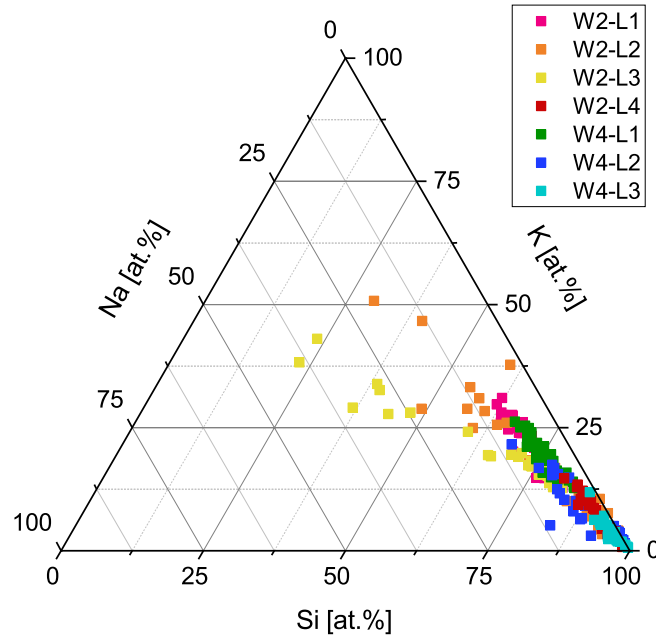


Figure 4.19 : Ternary diagram displaying normalized atomic composition for the elements Si, K and Na of all 7 lamellae.

### 4.3.7 Structure of the ASR products

Diffraction patterns of selected areas were analysed. In the case of samples with a crack width < 200nm an analysis of the product alone was impossible and the results where thus not considered. The early stage granular products showed an amorphous structure in every case. A weak diffraction pattern was observed for only one sample, the platey product in W4-L1 as seen in Figure 4.20. In Figure 4.20 (right) the defined ring shape is typical for nanocrystalline material. In this case, the ring is more intense (but not very bright) in some areas, indicating a preferential orientation of the formed nanocrystals.

The lack of a diffraction pattern in the case of the granular product and the weak one in case of the platey one indicates that the products are amorphous or nano-crystalline. So far, little is known about the structure of these products. Raman microscopy of amorphous ASR products formed in aggregates shows that they are dominated by $Q^2$ (chains of $SiO_2$ tetrahedra) and $Q^3$ (layers of silicon tetrahedra) sites [22]. Neither $Q^1$ nor $Q^4$ sites are present. The broad Raman bands indicate a structure with a relatively low degree of order. This is in line with the presented results of SAED.
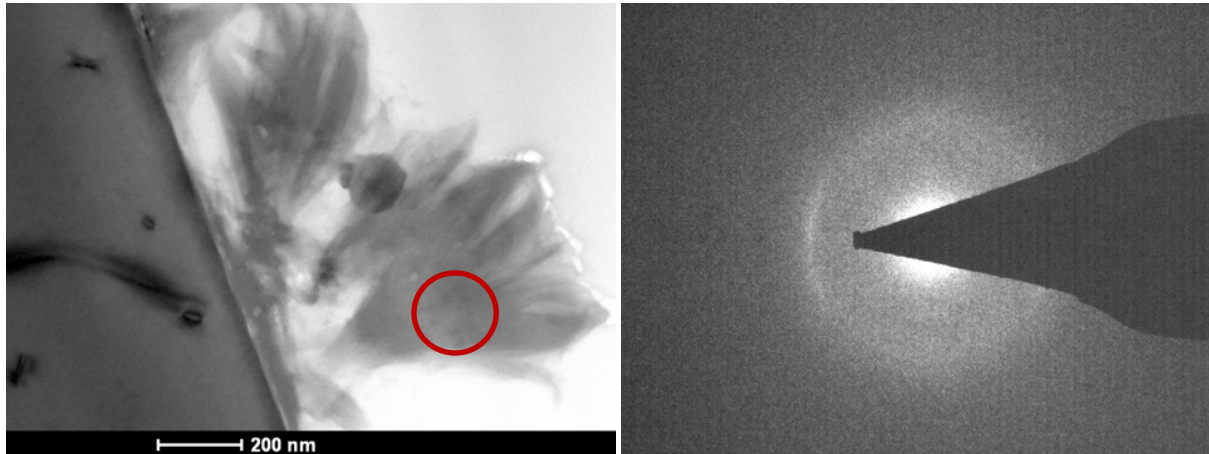
Figure 4.20 : Electron diffraction pattern (right) of the platey product from W4-L1 (left).

## 4.4     Conclusion

Observation of early stage ASR products is possible using the method described in chapter 3. It is clear here that we are observing in each lamella different stages of the ASR formation, not fully linked to the time spent in accelerated formation. The heterogeneity of the product gives a good insight on the formation process of the product, highlighting the different roles of the calcium and the alkali. The following points emerge from this study :

- ASR products are forming within preexisting cracks of the aggregates, close to the cement paste boundary, due to pH and silica gradients [105] as in Figure 4.21.
- Two ASR product types already exist at early age: a granular – amorphous product and a platey – nanocrystalline one. Presence of one rather than the other likely depends on ageing and eventually the local availability of reactants.
- The distribution of alkali and calcium is quite inhomogeneous. The inhomogeneity is likely related to alkali penetration of the silica, and thus to the product morphology: the granular product has a slightly higher calcium content than the platey one. A less dense network allows for increased penetration of the alkali.
- The difference in morphology in these samples was not influenced by the alkaline species present. Both granular and platey product exhibited a K/Na ratio of average 3.0, mirroring cement composition.
- Significant expansion is already observed in the presence of amorphous product mainly, at 60°C.
- Calcium is very quickly incorporated into the ASR product.
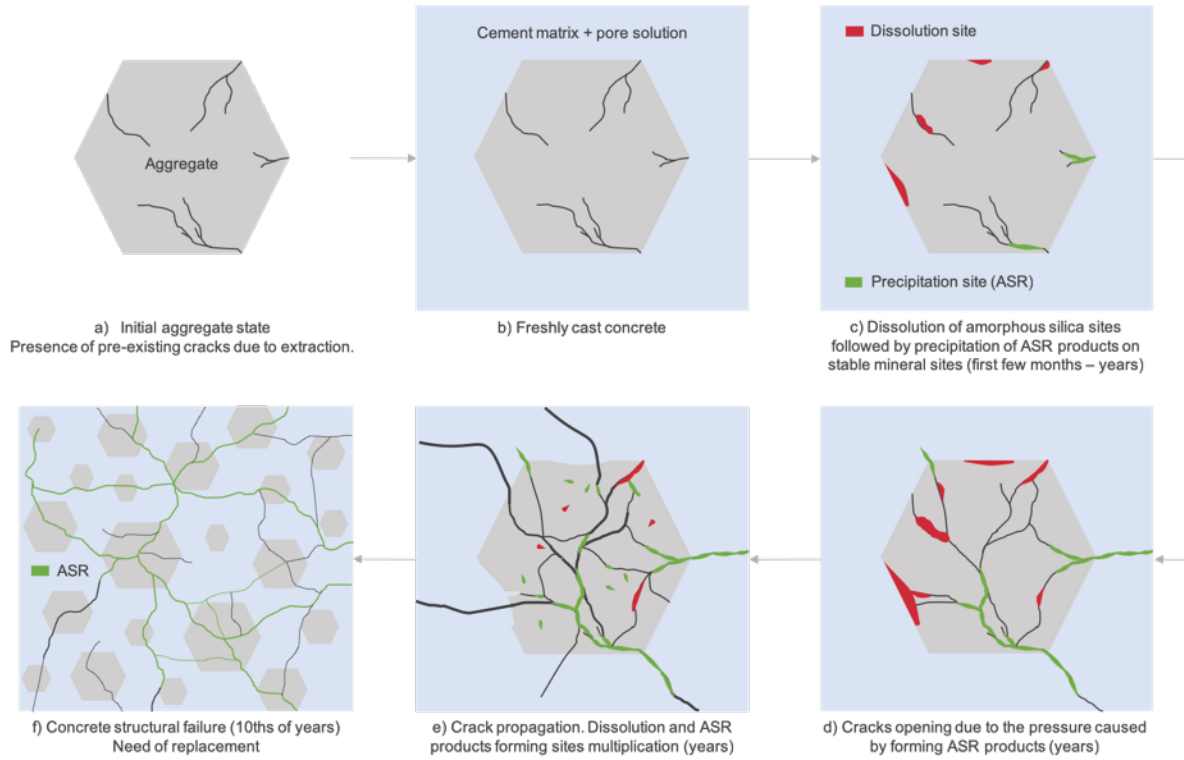
Figure 4.21 : Scheme of the ASR phenomenon evolution in concrete.

# Chapter 5　Early-stage　ASR　product evaluation in concrete exposed to more field-realistic accelerated conditions.

**Note : This chapter is based on an article in preparation for submission to a peer-reviewed journal.**

Contribution of the doctoral candidate : Conceptualization, Methodology, Formal analysis, Investigation, Writing of the first manuscript draft.

## Abstract

ASR formation is a long process in real life structures. The first signs generally occur after one or a few decades of service life. Fortunately, methods and standards have been developed in laboratories to accelerate the reaction and assess the expansion evolution in the frame of a few months. These accelerated conditions laboratory tests offer a good prediction for given concrete mixes. However, due to the boundary conditions changes and accelerated kinetics, the test failed in some cases to predict the real-life behavior. More field realistic accelerated conditions are needed. In this study, the early stage ASR product formation at 38°C instead of 60°C in the standards and stored in pore solution instead of water vapour to avoid too significant alkali leaching which have an impact on small samples, is investigated. It is explored if a change in these accelerated conditions have an impact on the morphology, composition and structure.

## 5.1    Introduction

ASR induces degradation of the concrete in the long term, after decades of service life, even though the first signs might be detected after a few years. Studying the phenomena is thus a challenge, and accelerated conditions have been used. Acceleration of the reaction rate is obtained by increasing the test conditioning temperature, to 50°C or 60°C in most standards ([97], ASTM C 1293 and 1567).

Temperature is an important factor known to increase reaction kinetics, and in the particular case of ASR, it might alter the gel development by modifying the morphology of the products [107]. Concerning the structure, the crystalline ASR product synthesized by Shi [46][47] was shown to have a change in d-spacing for the first XRD peaks, with a change of the temperature. In a more straightforward way, the temperature effect is directly seen when analysing the expansion curves of a given concrete mix. At lower temperature like 38°C, the reaction is delayed and some systems may behave differently compared to 60°C proposed by most standards [98][108][109]. Comparison between the ASR products formed at early age in accelerated standard and in more field realistic conditions has to the author knowledge not been evaluated so far. This study aims to address the differences observed between ASR product formed at 38°C and 60°C, before and after the first signs of ASR are detected.

## 5.2    Material and method

It is clear that the environmental conditions play a significant role. The onset of swelling is delayed approximately 4 months at 38°C, in comparison with 60°C. The samples stored in water vapour (WV) swell for a few months, but finally reach a plateau after 2 to 6 months Figure 5.1, which is less observed for samples stored in pore solution (PS) [98].
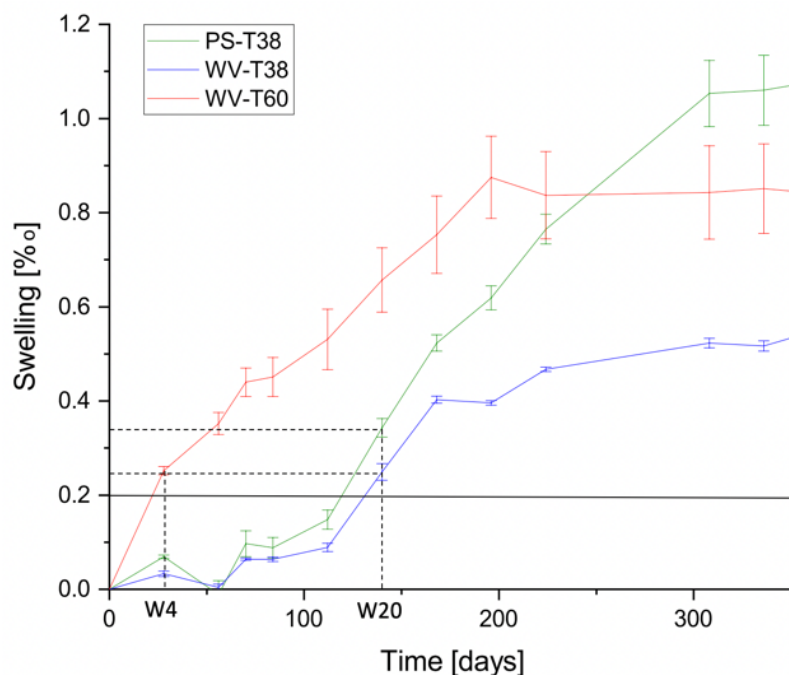


Figure 5.1 : Relative expansion of the concrete prisms as a function of time, in three different conditioning : in pore solution and 38°C, in water vapour and 38°C, in water vapour and 60°C.

This behavior indicates the leaching of the alkaline species from the concrete. The concrete depleted in alkali decreases the ASR formation rate and thus the expansion. It is confirmed by Inductively Coupled Plasma – Optical Emission Spectrometry (ICP-OES) analysis reported in Table 5.1. The alkali concentration measured in the water from the storage box increased drastically: K concentrations tripled and Na quintupled, after 9 months. These alkalis necessarily come from the leaching of the concrete prisms at high temperature. When the prisms are stored in pore solution, the alkali leaching is limited and thus provides a more realistic swelling behavior in the long term. Leaching occurs in real structures, but it only affects a small part of the total concrete volume.

Samples at 60°C were collected after 2 and 4 weeks in accelerated conditions (collected and analysed samples from chapter 4). To have a point of comparison between the ASR product formation at both temperatures, it was decided the 38°C samples should be collected at a time when they had a similar expansion to the 4 weeks 60°C samples. The later was showing an expansion of approximately 0.3‰, corresponding to a collection time of 20 weeks at 38°C, as seen in Figure 5.1. For the 2 weeks samples at 60°C, expansion was not measured, but was necessarily below 0.3‰, or even non-existing yet. Considering that, 38°C samples after 4 weeks in accelerated conditions are also analysed. There is no clear sign of expansion, but ASR products are present before the expansion is seen.

The expansion state for both 38 and 60°C prisms is the same at W20 and W4 respectively, and the differences or similarities in their ASR products can be assessed.

Table 5.1 : ICP-OES measurements of the solution from the accelerated tests boxes, after 1 and 10 months, to investigate the alkali leaching.

| Sample | Month | Al [mg/l] | Ca [mg/l] | K [mg/l] | Mg [mg/l] | Na [mg/l] | Si [mg/l] | pH |
|---|---|---|---|---|---|---|---|---|
| PS-T38 | 1 | 1,64 | 47,6 | 8350 | - | 1890 | 1,74 | 13,29 |
| | 10 | 6,92 | 5,64 | 9010 | <0.5 | 2110 | 311 | 12,95 |
| WV-T38 | 1 | - | 130 | 828 | - | 141 | 0,266 | 12,48 |
| | 10 | <0.5 | 1,77 | 3950 | <0.5 | 727 | 233 | 11,11 |
| WV-T60 | 1 | - | 173 | 1900 | - | 334 | 0,492 | 12,75 |
| | 10 | 0,821 | <0.5 | 6280 | <0.5 | 1840 | 1040 | 12,81 |

## 5.3    Results and discussion

### 5.3.1   General

From the nine lamellae prepared and analysed, two revealed very few to no ASR product in their crack (both at 4 weeks in water vapour and 38°C). Only traces of Ca and K are visible with the EDS analysis at the aggregate walls, suggesting the very beginning of the product formation. Due to the scarce product quantity, no quantitative analysis was done, and the results are not presented. The fact that ASR product is very scarce is

not surprising since at 38°C, and after only 4 weeks in accelerated conditions, no swelling occurred as seen in Figure 5.1.

In another case, one lamella contains quite a lot of product with an extremely high Ca content compared to the alkali and silica contents. The Ca/Si ratio ranges between 1.0 and 1.2. From the morphology, which is very fibrillar, with thin junctions in Figure 5.2, and the compositional analysis, it is clear that the product is C-S-H. These three lamellae are not included in the following results part and in Figure 5.3.
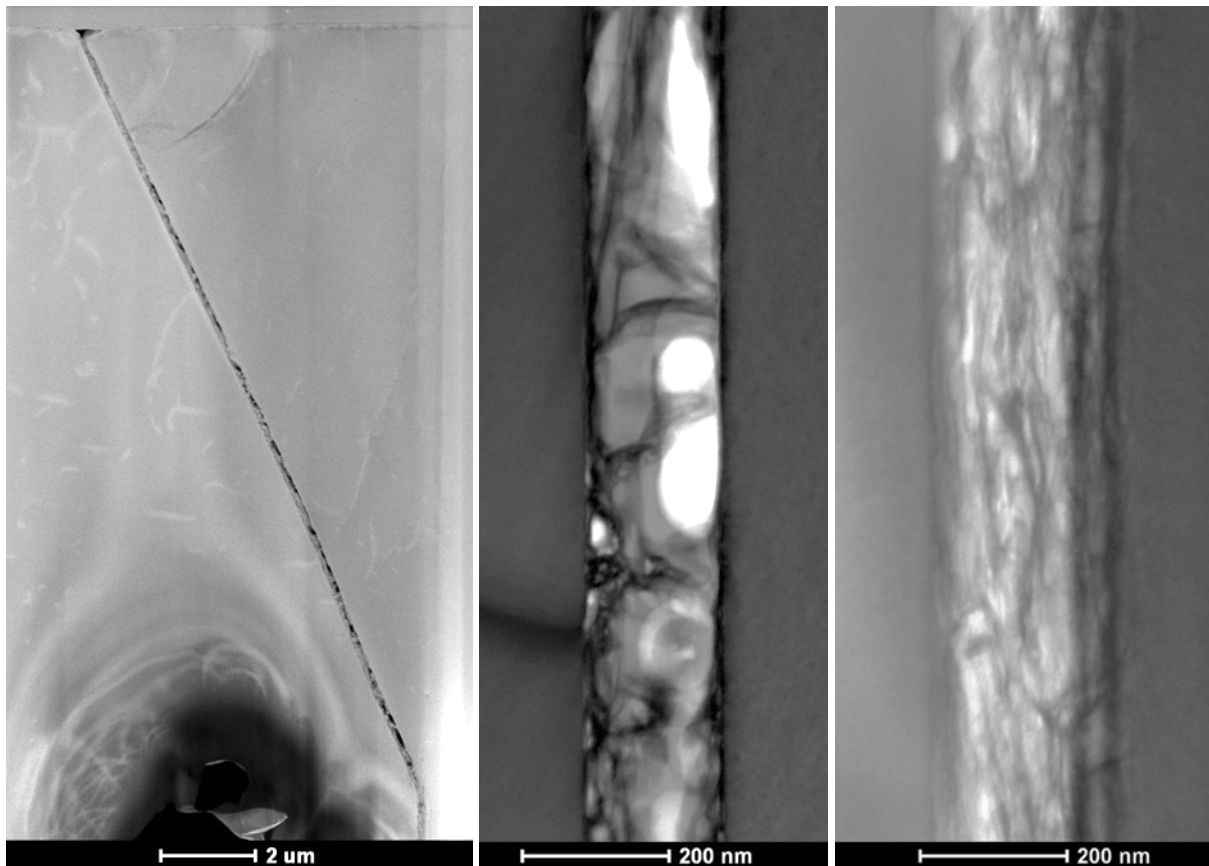


Figure 5.2 : BF and DF images of the product present in an aggregate crack after 4 weeks in water vapour at 38°C.

The other six lamellae showed cracks partially or totally filled with ASR product. The composition of their product is shown in the ternary diagram Figure 5.3. From these results, four groups G1 to G4 are identified :

- The high alkali and low Si content product (G1).
- The high calcium content ASR product (G2).
- The classical ASR product composition, with a similar alkali and Ca content, only slight variations (G3).
- The slightly higher alkali content ASR product (G4).

Each group characteristics are investigated in the following subparts.
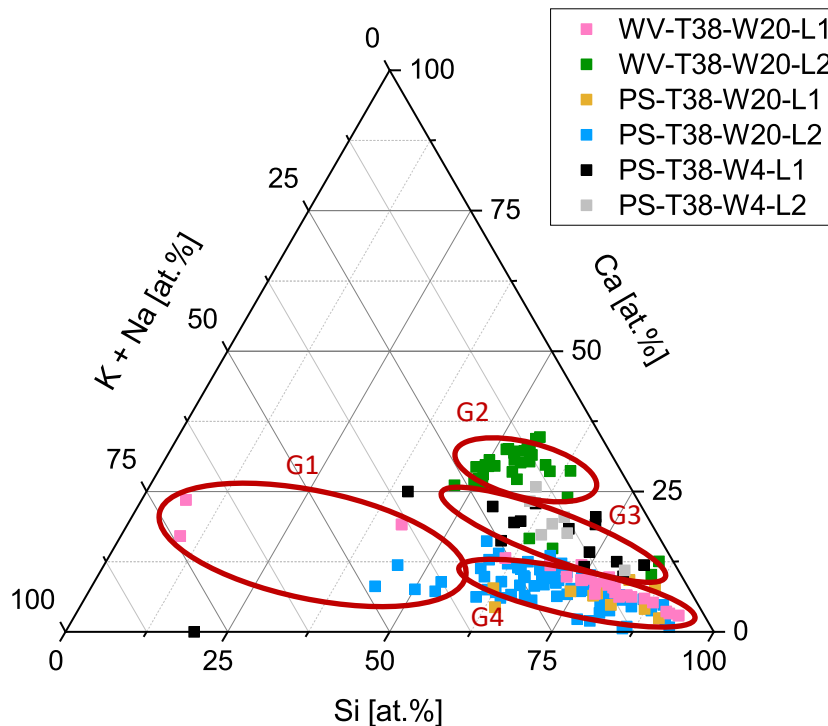
Figure 5.3 : Ternary diagram showing the normalized ASR product atomic percent composition in terms of Si, Ca and alkali, for six lamellae. One point represents a small analysed area of the product. Four groups of composition are identified.

## 5.3.2   High alkali and low Si content product G1

In contrast with the results from chapter 4, in which the samples were accelerated at 60°C instead of 38°C, the products morphology is not distinguishable anymore, as seen in Figure 5.4. There is no evidence of a granular or a platey morphology as reported at 60°C, despite the compositional differences and the previous link found between granular product and higher calcium content, and platey product associated with similar Ca/Alkali content.

An explanation is the slower kinetics due to the lower temperature, which favors the nucleation of the product rather than its growth, and leads to a denser product. Because of the slow growth rate at lower temperature, saturation is more easily reached (dissolution rate is closer to reaction rate), similarly to C-S-H [110].

The only product found is in a granular form, which could be a precursor of the ASR product, because of its high alkali but low Si content as well as its morphology (as seen in Figures 5.5 and 5.7). It contains a very low amount of Si and a lot of alkali, Alk/Si ratio ranging from 1.0 to 7.0 instead of the usual 0.2 to 0.35. It suggests that it is forming before the ASR product, and that it is a transitional formation stage, before uptaking more Si and forming the typical ASR product, or it could be due to precipitation during drying. Although the granular microstructure looks similar to the one of the ASR product observed at 60°C, their scale is not the same (nanometers order for 38°C vs. tenths of nanometers order for 60°C). At 60°C no precursor product could be clearly observed.
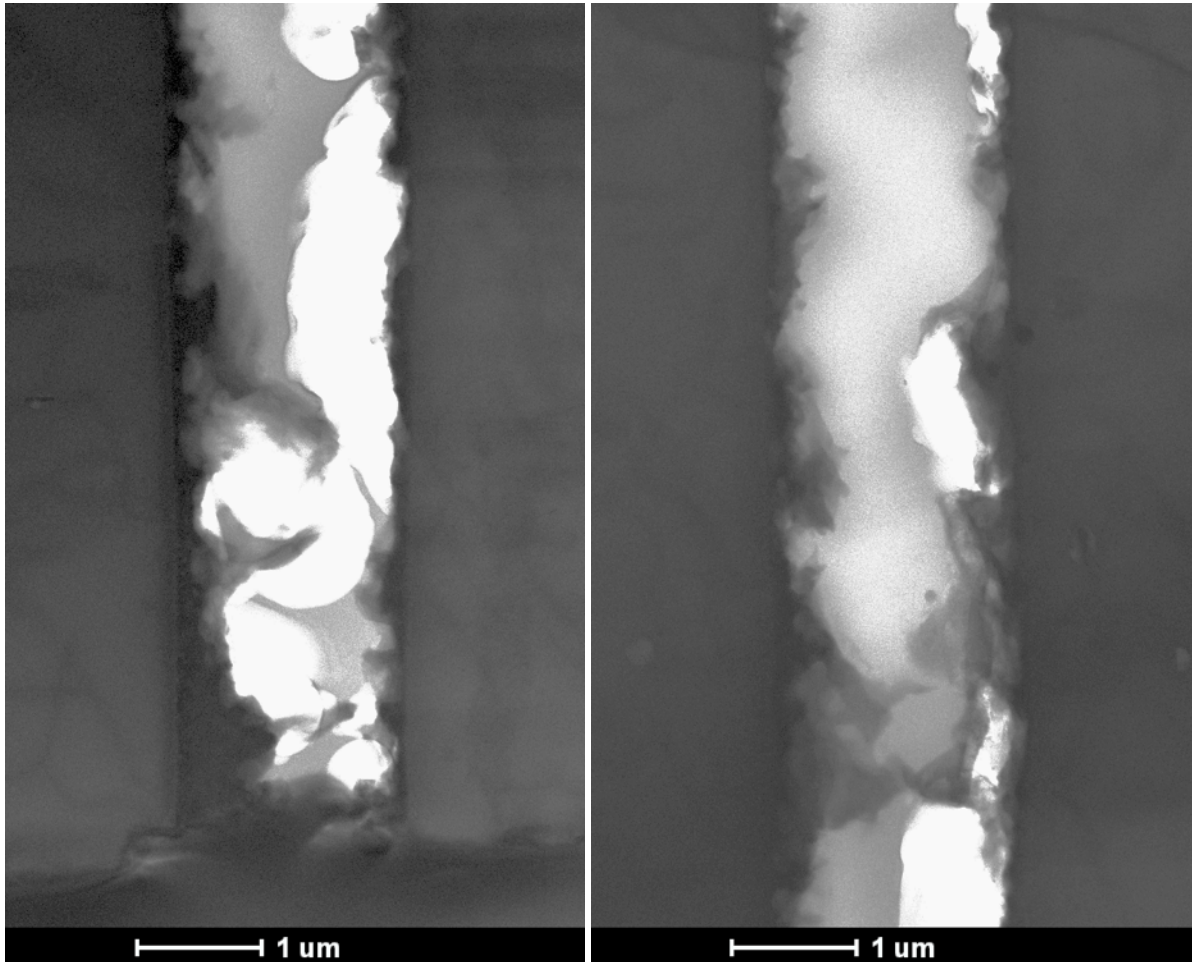
Figure 5.4 : ASR product partially filled crack, after 20 weeks in water vapour and 38°C. The product morphology is smooth.

An example is given in Figure 5.5, in which the composition is analysed for the precursor product (ASR 1), an overlap of precursor and ASR product (ASR 2 and 3) and ASR product (ASR 4). The results presented in Figure 5.6 clearly show the change of composition from a high alkali content to an enrichment in Si and a Ca/alkali ratio tending to 1. The composition of the precursor product is confirmed by the example of Figure 5.8, which composition also show a high alkali content. The analysed area is more clearly seen in Figure 5.7.
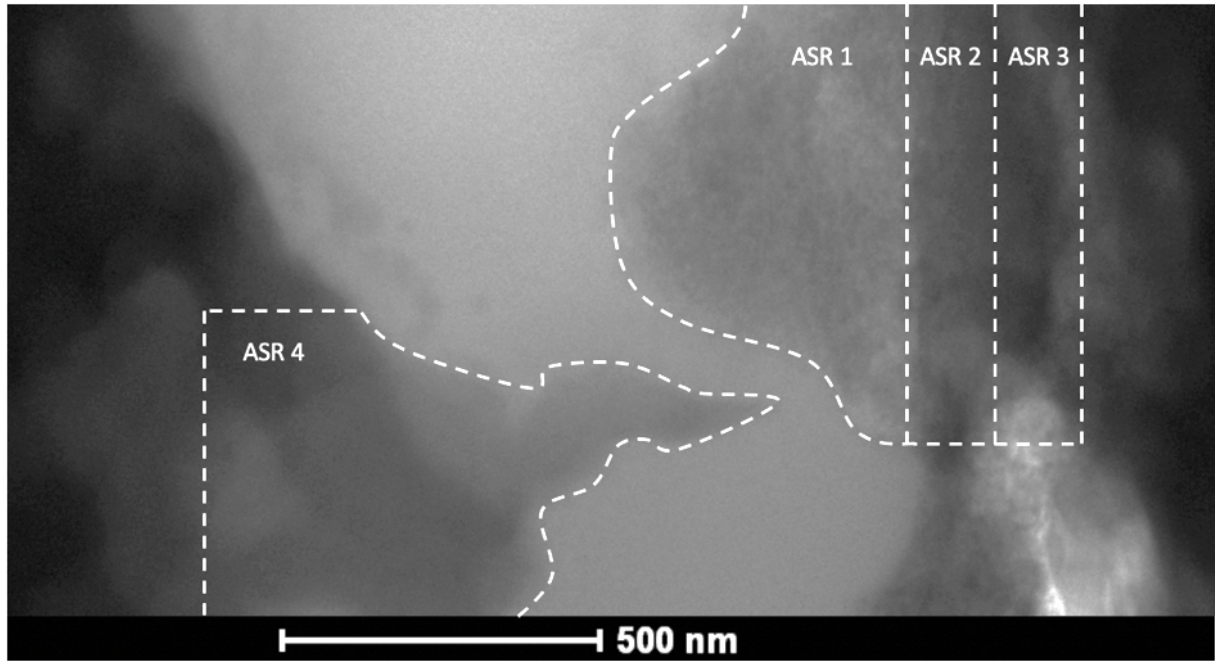
Figure 5.5 : High magnification view of an area from Figure 5.4, in which different morphologies are distinguishable : ASR 1 has a granular texture whereas ASR 4 has a smooth texture.
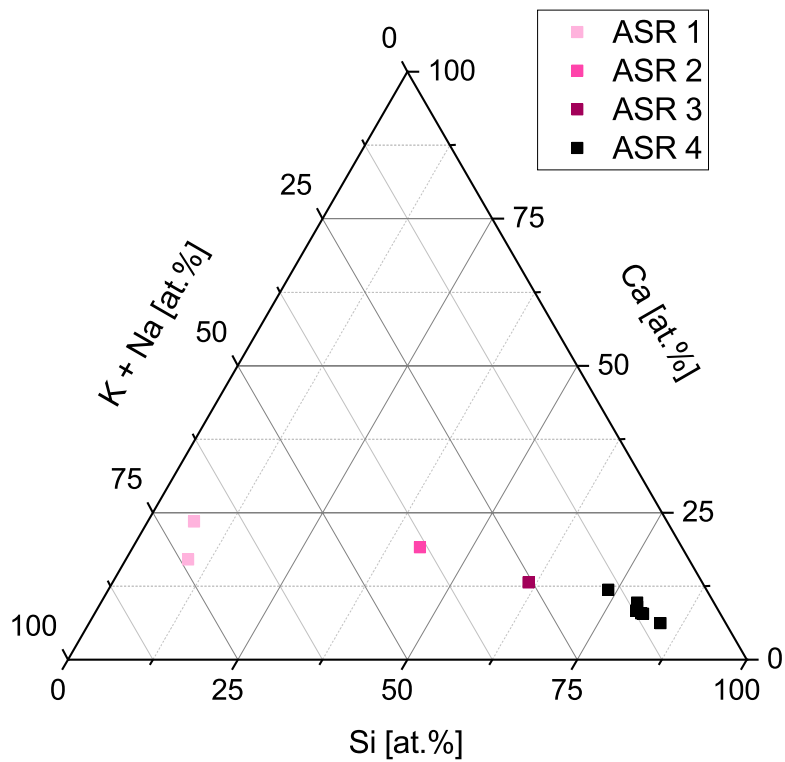


Figure 5.6 : Ternary diagram showing the normalized ASR product atomic percent composition in terms of Si, Ca and alkali, of the area defined in Figure 5.5 : ASR 1, 2, 3 and 4. There is a clear change in composition between the granular and smooth product.
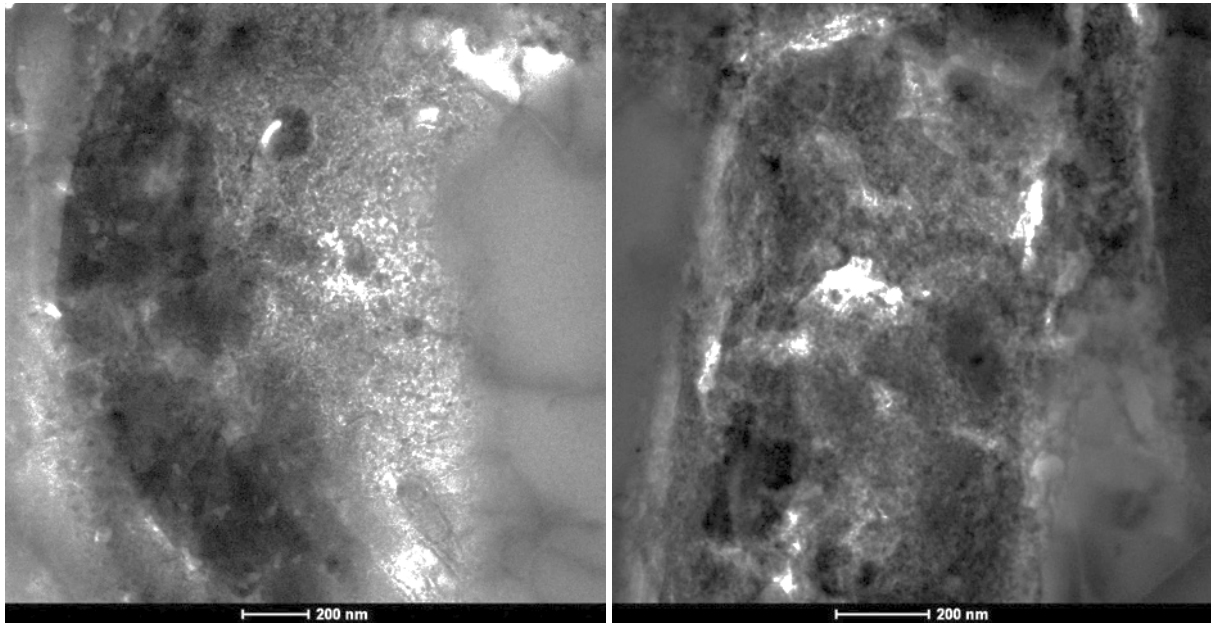
Figure 5.7 : Granular morphology of ASR product after 20 weeks in pore solution and 38°C accelerated conditions.
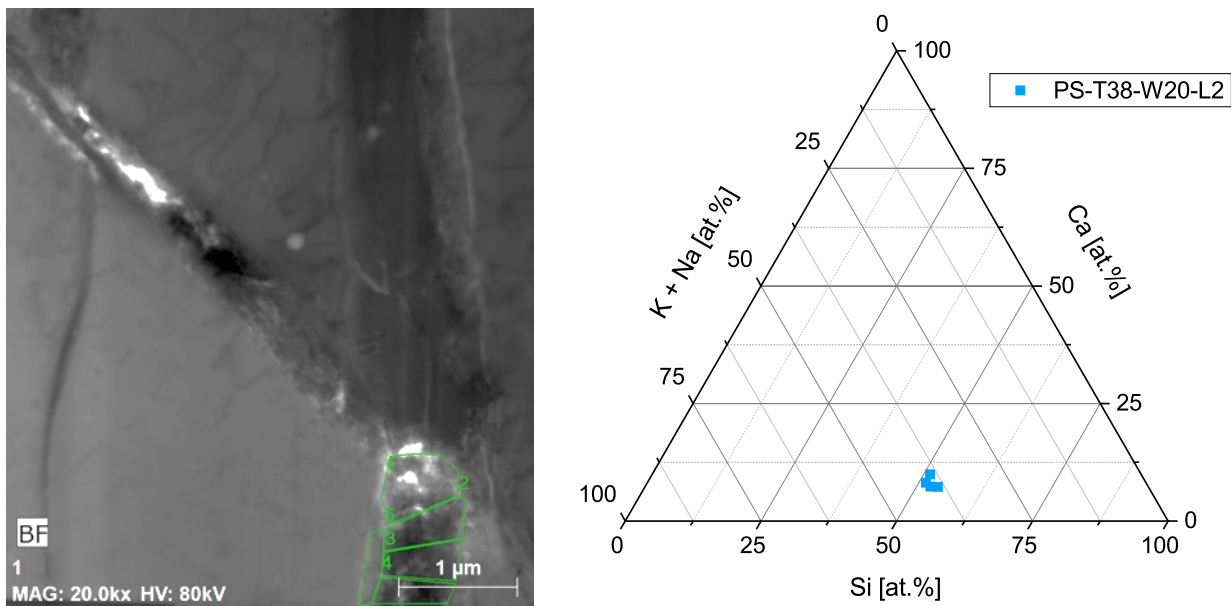


Figure 5.8 : BF image displaying the analysed green area containing the granular morphology ASR product (left) and their composition in the ternary diagram showing the normalized ASR product atomic percent composition in terms of Si, Ca and alkali (right).

Furthermore, in the case of samples which stayed 4 weeks in accelerated conditions, high alkali and low Si content product is also observed. Very little ASR product is present in the crack, with only a thin layer of a few nm partially covering the aggregate walls. It is more easily seen with the EDS analysis Figure 5.11. From the EDX analysis, an inhomogeneity between calcium and potassium is visible (Figure 5.9 right and Figure 5.10). The quantification confirms the inhomogeneity, with a high calcium content in the bulk product and a potassium ionic concentration increase around the product, at the external rim of the product. Far from the

product, the Ca concentration even drops to 0, with only silicon and alkali ions remaining. Unlike at W20, the product is present in too small quantities at W4 to have a resolution good enough to interpret the morphology.

At W4, in contrast to W20, it is easier to distinguish the different zones, because there is very little product : the ASR product containing high Ca content and the surroundings containing high alkali content, Figure 5.11. At W20, even though the lamella is thin, because there is much more product the different layers overlap and it is more complicated to separate the zones. This overlapping (with alkali-rich precursor product) is a possible explanation to why the ASR products majority tends to contain more alkali (in opposition to the less ASR dense areas). With time, the ASR product continue to form, and thus densify, leaving less alkali rich areas and more Ca rich areas. Alkali are progressively replaced by the forming ASR product, uptaking Ca instead.

In addition, the structure of the precursor product was found to be amorphous.
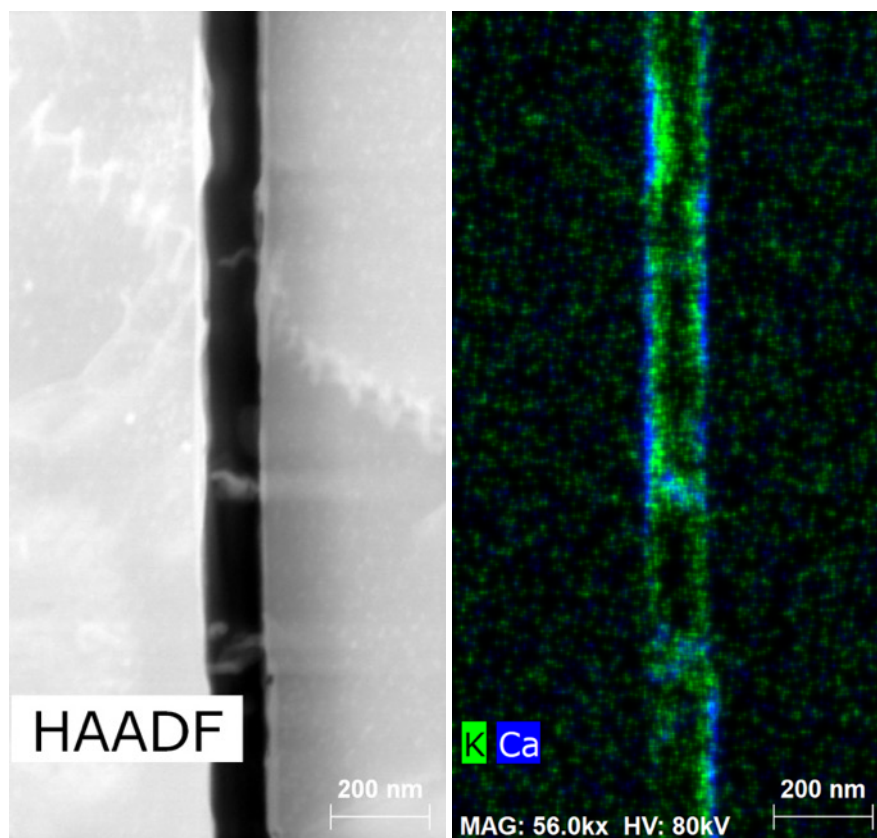


Figure 5.9 : DF image of a crack after 4 weeks in pore solution and 38°C (left) and its EDX Ca and K mapping distribution (right).
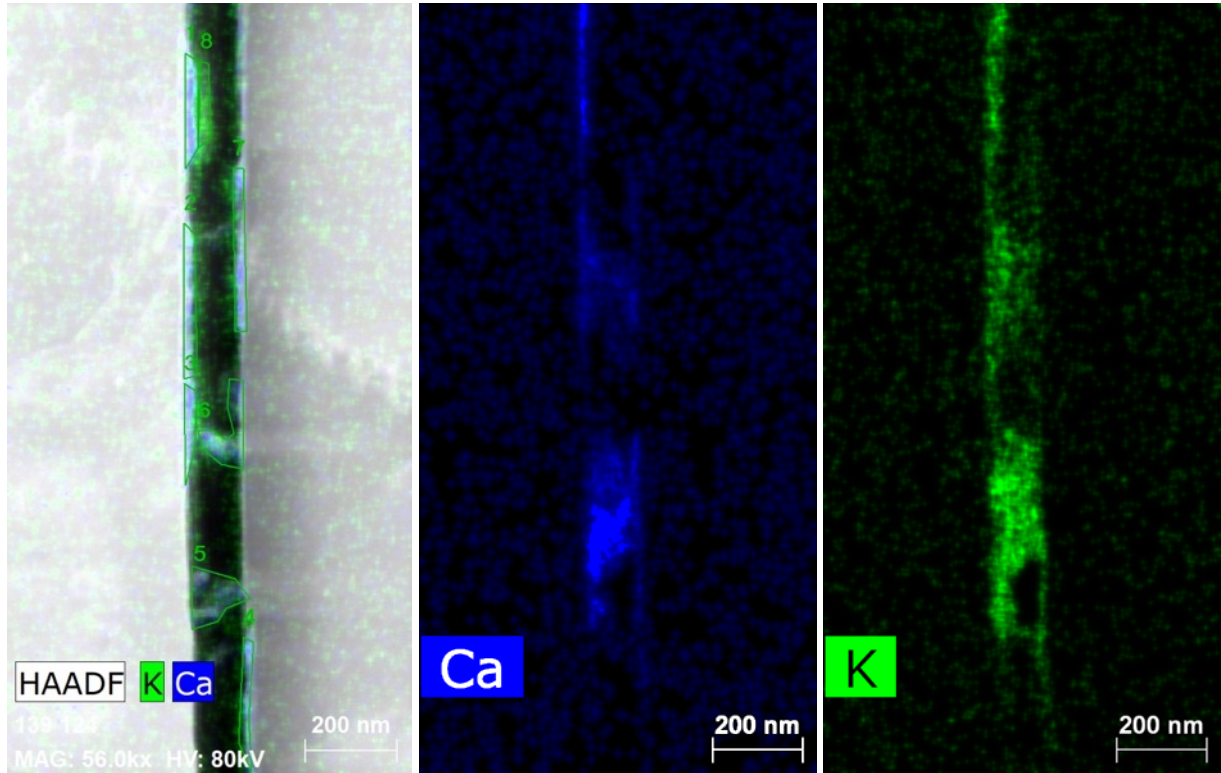
Figure 5.10 : DF image and Ca-K distribution of a crack after 4 weeks in pore solution and 38°C (left). Ca (middle) and K (right) EDX mapping distribution.
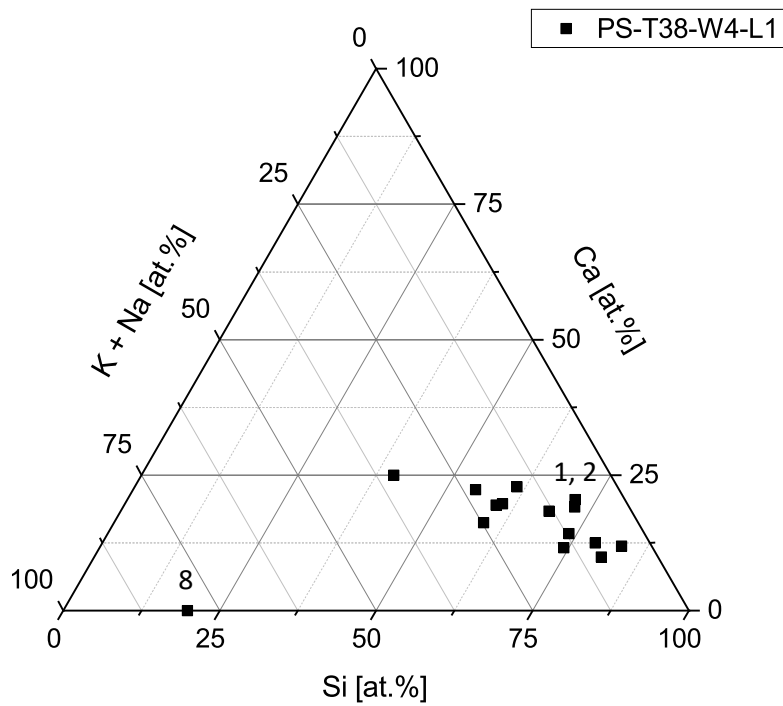


Figure 5.11 : Ternary diagram showing the normalized ASR product atomic percent composition in terms of Si, Ca and alkali, of the ASR product present in a crack after 4 weeks in pore solution and 38°C. The analysis corresponds partly to the defined green areas in Figure 5.10 (left), as clearly specified by the number 1, 2 and 8 for example. Number 8 corresponds to an area containing mainly K as seen in Figure 5.10.

### 5.3.3 High Ca content ASR product G2.

A high Ca content was found in the product, except for the product in area 1 in Figure 5.12, which contained an equal amount of Ca and alkali, probably due to less ASR product quantity and contribution of alkali accumulating at the product rim.

Despite the presence of a different morphology, as seen in Figure 5.12 (middle and right) and indicated by the arrows, no significant difference in composition was observed between the areas containing the fibrillar/granular and the smooth morphology.

There are three hypotheses to explain the high calcium content in WV-T38-W20-L2 lamella :

- Calcium has replaced the alkali over time. At the beginning of the reaction there is a lot of alkali and as things progress the product forms and age, alkali ions are replaced with calcium ions, and the product is also densifying.
- Alkali have leached out.
- C-S-H has also grown in the area and is taken into account in the analysis.

Even though the morphology of the granular/fibrillar product from Figure 5.12 is similar to the one of C-S-H, it is unlikely to be it. As reported above, no significant calcium increase was found in this product in comparison with the smooth product in the middle of the crack.
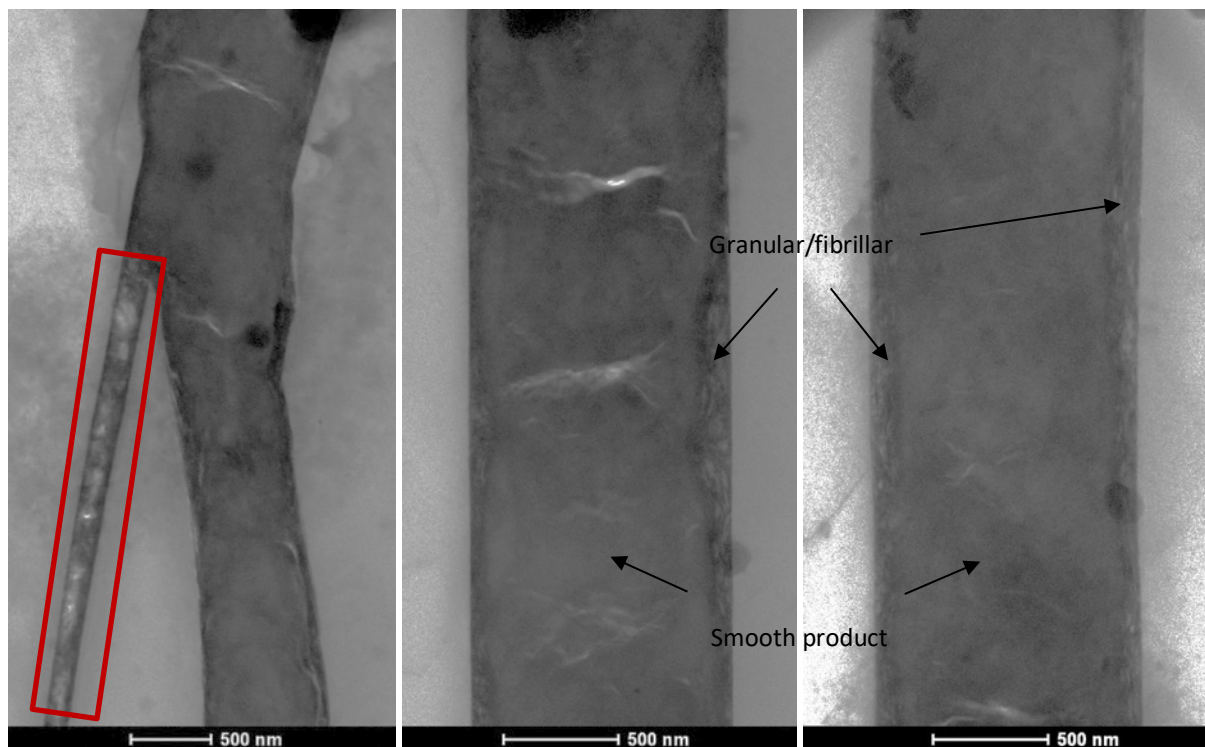


Figure 5.12 : BF images of a crack after 20 weeks in water vapour and 38°C. A thinner and less filled crack is highlighted by area 1 (left). Smooth and granular/fibrillar product is distinguishable (middle and right).

### 5.3.4 Classical ASR product composition, with a similar alkali and Ca content G3.

This composition was found in samples exposed to accelerated conditions after 4 weeks only Figure 5.13, and not after 20 weeks. In this particular case, the compositional results are in fact an average between two distinct compositions. The ASR product found has a higher calcium content, but when the analysis is done, because of the scarce product quantity, alkali present in the surroundings of the product are taken into account, Figures 5.9 and 5.10 (see explanation 5.3.2).
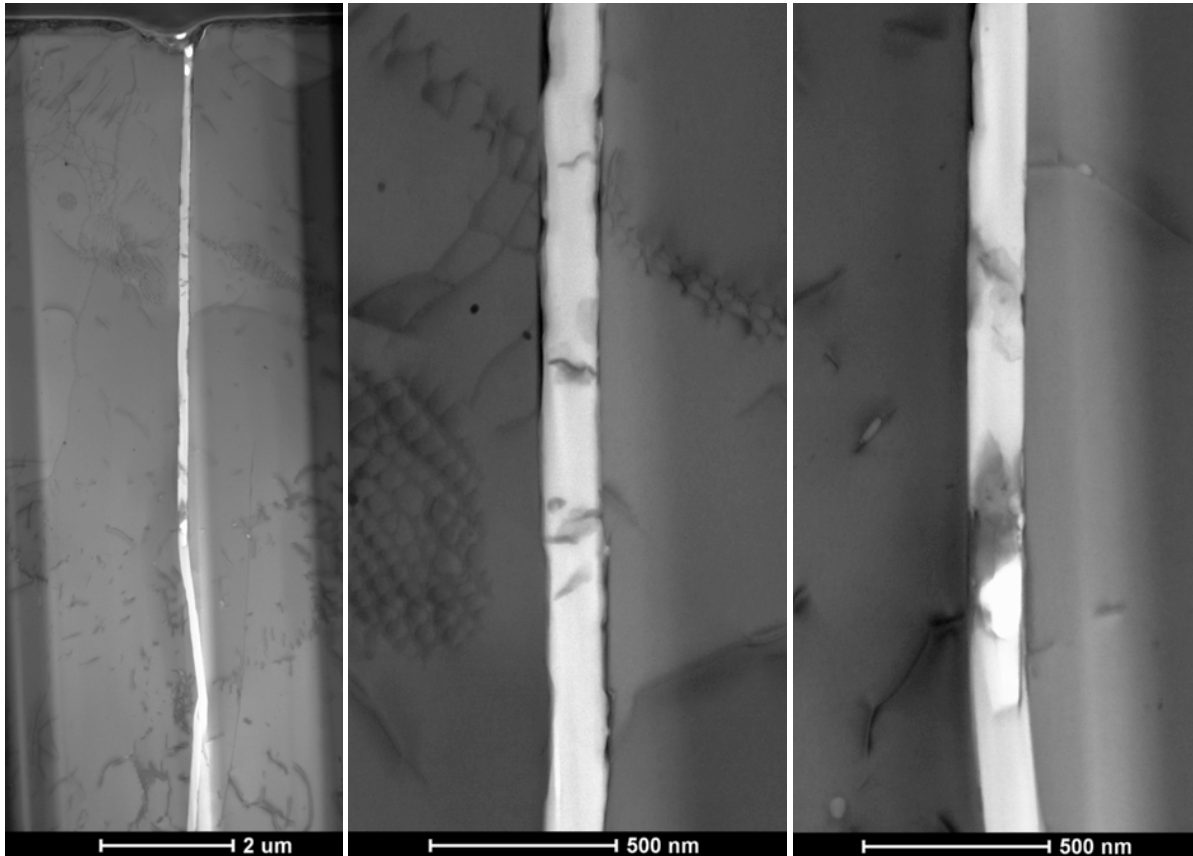


Figure 5.13 : BF images of a crack after 4 weeks in pore solution and 38°C. Very few ASR product is present.

### 5.3.5 Slightly higher alkali content ASR product G4.

The samples containing a slightly higher alkali content than the usual Ca/alkali ratio of 1, also always contained areas with precursor product as introduced in subsection 3.3, in addition to the smooth and dense ASR product. The most obvious explanation of this slightly higher alkali content is that in the analysis, not only the ASR product is being analysed but a mix of both ASR and precursor products. It is qualitatively confirmed by the presence of voids or less product-thick areas as seen in Figure 5.14, in contrast to the product found in Figure 5.12 which fills the space available in the crack. These changes in composition are hypothetically due to densification of ASR product in the crack and consideration of the different ASR growth stages with time. Very thin cracks were also found to be filled with ASR product as in Figure 5.15.
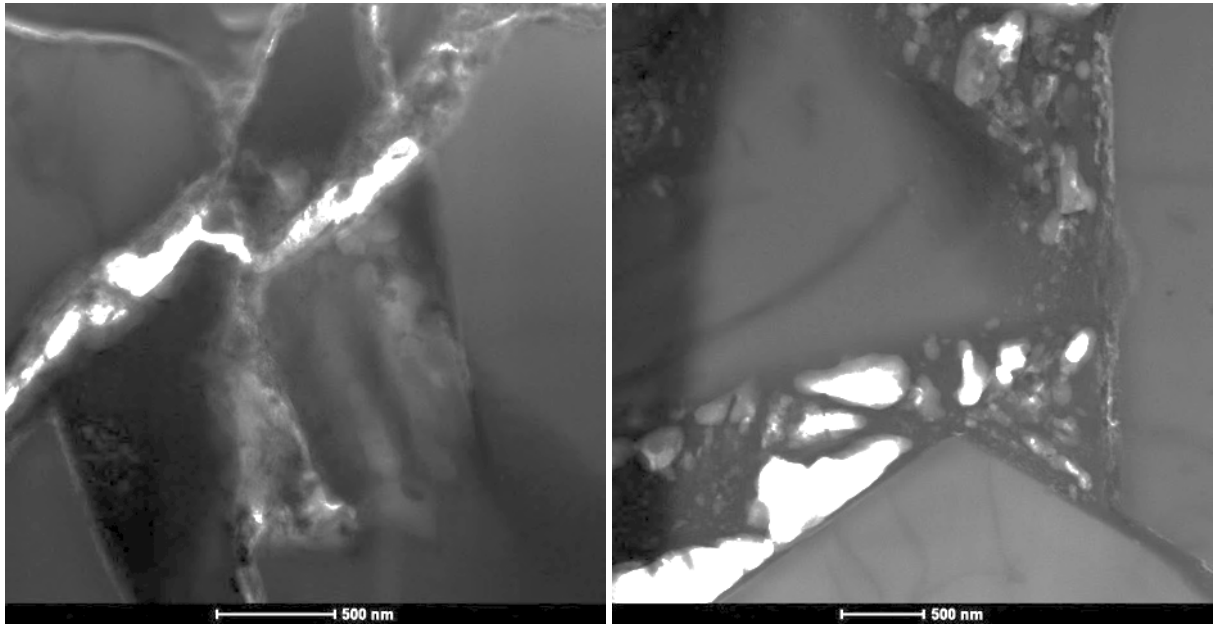
Figure 5.14 : BF images of a crack after 20 weeks in pore solution and 38°C (left and right). The morphology is difficult to assess, but some areas look smooth and dense, whereas others look scarce.
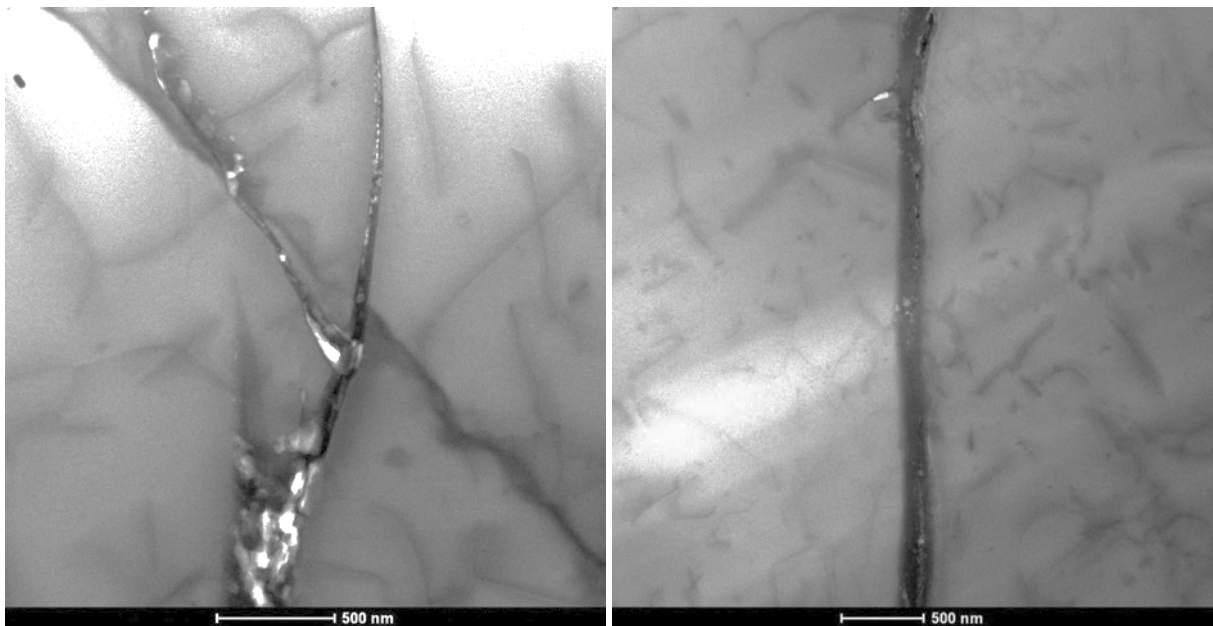


Figure 5.15 : BF images of a crack after 20 weeks in pore solution and 38°C (left and right). Thin cracks containing ASR products.

In the case of a very thin crack Figure 5.16, red rectangle, in which there is not much damage yet, nearly only alkali (in this case K) are present. This can be seen in the ternary diagram Figure 5.17 in which the average composition of the thin crack area from Figure 5.16 is analysed. A Ca/(K+Na) ratio of 0.13 only is found, and represented by a single dot in Figure 5.17.

The silica content is high due to the contribution of the quartz aggregate in the analysis. Analysing very thin cracks makes it impossible to only determine the composition of the product itself. From our previous findings though, it is believed that mainly alkali are present, similarly to the composition of area 8 in Figure 5.11.

The structure of the product containing slightly more alkali than calcium (G4) is also found to be amorphous.
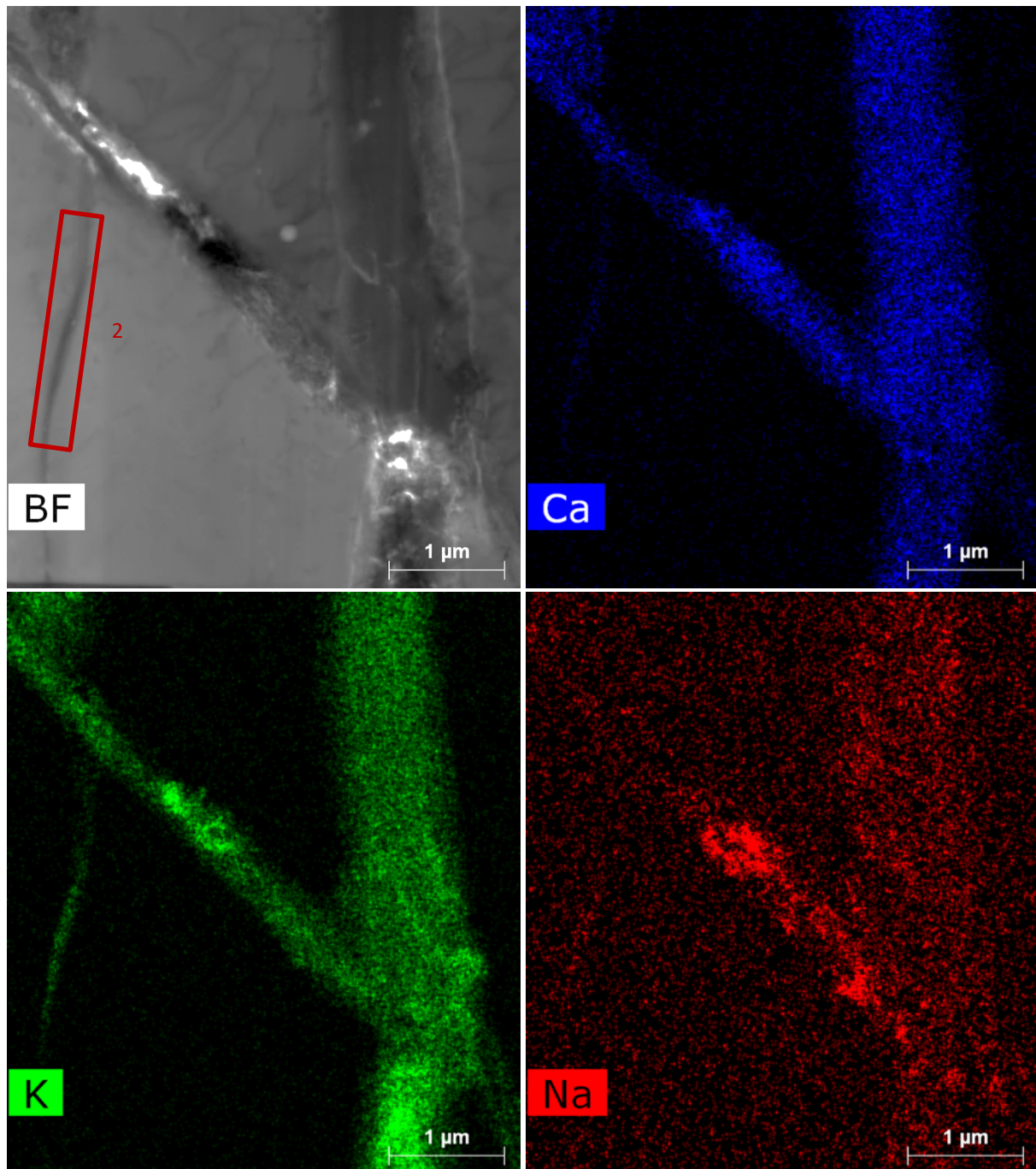


Figure 5.16 : EDX mapping analysis displaying the qualitative distribution of Ca, K and Na in reference to the BF image. In the case of the very thin crack (area 2), nearly no Ca was found as evidenced in Figure 5.17.
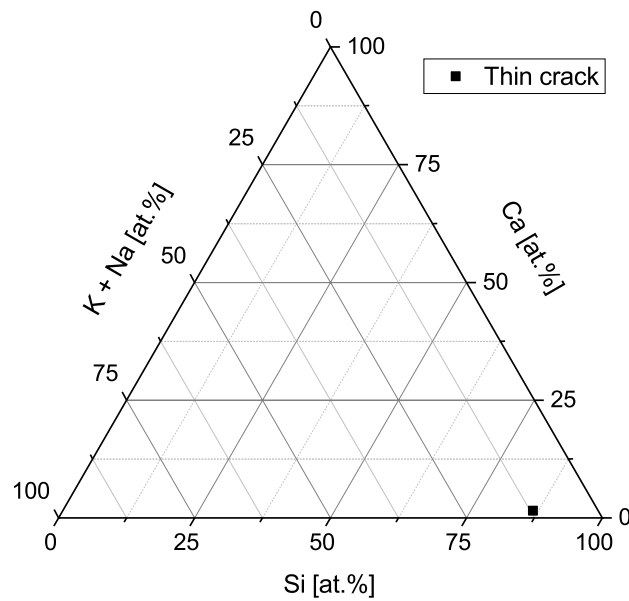
Figure 5.17 : Ternary diagram showing the normalized ASR product atomic percent composition in terms of Si, Ca and alkali, of the ASR product present in the very small crack (area 2) from Figure 5.16, after 20 weeks in pore solution and 38°C.

## 5.4    Conclusion

The following points can be concluded for the product formation at 38°C :

- There is formation of a precursor product, mainly containing alkali.
- There is then a calcium enrichment of the product, leading to a very distinct ASR product composition, similar to that at 60°C.
- The structure of both the precursor and the ASR product is amorphous.
- No platey morphology is seen at 38°C.

Based on the results and discussion in the previous section, and also supported by the results from chapter 4, a hypothesis about the product composition evolution is proposed in the ternary diagram in Figure 5.18 :

- At the very beginning, only alkali are present in solution in thin preexisting cracks. (chapter 4)
- A pre-product starts to form when a high enough Si and Ca content is reached in the pore solution (G1)
- Formation of ASR product, mixed with precursor product (G4)
- Continuous ASR product formation filling the crack (G3)
- Compacity increase of ASR product, replacement of alkali by Ca, no more pre-product present (G2)
- Destabilization of ASR product due to high Ca content in the pore solution and formation of C-S-H [39].
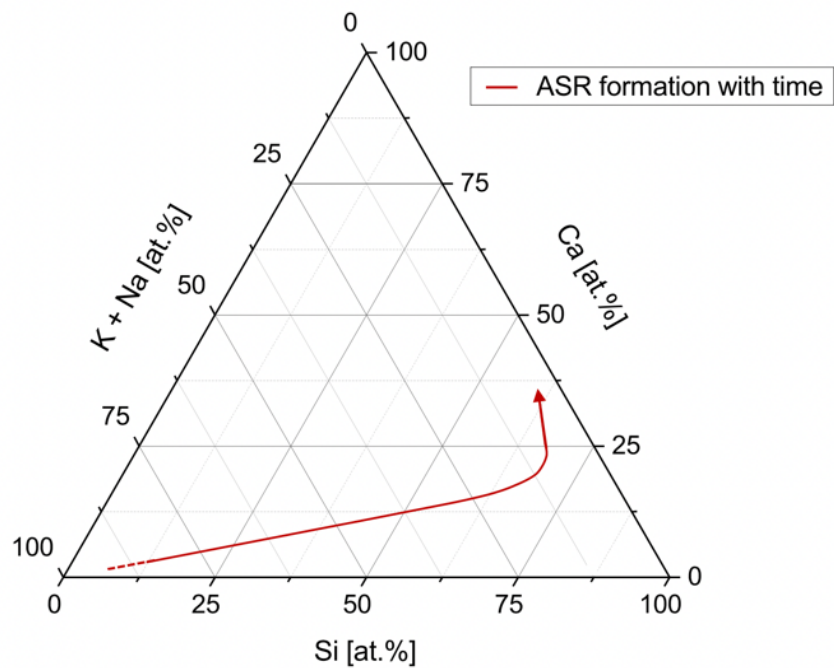
Figure 5.18 : Ternary diagram showing a theoretical composition of ASR product with time, in terms of normalized atomic percent composition of Si, Ca and alkali. A pre-product in solution containing mainly alkali enriches with Si and Ca to form ASR product, and finally destabilizes when a too high Ca concentration in the pore solution is reached, to form low Ca C-S-H.

# Chapter 6 The effect of SCM addition on ASR early-stage product formation.

**Note : This chapter is based on an article in preparation for submission to a peer-reviewed journal.**

Contribution of the doctoral candidate : Conceptualization, Methodology, Formal analysis, Investigation, Writing of the first manuscript draft.

## Abstract

Concrete shows no expansion in the first year of testing in accelerated conditions with addition of FA or LC3. Understanding the mechanisms behind this is crucial to further develop efficient concrete mix designs.

In this study, ASR products are analysed as early as possible inside concrete mixes containing FA and LC3, combining FIB, TEM and EDS microscopy techniques. Even though there is no expansion, some product is present, as early as 20 weeks in accelerated conditions according to the Swiss standard test SIA 2042.

The formation of typical ASR product and presence of N(K)-A-S-H products (perhaps zeolites) in the same crack is observed. The amount of product found in LC3 and FA samples is significantly lower than in OPC concrete. With alkali addition in LC3 mix, more product was found, similarly to the FA mix. The ASR products contain no alumina, and tend to contain less alkali than the products found in OPC concrete.

## 6.1    Introduction

The use of FA or calcined clay (LC3) as a replacement of a portion of ordinary Portland cement has proved beneficial from several perspectives. For FA, two major reasons are to adjust the granularity of the fine aggregate and partially replace the cement [111]. Moreover, FA  facilitates pumping, slows setting time, improves workability, and minimizes hydration heat in concrete [112]. The LC3 concrete has a strength as good as a usual OPC concrete [113][114][115][116][117], reduces $CO_2$ emissions [113][118], raw materials are available in many developing countries, and last but not least, its durability properties like resistance to carbonation, chloride ingress or ASR formation are improved [115][119][120].

ASR is an issue for many structures. Due to the recent development of LC3 cement systems, there have been only a few studies on their durability and more specifically on ASR formation [113], [119]. LC3 appears to be particularly promising for reducing deleterious ASR. It has been shown the addition of SCM like FA or metakaolin (LC3) has an efficient preventative impact against alkali silica reaction in concrete [121][122][123][124][125][126][127][128][129][130][131][132][133][134][135][136]  mainly  due  to  a decrease in pore solution alkalinity. It has been shown that alumina released into the pore solution by the calcined clay reaction directly hinders the breakdown of reactive siliceous minerals [137].

Nevertheless, the role of alumina in decreasing ASR expansive behavior is not fully understood and its relation to ASR product formation is unclear. In this study, the products present at early stage in concrete containing FA or LC3 was successfully analysed, despite their scarcity, by a combination of FIB, TEM and EDX. The results are compared with OPC samples accelerated in the same conditions, 60°C and water vapour.

## 6.2    Materials and method

The concrete samples produced in the lab and exposed to accelerated conditions were prepared in 4 batches, all containing Praz aggregate :

- PC + Fly Ash (FA) concrete.
- PC + Calcined Clay and Limestone (LC3) concrete.
- PC + Calcined Clay and Limestone (LC3) concrete (boosted in alkali to reach a $Na_2O_{Eq.}$ of 0.8%).
- PC + Calcined Clay and Limestone (LC3) concrete (boosted in alkali to reach a $Na_2O_{Eq.}$ of 1.25%).

The composition of the batches is summarized in Table 6.1 :

Table 6.1 : Raw materials proportions for each concrete mix, omitting the aggregate proportions.

| In wt% | Cement | Siliceous FA | Calcined Clay | Limestone | $Na_2O_{Eq.}$ |
|---|---|---|---|---|---|
| OPC | 100 | 0 | 0 | 0 | 0.83 |
| FA | 70 | 30 | 0 | 0 | 0.77 |
| LC3 | 55 | 0 | 30 | 15 | 0.57 |
| LC3 0.8% | 55 | 0 | 30 | 15 | 0.8 |
| LC3 1.25% | 55 | 0 | 30 | 15 | 1.25 |

Four concrete prisms were prepared according to SIA 2042 Swiss standard for each batch. The maximum aggregate sieve size was 22.4 mm. 401 kg/m$^3$ of PC + substitution material) and 1770 kg/m$^3$ of aggregates at a w/c of 0.46 were used for concrete production. The samples were cast in the form of 70x70x281 mm$^3$ prisms. Three prisms are kept to evaluate swelling and one to collect samples for microscopic analysis. The samples were boosted with Na$_2$OH to reach a 1.25% and 0.8 % Na$_2$OH$_{eq.}$ content (see Table 6.1), in contrast to 0.57% (LC3) and 0.77% (FA) Na$_2$OH$_{eq.}$ when not boosted. The accelerated conditions were: 1 day curing in molds, then the prisms were demolded and kept in water vapour at 60°C.

After 20 weeks, in accelerated conditions, samples were cut from the middle of the prisms, dried for 3 days in air at 40°C, impregnated with epoxy and polished according to the method described in chapter 3, with SEM, FIB and STEM analysis.

## 6.3    Results and discussion

### 6.3.1   Expansion test

A sample was taken after 20 weeks (146 days), in the accelerated conditions, for each mix. According to the swelling results from Figure 6.1, there was no expansion for FA or LC3 mixes samples. In the same condition, the OPC sample has already expanded more than 0.6 ‰. It indicates a clear mitigation with addition of SCM's, as reported in the literature (see 6.1).
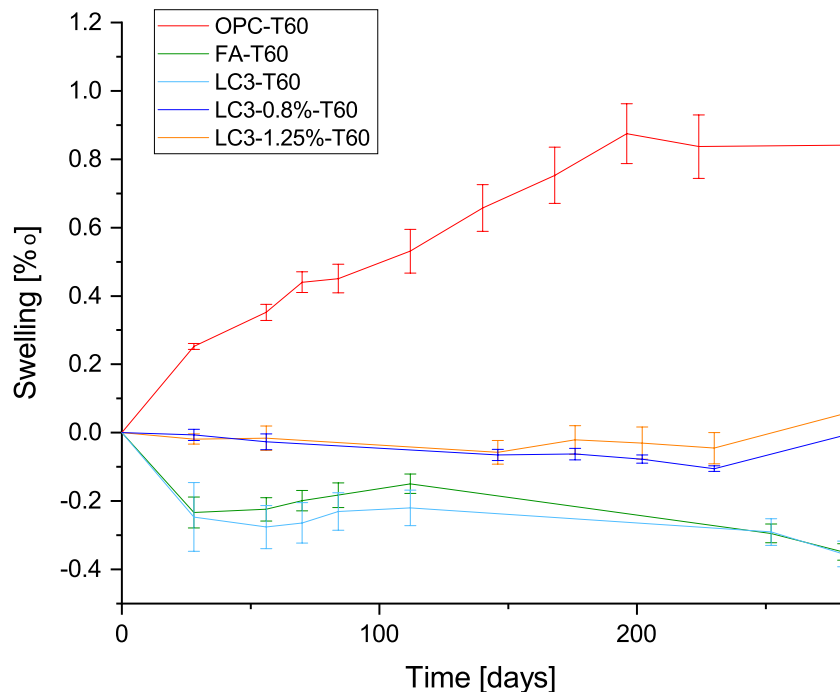


Figure 6.1 : Expansion curves of OPC and SCM concrete mixes as a function of time.

## 6.3.2   General

Out of the 13 successful lamellae prepared for analysis, ASR product could only be found in 6. ASR product was difficult to find in all samples, particularly in LC3 and LC3 0.8%. It was nearly never found in SiO2 mineral phases, but rather each time at the interface between quartz and mica (or zeolite). Therefore, in most cases in the analysed crack, ASR product was intermixed with other mineral phases such as mica, feldspar, and (N)K-A-S-H products (maybe zeolites) Figure 6.2, as confirmed by the compositions in Figure 6.3. In some cases, Mg was also present, and it was not distributed in the exact same area as any other element as seen in Figure 6.4.
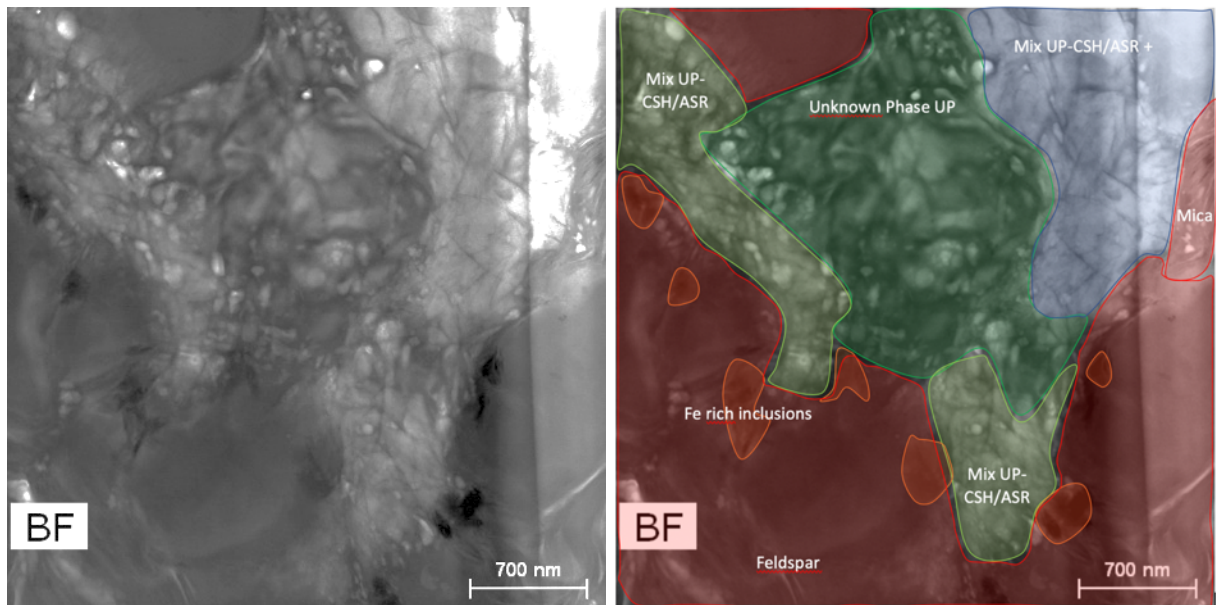


Figure 6.2 : BF image of different phases intermixing (left) and interpretation after EDX analysis (right).
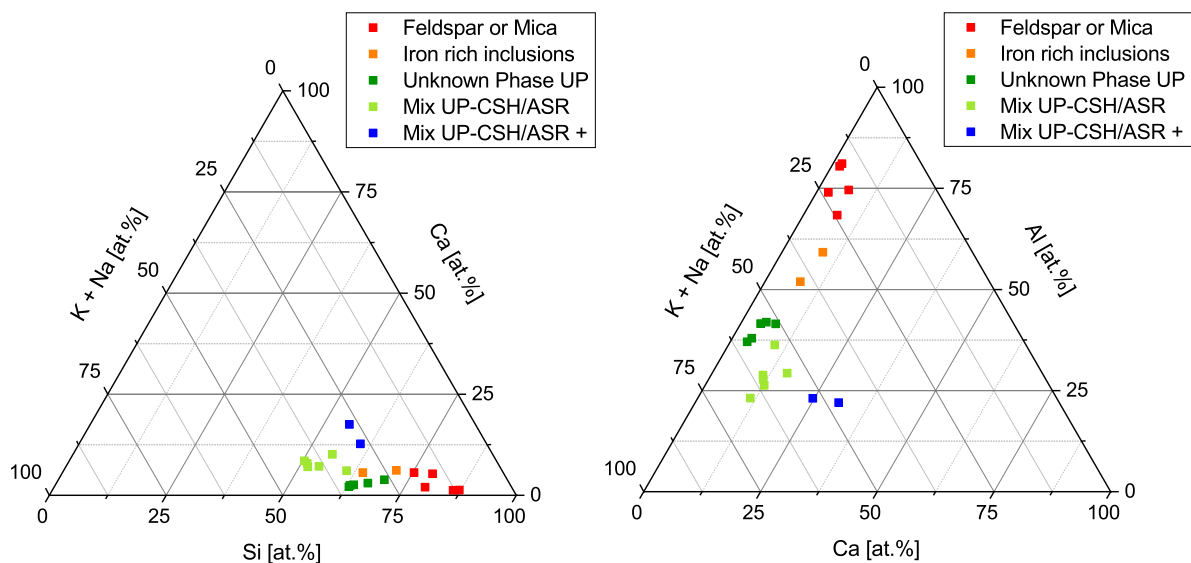


Figure 6.3 : Ternary diagram showing the normalized atomic percent composition in terms of Si, Ca and K+Na (left) and Ca, Al and K+Na (right), for the products in Figure 6.2. One point represents a small analysed area of the product
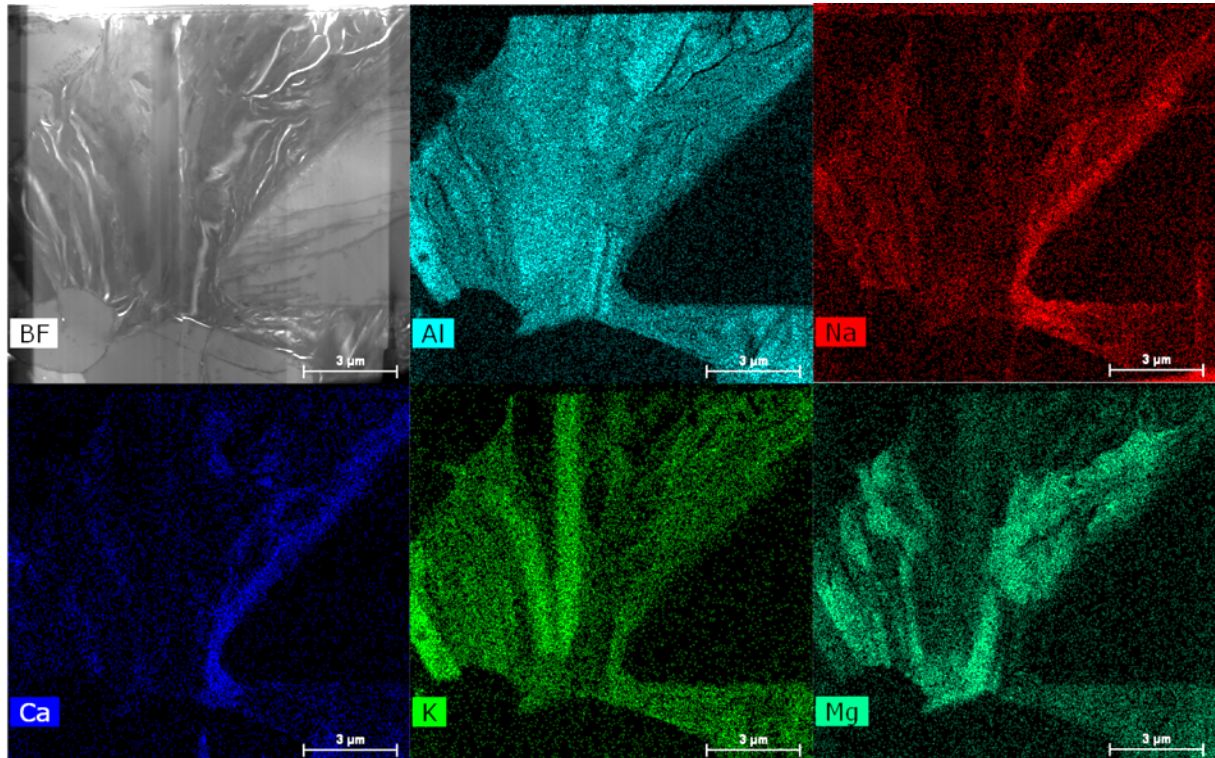
Figure 6.4 : BF and elemental mapping of a lamella containing many different phases like mica, feldspar, zeolites and probably ASR product, intermixed.

From the 6 lamellae having distinguishable ASR product, 2 were from the FA sample, 1 from LC3, 1 from LC3 0.8% and 2 from LC3 1.25%. The normalized compositions in terms of Si, Ca and alkali are shown in the ternary diagram Figure 6.5.

It is known that Al present in SCM's inhibits the expansion of the concrete [138][139][140]. However, there was no detectable uptake of Al (or other elements than Si, Ca and alkalis (Na, K)) in any of the ASR products. The composition and morphology of the products remained generally similar to that in the OPC samples.
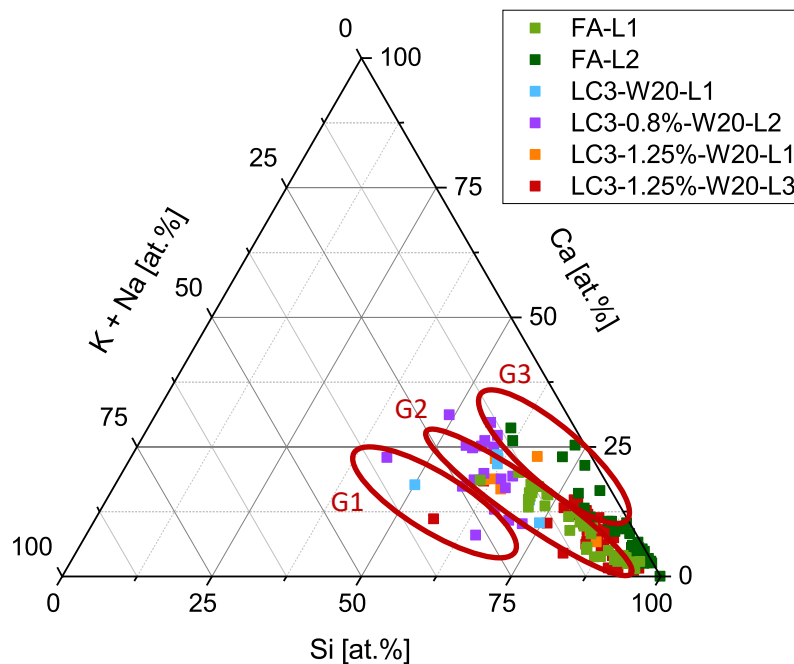
Figure 6.5 : Ternary diagram showing the normalized atomic percent composition in terms of Si, Ca and alkali, for all the distinguishable ASR products found in the 6 lamellae. 3 groups of composition are identified (G1, G2 and G3).

Based on the results displaying the products composition, 3 groups are identified:

- High alkali content product (G1)
- Similar alkali and calcium content product (G2)
- High calcium content product (G3)

The characteristics of each group are discussed in the following subsections.

### 6.3.3   High alkali content ASR product G1

The higher alkali content in some areas is considered to be due to the contribution of the neighbouring phases. As previously mentioned, ASR product is often intermixed or sharing an interface with mica, feldspar or zeolites, which do not contain any calcium but do contain alkali (Figures 6.6 and 6.7). Despite a precise analysis of the zone, it is not excluded that the alkali from another phase are taken into account in the ASR analysis. This was similarly reported in OPC samples, with the contribution of Si due to the quartz neighbouring phase. In the case of Si, it is less problematic when comparing the ratio between alkali and calcium. The small number of points in G1 were seen to be all in the neighbourhood of an alkali containing phase.
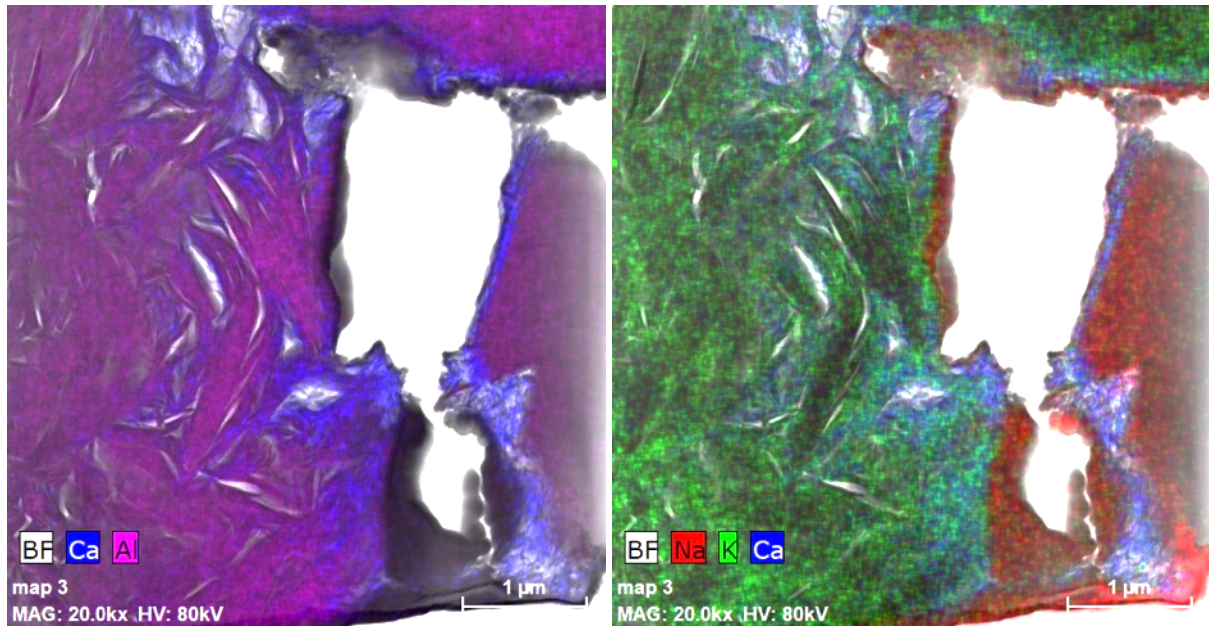
Figure 6.6 : BF and elemental distribution of Ca and Al (left) and Na, K and Ca (right) in the lamella LC3-0.8%-W20-L2. ASR product is present where the Ca is located and surrounded by Al and alkali rich phases.
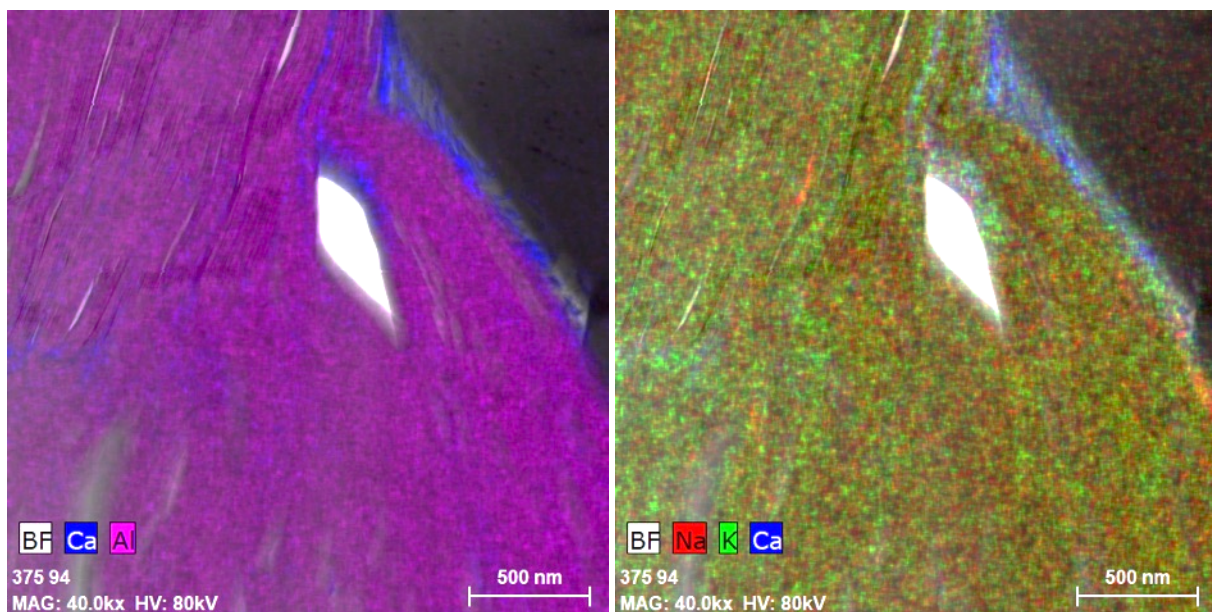


Figure 6.7 : BF and elemental distribution of Ca and Al (left) and Na, K and Ca (right) in the lamella LC3-W20-L1. ASR product is present where the Ca is located.

### 6.3.4   Similar alkali/Ca content ASR product G2

These are the typical ASR product composition with a Ca/Si and (K+Na)/Si ratio both of approximately 0.2 to 0.3 (see chapter 4 and 5), presenting in this case a granular morphology Figures 6.8 and 6.9. This product only contained Si, Ca and alkali, without any other elements in significant amounts. The small amount of product in each sample did not allow the use of electron diffraction to determine crystallinity, but from the morphology and the results in previous chapter 4 and 5, the ASR product is probably amorphous, since its morphology is granular and not platey.
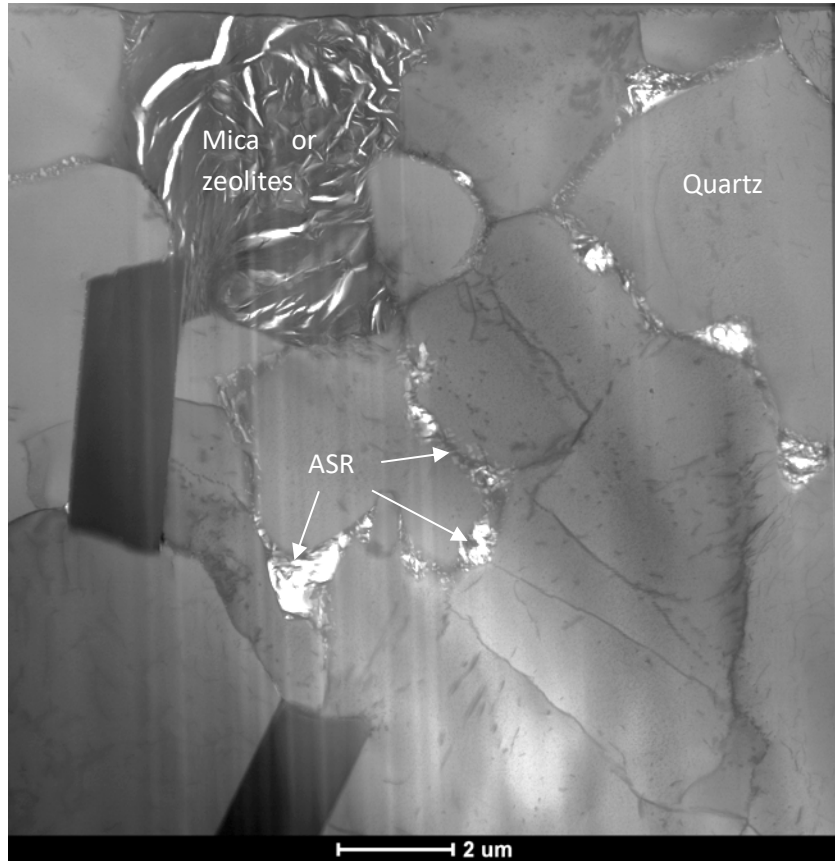
Figure 6.8 : Overview of the lamella FA-W20-L1, with presence of ASR product at the grain boundaries, forming pockets in some areas.
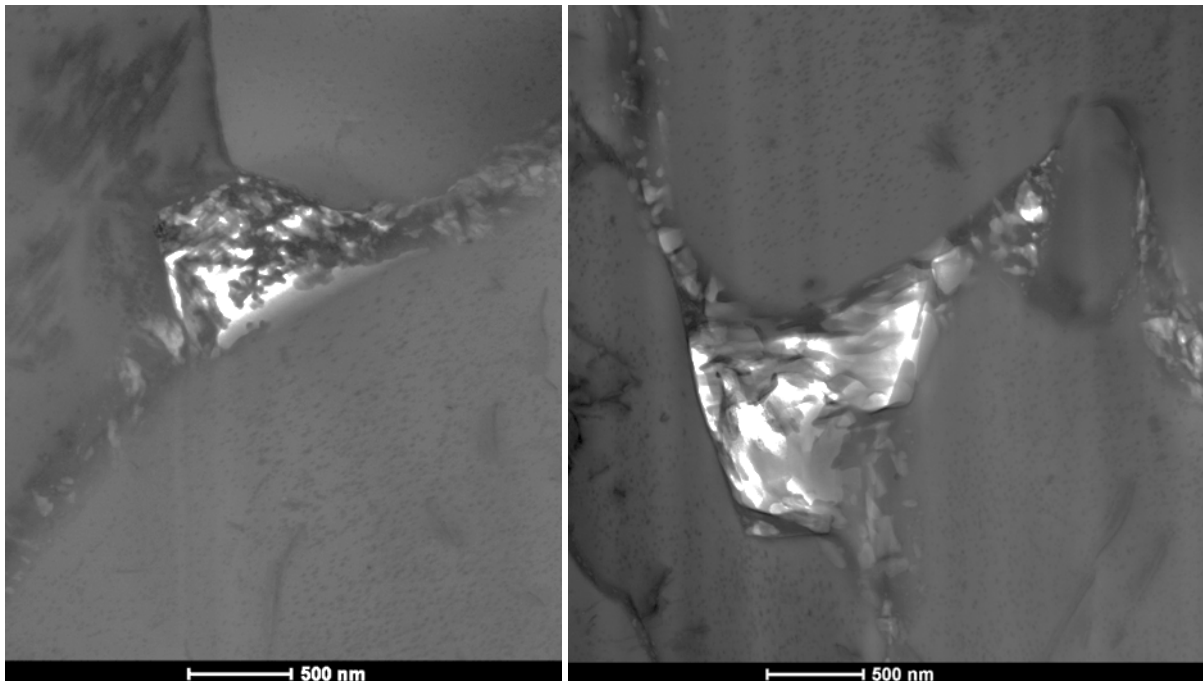


Figure 6.9 : In lamella FA-W20-L1, close view of ASR gel pockets from Figure 6.8

## 6.3.5    High Ca content ASR product G3

Higher calcium content product occurred mainly in one sample. The crack was mostly empty, and a first look at the morphology indicates it might be C-S-H because it looks like foils or fibrils (see Figure 6.10). The composition also suggests it might be C-S-H, despite a very low Ca/Si ratio. In some areas, no alkali is present, whereas in some others, alkali are more present, but with a Ca/(K+Na) ratio of approximately 2 (Figure 6.5).

The formation of C-S-H inside an aggregate crack suggests that there is a higher calcium concentration in the pore solution, due to the lower alkalinity [141]. Lower alkalinity is expected in the samples since additional silica provided by the SCMs has been demonstrated to lower the pore solution alkalinity [142][143].
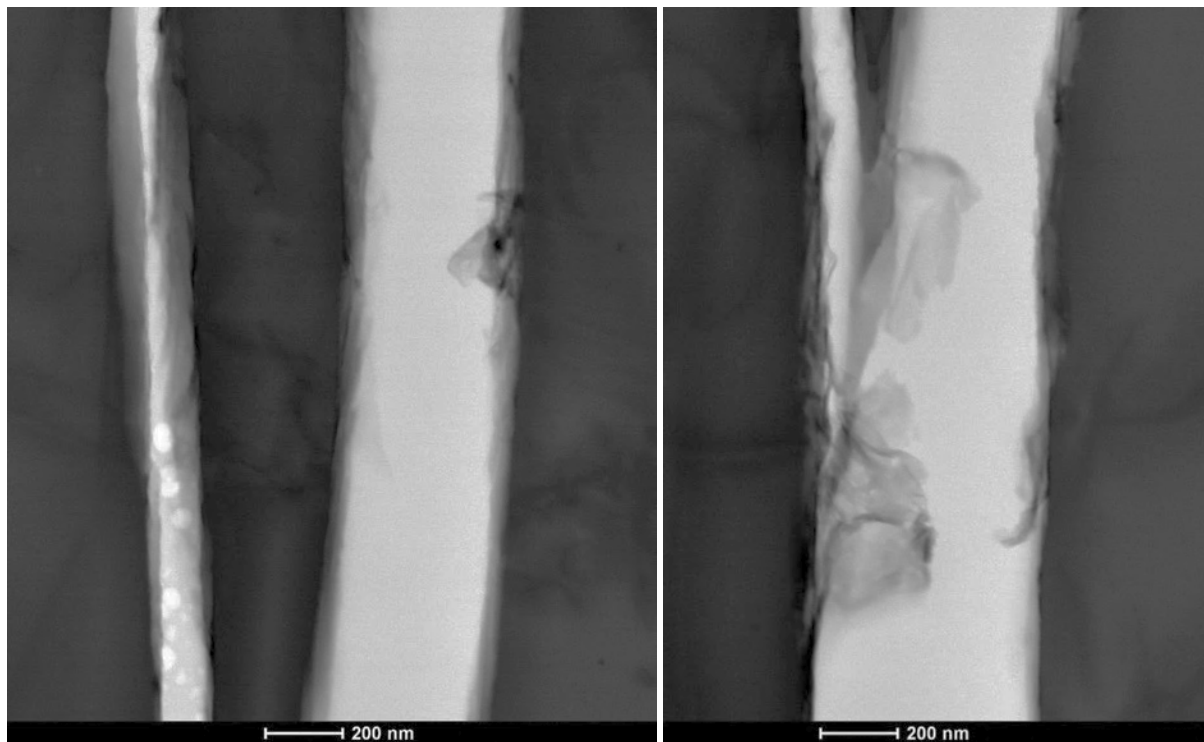


Figure 6.10 : BF images of the product found in lamella FA-W20-L2.

## 6.3.6    Effect of Al

The role of Al in the formation of ASR products is of great interest since it appears to be important in reducing expansion.  Figure 6.11 shows the analyses in another ternary diagram including Al, 2 groups can be identified :

- ASR products without Al

Most of the products analysed did not show any Al incorporation, especially in areas where the product could be isolated or was not in contact with Al rich phases. Al is considered to only be present in traces when its atomic percent composition is below 12 in ternary diagram Figure 6.12. In this case the percentage is normalized among Ca, Al and alkali, with exclusion of Si, explaining such a high percentage and high threshold for considering it as traces. A comparison with OPC samples gives a point of comparison (see 6.3.4).

- ASR products with small amount of Al

The purple points from the sample LC3-0.8%-W20-L2 appeared to contain a significant amount of Al, but it is because of the neighbouring mineral phases containing Al. In LC3-0.8%-W20-L2, the product is located in a mica and/or feldspar mineral phase. Due to the scarce quantity of product, it is not possible to analyse an area which does not partly take into account these phases. A few points from the other samples also had an interface with an Al rich mineral phase, which immediately resulted in a slight increase of the calcium content in the ASR product analysis. It is also seen in the ternary diagram showing the product atomic percent composition normalized between Ca, Al and alkali (excluding thus the Si) Figure 6.12.
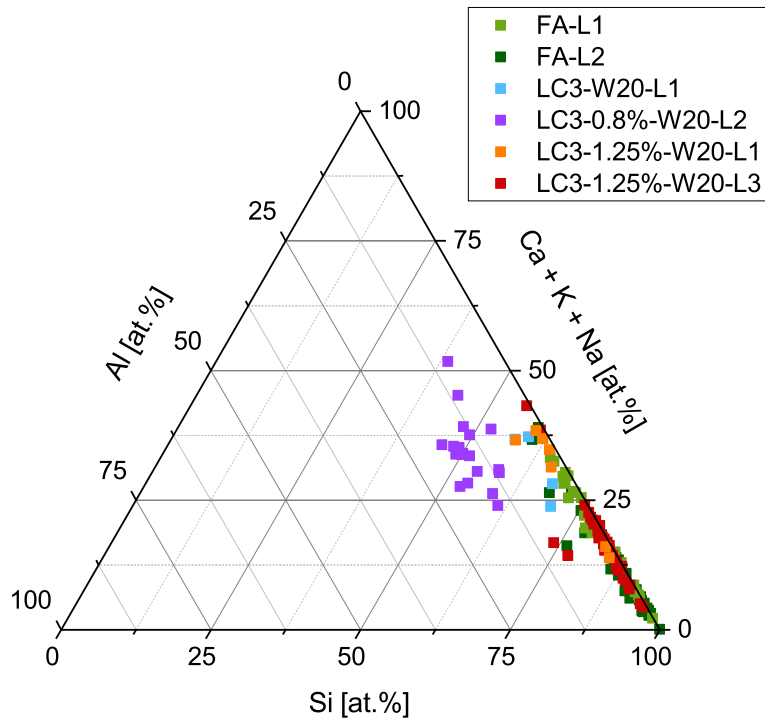


Figure 6.11 : Ternary diagram showing the normalized atomic percent composition in terms of Si, Ca+alkali and Al for all the distinguishable ASR products found in the 6 lamellae.
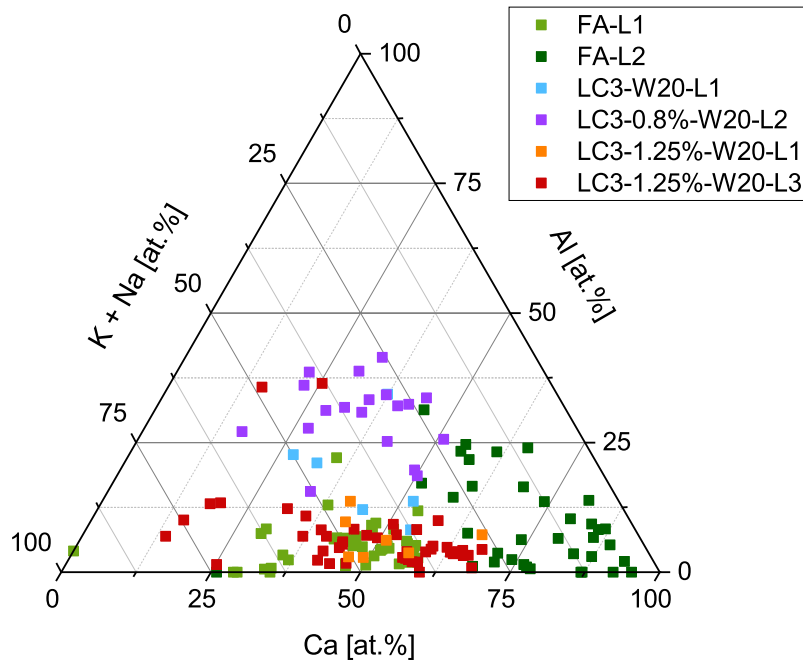
Figure 6.12 : Ternary diagram showing the normalized atomic percent composition in terms of Ca, Al and alkali, for all the distinguishable ASR products found in the 6 lamellae.

An interesting point is that ASR product is often associated in the crack with other phases, like mica or (N)K-A-S-H. Cracks in this phase were not observed in OPC samples and the (N)K-A-S-H composition is differing from a typical feldspar. It is possibly the result of zeolite formation, since the acceleration was done at a rather high temperature, 60°C. Such zeolite formation is consuming alkali from the pore solution.

An example of the two phases coexisting in a crack is given in Figure 6.14. The phases are easily distinguishable from the EDX mappings in Figure 6.15. From the SEM analysis in Figure 6.13, only a slight increase of K and Ca could be detected, and was presumed to contain ASR product.
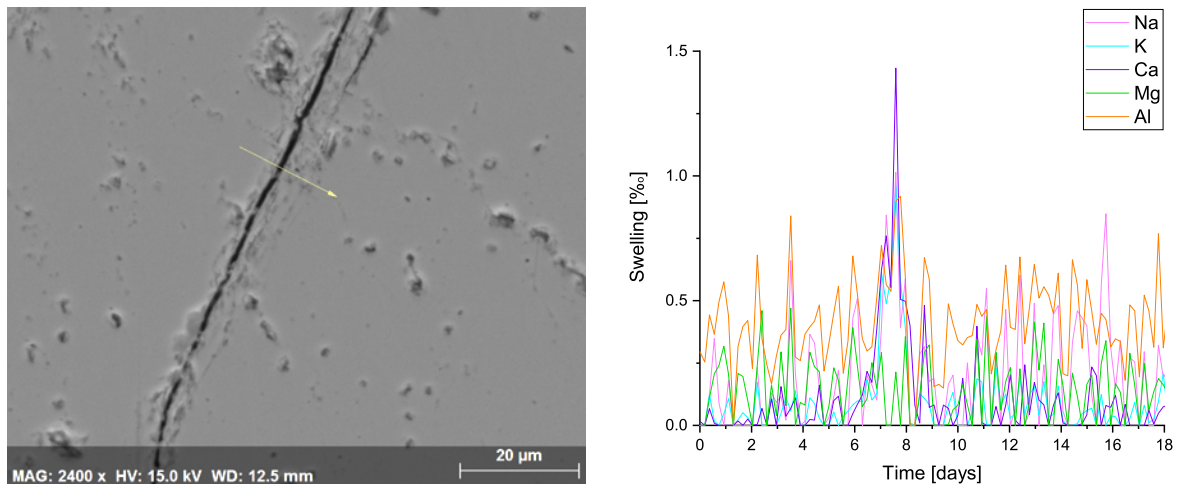


Figure 6.13 : SEM image with EDX line scan location of a crack in LC3-1.25%-W20-L1 (left) and the compositional result of the line scan (right)
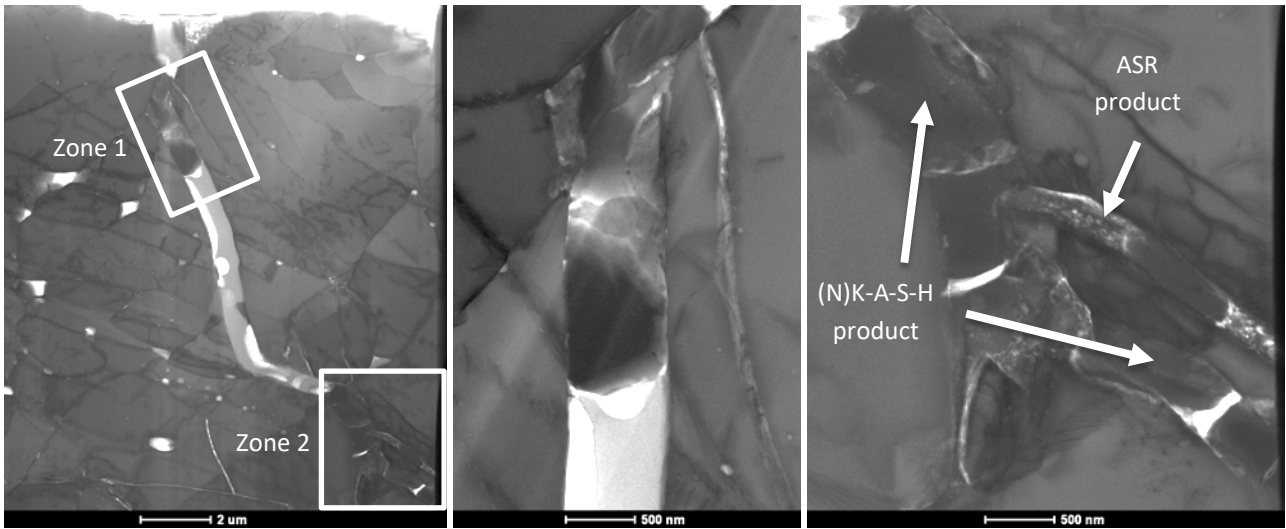
Figure 6.14 : BF images of LC3-1.25%-W20-L1 crack. Overview (left), zone 1 (middle) and zone 2 (right).
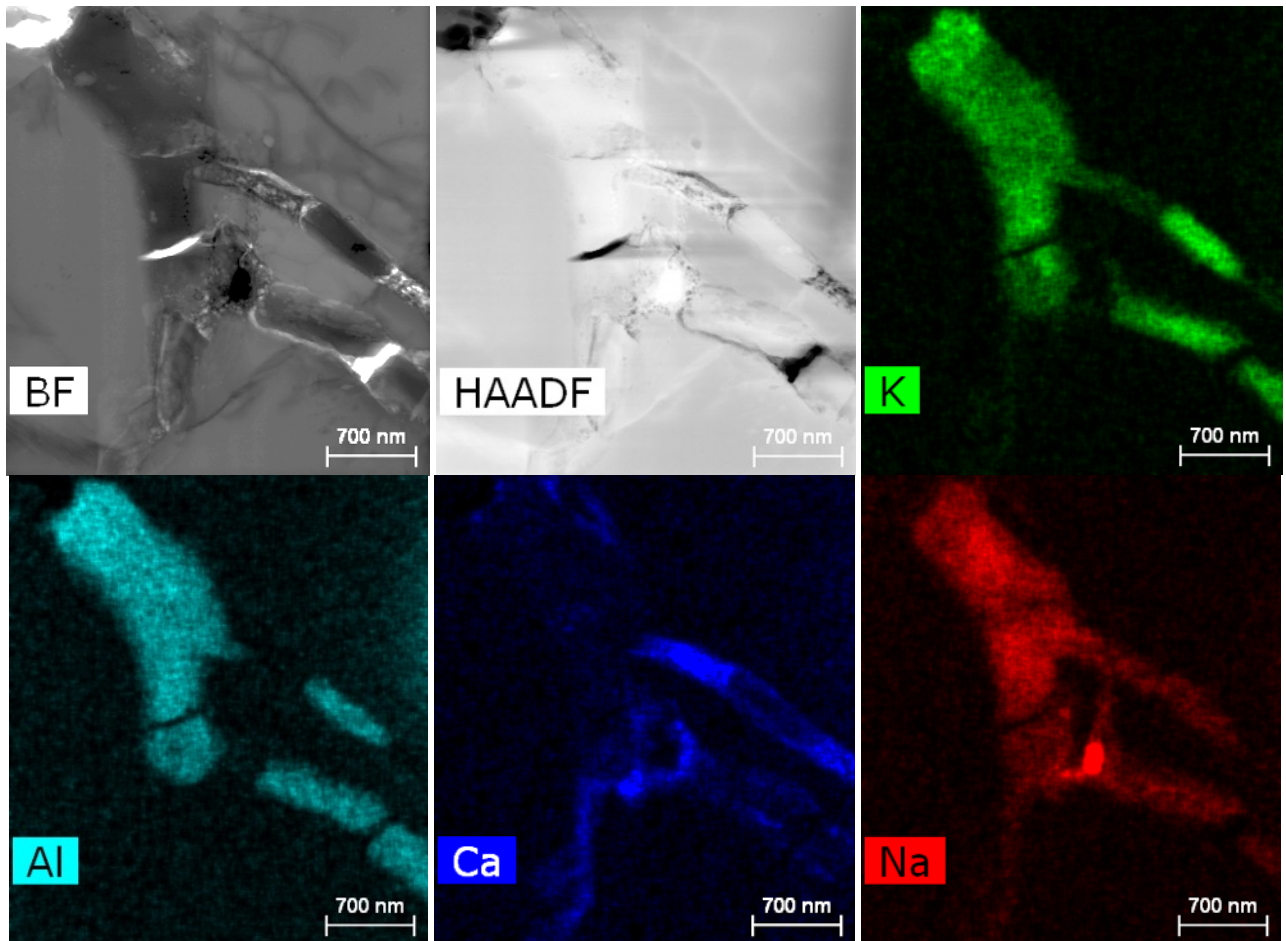


Figure 6.15 : BF, HAADF images and elemental distribution of K, Al, Ca and Na, in the lamella LC3-1.25%-W20-L1. ASR product is present where the Ca is located and surrounded by Al and alkali rich phases.

Table 6.2 : Atomic percent composition of areas selected in the LC3-1.25%-W20-L1 crack from Figure 6.15. In blue, composition of ASR product.

| [At. %] | O | Ca | Al | Si | Na | Mg | K | Ca/Si | (K+Na)/Si | Al/Si | Mg/Si |
|---|---|---|---|---|---|---|---|---|---|---|---|
| 1 | 52,59 | 0,13 | 8,06 | 26,20 | 7,00 | 0,09 | 5,84 | 0,00 | 0,49 | 0,31 | 0,00 |
| 2 | 51,38 | 1,23 | 4,04 | 34,62 | 5,24 | 0,22 | 3,18 | 0,04 | 0,24 | 0,12 | 0,01 |
| 3 | 52,45 | 9,41 | 1,71 | 27,93 | 5,40 | 0,04 | 2,75 | 0,34 | 0,29 | 0,06 | 0,00 |
| 4 | 48,23 | 0,72 | 7,58 | 27,39 | 4,29 | 0,34 | 11,17 | 0,03 | 0,56 | 0,28 | 0,01 |
| 5 | 58,89 | 0,00 | 8,53 | 25,17 | 3,94 | 0,01 | 3,44 | 0,00 | 0,29 | 0,34 | 0,00 |
| 6 | 58,59 | 0,12 | 8,01 | 23,75 | 5,53 | 0,18 | 3,73 | 0,00 | 0,39 | 0,34 | 0,01 |
| 7 | 57,41 | 0,05 | 8,09 | 23,22 | 7,32 | 0,11 | 3,74 | 0,00 | 0,48 | 0,35 | 0,00 |

In this lamella LC3-1.25%-W20-L1, there is a clear distinction between usual ASR product and (N)K-A-S-H product, in terms of morphology and composition. ASR has a granular morphology with a typical Ca/Si and (Na+K)/Si ratio between 0.25 to 0.35 at.%, with no Al and Mg (see Table 6.2, area 3). Parallelly, N(K)-A-S-H has a very smooth and homogeneous morphology with a (Na+K)/Si ratio between 0.29 to 0.49 at.% and Al/Si ratio between 0.25 to 0.35 at.%, with no Ca and Mg (Table 6.2). In some other cases, presence of Mg is found in the product.

### 6.3.7 Comparison with OPC samples

Comparing the results from LC3 and FA samples with OPC samples is necessary to clarify the possible impact of these SCM's on ASR formation.

There is a tendency of ASR product in SCM's samples to contain more calcium than in OPC as seen in Figure 6.16, or rather less alkali. To simplify and confirm it, the Ca to alkali ratio is plotted and a linear regression for each batch (SCM vs OPC) is calculated. The slope for the SCM data is two times greater than for OPC data indicating a stronger calcium proportion at higher ratio as seen in Figure 6.17. The $R^2$ coefficients are identical indicating a similarly good fit reliability. The difference in Ca/(K+Na) ratio becomes more clearly visible with higher Ca and alkali content.
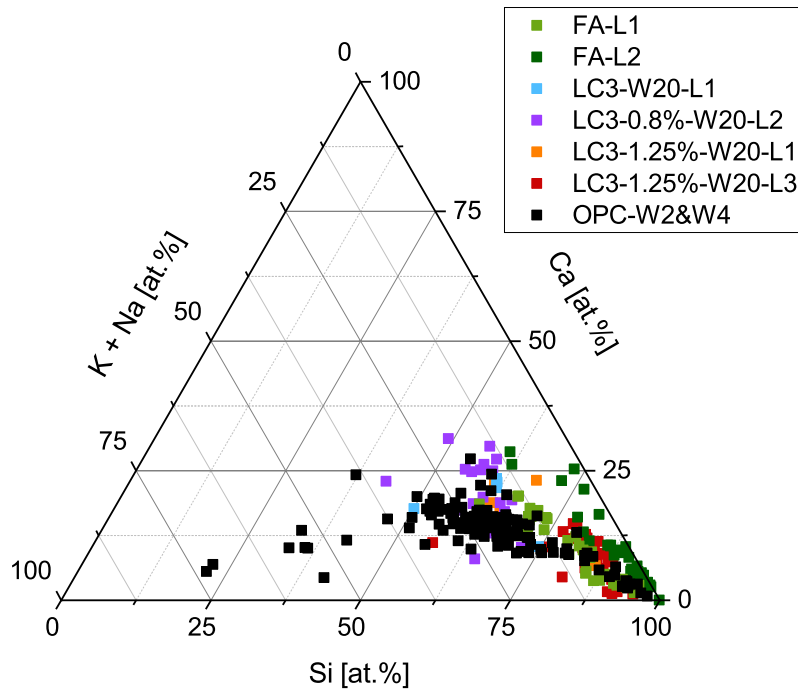
Figure 6.16: Ternary diagram showing the normalized atomic percent composition in terms of Si, Ca and alkali, for all the distinguishable ASR products found in the 6 lamellae and ASR products from OPC concrete in similar accelerated conditions.
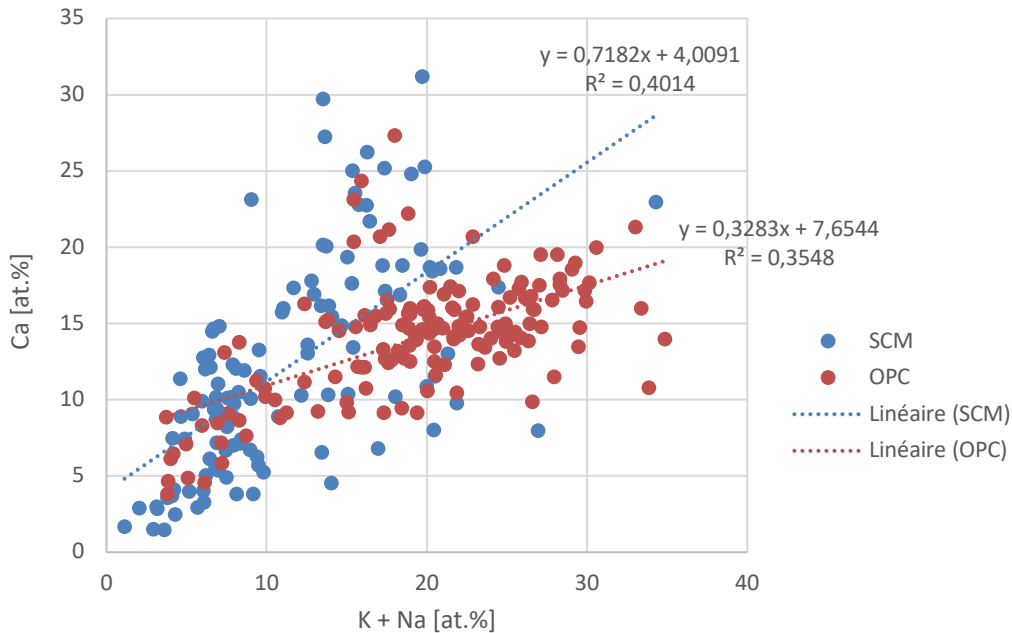


Figure 6.17: Ca/(K+Na) ratio comparison between ASR products found in SCM and OPC samples.

Running a two-samples t-test assuming unequal variance between the Ca/(K+Na) ratio of SCM and OPC sample data, in Table 6.3, show that our t statistics > t critical therefore our hypothesis of unequal variance is invalid. Indeed, we can see the variance are quite similar, indicating a good reliability. The calculated means for SCM and OPC show a significantly higher Ca/(K+Na) ratio, confirming our previous results.

Table 6.3 : Two-samples t-test of unequal variance between SCM and OPC samples.

|  | SCM | OPC |
|---|---|---|
| Mean Ca/(K+Na) | 1,14 | 0,80 |
| Variance | 0,24 | 0,10 |
| Observations | 118 | 153 |
| Hypothetic difference of the means | 0 | |
| Freedom degree | 187 | |
| t statistics | 6,61 | |
| P(T≤t) unilateral | 1,99E-10 | |
| t critical value (unilateral) | 1,65 | |
| P(T≤t) bilateral | 3,98E-10 | |
| t critical value (bilateral) | 1,97 | |

A possible explanation is that alkali are less available in the pore solution because there are consumed by other reactions, like zeolites formation [144][145] or alkali sorption in C-S-H [146][147]. The latter is proposed to be due to Al incorporation in C-S-H structure by substitution of Si atoms [148]. This substitution leaves a negative charge that must be balanced by a positive charge coming from the alkali for example. However, alkali fixation by C-S-H is reported to not be very much enhanced by Al incorporation [149][150] and zeolite formation is reported to happen only at high temperature so far (80°C) and not at 40°C [151]. In our case, at 60°C, the temperature could be high enough to have zeolite precursor formation.

According to Figueira et al. "MK is very effective in reducing $Ca(OH)_2$ and reducing ionic mobility [132][133][135][136][128]. Others have shown that the hydration products formed in the pozzolanic reaction of MK had the ability to absorb alkalis, which is an inhibition factor of ASR by MK [139][152]." Our results favor the second hypothesis for ASR mitigation.

It is also clear from Figure 6.18 that there is no significant Al incorporation in ASR product in SCM samples by comparison with OPC samples. The eventual increase is too low to be detected and can easily be due to Al absorption on the silica surface as reported by [137][45], which is necessarily taken into account in the STEM EDX analysis. A shift of the OPC samples towards higher alkali and lower Ca content is also clearly visible in Figure 6.18, confirming the previous paragraph statement.
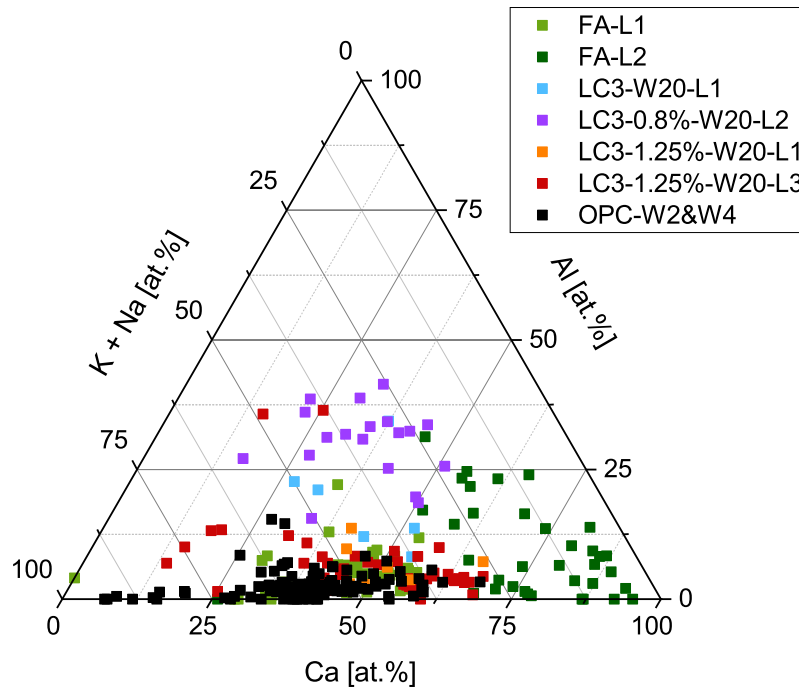
Figure 6.18 : Ternary diagram showing the normalized atomic percent composition in terms of Ca, Al and alkali, for all the distinguishable ASR products found in the 6 lamellae and ASR products from OPC concrete in similar accelerated conditions.

## 6.4    Conclusion

After 20 weeks in accelerated conditions, no expansion was observed, and very little ASR product was found in FA and LC3 samples. The rare occurrence of ASR product makes its analysis difficult, however the composition of some areas was analysed. To conclude :

- There is no Al uptake in ASR product.
- There is slightly more calcium (less alkali) in ASR product in SCM's samples compared to OPC
- It is easier to find ASR product in FA and LC3-1.25% than in LC3 and LC3-0.8%.
- There is much less ASR product in SCM's samples compared to OPC.

The morphology of ASR product in SCM samples is the same as the granular product found in OPC samples. Unfortunately, the crystallinity of the product could not be assessed due to the product scarcity.

# Chapter 7  Characterization of synthetic and on-field ASR products by electron microscopy

**Note : This chapter is based on a conference paper published in a peer-reviewed proceeding.**

Contribution of the doctoral candidate : Conceptualization, Methodology, Formal analysis, Investigation, Writing of the first manuscript draft.

## Abstract

The composition and structures of ASR products located in aggregates and cement paste can vary substantially. In a novel approach using SEM, FIB and TEM, the formation of early stage products could be studied. In this study, late stage and synthetic products are analysed using the same method : the morphology, composition and structure of three synthesized ASR products with various alkali content and four field products from different structures in Switzerland are defined. Morphology and structure are linked in synthetic samples : platey products are crystalline corresponding to K- or Na-shlykovite, and fibrillar/granular products are nanocrystalline, corresponding to ASR-P1 and/or eventually C-S-H. In field samples, platey products are weakly crystalline whereas the granular products are amorphous. Synthetic and field samples are quite similar in terms of overall composition. Finally, when comparing with early stage ASR products from laboratory samples, their composition is also very similar, despite differences in their morphology and structure.

***Keywords***: *Alkali-silica reaction, composition, electron microscopy, morphology, structure*

## 7.1    Introduction

Alkali-Silica Reaction (ASR) occurring in concrete structures is one of the main issues impairing concrete durability. Metastable silicates present in aggregates are dissolved by hydroxyl ions present in the alkaline pore solution of the concrete. The dissolved silica then forms precipitates with water, calcium and alkali ions resulting in the formation of reaction products, which induce stress in the aggregates and subsequent cracking. A preliminary survey indicates that in Switzerland, more than 400 structures are affected [8].

There is a great need to improve our knowledge about ASR formation in order to prevent it. Even though the basics of mechanisms are known, there are still many open questions regarding the role of the environment, the role of the different components, and the ageing behaviour, as well as the reactivity of the mineral phases. It is difficult to determine if a given aggregate/cement combination is deleteriously expansive due to the very slow nature of reaction in Switzerland's climate, despite the existence of testing standards [153]. Swiss aggregates are an issue concerning ASR occurrence as they often contain minerals which are vulnerable to ASR: around 90% of the aggregates were classified as potentially reactive by [9].

Some facts are nowadays extensively described: the chemistry of the reaction [30][11], the chemical composition of reaction products, which main components are Si, Ca, K and Na [16][17][18][19][20], the fact that ASR is not one product but that it forms several products [18][92][21][23][91][154]. So far, ASR products formed at late stage have been analysed once they are present in large quantities in big cracks (> 20 μm). A comparison between the early stage and late stage ASR product formation is needed for a better understanding of the mechanism of cracking. The very low amount of product found at early stage or in small cracks in field samples makes its analysis difficult, parallelly increasing interest in comparison between the early stage products and synthetic ASR products from laboratory synthesis produced by Shi [46]. In this study, a comparison between laboratory concrete samples, field concrete structures and synthetic samples opens a possibility of a more in depth and comprehensive characterisation [40], as synthetic samples can be produced in large quantities.

## 7.2    Materials and methods

### 7.2.1   SEM analysis and FIB cutting for field samples

**Samples**

A total of four different field samples were collected in Switzerland for this study, all severely affected by ASR. They were collected from :

1.  A gravity dam from Canton of Valais built in 1950, at 1850 m of altitude.
2.  A retaining wall at the Wall pass in Meiringen (Bern canton), about 40 years old, at around 1000 m of altitude.
3.  A bridge in a village from Saint Gallen canton, 500 m of altitude.
4.  A church from Canton of Valais, built in 1974, 670 m of altitude.

The samples are respectively named Dam, Wall, Bridge and Church in this study, and two lamellae were prepared for each : L1 and L2. Each region of interest was selected according to the following criteria, as already mentioned in chapter 3 :

- \> 100 µm away from the interface aggregate/cement matrix
- In the outer 2 mm of the aggregate
- In a crack < 1.5 µm
- In a $SiO_2$ mineral phase

**Preparation**

The regions of interest in the samples were located first by SEM imaging and the presence of ASR product was confirmed by energy-dispersive X-ray spectroscopy (EDX). A line scan is made across the crack and an increase of calcium and alkalis content of a few atomic percent (mostly from 1 to 5 percent) is looked for to confirm the presence of ASR in the thin crack (< 2 µm). Once localized, the region of interest is cut perpendicular to the crack, using a focused ion beam (FIB). Thinning of the lamella (see Figure 7.1) is done at progressively decreasing voltages and currents, ranging from 30kV-27nA down to 5kV-80pA, in order to optimize the time spent and to prevent beam damage. A thin lamella of approximate dimensions 10x12µm and thickness 200nm is obtained and welded to a TEM grid for further analysis regarding composition and structure.
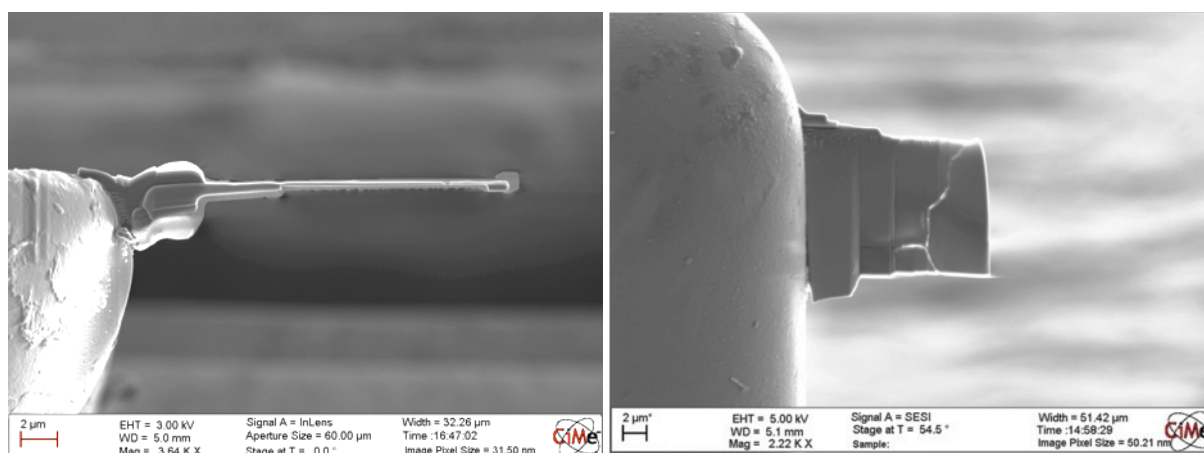


Figure 7.1 : TEM lamella after thinning in the FIB top view (left) and side view (right).

## 7.2.2  TEM grid preparation for synthetic samples

**Samples**

Three different samples  termed SNC, $SK_{0.25}N_{0.25}C$ (SKNC) and SKC from [46] were investigated, where the major phases are Na-shlykovite, ASR-P1 and K-shlykovite, respectively, based on powder X-ray diffraction analysis. They were synthesized at a temperature of 80°C. In this paper, they are respectively renamed SNC, SKNC and SKC. The reaction products contained silicon (S), calcium (C), potassium (K) and/or sodium (N) in various quantities, which will be assessed in the results.

**Preparation**

The synthetic powder was dispersed in ethanol, and a drop of the solution is placed on a Holey Carbon film copper grid, 200 mesh, 50 microns, for the STEM analysis. When dried out, the grid is stored under high vacuum.

### 7.2.3  STEM analysis

The product was studied in STEM mode (scanning TEM mode) for EDX measurements. Diffraction patterns were obtained from specific areas of the sample using selected area electron diffraction (SAED). The parameters used for analysis with STEM are also important to preserve the product, analysis is performed at a rather low voltage, 80kV instead of the usual 200kV, and the cumulative electron dose was kept low, below $5 \times 10^2$ e/Å$^2$, when compared with [155].

For EDX measurements, the sample is tilted by 20° to improve X-rays collection efficiency and a defocus of approximately 200nm is used to avoid beam damage. The analysis is then done after selecting the region of interest.

## 7.3      Results and discussion

### 7.3.1  Morphology and structure

**SNC**
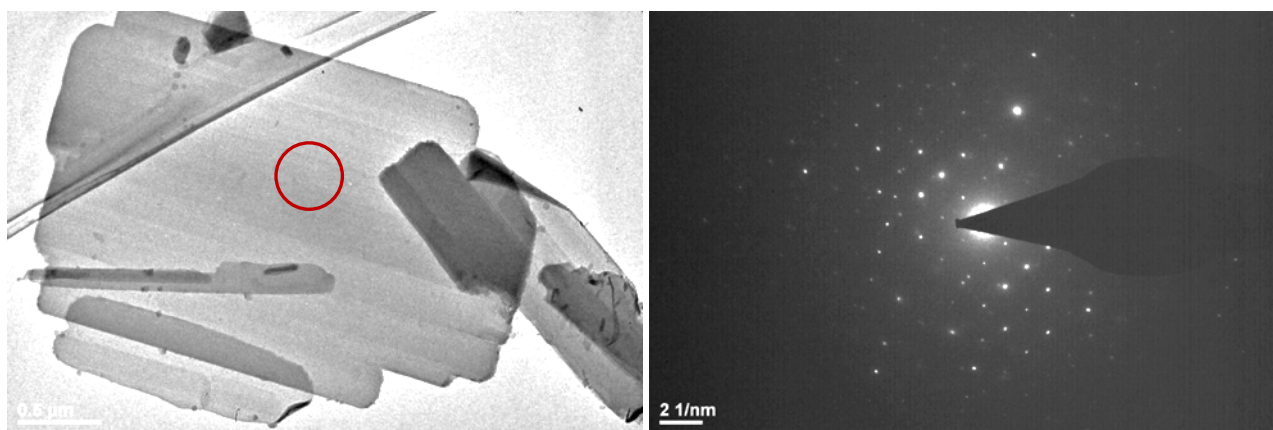


Figure 7.2 : Platelet-like Na-shlykovite structure of SNC sample (left) and diffraction pattern from the red zone (right)
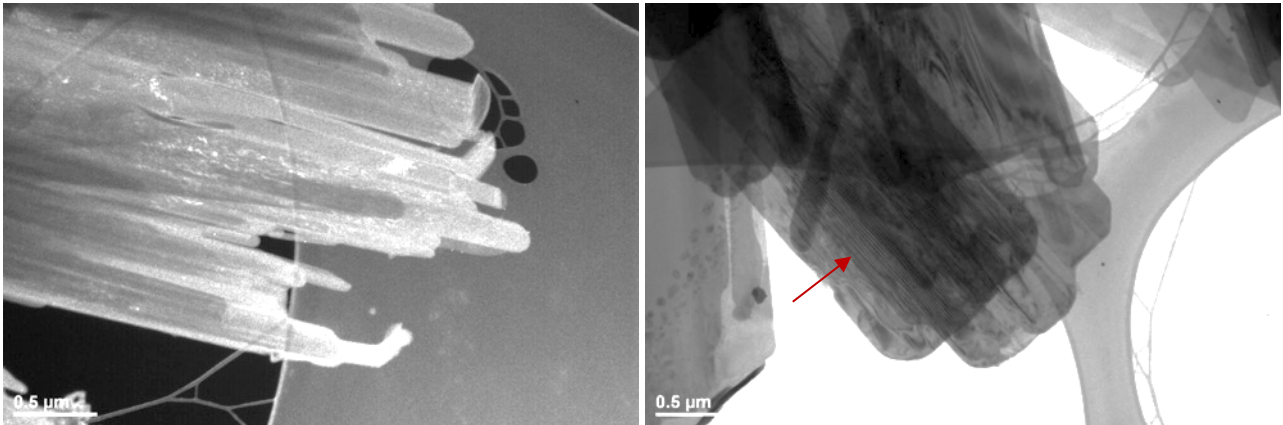
Figure 7.3 : Dark field image showing the micro-crystallinity of the Na-shlykovite (left) and bright field image showing atomic planes alignments (right, red arrow)

In SNC sample, ASR products have the following characteristics based on STEM analysis:

- A very well-defined platelet-like or rod-like structure corresponding to Na-shlykovite as seen in Figure 7.2 (left) and Figure 7.3 (left)
- It is crystalline (Figure 7.2 (right)).
- In dark field, the micro-crystalline nature of the rods is clearly seen by the brighter areas which show crystallographic planes with the same orientation (Figure 7.3 (left)). Additional features could be observed in Figure 7.3 (right), such as atomic plane alignment, in line with the layered-silicate structure of Na-shlykovite reported in [46].

**SKC**
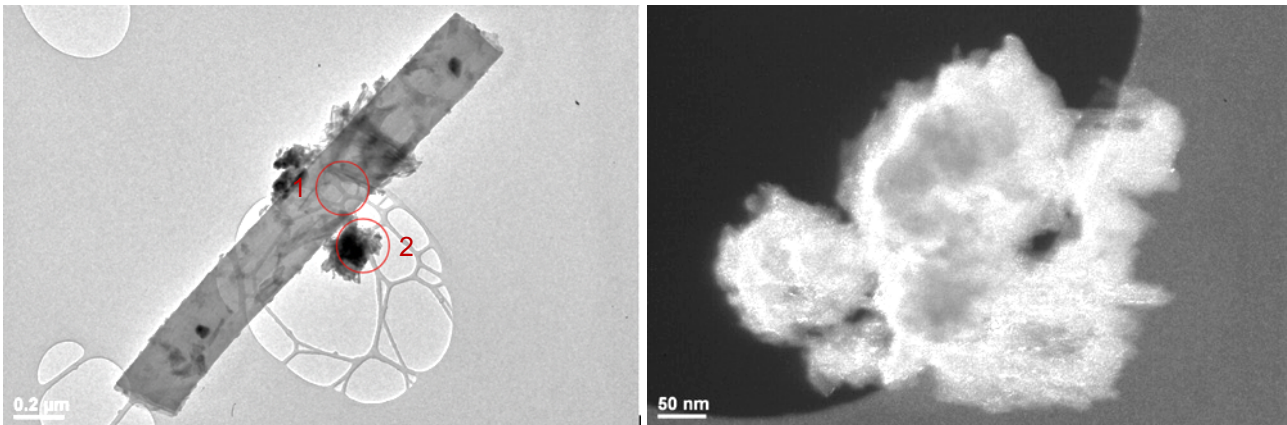


Figure 7.4 : Two different products types. Platelet-like K-shlykovite (circle 1) and fluffy product (circle 2) (left) and dark field image showing the nanocrystalline structure of the SKC ASR product granular structure (right).
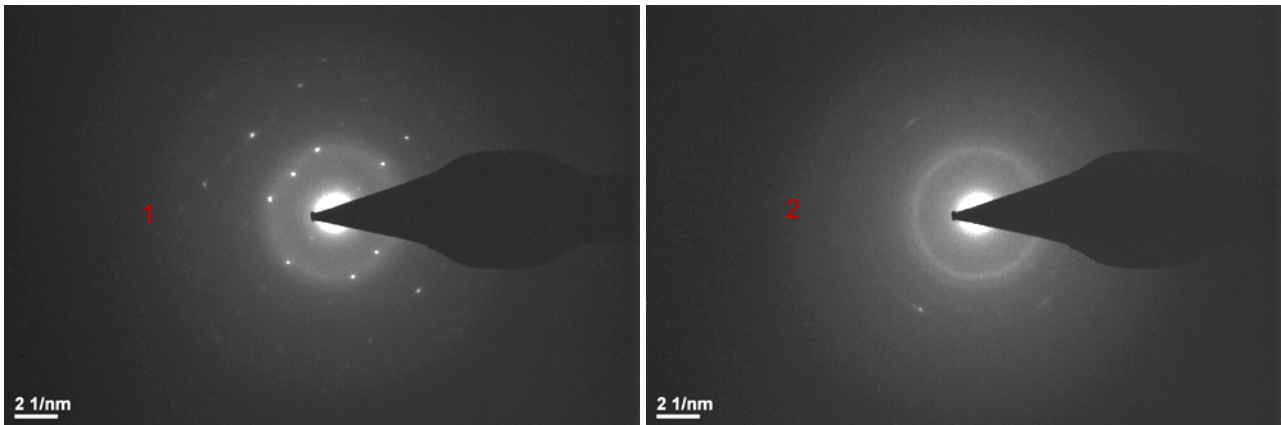
Figure 7.5 : Diffraction patterns showing crystallinity of the analysed area 1 (left) and the weak nano-crystallinity of the analysed area 2 (right).
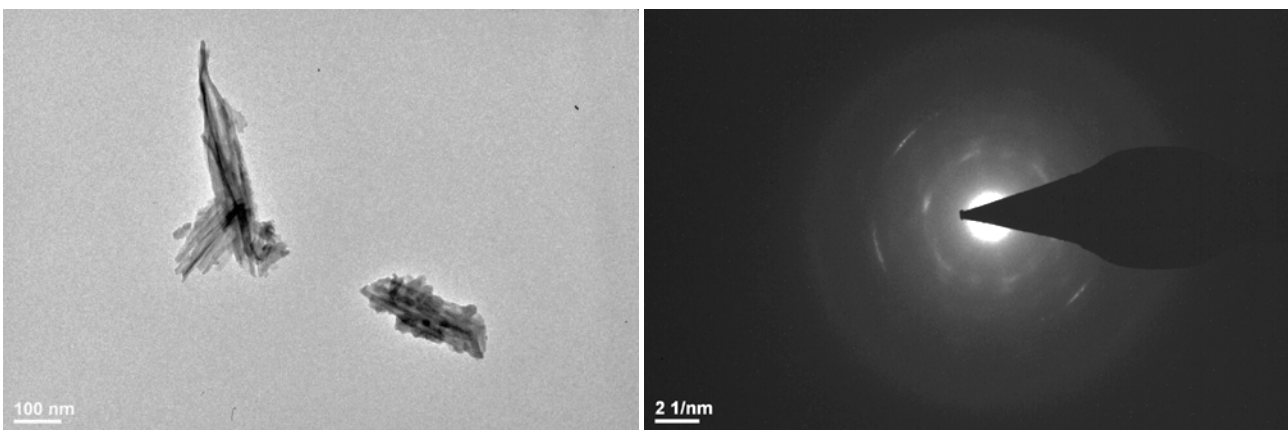


Figure 7.6 : Fibrillar product ASR-P1 (left) and corresponding nanocrystalline diffraction pattern (right).

In SKC sample, ASR products have the following characteristics based on STEM analysis:

- They present different structures. Only one occurrence of platelet-like product (corresponding K-shlykovite) as in Figure 7.4 (right) was found, whereas the rest of the products were found to have a fibrillar structure (likely to be ASR-P1 or CSH) in Figure 7.6 (left) or a more fluffy (or granular) appearance (likely to be ASR P1 or C-S-H) like in Figure 7.4 (right), since K-shlykovite and ASR-P1 can co-precipitate with C-S-H as observed from experiments and also predicted by thermodynamic modelling [39].

- All products are crystalline but at different scales as can be clearly seen in Figure 7.5 and Figure 7.6 (right). The fluffy and fibrillar product (ASR-P1) shows a very interesting nanocrystalline diffraction pattern (Figure 7.5 (right) and Figure 7.6 (right)), whereas the platelet-like product (K-shlykovite) shows a crystalline diffraction pattern with a clear orientation (Figure 7.5 (left)).

**SKNC**
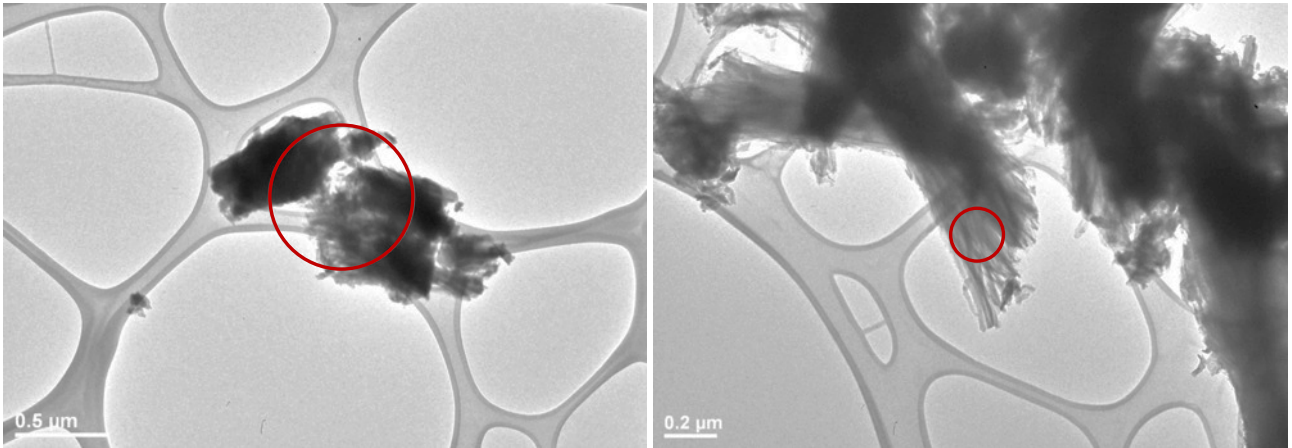
Figure 7.7 : Granular (left) or fibrillar ASR-P1 (right) morphology of SKNC sample.
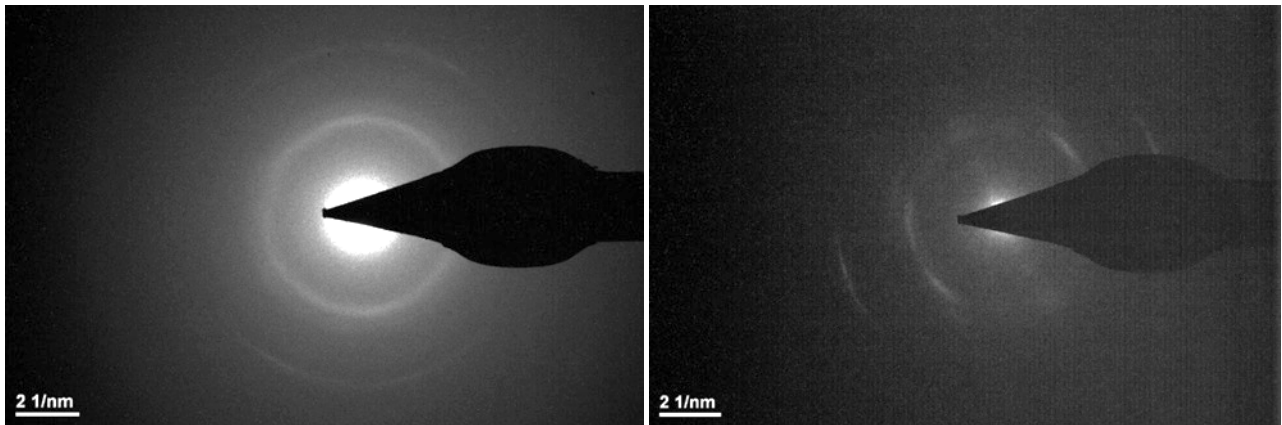


Figure 7.8 : Diffraction patterns of Figure 7.7 left red zone (left) and Figure 7.7 right red zone (right).

In SKNC sample, ASR products have the following characteristics based on STEM analysis:

- Most of the observed ASR products present what in 2D looks like a fibrillar morphology (Figure 7.7). In the more agglomerated areas, the product is densely packed and so the morphology cannot be clearly seen (Figure 7.7 (left)).
- All products are nanocrystalline as seen in Figure 7.8.

**Field samples**
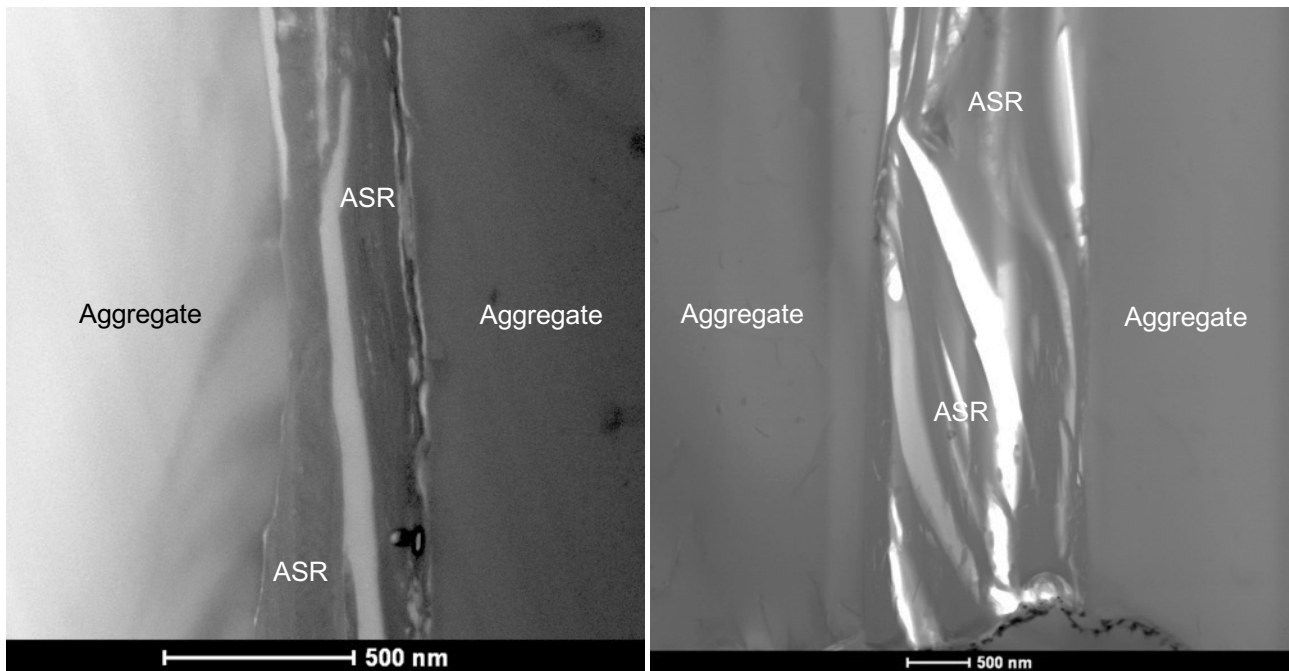


Figure 7.9 : Dam L2 (left) and L1 (right) samples morphologies.

In the case of the sample Dam, the product morphology is harder to assess compared to the synthetic one, indicating that the structure of these products is less ordered. In Figure 7.9 (left), L2 sample, no specific morphology appears, even though the product seems to be oriented parallel to the product/aggregate interface. The clefts were already present before beam exposure. For L1 (Figure 7.9 (right)) the platelet-like product morphology is visible, and also oriented parallelly to the product/aggregate interface. According to their diffraction pattern, both products were found to be amorphous.
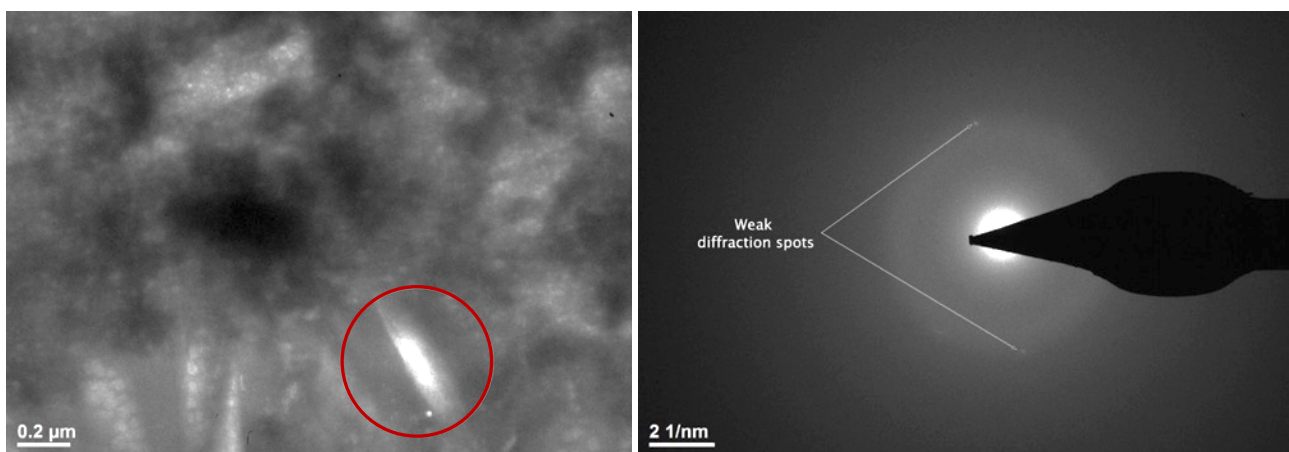


Figure 7.10 : Wall L2 amorphous (granular morphology) and crystalline (platelet-like morphology) (left) and diffraction pattern from the red zone showing a weak crystallinity (right).

Figure 7.11 : Wall L1 showing platelet-like morphology (but amorphous) (left) and Wall L2 showing the intermixing of both granular/globular and platelet-like morphologies (right).

Two clear morphologies are visible in the Wall samples. In L1 Figure 7.11 (left), only platelet-like product was found, and in L2 Figure 7.11 (right) granular and platelet-like products were found.

Analysing the electron diffraction patterns with SAED, the products present in the Dam samples and the granular product in the Wall samples were found to be amorphous. However, SAED performed on the platelet-like product in Wall sample L2 showed a diffraction pattern with two weak diffracting spots as seen in Figure 7.10.

The weakness of the diffraction spots indicates there is a low amount of ordered material in the analysed zone and it can be due to the following reasons:

- The product is only partially crystalline inducing very few diffracted electrons and thus a weak intensity.

- Even if used beam STEM operating conditions aimed at preserving the ASR products, it could have been slightly damaged by electron beam, resulting in observation of weaker crystalline product [23].

In the Church sample also, two morphologies are present. It is particularly visible in L1 Figure 7.12, in which the long platelets are intermixed with the less dense granular product.

In Church L2, the granular product is located at the aggregate wall interface, with on top what seems to be platey product Figure 7.13 (a). The platelets shape is more obvious in Figure 7.13 (c) where the separation of the platelets is seen in the upper right corner.
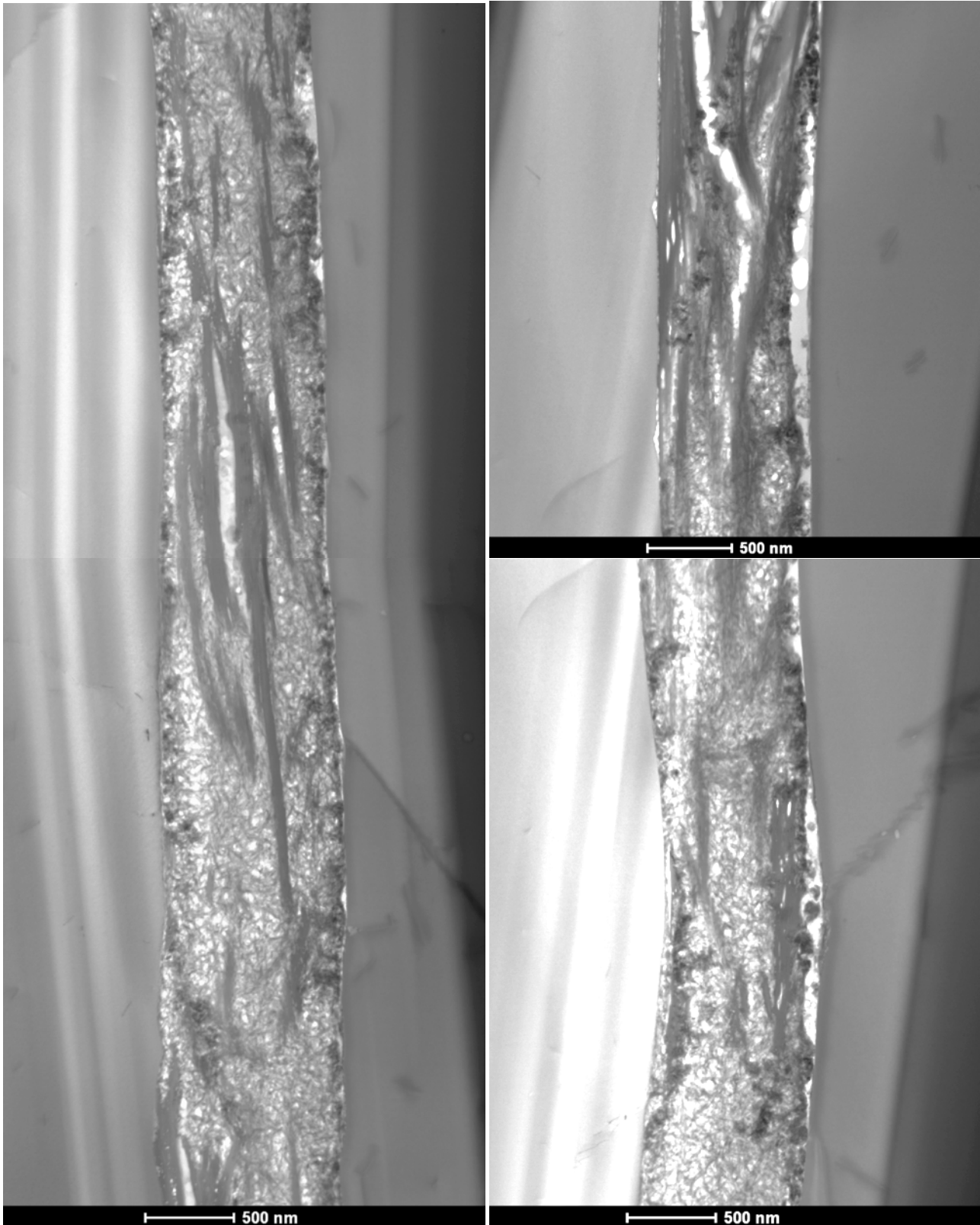
Figure 7.12 : Church L1 crack in which two ASR products morphologies are distinguished : platey and granular.
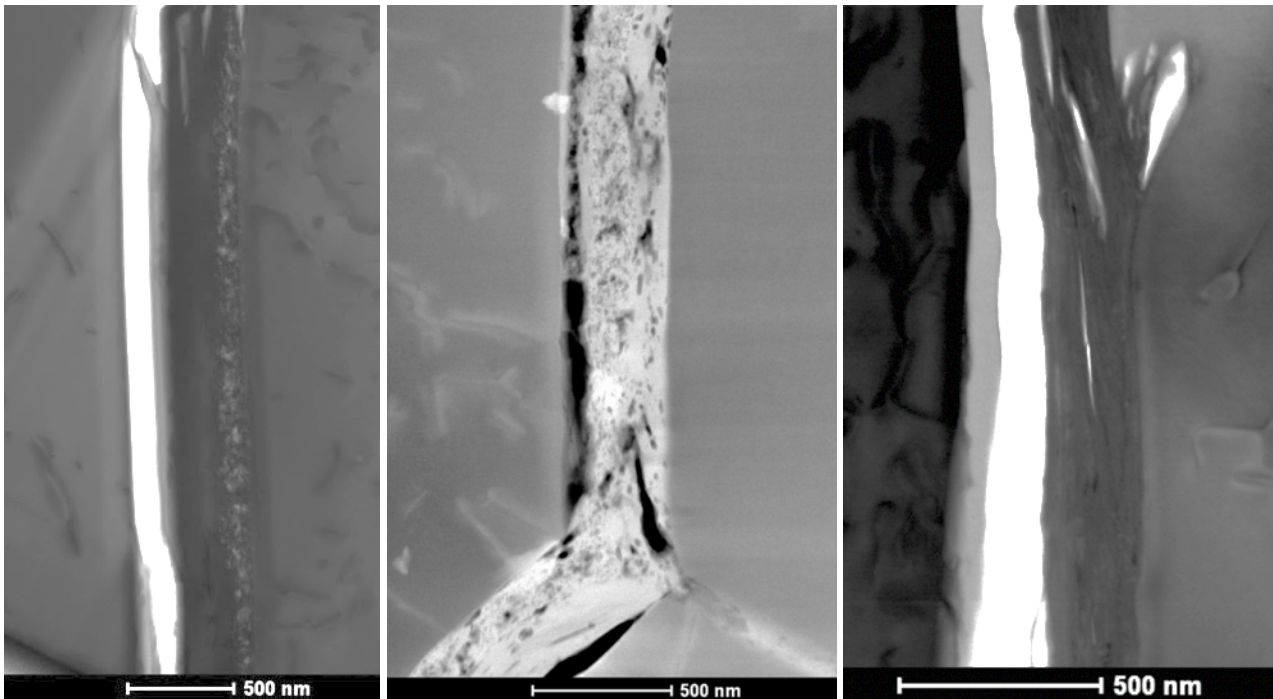
Figure 7.13 : Church L2 BF image showing granular product on the right side of the aggregate wall with platey product over it (left), HAADF image showing mainly granular product (middle) and BF image showing platey product (right)

The sample collected on the bridge in Valais was severely affected by ASR. In this particular case the product studied was located in a large vein, and considered as late-stage ASR product. It has a platey morphology as seen in Figure 7.14. The platelets are easily distinguished and they exhibit a crystalline structure as shown by the dots present in the diffraction pattern from Figure 7.15. Compared to the rest of the field samples, the bridge ASR product crystallinity is strong, probably due to the fact it is some second-stage thus aged product. Crystallinity is probably favored with ageing, as also noticed in field concrete [22].
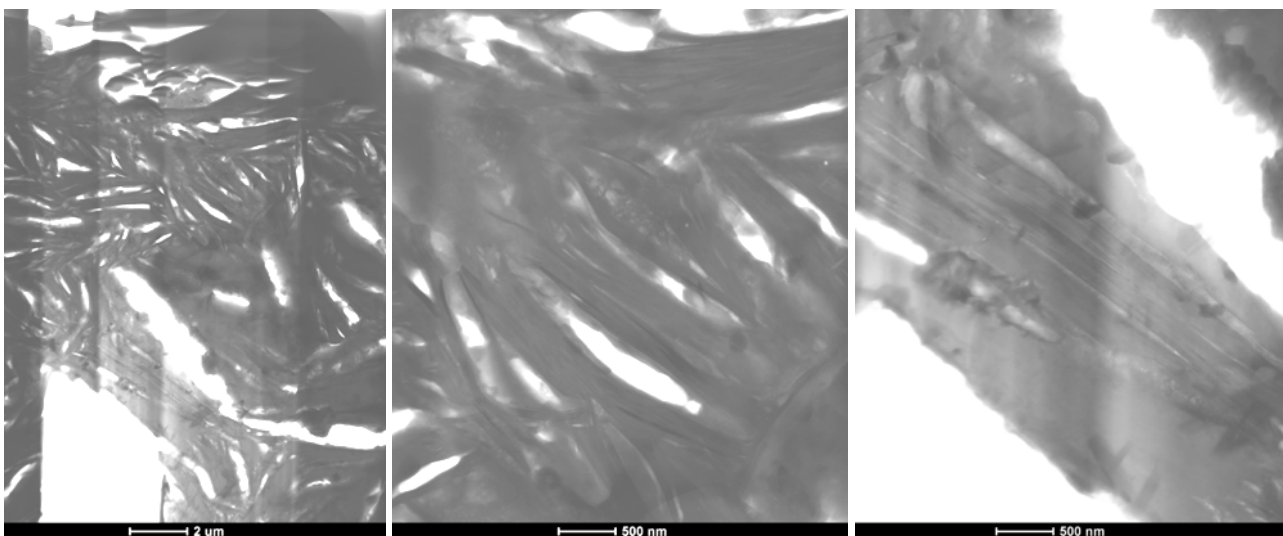


Figure 7.14 : Bridge L1 showing platelets entanglement in a general view (left) and at higher magnification (middle) and (right).
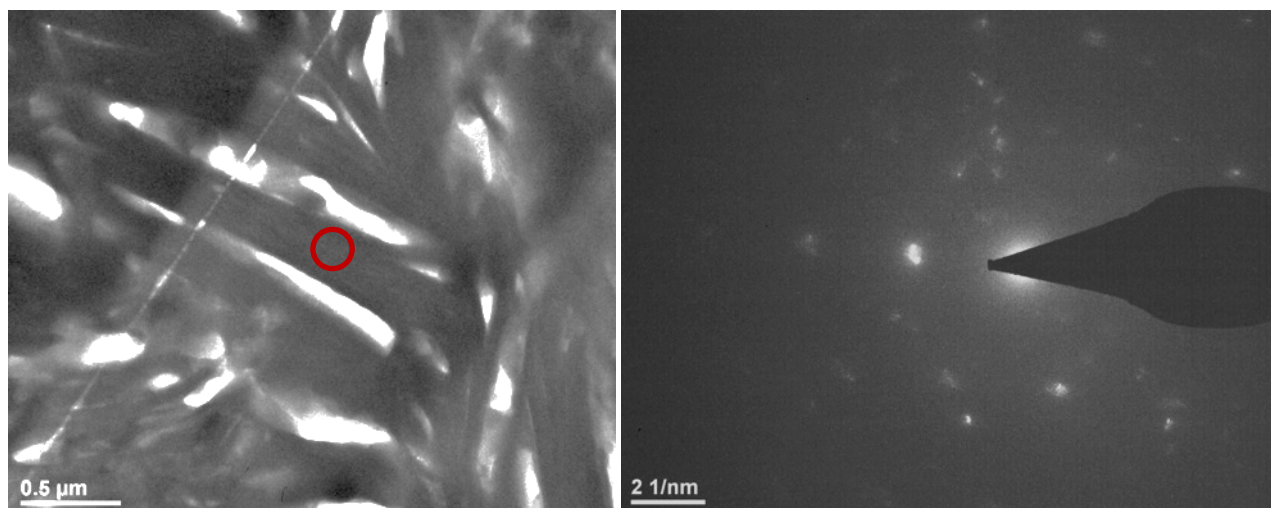
Figure 7.15 : Bridge L1 area selection in red with SAED aperture (left) and the resulting crystalline structure (right)

## 7.3.2   Composition

The compositions presented in Table 7.1 are very similar between the different analysed particles (L1 to L4) of each synthetic product, and also between the three synthetic products themselves. Only SKC seems to have a variation in the Ca/Si ratio, which suggests in this sample that one phase of ASR product contains more calcium (ASR P1) than the other (Schlykovite), or eventually indicates a coprecipitation of C-S-H [39]. L1 has a slightly lower calcium content compared to L2 and L3. If linked with the morphology and structure, L1 was the only particle to present a morphology in a platelet form and a crystalline structure, similar to SNC, in line with the fact that both Na-shlykovite and K-shlykovite have ideal alkali/Si ratio of 0.25. The other particles or agglomerates found were all having the rod-like appearance of ASR-P1 and fluffy appearance of broken ASR P1 rods (not C-S-H due to the composition) with a microcrystalline structure, thus indicating calcium content might have a more significant role than alkali in the product formation. Both experimental studies and thermodynamic modelling showed that increasing the calcium content could destabilize the K-shlykovite to ASR-P1 and further to C-S-H [39].

The type of alkali and their proportion combination indicate to have an effect on the morphologies and structures as also reported in [46], since a difference in morphology and structure was observed between SNC and SNKC products, with no significant calcium but alkali content variation.

Table 7.1 : Normalized composition of synthetic and field samples ASR product for different particles or lamellae.

|  |  | Si | Ca | K | Na | **Ca/Si** | **(K+Na)/Si** |
|---|---|---|---|---|---|---|---|
|  |  | at. % | at. % | at. % | at. % | at. % | at. % |
|  | L1 average | 64,06 | 17,02 | 0,09 | 18,83 | **0,27** | **0,30** |
| SNC | L2 average | 67,25 | 15,74 | 0,06 | 16,95 | **0,23** | **0,25** |
|  | L3 average | 65,67 | 15,70 | 0,07 | 18,56 | **0,24** | **0,28** |

| | | | | | | |
|---|---|---|---|---|---|---|
| | L4 average | 64,23 | 15,09 | 0,03 | 20,65 | **0,23** | **0,32** |

| | | | | | | |
|---|---|---|---|---|---|---|
| SKC | L1 average | 66,76 | 16,20 | 16,90 | 0,13 | **0,24** | **0,26** |
| | L2 average | 62,83 | 21,99 | 14,80 | 0,38 | **0,35** | **0,24** |
| | L3 average | 61,47 | 22,90 | 15,34 | 0,29 | **0,37** | **0,25** |

| | | | | | | |
|---|---|---|---|---|---|---|
| SNKC | L1 average | 62,49 | 17,45 | 10,72 | 9,35 | **0,28** | **0,32** |
| | L2 average | 63,05 | 17,20 | 10,00 | 9,75 | **0,27** | **0,31** |
| | L3 average | 62,30 | 17,39 | 10,30 | 10,01 | **0,28** | **0,33** |
| | L4 average | 62,31 | 16,91 | 11,51 | 9,26 | **0,27** | **0,33** |

| | | | | | | |
|---|---|---|---|---|---|---|
| Dam | L1 average | 65,95 | 17,88 | 14,94 | 0,43 | **0,27** | **0,25** |
| | L2 average | 63,26 | 21,38 | 9,12 | 7,26 | **0,34** | **0,24** |

| | | | | | | |
|---|---|---|---|---|---|---|
| Wall | L1 average | 60,38 | 15,06 | 19,20 | 5,35 | **0,25** | **0,42** |
| | L2 average AP | 43,50 | 25,43 | 26,32 | 4,76 | **0,59** | **0,77** |
| | L2 average Mix | 50,90 | 20,74 | 24,55 | 3,80 | **0,41** | **0,56** |
| | L2 average CP | 56,80 | 23,35 | 18,19 | 1,66 | **0,41** | **0,35** |

| | | | | | | |
|---|---|---|---|---|---|---|
| Bridge | L1 average | 65,71 | 12,77 | 11,98 | 9,53 | **0,19** | **0,33** |
| | L2 average | 65,04 | 13,32 | 11,73 | 9,92 | **0,20** | **0,33** |
| | L3 average | 67,28 | 14,07 | 11,42 | 7,24 | **0,21** | **0,28** |

| | | | | | | |
|---|---|---|---|---|---|---|
| Church | L1 average | 55,74 | 22,75 | 11,21 | 10,30 | **0,41** | **0,39** |
| | L2 average | 62,93 | 23,10 | 11,04 | 5,03 | **0,37** | **0,26** |

Globally, the normalized concentrations are similar between the synthetic products, with an increase in calcium content for the ASR P1 phase. They also have similar composition with the field samples, when comparison is made for each morphology.

Wall L2 and Bridge L1, L2 and L3 samples are different from the other lamellae, it is not part of the early stage products but it is rather some second stage product (see definition of the two in chapter 3). Indeed, the ASR vein from where it was extracted is a few microns wide, and presence of amorphous and crystalline products could visually clearly be seen, based on the description from [21].
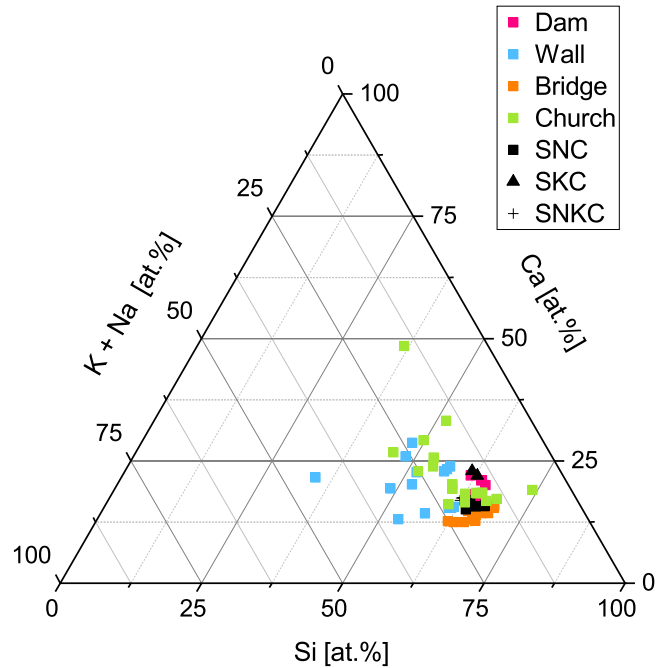


Figure 7.16 : Ternary diagram presenting the normalized composition of ASR products from field and synthetic samples.

The ternary diagram in Figure 7.16 shows the compositions in a more visual way, showing the similarity between all products discussed above, however, two groups tend to emerge. A group containing slightly more calcium than alkali, and a group containing less or the same amount of calcium compared to alkali.

For clarity purpose, the results are separated in two ternary diagrams :

- synthetic results (Figure 7.17)
- field results (with addition of accelerated laboratory results, for comparison, Figure 7.18)
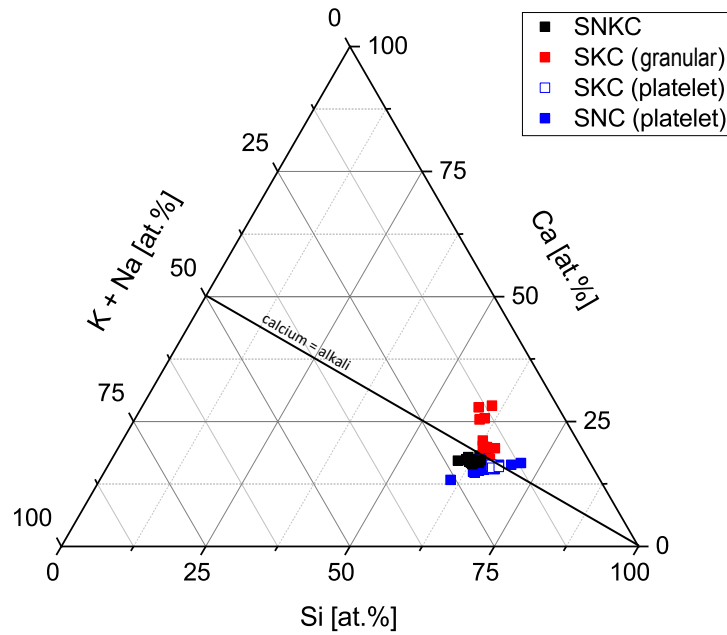
Figure 7.17 : Ternary diagram presenting the normalized composition of ASR products from synthetic samples.

The granular ASR phase (ASR P1) termed SKC (granular) in the ternary diagram Figure 7.17 clearly exhibits a higher calcium content than the rest of the products, as discussed in the previous paragraphs. The field and accelerated lab samples also exhibit the same behavior. The granular product pictured in red in the ternary diagram Figure 7.18 tend to contain a higher calcium content than the other samples, which contain themselves slightly more alkali than calcium.
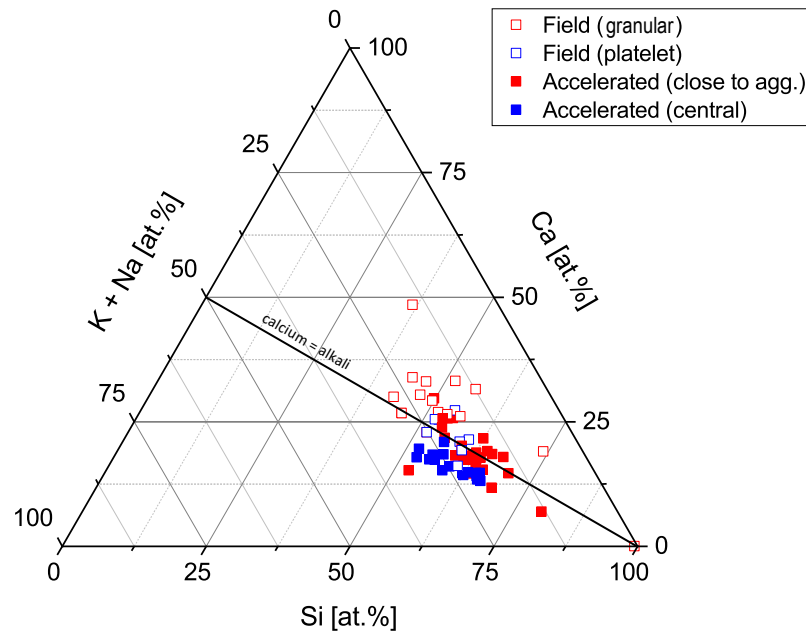


Figure 7.18 : Ternary diagram presenting the normalized composition of ASR products from field and laboratory accelerated samples.

In addition to the previous findings, there is a clear enrichment in calcium with time, as demonstrated by the compositional differences between the accelerated samples and the field samples. This was also hypothesized in chapter 5 with the results obtained at 38 °C, for which a greater gap between the alkali and calcium amount was observed. It was considered to be related to the formation steps of the product.

## 7.4    Conclusion

In this study, three synthesized ASR products with various alkali content as reported by [46] have been analysed by STEM to define their morphology, composition and structure. Four field products from different structures in Switzerland have also been analysed according to a new preparation method combining SEM, FIB and STEM described in [23] and in more details in chapter 3 of this thesis. The samples have been compared between each other and the following conclusions can be drawn from this preliminary study:

- ASR products are present in two very distinct morphologies: a platey and a granular morphology in both synthetic and field samples.
- The morphology is influenced by the calcium content and the initial K/Na molar ratio as seen in the synthetic samples.
- The granular product from field samples (ASR P1 in synthetic samples) contains more calcium than the platey products from field samples (schlykovite in synthetic samples), which themselves contain more alkali.
- In synthetic samples, the structure is linked to the morphology: platey products are crystalline corresponding to K- or Na-shlykovite, and fibrillar/granular products are nanocrystalline (due to fibrils size) corresponding to ASR-P1.
- In field samples, some platey products are weakly crystalline whereas the granular products are amorphous. Due to the low amount of product, crystallinity is difficult to assess.
- From the compositional results of the field and accelerated samples, there is an enrichment in calcium with time.
- Field, accelerated and synthetic samples exhibit similar composition and related morphologies. The structure is different, showing a much stronger crystallinity in synthetic samples than in field and accelerated samples.

As lastly stated, one main difference with the field, accelerated test and synthetic samples is that there is generally a higher degree of crystallinity in the synthetic samples than in the field (except the second-stage samples) or accelerated ones. Crystallinity is probably favored by time, as also observed in the field [22].

It is also affected by the high temperature and free of constraints environment and also quantity of material at disposal for the study.

Future research should focus on studying the behavior of the granular nanocrystalline ASR product. It is the one mainly encountered in the early stage concrete degradation and it has a role in the deterioration and expansion of concrete structures. Synthetic products offer a good base to study its water uptake and its

behavior in various environmental conditions, with enough available material quantities for analysis with different lab techniques.

## 7.5　Acknowledgements

# Chapter 8    Conclusions and perspectives

The major goal of this thesis was to characterize the early stage ASR product morphology, composition and structure by electron microscopy. It has been accomplished by mastering SEM, FIB and TEM techniques and choosing suitable samples. The main achievements are summarized in the following subsections, with a final discussion on the future needs or areas to develop.

## 8.1    Early-stage products characteristics and their meaning (chapter 4 & 5)

Observation of ASR products before they are macroscopically detected is made possible by a combination of SEM, FIB and TEM electron microscopy techniques. TEM allowed the analysis of in-situ ASR product cracks with minimalistic contribution of the neighbouring phases, and enables the collection of reliable data about the product.

In the Swiss-standard accelerated concrete samples (60°C), analysis clearly reveals that different ASR products are formed displaying a certain variation in chemical composition. Moreover, there is no clear-cut distinction between amorphous and crystalline ASR products. Both the morphology and the results obtained with SAED indicate that there is continuous transition between the two from clearly amorphous phases to various nanocrystalline ASR products to the well-crystallized ASR products as described for example in [48]. At the same time, this transition seems to be the result of maturation process with the amorphous phase representing the initial product.

The previous statement is confirmed by the evaluation of field-realistic accelerated concrete samples (40°C), in which only a precursor and an amorphous ASR product were found. The lower reaction kinetics lead to observation of different stages of the ASR formation. From the results, it is hypothesized there is first formation of a precursor product containing mainly alkali and a low quantity of calcium and silicon. The continuous dissolution of silica leads to the formation of an amorphous product mainly containing silicon, some calcium and alkali close to an equal quantity. Finally, a maturation process leads to the formation of a nanocrystalline or crystalline product, with similar composition as the amorphous product. The slight differences observed are believed to be due to an overlapping and mixing of the precursor product with the amorphous or crystalline product. The mechanism of ASR product formation seems to be a dissolution-formation process rather than a solid-state process in the aggregate matrix.

Only monitoring of the continuous process could settle the order of product formation. However, the time scale of ASR product formation and the difficulty of characterization without cutting the samples have prevented the implementation of such a method.

Concerning the role of the different phases, in the case of early stage product, no pure silico-alkaline product was found in the major cracks of aggregates. The only occurrences of alkali ions only without any calcium happened in very thin cracks which were not cracked opened and termed as crack tips. Such findings do suggest that alkali and calcium have different roles and effects, the first one more active in the dissolution and the second in the product formation. The mere presence of alkali is suggested to be insufficient to propagate cracks in concrete. More investigations are needed to confirm this hypothesis.

## 8.2     SCM's addition impact on ASR formation (chapter 6)

FA and LC3 cement replacement in concrete has proved to reduce the expansion due to ASR formation. In this work, it is shown the main effect of FA and LC3 addition is to hinder ASR product formation, without impacting its composition. The exact mechanisms leading to reduction of ASR product formation are still to be confirmed, but are linked to an alkali depletion and/or the presence of Al. The calcium is present in the product, and seems to be slightly more present. It indicates that calcium is available for ASR product formation, and that it is rather the alkali or the silica which are less available.

## 8.3     Relation to field & synthetic samples and their relevance (chapter 7)

It is confirmed that ASR found in accelerated samples is similar to the one from the field samples. Both amorphous and crystalline products are found in the field, with similar composition to the accelerated samples. The main difference is that there is much more crystalline product in the field samples as these are much older, and crystallinity is much stronger, indicating aging of the product does have an impact on the product morphology and structure if not on the composition. A future focus should be made on the amorphous product since it is the one mostly present at the beginning of the reaction, also after expansion is already observed.

Synthetic samples also showed a good analogy with early stage products. Mainly crystalline products were synthesized, but an amorphous to nanocrystalline product ASR P1 showed good correlation with the early stage product. The scale of production in comparison to field samples provides a new range of opportunities to study the product formation with techniques requiring substantial quantities of material.

## 8.4     Perspectives and future work

The implementation of an effective electron microscopy techniques combination is and will be useful to study other products formation at nanoscale in concrete.

Now the method for sample investigation is well established, further investigations of ASR early stage product formation in various mineral phases should be pursued, to detect any difference, any specific action or interaction with the aggregate structure.

There is a heterogeneity of the ASR product at microscale, which has been detected by synchrotron analysis [59], but also at nanoscale as detected in this thesis work. This interesting finding could not be investigated with the techniques proposed in the thesis. ASR being sensitive to the electron beam, it is not possible to

study the structure with High Resolution TEM (HRTEM). Atom Probe Tomography was tested to study the atomistic scale distribution of elements present in ASR product (see Appendix 1). The sample preparation was very successful, however, the ASR product being a not so stable solid, the analysis of the tips only led to one result, which was not enough to draw a conclusion. Also, progress on this newly developing technique will probably open possibilities in the near future, even for versatile materials.

A very important parameter still has to be evaluated to confirm hypotheses exposed in the thesis, and bring new insight on the mechanism of expansion : time. It has been for long impossible to see the live evolution of natural phenomena in a given environment, but very powerful techniques combining high end electron microscopic techniques with a possibility to preserve the environmental conditions are nowadays available. It includes for example Environmental Transmission Electron Microscopy (ETEM) and Liquid Phase Electron Microscopy (LPEM). Knowing at which stage of the reaction the cracking occurs and the state of ASR product at a given time is crucial to progress in the reaction knowledge.

# References

[1]     'Learning from the Genoa bridge collapse', *Institution of Civil Engineers (ICE)*, Jan. 03, 2019. https://www.ice.org.uk/news-and-insight/the-civil-engineer/january-2019/learning-from-the-genoa-bridge-collapse (accessed Nov. 19, 2021).

[2]     B. Fournier and M.-A. Bérubé, 'Alkali-aggregate reaction in concrete: a review of basic concepts and engineering implications', *Can. J. Civ. Eng.*, vol. 27, no. 2, pp. 167–191, Apr. 2000, doi: 10.1139/l99-072.

[3]     I. Fernandes *et al.*, 'Alkali–silica reactivity of some common rock types. A global petrographic atlas', *Quarterly Journal of Engineering Geology and Hydrogeology*, vol. 46, no. 2, pp. 215–220, May 2013, doi: 10.1144/qjegh2012-065.

[4]     S. Diamond, 'ALKALI AGGREGATE REACTIONS IN CONCRETE. AN ANNOTATED BIBLIOGRAPHY 1939-1991', 1992.

[5]     T. E. Stanton, 'A study of alkali-aggregate reactivity', *Proc. Amer. Soc. Civ. Eng*, vol. 66, pp. 1781–1792, 1940.

[6]     T. E. Stanton, 'Influence of cement and aggregate on concrete expansion', *Engineering News-Record*, 1940.

[7]     T. E. Stanton, 'Expansion of Concrete through Reaction between Cement and Aggregate', *Transactions of the American Society of Civil Engineers*, vol. 107, no. 1, pp. 54–84, Jan. 1942, doi: 10.1061/TACEAT.0005540.

[8]     C. Merz, F. Hunkeler, and A. Griesser, 'Schäden durch Alkali-Aggregat-Reaktion an Betonbauten in der Schweiz', 2006.

[9]     C. Merz and A. Leemann, 'Validierung der AAR-Prüfungen für Neubau und Instandsetzung', *BUNDESAMT FUER STRASSENBAU (ASTRA)/OFFICE FEDERAL DES ROUTES (OFROU)*, no. 648, 2011.

[10]    S. Diamond, 'A review of alkali-silica reaction and expansion mechanisms 1. Alkalies in cements and in concrete pore solutions', *Cement and Concrete Research*, vol. 5, no. 4, pp. 329–345, Jul. 1975, doi: 10.1016/0008-8846(75)90089-7.

[11]    L. S. Dent Glasser and N. Kataoka, 'The chemistry of "alkali-aggregate" reaction', *Cement and Concrete Research*, vol. 11, no. 1, pp. 1–9, Jan. 1981, doi: 10.1016/0008-8846(81)90003-X.

[12]    S. Chatterji, 'Chemistry of alkali–silica reaction and testing of aggregates', *Cement and Concrete Composites*, vol. 27, no. 7, pp. 788–795, Aug. 2005, doi: 10.1016/j.cemconcomp.2005.03.005.

[13]    A. B. Poole, 'Alkali-silica reactivity mechanisms of gel formation and expansion', p. 8, 1992.

[14]    R. Dron, 'Thermodynamique de la réaction alcali-silice', *Bulletin de liaison des Laboratoires des Ponts et Chaussées*, no. 166, 1990.

[15]    K. R. Iler, 'The chemistry of silica', *Solubility, polymerization, colloid and surface properties and biochemistry of silica*, 1979.

[16]    R. Helmuth, D. Stark, S. Diamond, and M. Moranville-Regourd, 'Alkali-silica reactivity: an overview of research', *Contract*, vol. 100, p. 202, 1993.

[17]    M. Brouxel, 'The alkali-aggregate reaction rim: Na2O, SiO2, K2O and CaO chemical distribution', *Cement and Concrete Research*, vol. 23, no. 2, pp. 309–320, Mar. 1993, doi: 10.1016/0008-8846(93)90096-R.

[18]    N. Thaulow, U. H. Jakobsen, and B. Clark, 'Composition of alkali silica gel and ettringite in concrete railroad ties: SEM-EDX and X-ray diffraction analyses', *Cement and Concrete Research*, vol. 26, no. 2, pp. 309–318, Feb. 1996, doi: 10.1016/0008-8846(95)00219-7.

[19]    S. A. Marfil and P. J. Maiza, 'Deteriorated pavements due to the alkali–silica reaction: A petrographic study of three cases in Argentina', *Cement and concrete research*, vol. 31, no. 7, pp. 1017–1021, 2001.

[20]    M. Kawamura and K. Iwahori, 'ASR gel composition and expansive pressure in mortars under restraint', *Cement and Concrete Composites*, vol. 26, no. 1, pp. 47–56, Jan. 2004, doi: 10.1016/S0958-9465(02)00135-X.

[21]    A. Leemann, T. Katayama, I. Fernandes, and M. A. T. M. Broekmans, 'Types of alkali–aggregate reactions and the products formed', *Proceedings of the Institution of Civil Engineers - Construction Materials*, vol. 169, no. 3, pp. 128–135, Feb. 2016, doi: 10.1680/jcoma.15.00059.

[22]    A. Leemann, Z. Shi, and J. Lindgård, 'Characterization of amorphous and crystalline ASR products formed in concrete aggregates', *Cement and Concrete Research*, vol. 137, p. 106190, Nov. 2020, doi: 10.1016/j.cemconres.2020.106190.

[23]    E. Boehm-Courjault, S. Barbotin, A. Leemann, and K. Scrivener, 'Microstructure, crystallinity and composition of alkali-silica reaction products in concrete determined by transmission electron microscopy', *Cement and Concrete Research*, vol. 130, p. 105988, Apr. 2020, doi: 10.1016/j.cemconres.2020.105988.

[24]    L. J. Struble and S. Diamond, 'Swelling Properties of Synthetic Alkali Silica Gels', *Journal of the American Ceramic Society*, vol. 64, no. 11, pp. 652–655, 1981, doi: 10.1111/j.1151-2916.1981.tb15864.x.

[25]    L. Struble and S. Diamond, 'Influence of cement alkali distribution on expansion due to alkali-silica reaction', in *Alkalies in concrete*, ASTM International, 1986.

[26]    S. Chatterji, 'Mechanisms of alkali-silica reaction and expansion', in *Proceedings of the 8th International Conference on Alkali-Aggregate Reaction, Kyoto, Japan*, 1989, pp. 101–105.

[27]    R. Dron, F. Brivot, and T. Chaussadent, 'Mécanisme de la réaction alcali-silice', *BULLETIN-LABORATOIRES DES PONTS ET CHAUSSEES*, pp. 61–68, 1998.

[28]    M. Prezzi, P. J. M. Monteiro, and G. Sposito, 'Alkali-Silica Reaction, Part I: Use of the Double-Layer Theory to Explain the Behavior of Reaction-Product Gels', *MJ*, vol. 94, no. 1, pp. 10–17, Jan. 1997, doi: 10.14359/280.

[29]    E. Garcia-Diaz, J. Riche, D. Bulteel, and C. Vernet, 'Mechanism of damage for the alkali–silica reaction', *Cement and Concrete Research*, vol. 36, no. 2, pp. 395–400, Feb. 2006, doi: 10.1016/j.cemconres.2005.06.003.

[30]    S. Chatterji, 'The role of Ca(OH)2 in the breakdown of Portland cement concrete due to alkali-silica reaction', *Cement and Concrete Research*, vol. 9, no. 2, pp. 185–188, Mar. 1979, doi: 10.1016/0008-8846(79)90024-3.

[31]    S. Urhan, 'Alkali silica and pozzolanic reactions in concrete. Part 1: Interpretation of published results and an hypothesis concerning the mechanism', *Cement and Concrete Research*, vol. 17, no. 1, pp. 141–152, Jan. 1987, doi: 10.1016/0008-8846(87)90068-8.

[32]     S. Chatterji, N. Thaulow, and A. D. Jensen, 'Studies of alkali-silica reaction, part 6. Practical implications of a proposed reaction mechanism', *Cement and Concrete Research*, vol. 18, no. 3, pp. 363–366, May 1988, doi: 10.1016/0008-8846(88)90070-1.

[33]     S. Chatterji, N. Thaulow, and A. D. Jensen, 'Studies of alkali-silica reaction. part 5. Verification of a newly proposed reaction mechanism', *Cement and Concrete Research*, vol. 19, no. 2, pp. 177–183, Mar. 1989, doi: 10.1016/0008-8846(89)90081-1.

[34]     H. Wang and J. E. Gillott, 'Mechanism of alkali-silica reaction and the significance of calcium hydroxide', *Cement and Concrete Research*, vol. 21, no. 4, pp. 647–654, Jul. 1991, doi: 10.1016/0008-8846(91)90115-X.

[35]     T. Ichikawa and M. Miura, 'Modified model of alkali-silica reaction', *Cement and Concrete Research*, vol. 37, no. 9, pp. 1291–1297, Sep. 2007, doi: 10.1016/j.cemconres.2007.06.008.

[36]     R. Dron and F. Brivot, 'Thermodynamic and kinetic approach to the alkali-silica reaction. Part 1: Concepts', *Cement and Concrete Research*, vol. 22, no. 5, pp. 941–948, Sep. 1992, doi: 10.1016/0008-8846(92)90118-F.

[37]     F. A. Rodrigues, P. J. M. Monteiro, and G. Sposito, 'The alkali-silica reaction: The surface charge density of silica and its effect on expansive pressure', *Cement and Concrete Research*, vol. 29, no. 4, pp. 527–530, Apr. 1999, doi: 10.1016/S0008-8846(98)00220-8.

[38]     M. D. Thomas, B. F. Fournier, and K. J. Folliard, 'Alkali-Aggregate Reactivity (AAR) Facts Book', 2013.

[39]     Z. Shi and B. Lothenbach, 'The role of calcium on the formation of alkali-silica reaction products', *Cement and Concrete Research*, vol. 126, p. 105898, Dec. 2019, doi: 10.1016/j.cemconres.2019.105898.

[40]     Z. Shi and B. Lothenbach, 'The combined effect of potassium, sodium and calcium on the formation of alkali-silica reaction products', *Cement and Concrete Research*, vol. 127, p. 105914, Jan. 2020, doi: 10.1016/j.cemconres.2019.105914.

[41]     F. Rajabipour, E. Giannini, C. Dunant, J. H. Ideker, and M. D. A. Thomas, 'Alkali–silica reaction: Current understanding of the reaction mechanisms and the knowledge gaps', *Cement and Concrete Research*, vol. 76, pp. 130–146, Oct. 2015, doi: 10.1016/j.cemconres.2015.05.024.

[42]     R. B. Figueira *et al.*, 'Alkali-silica reaction in concrete: Mechanisms, mitigation and test methods', *Construction and Building Materials*, vol. 222, pp. 903–931, Oct. 2019, doi: 10.1016/j.conbuildmat.2019.07.230.

[43]     T. C. Powers and H. H. Steinour, 'An Interpretation of Some Published Researches on the Alkali-Aggregate Reaction Part 1-The Chemical Reactions and Mechanism of Expansion', *JP*, vol. 51, no. 2, pp. 497–516, Feb. 1955, doi: 10.14359/11691.

[44]     R. Dron and F. Brivot, 'Thermodynamic and kinetic approach to the alkali-silica reaction. Part 2: Experiment', *Cement and Concrete Research*, vol. 23, no. 1, pp. 93–103, Jan. 1993, doi: 10.1016/0008-8846(93)90139-Z.

[45]     M. Bagheri, 'Aggregate dissolution in different pore solutions', *Infoscience*, 2021. https://infoscience.epfl.ch/record/286802 (accessed Jul. 02, 2021).

[46]     Z. Shi, G. Geng, A. Leemann, and B. Lothenbach, 'Synthesis, characterization, and water uptake property of alkali-silica reaction products', *Cement and Concrete Research*, vol. 121, pp. 58–71, Jul. 2019, doi: 10.1016/j.cemconres.2019.04.009.

[47]    Z. Shi, A. Leemann, D. Rentsch, and B. Lothenbach, 'Synthesis of alkali-silica reaction product structurally identical to that formed in field concrete', *Materials & Design*, vol. 190, p. 108562, May 2020, doi: 10.1016/j.matdes.2020.108562.

[48]    G. Geng *et al.*, 'Atomistic structure of alkali-silica reaction products refined from X-ray diffraction and micro X-ray absorption data', *Cement and Concrete Research*, vol. 129, p. 105958, Mar. 2020, doi: 10.1016/j.cemconres.2019.105958.

[49]    W. Wieker, C. Hübert, and R. Ebert, 'Contribution to the chemical reaction mechanism of the alkali-aggregate reaction', 1996.

[50]    S. Diamond, J. Barneyback, and L. J. Struble, 'Physics and chemistry of alkali-silica reactions', Purdue Univ., Lafayette, IN (USA), DOE/CS/40222-3; CONF-8103111-1, Jan. 1981. Accessed: Dec. 09, 2021. [Online]. Available: https://www.osti.gov/biblio/5680311

[51]    J. Lindgård, Ö. Andiç-Çakır, I. Fernandes, T. F. Rønning, and M. D. A. Thomas, 'Alkali–silica reactions (ASR): Literature review on parameters influencing laboratory performance testing', *Cement and Concrete Research*, vol. 42, no. 2, pp. 223–243, Feb. 2012, doi: 10.1016/j.cemconres.2011.10.004.

[52]    A. Gholizadeh-Vayghan, F. Rajabipour, M. Khaghani, and M. Hillman, 'Characterization of viscoelastic behavior of synthetic alkali–silica reaction gels', *Cement and Concrete Composites*, vol. 104, p. 103359, Nov. 2019, doi: 10.1016/j.cemconcomp.2019.103359.

[53]    A. Gholizadeh Vayghan, F. Rajabipour, and J. L. Rosenberger, 'Composition–rheology relationships in alkali–silica reaction gels and the impact on the gel's deleterious behavior', *Cement and Concrete Research*, vol. 83, pp. 45–56, May 2016, doi: 10.1016/j.cemconres.2016.01.011.

[54]    H. Du and K. H. Tan, 'Effect of particle size on alkali–silica reaction in recycled glass mortars', *Construction and Building Materials*, vol. 66, pp. 275–285, Sep. 2014, doi: 10.1016/j.conbuildmat.2014.05.092.

[55]    S. Chatterji, N. Thaulow, and A. D. Jensen, 'Studies of alkali-silica reaction. Part 4. Effect of different alkali salt solutions on expansion', *Cement and Concrete Research*, vol. 17, no. 5, pp. 777–783, Sep. 1987, doi: 10.1016/0008-8846(87)90040-8.

[56]    T. Knudsen and N. Thaulow, 'Quantitative microanalyses of alkali-silica gel in concrete', *Cement and Concrete Research*, vol. 5, no. 5, pp. 443–454, Sep. 1975, doi: 10.1016/0008-8846(75)90019-8.

[57]    A. Leemann, G. Le Saout, F. Winnefeld, D. Rentsch, and B. Lothenbach, 'Alkali–Silica Reaction: the Influence of Calcium on Silica Dissolution and the Formation of Reaction Products', *Journal of the American Ceramic Society*, vol. 94, no. 4, pp. 1243–1249, 2011, doi: 10.1111/j.1551-2916.2010.04202.x.

[58]    R. Dähn *et al.*, 'Application of micro X-ray diffraction to investigate the reaction products formed by the alkali–silica reaction in concrete structures', *Cement and Concrete Research*, vol. 79, pp. 49–56, Jan. 2016, doi: 10.1016/j.cemconres.2015.07.012.

[59]    G. Geng *et al.*, 'An in-situ 3D micro-XRD investigation of water uptake by alkali-silica-reaction (ASR) product', *Cement and Concrete Research*, vol. 141, p. 106331, Mar. 2021, doi: 10.1016/j.cemconres.2020.106331.

[60]    H. Maraghechi, F. Rajabipour, C. G. Pantano, and W. D. Burgos, 'Effect of calcium on dissolution and precipitation reactions of amorphous silica at high alkalinity', *Cement and Concrete Research*, vol. 87, pp. 1–13, Sep. 2016, doi: 10.1016/j.cemconres.2016.05.004.

[61]    K. E. Kurtis and P. J. M. Monteiro, 'Chemical additives to control expansion of alkali-silica reaction gel: proposed mechanisms of control', *Journal of Materials Science*, vol. 38, no. 9, pp. 2027–2036, May 2003, doi: 10.1023/A:1023549824201.

[62]    X. Hou, L. J. Struble, and R. J. Kirkpatrick, 'Formation of ASR gel and the roles of C-S-H and portlandite', *Cement and Concrete Research*, vol. 34, no. 9, pp. 1683–1696, Sep. 2004, doi: 10.1016/j.cemconres.2004.03.026.

[63]    T. Kim and J. Olek, 'Chemical Sequence and Kinetics of Alkali-Silica Reaction Part I. Experiments', *Journal of the American Ceramic Society*, vol. 97, no. 7, pp. 2195–2203, 2014, doi: 10.1111/jace.12992.

[64]    T. Kim and J. Olek, 'Chemical Sequence and Kinetics of Alkali–Silica Reaction Part II. A Thermodynamic Model', *Journal of the American Ceramic Society*, vol. 97, no. 7, pp. 2204–2212, 2014, doi: 10.1111/jace.12830.

[65]    T. Kim, J. Olek, and H. Jeong, 'Alkali–silica reaction: Kinetics of chemistry of pore solution and calcium hydroxide content in cementitious system', *Cement and Concrete Research*, vol. 71, pp. 36–45, May 2015, doi: 10.1016/j.cemconres.2015.01.017.

[66]    J. Duchesne and E. J. Reardon, 'Measurement and prediction of portlandite solubility in alkali solutions', *Cement and Concrete Research*, vol. 25, no. 5, pp. 1043–1053, Jul. 1995, doi: 10.1016/0008-8846(95)00099-X.

[67]    W. C. Hansen, 'Studies Relating To the Mechanism by Which the Alkali-Aggregate Reaction Produces EXPANSION IN CONCRETE . . . . . .', *JP*, vol. 40, pp. 213–228, Jan. 1944, doi: 10.14359/8657.

[68]    M. Thomas, 'The role of calcium hydroxide in alkali recycling in concrete', *Materials Science of Concrete Special*, pp. 225–236, 2001.

[69]    A. Sellier, E. Bourdarot, S. Multon, M. Cyr, and E. Grimal, 'Combination of Structural Monitoring and Laboratory Tests for Assessment of Alkali-Aggregate Reaction Swelling: Application to Gate Structure Dam', *MJ*, vol. 106, no. 3, pp. 281–290, May 2009, doi: 10.14359/56553.

[70]    N. Courtois, 'Étude de la réaction alcali-silice au sein de bétons formulés pour le conditionnement de concentrats d'évaporation', p. 311, 2020.

[71]    E. Riecke, 'Über das gleichwicht zwischen einem festen, homogenen deformierten körper und einer flüssigen phase. Insbesondere über die Depression des Schmelzpunktes durch einseitige Spannung', *Nachr. Kgl. Ges. Wiss. Göttingen, Mathm.+ Naturwiss.*, vol. 4, pp. 278–284, 1894.

[72]    P. W. Brown and H. F. W. Taylor, 'The role of ettringite in external sulfate attack', *Materials Science of Concrete: Sulfate Attack Mechanisms, The American Ceramic Society*, pp. 73–98, 1999.

[73]    T. Honorio, O. M. Chemgne Tamouya, Z. Shi, and A. Bourdot, 'Intermolecular interactions of nanocrystalline alkali-silica reaction products under sorption', *Cement and Concrete Research*, vol. 136, p. 106155, Oct. 2020, doi: 10.1016/j.cemconres.2020.106155.

[74]    L. Struble and S. Diamond, 'Unstable swelling behaviour of alkali silica gels', *Cement and Concrete Research*, vol. 11, no. 4, pp. 611–617, Jul. 1981, doi: 10.1016/0008-8846(81)90091-0.

[75]    'Easymetal website'. [Online]. Available: https://www.easymetal.com/en/technologies/reverse-osmosis/the-principle-of-reverse-osmosis.html

[76]    S. Chatterji, 'An accelerated method for the detection of alkali-aggregate reactivities of aggregates', *Cement and Concrete Research*, vol. 8, no. 5, pp. 647–649, Sep. 1978, doi: 10.1016/0008-8846(78)90047-9.

[77]     G. Davies and R. E. Oberholster, 'Alkali-silica reaction products and their development', *Cement and Concrete Research*, vol. 18, no. 4, pp. 621–635, Jul. 1988, doi: 10.1016/0008-8846(88)90055-5.

[78]     J. Liaudat, C. M. López, and I. Carol, 'DIFFUSION-REACTION MODEL FOR ALKALI-SILICA REACTION IN CONCRETE', p. 11.

[79]     S. Chatterji, A. D. Jensen, N. Thaulow, and P. Christensen, 'Studies of alkali-silica reaction. Part 3. Mechanisms by which NaCl and Ca(OH)2 affect the reaction', *Cement and Concrete Research*, vol. 16, no. 2, pp. 246–254, Mar. 1986, doi: 10.1016/0008-8846(86)90141-9.

[80]     M. Prezzi, P. J. M. Monteiro, and G. Sposito, 'Alkali-Silica Reaction; Part 2: The Effect of Chemical Additives', *MJ*, vol. 95, no. 1, pp. 3–10, Jan. 1998, doi: 10.14359/346.

[81]     J. Lombardi, A. Perruchot, P. Massard, and C. Larive, 'Study of Ca-Si gels, products of Alkali silica reaction', *10th ICAAR, Melbourne*, pp. 18–23, 1996.

[82]     H. Hornain and J. P. Bournazel, 'Réaction alcali-silice; point sur les mécanismes de gonflement', *Journée scientifique AFGC-DRAST sur l'alcali-réaction, ESPCI*, vol. 21, 1999.

[83]     J. M. Ponce and O. R. Batic, 'Different manifestations of the alkali-silica reaction in concrete according to the reaction kinetics of the reactive aggregate', *Cement and Concrete Research*, vol. 36, no. 6, pp. 1148–1156, Jun. 2006, doi: 10.1016/j.cemconres.2005.12.022.

[84]     N. Marinoni, M. Voltolini, L. Mancini, and F. Cella, 'Influence of aggregate mineralogy on alkali–silica reaction studied by X-ray powder diffraction and imaging techniques', *J Mater Sci*, vol. 47, no. 6, pp. 2845–2855, Mar. 2012, doi: 10.1007/s10853-011-6114-3.

[85]     N. Castro, B. E. Sorensen, and M. A. T. M. Broekmans, 'Assessment of Individual ASR-Aggregate Particles by XRD', in *Proceedings of the 10th International Congress for Applied Mineralogy (ICAM)*, Berlin, Heidelberg, 2012, pp. 95–102. doi: 10.1007/978-3-642-27682-8_13.

[86]     A. Abd-Elssamd, Z. J. Ma, H. Hou, and Y. Le Pape, 'Influence of mineralogical and chemical compositions on alkali-silica-reaction of Tennessee limestones', *Construction and Building Materials*, vol. 261, p. 119916, Nov. 2020, doi: 10.1016/j.conbuildmat.2020.119916.

[87]     W. F. Cole and C. Lancucki, 'Products formed in an aged concrete the occurrence of okenite', *Cement and Concrete Research*, vol. 13, no. 5, pp. 611–618, 1983.

[88]     L. De Ceukelaire, 'The determination of the most common crystalline alkali-silica reaction product', *Materials and Structures*, vol. 24, no. 3, pp. 169–171, 1991, doi: 10.1007/BF02472981.

[89]     K. Peterson, D. Gress, T. Van Dam, and L. Sutter, 'Crystallized alkali-silica gel in concrete from the late 1890s', *Cement and Concrete Research*, vol. 36, no. 8, pp. 1523–1532, 2006.

[90]     C. J. Benmore and P. J. M. Monteiro, 'The structure of alkali silicate gel by total scattering methods', *Cement and Concrete Research*, vol. 40, no. 6, pp. 892–897, Jun. 2010, doi: 10.1016/j.cemconres.2010.02.006.

[91]     A. Leemann and P. Lura, 'E-modulus of the alkali–silica-reaction product determined by micro-indentation', *Construction and Building Materials*, vol. 44, pp. 221–227, Jul. 2013, doi: 10.1016/j.conbuildmat.2013.03.018.

[92]     T. Katayama, 'Petrographic study of the alkali-aggregate reactions in concrete', *Graduate School of Science, University of Tokyo, Department of Earth and Planetary Science*, 2012.

[93]     E. Boehm-Courjault and A. Leemann, *Characterization of ASR products by SEM and TEM*. 2017.

[94]     A. Leemann and B. Münch, 'The addition of caesium to concrete with alkali-silica reaction: Implications on product identification and recognition of the reaction sequence', *Cement and Concrete Research*, vol. 120, pp. 27–35, Jun. 2019, doi: 10.1016/j.cemconres.2019.03.016.

[95]     I. G. Richardson, 'Electron microscopy of cements', *Structure and performance of cements*, pp. 500–556, 2002.

[96]     A. Bazzoni, 'Study of early hydration mechanisms of cement by means of electron microscopy', EPFL, Lausanne, 2014. doi: 10.5075/epfl-thesis-6296.

[97]     'SIA 2042-C1 (2012) - Prévention de la réaction alcalis-granulats (RAG) des ouvrages en béton'. Accessed: Jun. 29, 2021. [Online]. Available: https://www.sia.ch/fileadmin/content/download/sia-norm/korrigenda_sn/2042-C1_2015_f.pdf

[98]     L. Sofia, T. Chappex, and C. Dunant, 'A Robust Testing Protocol for the Assessment of ASR Reactivity of Concrete', *Swelling Concrete in Dams and Hydraulic Structures: DSC 2017*, p. 153, 2017.

[99]     B. A. CARTER, D. B. Williams, C. B. Carter, and D. B. Williams, *Transmission Electron Microscopy: A Textbook for Materials Science. Basics. I*, vol. 2. Springer Science & Business Media, 1996.

[100]    'R. Dron, F. Brivot, T. Chaussadent. Mécanisme de la réaction alcali-silice. BBulletin des laboratoires des ponts et chaussées - 214 - Mars-Avril 1998'. Accessed: Mar. 22, 2021. [Online]. Available: https://www.ifsttar.fr/collections/BLPCpdfs/blpc__214_61-68.pdf

[101]    D. Bulteel, E. Garcia-Diaz, C. Vernet, and H. Zanni, 'Alkali–silica reaction: A method to quantify the reaction degree', *Cement and Concrete Research*, vol. 32, no. 8, pp. 1199–1206, Aug. 2002, doi: 10.1016/S0008-8846(02)00759-7.

[102]    S. Diamond, 'A review of alkali-silica reaction and expansion mechanisms 2. Reactive aggregates', *Cement and Concrete Research*, vol. 6, no. 4, pp. 549–560, Jul. 1976, doi: 10.1016/0008-8846(76)90083-1.

[103]    S. Barbotin, 'Characterization of initial ASR products by SEM, FIB and STEM-EDX', p. 7, 2019.

[104]    'SIA 2042 (2012) - Prévention de la réaction alcalis-granulats (RAG) des ouvrages en béton.pdf'.

[105]    G. D. Guthrie and J. W. Carey, 'A thermodynamic and kinetic model for paste–aggregate interactions and the alkali–silica reaction', *Cement and Concrete Research*, vol. 76, pp. 107–120, Oct. 2015, doi: 10.1016/j.cemconres.2015.05.004.

[106]    J. Duchesne and E. Reardon, 'Measurement and prediction of portlandite solubility in alkali solutions', *undefined*, 1995, Accessed: Sep. 27, 2021. [Online]. Available: https://www.semanticscholar.org/paper/Measurement-and-prediction-of-portlandite-in-alkali-Duchesne-Reardon/34cbcdd131c76be30dce728457f0472b798ac66b

[107]    F. M. Maia Neto *et al.*, 'Considerations on the effect of temperature, cation type and molarity on silica degradation and implications to ASR assessment', *Construction and Building Materials*, vol. 299, p. 123848, Sep. 2021, doi: 10.1016/j.conbuildmat.2021.123848.

[108]    Y. Kawabata, C. Dunant, K. Yamada, and K. Scrivener, 'Impact of temperature on expansive behavior of concrete with a highly reactive andesite due to the alkali–silica reaction', *Cement and Concrete Research*, vol. 125, p. 105888, Nov. 2019, doi: 10.1016/j.cemconres.2019.105888.

[109]    B. P. Gautam and D. K. Panesar, 'The effect of elevated conditioning temperature on the ASR expansion, cracking and properties of reactive Spratt aggregate concrete', *Construction and Building Materials*, vol. 140, pp. 310–320, Jun. 2017, doi: 10.1016/j.conbuildmat.2017.02.104.

[110]    A. Ouzia and K. Scrivener, 'The needle model: A new model for the main hydration peak of alite', *Cement and Concrete Research*, vol. 115, pp. 339–360, Jan. 2019, doi: 10.1016/j.cemconres.2018.08.005.

[111]    G. Xu and X. Shi, 'Characteristics and applications of fly ash as a sustainable construction material: A state-of-the-art review', *Resources, Conservation and Recycling*, vol. 136, pp. 95–109, Sep. 2018, doi: 10.1016/j.resconrec.2018.04.010.

[112]    K. Wesche, *Fly ash in concrete: properties and performance*. CRC Press, 1991.

[113]    K. Scrivener, F. Martirena, S. Bishnoi, and S. Maity, 'Calcined clay limestone cements (LC3)', *Cement and Concrete Research*, vol. 114, pp. 49–56, Dec. 2018, doi: 10.1016/j.cemconres.2017.08.017.

[114]    L. M. Vizcaíno-Andrés, S. Sánchez-Berriel, S. Damas-Carrera, A. Pérez-Hernández, K. L. Scrivener, and J. F. Martirena-Hernández, 'Industrial trial to produce a low clinker, low carbon cement', *Mater. construcc.*, vol. 65, no. 317, p. e045, Mar. 2015, doi: 10.3989/mc.2015.00614.

[115]    Y. Dhandapani, T. Sakthivel, M. Santhanam, R. Gettu, and R. G. Pillai, 'Mechanical properties and durability performance of concretes with Limestone Calcined Clay Cement (LC3)', *Cement and Concrete Research*, vol. 107, pp. 136–151, May 2018, doi: 10.1016/j.cemconres.2018.02.005.

[116]    S. Bishnoi, S. Maity, A. Mallik, S. Joseph, and S. Krishnan, 'Pilot scale manufacture of limestone calcined clay cement : The Indian experience', *Indian Concrete Journal*, vol. 7, pp. 22–28, Jul. 2014.

[117]    A. C. Emmanuel, P. K. Haldar, S. Maity, and S. Bishnoi, 'Second pilot production of limestone calcined clay cement in India: The experience', vol. 90, pp. 57–63, May 2016.

[118]    R. Gettu *et al.*, 'Influence of supplementary cementitious materials on the sustainability parameters of cements and concretes in the Indian context', *Mater Struct*, vol. 52, no. 1, p. 10, Jan. 2019, doi: 10.1617/s11527-019-1321-5.

[119]    Q. D. Nguyen, T. Kim, and A. Castel, 'Mitigation of alkali-silica reaction by limestone calcined clay cement (LC3)', *Cement and Concrete Research*, vol. 137, p. 106176, Nov. 2020, doi: 10.1016/j.cemconres.2020.106176.

[120]    W. Hanpongpun, 'Investigation of the use of Limestone Calcined Clay Cement (LC3) applied to Thailand', *Infoscience*, 2019. https://infoscience.epfl.ch/record/262808 (accessed Oct. 18, 2020).

[121]    R. Detwiler, 'The Role of Fly Ash Composition in Reducing Alkali-Silica Reaction', p. 35.

[122]    F. Bektas, L. Turanli, T. Topal, and M. C. Goncuoglu, 'Alkali reactivity of mortars containing chert and incorporating moderate-calcium fly ash', *Cement and Concrete Research*, vol. 34, no. 12, pp. 2209–2214, Dec. 2004, doi: 10.1016/j.cemconres.2004.02.007.

[123]    S. Kandasamy and M. H. Shehata, 'The capacity of ternary blends containing slag and high-calcium fly ash to mitigate alkali silica reaction', *Cement and Concrete Composites*, vol. 49, pp. 92–99, May 2014, doi: 10.1016/j.cemconcomp.2013.12.008.

[124]    Y. Kawabata and K. Yamada, 'The mechanism of limited inhibition by fly ash on expansion due to alkali–silica reaction at the pessimum proportion', *Cement and Concrete Research*, vol. 92, pp. 1–15, Feb. 2017, doi: 10.1016/j.cemconres.2016.11.002.

[125]    P. R. Rangaraju and J. Desai, 'Effectiveness of Fly Ash and Slag in Mitigating Alkali–Silica Reaction Induced by Deicing Chemicals', *J. Mater. Civ. Eng.*, vol. 21, no. 1, pp. 19–31, Jan. 2009, doi: 10.1061/(ASCE)0899-1561(2009)21:1(19).

[126]    M. H. Shehata and M. D. A. Thomas, 'The effect of fly ash composition on the expansion of concrete due to alkali–silica reaction', *Cement and Concrete Research*, vol. 30, no. 7, pp. 1063–1072, Jul. 2000, doi: 10.1016/S0008-8846(00)00283-0.

[127]    M. H. Shehata and M. D. A. Thomas, 'Use of ternary blends containing silica fume and fly ash to suppress expansion due to alkali–silica reaction in concrete', *Cement and Concrete Research*, vol. 32, no. 3, pp. 341–349, Mar. 2002, doi: 10.1016/S0008-8846(01)00680-9.

[128]    Z. Shi, C. Shi, J. Zhang, S. Wan, Z. Zhang, and Z. Ou, 'Alkali-silica reaction in waterglass-activated slag mortars incorporating fly ash and metakaolin', *Cement and Concrete Research*, vol. 108, pp. 10–19, Jun. 2018, doi: 10.1016/j.cemconres.2018.03.002.

[129]    K. Turk, C. Kina, and M. Bagdiken, 'Use of binary and ternary cementitious blends of F-Class fly-ash and limestone powder to mitigate alkali-silica reaction risk', *Construction and Building Materials*, vol. 151, pp. 422–427, Oct. 2017, doi: 10.1016/j.conbuildmat.2017.06.075.

[130]    F. Xiao-xin, F. Nai-qian, and H. Dong, 'Effect of the composite of natural zeolite and fly ash on alkali-silica reaction', *J. Wuhan Univ. Technol.-Mat. Sci. Edit.*, vol. 18, no. 4, p. 93, Dec. 2003, doi: 10.1007/BF02838402.

[131]    I. García-Lodeiro, A. Palomo, and A. Fernández-Jiménez, 'Alkali–aggregate reaction in activated fly ash systems', *Cement and Concrete Research*, vol. 37, no. 2, pp. 175–183, Feb. 2007, doi: 10.1016/j.cemconres.2006.11.002.

[132]    R. D. Moser, A. R. Jayapalan, V. Y. Garas, and K. E. Kurtis, 'Assessment of binary and ternary blends of metakaolin and Class C fly ash for alkali-silica reaction mitigation in concrete', *Cement and Concrete Research*, vol. 40, no. 12, pp. 1664–1672, Dec. 2010, doi: 10.1016/j.cemconres.2010.08.006.

[133]    T. C. Esteves, R. Rajamma, D. Soares, A. S. Silva, V. M. Ferreira, and J. A. Labrincha, 'Use of biomass fly ash for mitigation of alkali-silica reaction of cement mortars', *Construction and Building Materials*, vol. 26, no. 1, pp. 687–693, Jan. 2012, doi: 10.1016/j.conbuildmat.2011.06.075.

[134]    K. A. Schumacher and J. H. Ideker, 'New Considerations in Predicting Mitigation of Alkali-Silica Reaction Based on Fly Ash Chemistry', *J. Mater. Civ. Eng.*, vol. 27, no. 4, p. 04014144, Apr. 2015, doi: 10.1061/(ASCE)MT.1943-5533.0001021.

[135]    Ş. Yazıcı, H. Ş. Arel, and D. Anuk, 'Influences of Metakaolin on the Durability and Mechanical Properties of Mortars', *Arab J Sci Eng*, vol. 39, no. 12, pp. 8585–8592, Dec. 2014, doi: 10.1007/s13369-014-1413-z.

[136]    R. Pouhet and M. Cyr, 'Alkali–silica reaction in metakaolin-based geopolymer mortar', *Mater Struct*, vol. 48, no. 3, pp. 571–583, Mar. 2015, doi: 10.1617/s11527-014-0445-x.

[137]    T. Chappex and K. L. Scrivener, 'The influence of aluminium on the dissolution of amorphous silica and its relation to alkali silica reaction', *Cement and Concrete Research*, vol. 42, no. 12, pp. 1645–1649, Dec. 2012, doi: 10.1016/j.cemconres.2012.09.009.

[138]    R. Hay and C. P. Ostertag, 'On utilization and mechanisms of waste aluminium in mitigating alkali-silica reaction (ASR) in concrete', *Journal of Cleaner Production*, vol. 212, pp. 864–879, Mar. 2019, doi: 10.1016/j.jclepro.2018.11.288.

[139]    W. Aquino, D. A. Lange, and J. Olek, 'The influence of metakaolin and silica fume on the chemistry of alkali–silica reaction products', *Cement and Concrete Composites*, vol. 23, no. 6, pp. 485–493, Dec. 2001, doi: 10.1016/S0958-9465(00)00096-2.

[140]    J. Duchesne and M.-A. Bérubé, 'Long-term effectiveness of supplementary cementing materials against alkali–silica reaction', *Cement and Concrete Research*, vol. 31, no. 7, pp. 1057–1063, Jul. 2001, doi: 10.1016/S0008-8846(01)00538-5.

[141]    S. Song and H. M. Jennings, 'Pore solution chemistry of alkali-activated ground granulated blast-furnace slag11This paper was originally submitted to Advanced Cement Based Materials. The paper was received at the Editorial Office of Cement and Concrete Research on 12 November 1998 and accepted in final form on 16 November 1998.', *Cement and Concrete Research*, vol. 29, no. 2, pp. 159–170, Feb. 1999, doi: 10.1016/S0008-8846(98)00212-9.

[142]    A. M. Boddy, R. D. Hooton, and M. D. A. Thomas, 'The effect of product form of silica fume on its ability to control alkali–silica reaction', *Cement and Concrete Research*, vol. 30, no. 7, pp. 1139–1150, Jul. 2000, doi: 10.1016/S0008-8846(00)00297-0.

[143]    A. M. Boddy, R. D. Hooton, and M. D. A. Thomas, 'The effect of the silica content of silica fume on its ability to control alkali–silica reaction', *Cement and Concrete Research*, vol. 33, no. 8, pp. 1263–1268, Aug. 2003, doi: 10.1016/S0008-8846(03)00058-9.

[144]    K.-J. Hünger, 'The contribution of quartz and the role of aluminum for understanding the AAR with greywacke', *Cement and Concrete Research*, vol. 37, no. 8, pp. 1193–1205, Aug. 2007, doi: 10.1016/j.cemconres.2007.05.009.

[145]    K.-J. Hünger, J. Kronemann, C. Hübert, and Y. Scholz, 'On the mechanism of ASR inhibition by Si and Al containing SCMs', 2015, pp. 437–451. Accessed: Jul. 02, 2021. [Online]. Available: https://opus4.kobv.de/opus4-UBICO/frontdoor/index/index/docId/21300

[146]    S.-Y. Hong and F. P. Glasser, 'Alkali binding in cement pastes: Part I. The C-S-H phase', *Cement and Concrete Research*, vol. 29, no. 12, pp. 1893–1903, Dec. 1999, doi: 10.1016/S0008-8846(99)00187-8.

[147]    S.-Y. Hong and F. P. Glasser, 'Alkali sorption by C-S-H and C-A-S-H gels: Part II. Role of alumina', *Cement and Concrete Research*, vol. 32, no. 7, pp. 1101–1111, Jul. 2002, doi: 10.1016/S0008-8846(02)00753-6.

[148]    G. K. Sun, J. F. Young, and R. J. Kirkpatrick, 'The role of Al in C–S–H: NMR, XRD, and compositional results for precipitated samples', *Cement and Concrete Research*, vol. 36, no. 1, pp. 18–29, Jan. 2006, doi: 10.1016/j.cemconres.2005.03.002.

[149]    T. Chappex and K. Scrivener, 'Alkali fixation of C–S–H in blended cement pastes and its relation to alkali silica reaction', *Cement and Concrete Research*, vol. 42, no. 8, pp. 1049–1054, Aug. 2012, doi: 10.1016/j.cemconres.2012.03.010.

[150]    E. L'Hôpital, B. Lothenbach, K. Scrivener, and D. A. Kulik, 'Alkali uptake in calcium alumina silicate hydrate (C-A-S-H)', *Cement and Concrete Research*, vol. 85, pp. 122–136, Jul. 2016, doi: 10.1016/j.cemconres.2016.03.009.

[151]    Z. Shi, B. Ma, and B. Lothenbach, 'Effect of Al on the formation and structure of alkali-silica reaction products', *Cement and Concrete Research*, vol. 140, p. 106311, Feb. 2021, doi: 10.1016/j.cemconres.2020.106311.

[152]    T. Ramlochan, M. Thomas, and K. A. Gruber, 'The effect of metakaolin on alkali–silica reaction in concrete', *Cement and Concrete Research*, vol. 30, no. 3, pp. 339–344, Mar. 2000, doi: 10.1016/S0008-8846(99)00261-6.

[153]    A. Leemann and C. Merz, 'An attempt to validate the ultra-accelerated microbar and the concrete performance test with the degree of AAR-induced damage observed in concrete structures', *Cement and Concrete Research*, vol. 49, pp. 29–37, Jul. 2013, doi: 10.1016/j.cemconres.2013.03.014.

[154]    A. Leemann, 'Raman microscopy of alkali-silica reaction (ASR) products formed in concrete', *Cement and Concrete Research*, vol. 102, pp. 41–47, Dec. 2017, doi: 10.1016/j.cemconres.2017.08.014.

[155]    C. Rößler, J. Stark, F. Steiniger, and W. Tichelaar, 'Limited-Dose Electron Microscopy Reveals the Crystallinity of Fibrous C–S–H Phases', *Journal of the American Ceramic Society*, vol. 89, no. 2, pp. 627–632, 2006, doi: 10.1111/j.1551-2916.2005.00714.x.

[156]    P. K. Mehta and P. J. Monteiro, *Concrete microstructure, properties and materials*. 2017.

[157]    W. F. Cole, C. J. Lancucki, and M. J. Sandy, 'Products formed in an aged concrete', *Cement and Concrete Research*, vol. 11, no. 3, pp. 443–454, 1981.

[158]    'ASTM 2002 C 294-98 Standard Descriptive Nomenclature for Constituents of Natural Mineral Aggregates.' American Society for Testing and Materials, West Conshohocken, PA, 2002.

[159]    'EN 2010 EN 932-3. Tests for General Properties of Aggregates—Part 3: Procedure and Terminology for Simplified Petrographic Description.' European Committee for Standardization (CEN), Brussels, 2010.

[160]    C. ASTM, '1293 Standard test method for determination of length change of concrete due to alkali–silica reaction', *West Conshohocken, PA: ASTM International*, 2008.

[161]    A. E. Eskridge, J. T. Klahorst, R. E. Klingner, and M. E. Kreger, 'Mitigation techniques for structures with premature concrete deterioration due to ASR/DEF', *ACI Materials Journal*, vol. 106, no. 3, p. 273, 2009.

[162]    J. H. Ideker, B. L. East, K. J. Folliard, M. D. Thomas, and B. Fournier, 'The current state of the accelerated concrete prism test', *Cement and Concrete Research*, vol. 40, no. 4, pp. 550–555, 2010.

[163]    T. Oey *et al.*, 'Calcium nitrate: A chemical admixture to inhibit aggregate dissolution and mitigate expansion caused by alkali-silica reaction', *Cement and Concrete Composites*, vol. 110, p. 103592, 2020.

[164]    M. Alnaggar, M. Liu, J. Qu, and G. Cusatis, 'Lattice Discrete Particle Modeling of acoustic nonlinearity change in accelerated alkali silica reaction (ASR) tests', *Materials and Structures*, vol. 49, no. 9, pp. 3523–3545, 2016.

[165]    Y. Kawabata, J.-F. Seignol, R.-P. Martin, and F. Toutlemonde, 'Macroscopic chemo-mechanical modeling of alkali-silica reaction of concrete under stresses', *Construction and Building Materials*, vol. 137, pp. 234–245, 2017.

[166]    M. Rashidi, A. Paul, C. Do, and K. E. Kurtis, 'The role of composition in the structure and water-binding in alkali-silica reaction sol and gel', *Cement and Concrete Research*, vol. 124, p. 105814, 2019.

[167]    A. Gholizadeh-Vayghan and F. Rajabipour, 'The influence of alkali–silica reaction (ASR) gel composition on its hydrophilic properties and free swelling in contact with water vapor', *Cement and Concrete Research*, vol. 94, pp. 49–58, Apr. 2017, doi: 10.1016/j.cemconres.2017.01.006.

[168]    J. H. M. Visser, 'Fundamentals of alkali-silica gel formation and swelling: Condensation under influence of dissolved salts', *Cement and Concrete Research*, vol. 105, pp. 18–30, 2018.

[169]    H. F. Taylor, *Cement chemistry*, vol. 2. Thomas Telford London, 1997.

[170]    C. Hu, B. P. Gautam, and D. K. Panesar, 'Nano-mechanical properties of alkali-silica reaction (ASR) products in concrete measured by nano-indentation', *Construction and Building Materials*, vol. 158, pp. 75–83, 2018.

[171]    T. Katayama, 'Late-expansive ASR in a 30-year old PC structure in eastern Japan', 2012.

[172]    G. Geng *et al.*, 'Mechanical behavior and phase change of alkali-silica reaction products under hydrostatic compression', *Acta Crystallographica Section B: Structural Science, Crystal Engineering and Materials*, vol. 76, no. 4, pp. 674–682, 2020.

[173]    A. Leemann, Z. Shi, M. Wyrzykowski, and F. Winnefeld, 'Moisture stability of crystalline alkali-silica reaction products formed in concrete exposed to natural environment', *Materials & Design*, vol. 195, p. 109066, 2020.

[174]    Z. Shi, S. Park, B. Lothenbach, and A. Leemann, 'Formation of shlykovite and ASR-P1 in concrete under accelerated alkali-silica reaction at 60 and 80 C', *Cement and Concrete Research*, vol. 137, p. 106213, 2020.

[175]    J. Lindgård *et al.*, 'The EU "PARTNER" Project—European standard tests to prevent alkali reactions in aggregates: final results and recommendations', *Cement and concrete research*, vol. 40, no. 4, pp. 611–635, 2010.

[176]    C. N. Borca *et al.*, 'The microXAS beamline at the Swiss Light source: towards nano-scale imaging', in *Journal of Physics: Conference Series*, 2009, vol. 186, no. 1, p. 012003.

[177]    W. Van Aarle *et al.*, 'Fast and flexible X-ray tomography using the ASTRA toolbox', *Optics express*, vol. 24, no. 22, pp. 25129–25147, 2016.

[178]    W. J. Palenstijn, K. J. Batenburg, and J. Sijbers, 'Performance improvements for iterative electron tomography reconstruction using graphics processing units (GPUs)', *Journal of structural biology*, vol. 176, no. 2, pp. 250–253, 2011.

[179]    D. F. Sanchez, D. Grolimund, M. Hubert, P. Bleuet, and J. Laurencin, 'A 2D and 3D X-ray M-diffraction and M-fluorescence study of a mixed ionic electronic conductor', *International Journal of Hydrogen Energy*, vol. 42, no. 2, pp. 1203–1211, 2017, doi: 10.1016/j.ijhydene.2016.11.094.

[180]    G. Ashiotis *et al.*, 'The fast azimuthal integration Python library: pyFAI', *Journal of applied crystallography*, vol. 48, no. 2, pp. 510–519, 2015.

[181]    Rasband, W. S., *ImageJ*. U. S. National Institutes of Health, Bethesda, Maryland, USA, 1997. [Online]. Available: https://imagej.nih.gov/ij/

[182]    A. Henderson, J. Ahrens, and C. Law, *The ParaView Guide*, vol. 366. Kitware Clifton Park, NY, 2004.

[183]    P. Bleuet, E. Welcomme, E. Dooryhée, J. Susini, J.-L. Hodeau, and P. Walter, 'Probing the structure of heterogeneous diluted materials by diffraction tomography', *Nature materials*, vol. 7, no. 6, pp. 468–472, 2008.

[184]    C. Zhang, L. Sorelli, B. Fournier, J. Duchesne, J. Bastien, and Z. Chen, 'Stress-relaxation of crystalline alkali-silica reaction products: Characterization by micro- and nanoindentation and simplified modeling', *Construction and Building Materials*, vol. 148, pp. 455–464, Sep. 2017, doi: 10.1016/j.conbuildmat.2017.05.069.

[185]    J. J. Timothy and G. Meschke, 'A cascade continuum micromechanics model for the effective elastic properties of porous materials', *International Journal of Solids and Structures*, vol. 83, pp. 1–12, 2016.

# Appendices

# Appendix 1 - Investigation of ASR product early-stage formation at aggregates walls in concrete

## 1.1 Introduction

Since the discovery of Alkali Silica Reaction degradation in the 1940s [7], great progress has been made regarding its characterization. It is generally described as a two steps reaction, involving :

- the dissolution of the aggregates silica
- the formation of an alkali-calcium-silica rich product leading to concrete cracking

Models for the dissolution-reaction mechanism [11][30][79][34][100][101] have been proposed, and agree on the basics of dissolution. The OH- ions present in the pore solution break the siloxane bonds of the amorphous or nanocrystalline silica which further reacts with the alkalis [10], [12], [102] and eventually the calcium. Models for the swelling mechanism (osmotic pressure [11][34], crystallization pressure [100], ion diffusion [3][8], double-layer [11][12]) have also been proposed. However, ASR has a complex nature which is not yet fully assessed. The relation between amorphous and crystalline nature of the products, which are often found to be intermixed in the same crack is still to be determined. The composition of the products, their homogeneity at nanoscale is also to be determined. Experimental evidences focused on the beginning of the reaction (early stage ASR formation) is needed to be able to understand and confirm the mechanism of concrete expansion due to the ASR formation process. The main goal was thus to determine if there is an ASR product inhomogeneity of calcium and potassium close to the aggregate interface. At early age, the product is present in very small amounts making its analysis difficult. A combination of Focus Ion beam and Atom Probe Tomography techniques is used to respectively prepare the samples and analyse the early stage reaction products.

## 1.2 Materials and method

Concrete samples prepared with Ordinary Portland Cement (OPC) were cast in the form of 70x70x281 mm prisms. These prisms were stored in water vapour (WV) at 60°C (T60) according to the Swiss standard SIA M 2042 [104] for ASR development evaluation. After 2 and 4 weeks in accelerated conditions, samples from the prisms were taken, dried for 3 days in air at 40°C, impregnated with epoxy and polished according to [23] method.

Samples from the field (OPC concrete) were also taken and prepared in the same way. Using a Scanning Electron Microscope (SEM), various areas of interest were localized, according to the following criteria:

- Located in the aggregate, a minimum of 100 µm away from the cement-aggregate interface
- Located between adjacent quartz grains

The area of interest, cracks containing ASR product, were then cut with a FIB. Very sharp tips were prepared out of the cut area, including the ASR/aggregate interface.

## 1.3     Results and discussion

The APT tips were successfully produced from the area of interest (example in Figures A1.1 and A1.2). Out of a few dozens of tips, only one could be measured. The composition found were in the awaited range (Figure A1.3), except for potassium. The overall composition in atomic % given in Table A1.1, is for calcium 14.6 and potassium 0.9. After comparison with general Transmission Electron Microscopy results, which atomic % composition is often very close and around the 14.6 value found for calcium, the question arises if this confirms the heterogeneity suspected for the product or if this is a problem with the measurement. To answer the question, more results are needed, but were not obtained.

The tips were mainly breaking at the interface or in the ASR product, suggesting the ASR phase is too unstable, probably too porous to conduct the measurements.

A method to stabilize the tips was thought of. Platinum was sputtered on the tips to improve their stability. A few dozens of tips were once more produced, with not enough successful measurement length to obtain results that could be analysed.
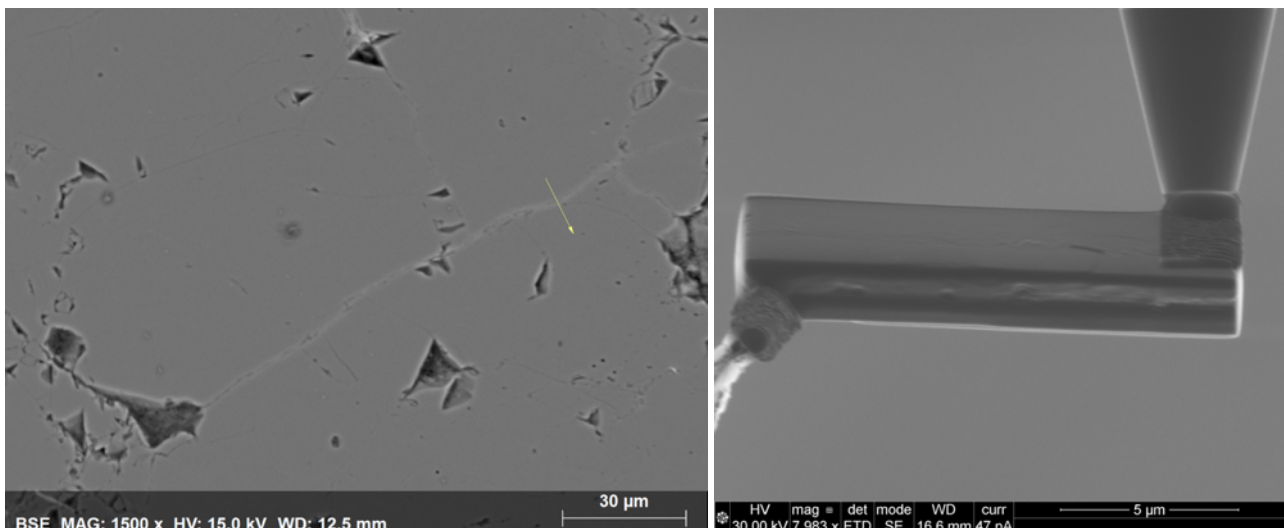


Figure A1.1 : Area of interest as viewed in SEM (left) and extracted using a FIB (right)
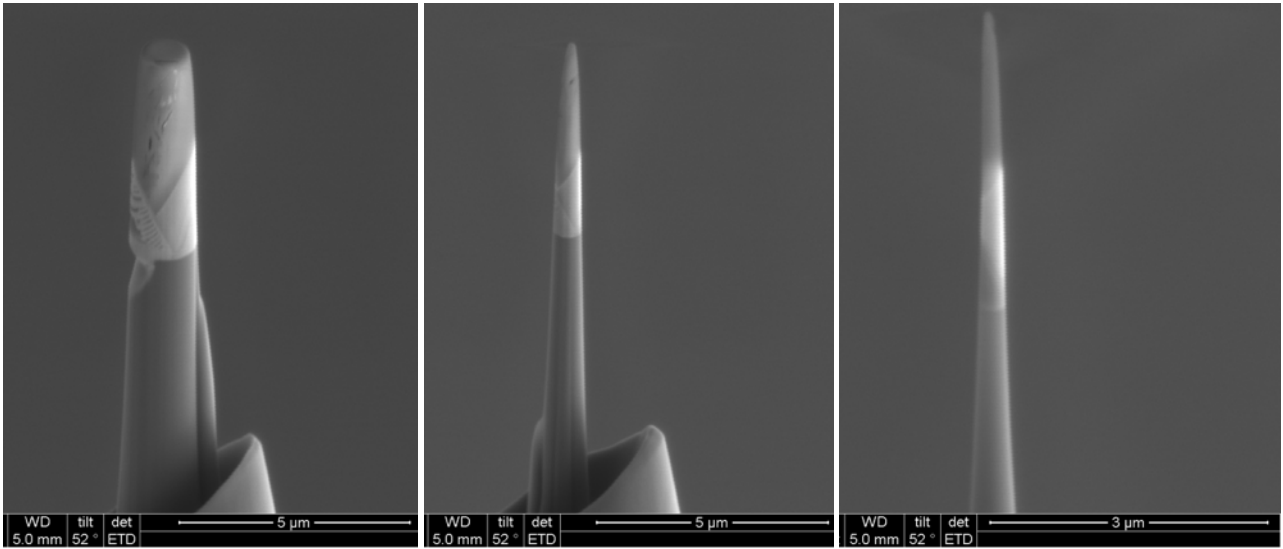
Figure A1.2 : Thinning of the tips (from left to right)
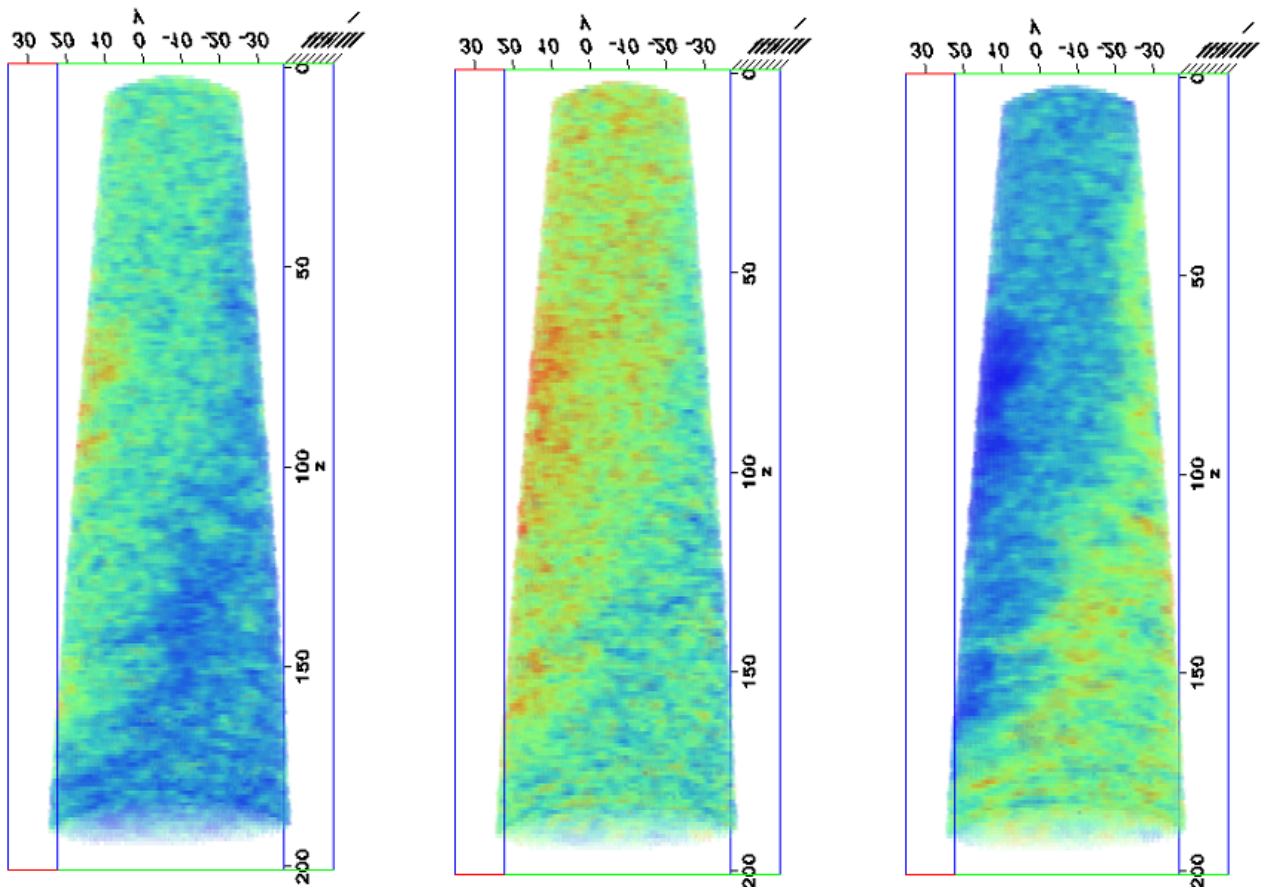


Si heatmap from

12 at% (blue) up to 42 at% (red)

O heatmap from

38 at% (blue) up to 66 at% (red)

Ca heatmap from

1 at% (blue) up to 37 at% (red)

Figure A1.3 : Heatmap showing the concentration of Silicon (left), Oxygen (middle) and Calcium (right)

Table A1.1 : Overall composition of the present elements

Over all composition (in at%, without element bumps)

| O | Si | Ca | K | and traces of Na, Mg, Al |
|---|----|----|---|--------------------------|
| 56.6 | 27.5 | 14.6 | 0.9 | |

## 1.4  Conclusion and perspectives

The very sensitive ASR product makes its analysis in APT difficult, the prepared tips being unstable and generally breaking at the beginning of the analysis. New methods to improve the stability of sensitive materials are needed to be able to analyse such materials in the future.

## 1.5  Acknowledgements

# Appendix 2 - An in-situ 3D micro-XRD investigation of water uptake by alkali-silica-reaction (ASR) product

*G. Geng, S. Barbotin, M. Shakoorioskooie, z. Shi, A. Leemann, D. Ferreira Sanchez, D. Grolimund, E. Wieland, R. Dähn*

## Abstract

The ASR products in concrete have various chemical compositions. It is yet unclear whether and how these products develop micro-expansion upon moisture ingress. This paper presents a 3D in-situ observation of the crystallography and volume change of an ASR-product-filled vein under varying relative-humidity (R.H.). The vein was observed to contain two layered nano-crystalline phases with distinct basal spacings, and was distributed heterogeneously in space. When R.H. changed from 10% to >38%, the basal spacing increased from 7.43 Å to 8.89 Å for one phase, whereas it remained constant (~10.9 Å) for the other. This is the first time that an ASR product is observed in-situ to exhibit crystal structural expansion during wetting process. However, the product-filled vein exhibited no noticeable swelling when R.H. varied from 10% to 97%. Our findings provide the first direct evidence that the moisturization-induced crystal structural change of ASR product may not be a plausible explanation to the macroscale concrete expansion.

## 2.1    Introduction

Alkali-silica-reaction (ASR) is a commonly known mechanism of concrete degradation, but its microscale origin is not widely known. The ASR products cause expansion in concrete in the presence of moisture, leading to crack formation and concrete degradation [156][157]. ASR-induced deterioration has been reported worldwide, and a global effort of investigating ASR exists since the mid-20th century [6][2]. Today, multiple standard testing methods have been established to evaluate the ASR reactivity of aggregates [158][159]. Limiting the alkali content of cement is also incorporated in construction codes to minimize the long-term ASR risk [160]. These measures are vastly helpful in construction practice, yet different testing methods may sometimes provide controversial results, and fail to predict the premature ASR degradation [161][162]. Meanwhile, computational simulations of ASR-induced material degradation have been frequently reported over the past 20 years [163][164][165]. Many of them are based on conceptual mechanisms that lack microscale validation. There is thus an urgent need to deepen our understanding of the microscale mechanism of the ASR process.

One of the most widely accepted hypotheses of ASR damage is the moisture-driven swelling [166][167][168] of the products which bear a general composition of sodium/potassium calcium silicate hydrates. Compared with the calcium silicate hydrate (C-S-H, the main hydration product in Portland cement concrete), the ASR gel has a much higher content of Na + K and a much lower content of Ca [168][154][40][169]. This compositional difference results in a higher degree of silicate polymerization in the ASR product ($Q^3$ dominant) than in C-S-H ($Q^1/Q^2$ dominant) [154][46]. It is proposed that ASR product expands upon up-taking water to its gel structure, leading to a local stress development and initiation of cracks in concrete [166][167][168]. This hypothesis has been challenged recently at least by two research evidences. First, large amounts of SEM data have indicated that the ASR product inside the reacted aggregates often exhibit a nano-crystalline nature. The product vein is a 'river' of nano-platelets that are tens of nanometers thick and micron-size wide [88][89][91]. These products are distinct from a gel-appearance, and their time-dependent mechanical property is yet to be justified [91][170].

Second, recent micro-XRD and micro-spectroscopic evidences have unveiled the high similarity between the nano-crystalline ASR product and shlykovite – a layer-silicate mineral [154][40][48][58][47][171]. They were both reproduced in recent laboratory synthesis attempts. Although multiple basal spacing values were found for ASR products from the field and lab-synthesis [172], it was noted that they all seem not able to swell or shrink upon a significant R.H. change [46][47][173]. Temperature is found to affect the formation of different types of crystalline ASR products with varying basal spacing, i.e., 12.0 Å (<40 °C), 10.8 Å (around 40 °C), and 13.1 Å (60–80 °C for K-shlykovite) [47][174][22]. Moreover, a significant hydrostatic compression pressure (>2 GPa) can also alter the basal spacing [172]. These evidences make it questionable whether moisture-induced swelling is the microscale source of expansive stress during the ASR damage.

To answer this question, a microscale in-situ observation of a vein filled with the ASR product and subject to R.H. change would provide unparalleled evidence. This paper reports exactly an approach of such kind. A vein filled with crystalline ASR product was carefully isolated from a degraded concrete and then investigated by synchrotron-based micro-XRD. The sample was exposed to an inert atmosphere ($N_2$) with a largely varying R.H. (10%, 38% and 97%). The combined use of micro-XRD and tomographic scanning allows reconstructing the XRD pattern of each voxel in the probed volume, which then enables monitoring the crystal structure of the product during the R.H. variation, along with its volumetric change (if any). The results provide a direct

evidence of whether the crystalline ASR product undergoes a structural swelling upon contacting moisture, and whether this leads to a volumetric change inside the product vein.

## 2.2    Methodology

### 2.2.1.  Materials

The ASR product was extracted from a laboratory-produced concrete cube exposed for 14 years to natural conditions in Valencia (Spain), with noticeable ASR degradation. The reactive aggregate is a silicified limestone [175]. This concrete was referred to as 'ES1' in our previous studies [48][172]. An iron hammer was used to gently crush the concrete. Via inspection under a stereoscopic optical microscope, a fragment with abundant ASR product veins on the fractural surface was selected. No resin impregnation was applied to the sample. A scanning electron microscope (Quanta 200 ESEM, FEI) at a pressure of $1.0–2.0 \times 10^{-5}$ mbar, an accelerating voltage of 15 kV and a beam current of 95–100 μA was used to locate the region of interest. An SSD detector (30 mm$^2$) from Bruker and Esprit energy software with PhiRhoZ quantification were operated for the energy-dispersive X-ray spectroscopy (EDS) analysis.

The region of interest was extracted with a plasma focused ion beam (Helios G4 PFIB DualBeam UXe, ThermoFisher Scientific). A ~50 μm wide product vein was spotted on the fractural surface. An SEM-EDS line-scan perpendicular to the vein (containing 24 points from the edge to the middle of the vein) indicated an average (Na + K)/Si = 0.40 and Ca/Si = 0.32. This product vein was then cut with the Xenon plasma ion beam at working currents ranging from 2 μA down to 0.2 μA. The extracted volume was a cuboid with edge lengths of 40–80 μm, containing part of an ASR product vein embedded in an aggregate (limestone) matrix (Figure A2.1a). It was then fixated to the tip of an aluminium pin using Pt as the welding material. A second step to clean the sample was operated in a focused ion beam (FIB, NVision 40 CrossBeam, Zeiss), at much lower currents ranging from 65 nA to 27 nA, with Gallium ion beam. The sample was then placed in a desiccator containing saturated NaOH solution as $CO_2$ and moisture trap, until it was measured two days later.



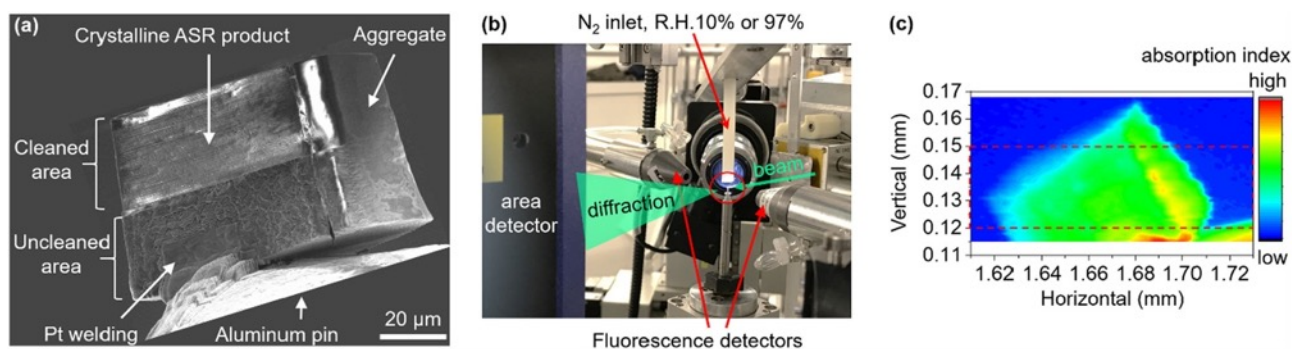Figure A2.1 : Overview of the sample and the beamline setup. (a) SEM image of the extracted volume. The surface was partly cleaned with FIB to expose the morphogen of the ASR product. (b) Sample placed on the sample stage between the beam upstream, XRD and fluorescence detectors, with a N2 flow approaching from top; (c) an absorption contrast image of the sample during the scanning, viewed from an angle slightly different from (a).

## 2.2.2. Micro-XRD tomography

The micro-XRD measurement was performed at the microXAS beamline of the Swiss Light Source (SLS) [176]. An incident beam of 14.6 keV energy was focused to ~1 μm × 1 μm using Kirkpatrick-Baez mirrors. As shown in Figure A2.1b, an Eiger4M area detector was used to record the diffraction pattern of the scanned region on the sample. The sample-to-plate distance and the position of the beam center were calibrated using the diffraction pattern of a standard material (LaB$_6$). A pair of fluorescence detectors was placed in equal distance on both sides of the sample with respect of the beam direction. The elemental concentrations in the scanned region were semi-quantified by averaging the signals from both fluorescence detectors, which was used to differentiate the ASR product from other phases. Reconstructions were conducted using the selected fluorescence signal with home-made python codes and the Astra Toolbox library, using the SIRT method and the parallel beam GPU code [177][178].

Using x-ray absorption contrast imaging, the sample was readily located during the scanning (Figure A2.1c). The raw XRD pattern contained the information of all materials along the beam path. Hence, a tomographic scanning manner was adopted to decouple the diffraction contributed by different parts of the sample. At each height (vertical position), horizontal scanning at a step size of 1 μm was combined with a rotational scanning at a step size of ~1.6°, covering an angle range of ~180°. The scanning of each slice took ~65 min. Such tomographic scans were conducted on multiple slices along the vertical direction. The overall investigated region is indicated by the red-dashed rectangle in Figure A2.1c.

To study the effect of R.H., the sample was blown from top using either pure (dry) N$_2$ or N$_2$ that passed through a water reservoir. The R.H. was measured as 10% (dry N$_2$) and 97% (water-saturated N$_2$), hereafter denoted as '*dry*' and '*wet*' conditions, respectively. For each R.H. condition, 21 consecutive slices were scanned. The step size between adjacent slices was 1.5 μm for the dry condition, and 1.2 μm for the wet condition (vertical position of each scanned slices available later in Figure A2.5). The N$_2$ blow was lastly removed to study the sample at ambient R.H., which was measured to be 38% in the experiment hutch, hereafter denoted as '*amb*' condition. Due to the limitation of experiment time, only four slices were studied at the ambient condition. The measurement started from *dry*, followed by *wet* and *amb* conditions. The sample was allowed one-hour equilibration each time after a R.H. change.

For the tomographic scan of each slice, one XRD pattern was collected for each horizontal position at each rotation angle. A set of home-made codes were used to translate these diffraction patterns to a diffractogram of intensity vs 2theta [179][180]. Matlab software was then used to reconstruct the slice using the diffraction intensity at each 2theta angle as the contrast. For each slice, this reconstruction resulted in three dimensional data, with the first and second dimensions corresponding to the x- and y-coordinates of the pixels on the slice, and the third dimension corresponding to the 2theta angle. This eventually yielded the XRD pattern of each point in the studied volume under various R.H. conditions. Spatial distribution of a certain phase on each slice was obtained through reconstruction using the integrated intensity of its characteristic XRD peaks (e.g. the basal peak) using a python code of simultaneous iterations reconstruction technique (SIRT) algorithm [177][178]. Open source packages *ImageJ* [181] and *Paraview* [182] were used for visualization.

## 2.3 Results and discussions

### 2.3.1 Micro-XRD of the ASR products

A projection of the sample is shown with Ca, absorption and Pt contrast (Figure A2.2a). In the Ca contrast image, the regions containing relatively high and low Ca content correspond to the calcite aggregate and the ASR product, respectively. The deposited Pt weld is clearly resolved on the surface of the sample. To analyse the influence of R.H. change to the crystal structure of the ASR product, three slices at different vertical positions were selected (Figure A2.2a). For each slice, the XRD at all horizontal positions and all rotational angles were summed as the overall XRD of this slice, denoted as *dry/wet/amb*_slice1/2/3 as shown in Figure A2.2b. Only slice3 was studied at *amb* condition due to limited synchrotron beamline time.
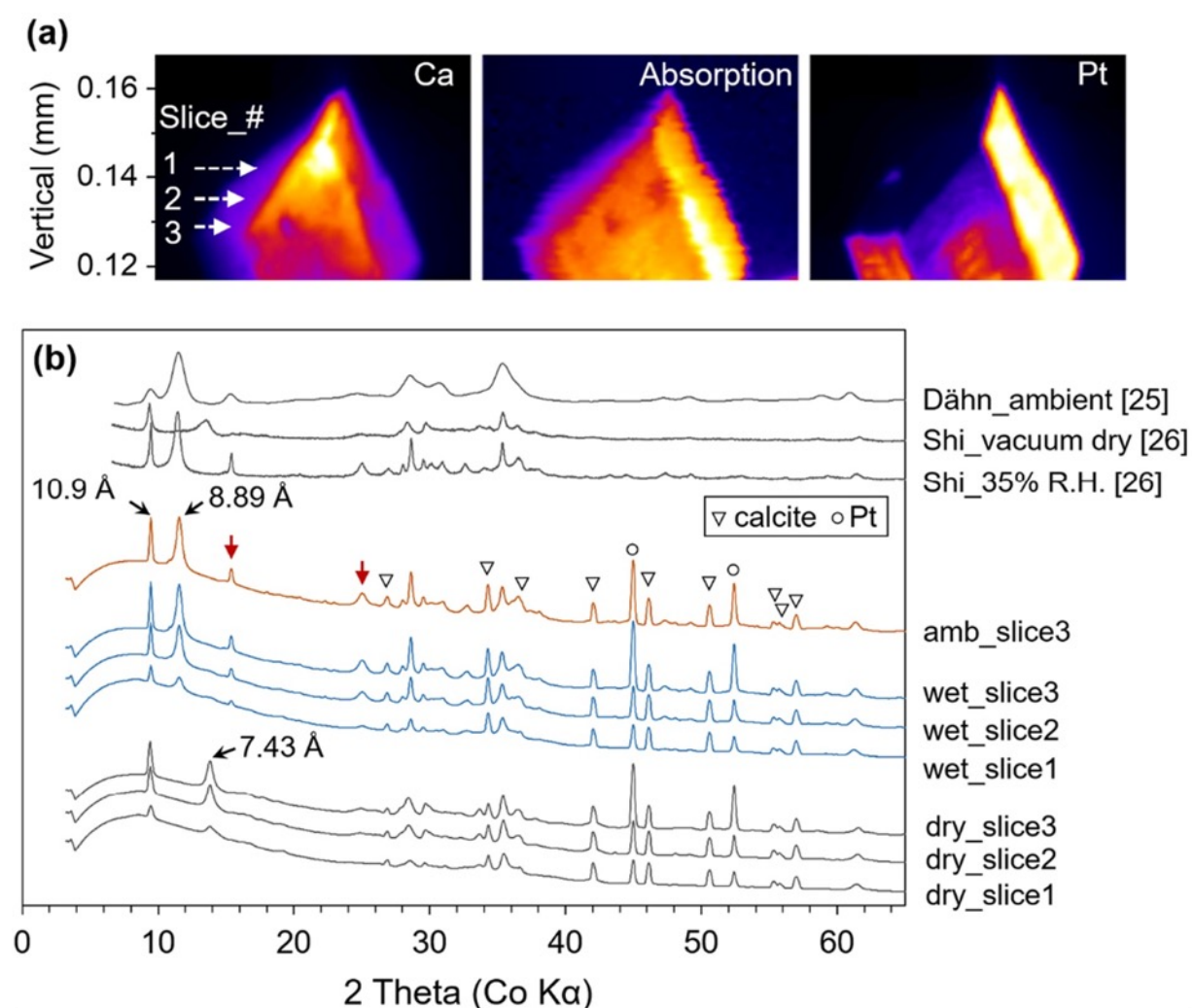


Figure A2.2 : XRD data of ASR products under different R.H. (10% for dry, 97% for wet and 38% for ambient). (a) Projections of the sample in Ca, absorption and Pt contrast, with the vertical positions of three selected slices labeled. (b) The XRD of the selected slices plotted together with reported data [58][47]. Diffraction peaks not from ASR are labeled with triangle (calcite) and circle (Pt). The 2theta angle of synchrotron beam was translated to the equivalent Co Kα value, according to the Bragg equation.

Under a certain R.H. condition, the diffraction patterns of ASR products were comparable among different slices (Figure A2.2b). The peak intensities of slice1 were weaker than those of slice2 and slice3, since there

was less solid material in slice1. The XRD of each slice typically contained the contribution from the ASR products, and from calcite (aggregate) and Pt as labeled in Figure A2.2b. Although not displayed in Figure A2.2, this finding holds true for all the scanned slices under a certain R.H., demonstrating that the crystal composition is comparable among different slices.

Two basal peaks were observed at $d \sim 10.9$ Å and 7.43 Å when the sample was dry (R.H. = 10%). Upon increasing R.H. to 97%, the 7.43 Å basal peak vanished while a new basal peak appeared at $d \sim 8.89$ Å. The 10.9 Å basal peak remained unchanged. Meanwhile, two new peaks appeared in the wet condition at 2theta of ~15° and ~25° (red arrows in Figure A2.2b). The peak at 29.5° was sharper and more intensive in the wet condition as compared with the dry condition. When R.H. subsequently dropped from 97% to 38% (*amb*), no noticeable change of the XRD was observed after 5 h of equilibration and measurement.

The basal spacing of the crystalline ASR product was found to be highly variable. In our previous work, ASR products exhibited similar layer structure as shlykovite, but with various basal peaks at $d \sim 8.6, 9.6, 10.6, 12.2$ and 13.4 Å [48][58][172]. For samples from different field sources, the dominant peak in all cases appears to be at $d \sim 12.2$ Å [48]. For lab synthesized shlykovite-type ASR samples at elevated temperature (e.g. 60 °C and 80 °C), a basal spacing larger than 13 Å was often observed [40]. When the synthesis temperature dropped to 40 °C, a product with basal peaks at 10.8 Å and 8.9 Å was reported [47]. These two basal spacings remained unchanged when R.H. was reduced to 35% (Figure A2.2b Shi_35% R.H.), yet a clear change took place when the sample was vacuum-dried for three days (Figure A2.2b Shi_vacuum dry) [47]. It is clearly shown in Figure A2.2b that the XRD of the 40 °C-synthesized sample are highly comparable to the results in this study. A previously reported micro-XRD data (Figure A2.2b Dähn_ambient) also resembles the results in this study at *wet* and *amb* condition, while the ~8.9 Å peak is much more dominant in the reported work [58].

In the reported lab-synthesis work [47], SEM observation and spectroscopic data indicated that the obtained ASR product seems to have a uniform morphology and chemical environment. However, the variation in the intensity ratio between the 10.9 Å and 8.89 Å (7.43 Å) peak and their distinct response to R.H. change indicate that they might come from two crystalline phases with similar layer structure but different basal spacings.

## 2.3.2   Tomographic reconstruction

To further investigate the source of the two basal peaks, the azimuthally integrated intensity was used to retrieve the spatial distribution of phases that produce them (hereafter denoted as phase basal_1 and basal_2, respectively). With the scanning tomographic X-ray powder diffraction technique, every voxel in the scanned volume should satisfy a powder diffraction condition [183]. The ASR products are nano-platelets with thickness of tens-of-nm, which is much smaller than the pixel size (1 µm × 1 µm). As shown by a raw pattern example (inset in Figure A2.3a), the diffraction rings of basal peak 10.9 Å (basal_1) and 7.43 Å (basal_2) are both continuous rings with approximately homogeneous distribution of intensity at all azimuthal angles, i.e. satisfying the powder diffraction condition. Meanwhile, this diffraction contrast reconstruction could not be applied to the aggregate since it exhibited a strongly spotty diffraction from large single-crystal calcite grains. As such, the whole scanned volume was reconstructed using the Ca fluorescence contrast, and segmented to ASR product and aggregate, i.e. the grey and orange volume in Figure A2.3a (partially transparent for viewing convenience).
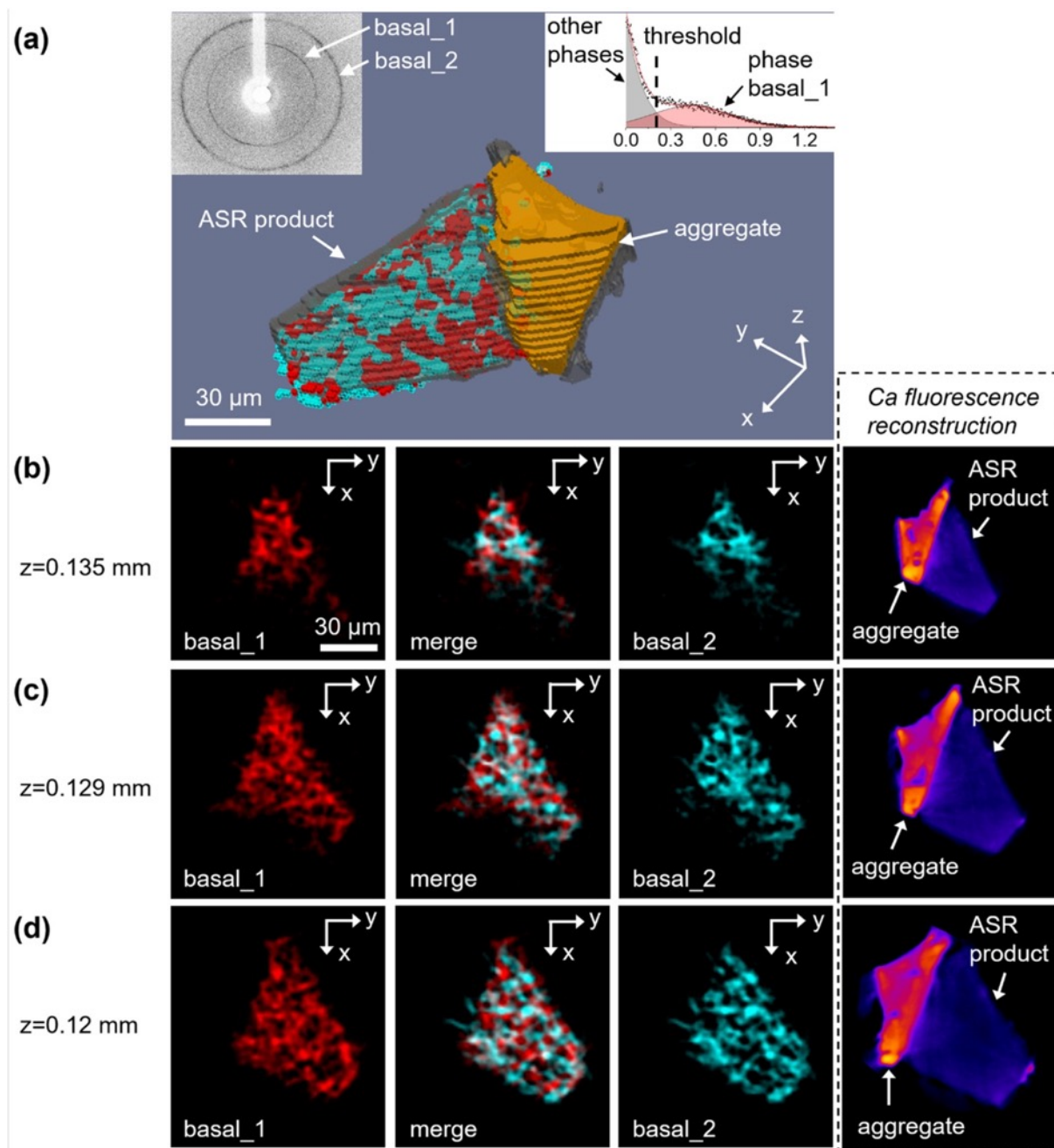
Figure A2.3 : Reconstructed spatial distribution of phases (in dry condition) that produce basal peaks 10.9 Å (basal_1, red) and 7.43 Å (basal_2, cyan). (a) Volume rendering of the ASR product (red and cyan) inside the whole scanned volume (reconstructed using Ca contrast). (b–d) Compared distribution of the phases basal_1 and basal_2 in three selected slices. A grey color in the merged image indicates the co-existence of both phases. The corresponding slices reconstructed with Ca Kα fluorescence signal are also display for comparison. Images reconstructed from diffraction contrast are binary-segmented.

A threshold-segmentation was applied to the ASR phases reconstructed with their basal peak diffraction contrast, which is well differentiated from other phases. An example of the basal_1 diffraction contrast histogram is shown by the inset in Figure A2.3a (right-hand-side). Inside the scanned volume, the basal_1 phase (red) and basal_2 phase (cyan) are intermixed in a sub-volume that is consistent with the location of the ASR product (Figure A2.1a). The distribution of basal_1 and basal_2 phases are further illustrated in three selected slices, together with slices reconstructed using the Ca fluorescence signal (Figure A2.3b–d). The Ca

contrast images demonstrate two regions with distinct Ca content, corresponding to aggregate (left) and ASR product (right). In each slice, both basal_1 and basal_2 phases spread within the region corresponding to the ASR product. The distribution of each phase, however, is not homogeneous. There are regions rich in a single phase, while between them are regions with no diffraction signal of this phase. When merging the distribution of basal_1 and basal_2, the vacancies in the distribution of one phase often host the other phase, though some regions seem to contain both phases (grey color region in Figure A2.3b–d). This suggests that the ASR products that produce the peak 10.9 Å (basal_1) and peak 7.43 Å (basal_2) are not the same. At the micron-scale, they are distributed differently inside an ASR product vein. Meanwhile, the distribution of Ca does not exhibit a similar heterogeneity as the distribution of basal_1 and basal_2, indicating that the two phases share similar content of Ca.

The diffraction-contrast reconstruction was applied also to the data in *wet* (97% R.H.) and *amb* (38% R.H.) conditions. For comparison, the reconstructed images of a slice at the vertical position of 0.130 ± 0.0005 mm are plotted together (Figure A2.4). The distribution of phase basal_1 in *dry*, *wet* and *amb* conditions are colored in red, green and blue, respectively (Figure A2.4a). A slight change in the measured vertical position in different R.H. conditions resulted in a few local variations in the distribution of basal_1. Apart from that, the overall size of the distributed area of phase basal_1 remains vastly unchanged, as indicated by the yellow dashed lines in Figure A2.4a.
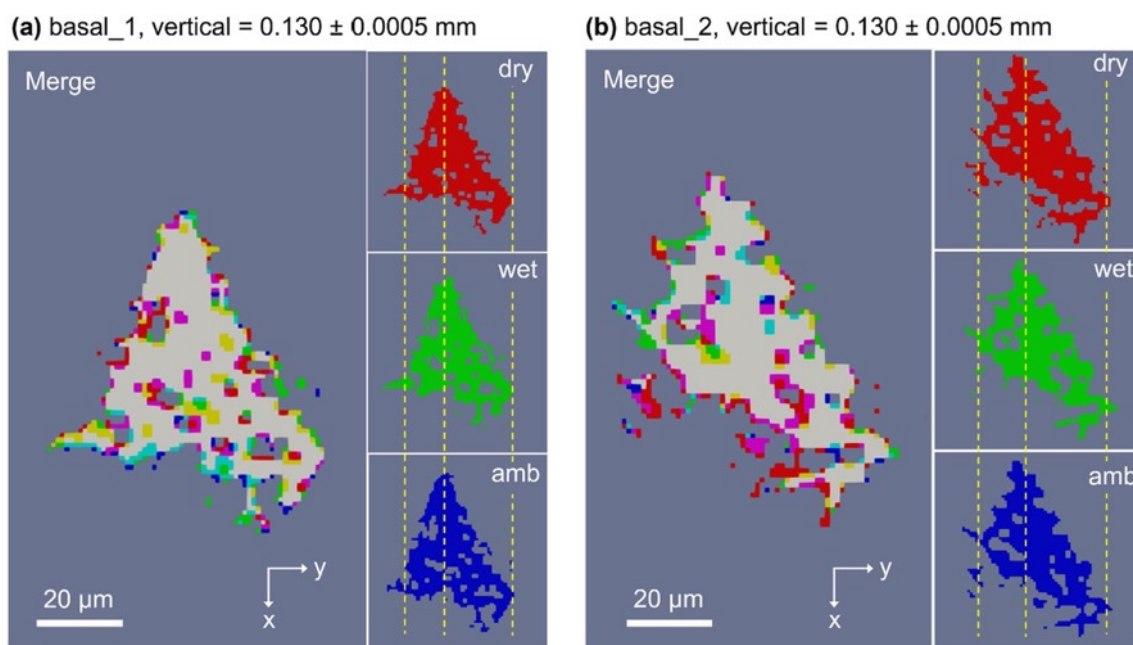


Figure A2.4 : Comparison of the micro-distribution of (a) phase basal_1 and (b) basal_2 under varying R.H. conditions. The yellow dashed lines are eye-guides of the size of the distributed area. Red, green and blue are used for the dry, wet and amb conditions, respectively. In the merged image, binary overlaps are represented by purple (red & blue), yellow (red & green) and cyan (blue & green). The grey area indicates an overlap of three basic colors.

The distribution of basal_2 in the *wet* and *amb* conditions were reconstructed using the intensity of the 8.89 Å peak in comparison to the 7.43 Å peak in dry condition. As shown in Figure A2.4b, the nearly identical distribution of basal_2 in all three R.H. conditions readily suggests that it is the same phase that produces peak 7.43 Å when dry and peak 8.89 Å when wet. In other words, the phase basal_2 has undergone an enlargement of basal spacing when R.H. increased from 10% to >38%. This is the first time that a microscale

ASR product has been observed to exhibit crystal structural expansion in an in-situ wetting process. Yet surprisingly, the spatial distribution of basal_2 exhibits nearly zero change during the wetting process, although the basal peak shift corresponds to a ~20% volume increase of the crystal structure. Otherwise stated, the crystal structural swelling of the ASR product basal_2 did not lead to a swelling of the product vein at microscale (Figure A2.4b).

The threshold segmentation was applied to all the reconstructed slices in different R.H. conditions. The volume (number of voxels) of phase basal_1 and basal_2 were counted and plotted as a function of the vertical positions, as shown in Figure A2.5a and b. For all slices, there is no clear change in volume for both basal_1 and basal_2 phases in all studied R.H. conditions. Their volume ratio at each vertical position is also consistent throughout R.H. changes (Figure A2.5c). These data again suggest that the microscale volume of the ASR product remained unchanged during R.H. variation, despite the change of their crystal structure size.
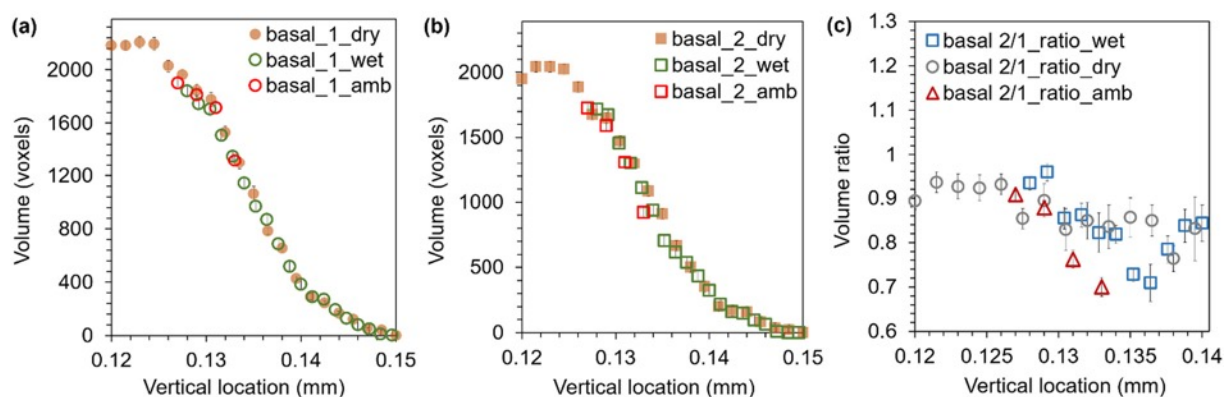


Figure A2.5 : Reconstructed volume (number of voxels) of phase basal_1 (a), basal_2 (b) and their ratios as a function of the vertical position in various R.H. conditions. The uncertainty is indicated by the error bar, which is estimated by varying the segmentation threshold value by ±5%. The volume ratio in (c) does not include slices with vertical location higher than 0.14 mm, since the volume is too small and the error bar thus too large.

### 2.3.3  Implications on moisture uptake by ASR product

The reconstructed 3D XRD data enables the diffractogram to be extracted from voxels that contain only phase basal_1 or basal_2, as shown in Figure A2.6a. The strong orientations of Pt and calcite have resulted in significant reconstruction artifacts in the XRD patterns. Therefore the 2theta ranges corresponding to calcite and Pt diffractions are masked in Figure A2.6a for viewing convenience. For phase basal_1, its diffractogram in wet and dry condition were mostly comparable. The 2theta positions of all diffraction peaks remained unchanged. Meanwhile, the (100) and (106) peaks were much sharper when basal_1 is wet, suggesting that the drying has resulted in a certain degree of amorphousness. For phase basal_2, the basal peak drifted significantly when R.H. changes from 10% to above 38%. A loss of crystallinity was also observed when phase basal_2 is dry, as indicated by the broadening of several sharp peaks that were present in wet condition.
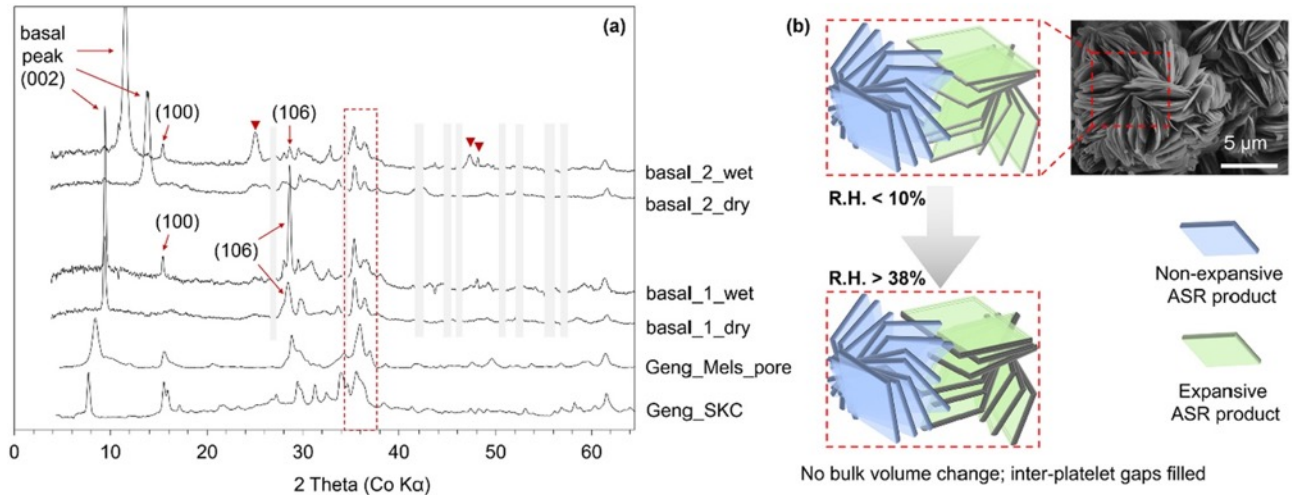
Figure A2.6 : (a) Decoupled XRD of phase basal_1 and basal_2 in dry and wet conditions, compared with published XRD of ASR-related phases [48]. The peaks corresponding to calcite and Pt peaks are masked by grey bars for viewing convenience. (b) An illustration of the micro-process of moisture uptake by the ASR product vein. The SEM image is adopted from [173].

For both basal_1 and basal_2 phases, their XRD are comparable to the XRD of previously studied shlykovite-type products [48] in the 2theta, especially in the group of strong diffraction from 34° to 38° (red dashed square in Figure A2.6a). This suggests that the two phases identified here share similar layer structure as other shlykovite-type products, whereas the basal spacing of the layers is smaller here. The similarity in chemical environment is consistent with the spectroscopic study of similar products synthesized in the lab [47]. On the other hand, the thickness of each shlykovite-type layer is ~9 Å [48]. If phase basal_2 has the same layer structure, it will need to adopt an extremely tight stacking to obtain such a small basal spacing (8.89 and 7.43 Å). Particularly, in dry condition, the dendritic tips of the silicate layer will need to penetrate into the 8-unit silicate ring of the adjacent layer, to reach a basal spacing as small as 7.43 Å. Meanwhile, some diffraction peaks in basal_2_wet were not observed in other shlykovite-type ASR products (red triangles in Figure A2.6a). Thus more study is needed to provide insight into the crystal structure of the swelling phase basal_2.

So far a group of basal spacings, ranging from 7.4 Å to 13.4 Å, have been reported for the crystalline ASR products from affected concrete. Among them, only the product with a ~8.9 Å basal spacing (wet condition) was observed here to shrink to ~7.4 Å upon severe drying. The basal spacings of the other products, ranging from ~10 Å to 13.5 Å, seem inert to the moisture change. Lab-synthesis attempts indicated that their basal spacings are more determined by the synthesis temperature [46][47]. A compression as high as 2 GPa was also proven to result in a permanent basal spacing reduction of ~1 Å for ASR products with basal spacing around 12.2 Å from field concrete samples [172]. In a real ASR product vein, all these products may exist at the same time, although they may have similar nano-platy morphology. It still remains largely unclear what leads to such a variation in the stacking behavior in different ASR products.

The bulk moduli of several polymorphs of ASR products range from 27 to 76 GPa as reported by our previous high-pressure XRD work [172], while the bulk modulus of the whole product vein is at the scale of ~10 GPa according to indentation results [91][170][184]. This indicates a porosity of 40% to 80% in the product vein, as roughly estimated by a Mori-Tanaka homogenization scheme of randomly oriented thin platelets [185]. Assuming an equal volume of phase basal_1 and basal_2, the volume ratio of basal_2 to the total product is

roughly in the range of 10% to 30%. Thus, the 20% crystal structural expansion of phase basal_2 is homogenized to a <6% volume change of the product vein, i.e. less than 2% increase on one spatial dimension. This value is comparable to the accuracy of our experimental approach here and therefore difficult to be established unambiguously in the present measurements.

Based on the above discussion, an illustration of the moisture-uptake in the studied ASR product vein is given in Figure A2.6b. The vein contains the agglomeration of expansive (basal_2) and non-expansive (basal_1) ASR nano-platelets. Starting from a dry state, the expansive product (basal_2) may uptake water into the interlayer during moisture ingress, resulting in an enlargement of basal spacing and the thickening of each platelet. However, this seems not to cause any expansion of the bulk volume of the product vein. A straightforward explanation is that the thickening of the nano-platelets only results in a shortening of the gaps between the platelets.

Our results suggest that the source of micro-expansive stress is not from the swelling of the crystalline ASR product during moisture ingress. The mechanism of ASR degradation thus awaits alternative explanations. A recent study showed that the early form of ASR products in nano-cracks of aggregate are often amorphous, in contrast to the nano-crystalline form when macro-expansion is already obvious [23]. It remains to be studied whether the amorphous early products may uptake water and generate swelling stress. It is also not investigated whether the recrystallization of early products is accompanied by a crystallization pressure. In the latter case, a pre-existing crack may open up due to localized crystal-growth before the whole crack/void is filled with product. This phenomenon has indeed been observed in a recent study [94].

## 2.4    Conclusions

In this work, a tomographic micro-XRD measurement was applied to a freshly extracted nano-crystalline ASR product vein in varying R.H. conditions, i.e. 10% (dry), 97% (wet) and 38% (ambient). The main conclusions are summarized as follows.

1) Two nano-crystalline phases with the same morphology were found intermixed inside an ASR product vein from a damaged concrete aggregate. They exhibit distinct basal spacings – one at 10.9 Å and the other at 7.43 Å when the sample was equilibrated in R.H. = 10%.

2) After the dry sample was exposed to R.H. = 97% for 1 h, the basal peak 7.43 Å shifted to 8.89 Å, indicating a moisture-driven enlargement of basal spacing. Meanwhile, the 10.9 Å peak remained unchanged. Both phases have a higher degree of crystallinity in wet condition than in dry condition. Both phases remained unchanged when R.H. dropped from 97% to 38%.

3) Despite the crystal structural expansion of one ASR product phase by uptaking water, the overall ASR product vein showed no sign of clear in-situ expansion at microscale of the studied sample. Therefore, the moisture ingress into nano-crystalline product veins may not explain the microscale origin of the expansive stress development in ASR degradation. Similar experiments are needed for more ASR product from affected concrete to justify the universality of this finding.
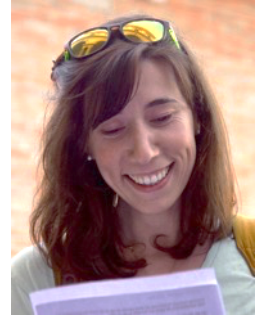
## 2.5    Acknowledgements

# Curriculum Vitae



## SOLÈNE BARBOTIN ALBINSKI

solene.barbotin@alumni.epfl.ch – s.barbotin@gmail.com

M.Sc. – Ph.D.

Ecole Polytechnique Fédérale de Lausanne

PERSONAL INFORMATION

| | |
|---|---|
| Date of birth : | 12.05.1990 |
| Gender : | Female |
| Nationality : | French |
| Status : | Married, 2 children |
| Languages : | French – Mothertongue |
| | English – Fluent C1 (CAE) |
| | Italian – Advanced B2 |
| | German – Advanced B1 |
| | Polish – Basic Knowledge |

EDUCATION

2017 – 2022     **Doctor of Science (Ph.D.)**

Ecole Polytechnique Fédérale de Lausanne (EPFL)

Construction Materials Laboratory (LMC)

2015 – 2016     **Emmanuel School of Mission (ESM)**

Paray-le-Monial, France

Theology and human sciences

| | |
|---|---|
| 2012 – 2014 | **Master of Science in Engineering (Materials Science)**<br><br>Ecole Polytechnique Fédérale de Lausanne (EPFL) |
| 2008 - 2012 | **Bachelor of Science in Engineering (Materials Science)**<br><br>Ecole Polytechnique Fédérale de Lausanne (EPFL) |

EMPLOYMENT HISTORY

| | |
|---|---|
| 2017 – 2021 | **Doctoral, Master and Bachelor courses teacher**<br><br>Alkali-Silica Reaction<br><br>Practical Work : Wood, Concrete casting, Concrete Hardening<br><br>Linear Algebra |
| 2014 - 2015 | **Scientific Collaborator**<br><br>Haute Ecole Spécialisée Bernoise d'Architecture, Bois et Génie Civil (BFH) |
| 2013 | **Intern for the company Corbat**<br><br>Haute Ecole Spécialisée Bernoise d'Architecture, Bois et Génie Civil (BFH) |
| 2013 | **Practical work Teacher**<br><br>Ecole Polytechnique Fédérale de Lausanne (EPFL)<br><br>Forging and precipitation Hardening in Metallurgy |

PUBLICATIONS

| | |
|---|---|
| In preparation | **Barbotin S**., Boehm-Courjault E., Scrivener K. The effect of SCM addition on ASR early-stage product formation. |
| In preparation | **Barbotin S**., Boehm-Courjault E., Leemann A., Scrivener K. Early-stage ASR products evaluation in laboratory concrete samples and comparison with field samples. To be submitted to *Cement and Concrete Research.* |

2021      Geng G., **Barbotin S.**, Shakoorioskooie M., Shi Z., Leemann A., Sanchez D. F., Grolimund D., Wieland E. & Dähn R. (2021). An in-situ 3D micro-XRD investigation of water uptake by alkali-silica-reaction (ASR) product. *Cement and Concrete Research*, *141*, 106331.

**Barbotin S**., Shi Z., Boehm-Courjault E., Leemann A., Scrivener K. (2021) Characterization of synthetic ASR products by TEM and comparison with on-field early stage ASR products. *16th International Conference on Alkali Aggregate Reaction in Concrete – ICAAR 2020-22, Lisboa, Portugal.*

2020      Boehm-Courjault E., **Barbotin S.**, Leemann A., & Scrivener K. (2020). Microstructure, crystallinity and composition of alkali-silica reaction products in concrete determined by transmission electron microscopy. *Cement and Concrete Research, 130, 105988.*

2019      **Barbotin S.**, Boehm-Courjault E., Leemann A., Scrivener K. (2019) Characterization of initial ASR products by SEM, FIB and STEM-EDX. *17th EMABM May 20-23, Toronto, Canada.*

2018      **Barbotin S.**, Boehm-Courjault E., Leemann A., Scrivener K. (2018) Characterization of ASR early stage reaction product using STEM-EDX and electron diffraction. *38th Cement and Concrete Science Conference, 10-11 September, Coventry, UK.*

INTERESTS

Volleyball, sailing/windsurfing

Scouting

Drawing & painting

Philosophy/psychology